



# Processes controlling the distribution of dissolved silicon isotopes ( $\delta^{30}\text{Si}$ ) in the Atlantic and the Southern Ocean

Nathalie Coffineau

## ► To cite this version:

Nathalie Coffineau. Processes controlling the distribution of dissolved silicon isotopes ( $\delta^{30}\text{Si}$ ) in the Atlantic and the Southern Ocean. Other. Université de Bretagne occidentale - Brest, 2013. English. NNT : 2013BRES0067 . tel-01630072

**HAL Id: tel-01630072**

**<https://theses.hal.science/tel-01630072>**

Submitted on 7 Nov 2017

**HAL** is a multi-disciplinary open access archive for the deposit and dissemination of scientific research documents, whether they are published or not. The documents may come from teaching and research institutions in France or abroad, or from public or private research centers.

L'archive ouverte pluridisciplinaire **HAL**, est destinée au dépôt et à la diffusion de documents scientifiques de niveau recherche, publiés ou non, émanant des établissements d'enseignement et de recherche français ou étrangers, des laboratoires publics ou privés.



université de bretagne  
occidentale



**THÈSE / UNIVERSITÉ DE BRETAGNE OCCIDENTALE**

*sous le sceau de l'Université européenne de Bretagne*

pour obtenir le titre de

**DOCTEUR DE L'UNIVERSITÉ DE BRETAGNE OCCIDENTALE**

*Mention : Chimie Marine*

**École Doctorale des Sciences de la Mer**

présentée par

**Nathalie COFFINEAU**

Préparée à l'Unité Mixte de Recherche 6539

Laboratoire de l'Environnement Marin (LEMAR)

Institut Universitaire Européen de la Mer (IUEM)

# "Processus contrôlant la distribution des isotopes du silicium dissous ( $\delta^{30}\text{Si}$ ) dans l'océan Atlantique et Indien"

**Thèse soutenue le 13 décembre 2013**

devant le jury composé de :

**Pascal Claquin**

Professeur, FRE 3484 CNRS BioMEA, Université de Caen Basse Normandie, France  
/ *rapporteur*

**Bernard Quéquiner**

Professeur, UMR 6535 CNRS, Université de la Méditerranée, Marseille, France /  
*rapporteur*

**Aude Leynaert**

Chercheur, LEMAR IUEM, Brest, France / *examinatrice*

**Dieter Wolf-Gladrow**

Professeur, Alfred Wegener Institute, Allemagne / *examinateur*

**Christina De La Rocha**

Professeur, LEMAR IUEM UBO Brest, France / *directrice de thèse*

**Philippe Pondaven**

Maitre de conférence, LEMAR IUEM, Brest, France / *encadrant*





université de bretagne  
occidentale



**PhD / UNIVERSITY OF BREST**

*Under the seal of European University of Brittany*

To obtain the title of

**DOCTOR OF UNIVERSITY OF BREST**

*Subject : Marine chemistry*

**Doctoral school of Marine Science**

Defended by

**Nathalie COFFINEAU**

Presented to Unité Mixte de Recherche 6539

Laboratory of marine environmental sciences (LEMAR)

European Institute of Marine Studies (IUEM)

# "Processes controlling the distribution of dissolved silicon isotopes ( $\delta^{30}\text{Si}$ ) in the Atlantic and the Southern Ocean"

**PhD defended 13<sup>th</sup> December 2013**

In the presence of the jury members:

**Pascal Claquin**

Professor, FRE 3484 CNRS BioMEA, University of Caen Basse Normandie, France  
/ *reporter*

**Bernard Quéquiner**

Professor, UMR 6535 CNRS, University of Marseille, France / *reporter*

**Aude Leynaert**

Researcher, LEMAR IUEM, Brest, France / *examiner*

**Dieter Wolf-Gladrow**

Professor, Alfred Wegener Institute, Germany / *examiner*

**Christina De La Rocha**

Professor, LEMAR IUEM UBO Brest, France / PhD supervisor

**Philippe Pondaven**

Senior lecturer, LEMAR IUEM, Brest, France / supervisor







*To my amazing family...*

# Acknowledgment

First of all I want to warmly thank Christina De La Rocha for welcoming me into LEMAR and for giving me the chance to tackle this PhD. I learned a lot about the crazy world of silicon isotopes, patience in the clean lab and the English language thanks to you. Thank you for your good mood and your jokes, for being available each time I needed it, for your good advice all the time, for being patient and passionate about science, and for being understanding and open-minded. Thanks for the nice and funny discussions we had while waiting in the Neptune room and also out of the lab, it was really nice to discover you out of work.

Secondly I want to warmly thank Philippe Pondaven for being my 2<sup>nd</sup> supervisor. Thank you for being so kind, patient and comprehensive. You were there and available each time I needed it and you taught me a lot about modelling. Thank you for your eternal good mood and your positive energy.

I want to give a lot of thanks to Manu, Yoan, Claire, Céline and Arnaud for their great help in the clean lab, with the Neptune and for their help with column protocols.

I especially want to thank Fred Jean for advising me to register at the university after the master's degree. Thanks to him I remained in science and succeeded to obtain a PhD.

And I would like to thank the people who shared these 3 years with me in Brest, in France or abroad:

I would like to massively thank Louis, Céline, Angélique, Marie, Cécile, Pieter, Aurélien and Anaïs for being such amazing friends! We shared crazy good times in Brest, good as well as bad. Without you guys nothing would have been possible. You made my time in Brest a really great and special moment I will never forget! "I gotta feeling that tonight's gonna be a good night".

I would like to extend a special thanks to the "women team": Morgane, Aurore, Mathilde, Clemence and the 2 Virginie for all lunches, fun, discussions, beach sessions and walk we shared!

Thank you Flora, Bérengère, Estelle, Stefan,... Team Geology for the nice times, Sunday coffees, great parties and more that we shared in Brest and your happiness.

Thank you Thomas, Violette, Julia, Fabien, Marie, Gaspard and Manon for being the best officemates and even more! Thank you for your joy, for the nice and fun time we shared in the office and outside, for coffee breaks and the discussions we had.

Thank you Aurélie and Morgane for your big smile, your kindness and our nice long discussions. Thank you Ffi for your happiness, craziness and positive energy. You helped me a lot.

Thanks to my friends who were with me during these 3 years: Christelle, Clarice, Kati, Mathieu, Morgan, Guillaume, Philou, Sandrine, Isaure... and anyone I have momentarily overlooked!

I want to very especially thank Riri, Ben and p'tite sirène for being such amazing friends with and from whom I had fun, good advice, crazy chats and help even if we were collectively scattered across all France during the time of my PhD.

I finally want to warmly thank the best: my amazing family "Les p'tit Coff"! You were my main support, always positive, comprehensive, amazing with me, helpful even if I was really hard to understand. I feel grateful for who you are.

## Abstract

### **Processes controlling the distribution of dissolved silicon isotopes ( $\delta^{30}\text{Si}$ ) in the Atlantic and the Southern Ocean.**

Use of silicon isotopes ( $\delta^{30}\text{Si}$ ) as a paleoceanographic proxy requires sound knowledge of the distribution and behaviour of silicon isotopes throughout the ocean. Over the past few years considerable effort has been made to map the silicon isotope composition ( $\delta^{30}\text{Si}$ ) of silicic acid (dissolved silicon, DSi) and biogenic silica (BSi) throughout the ocean.

Diatoms uptake DSi to build up their opal frustules (BSi). During this process, diatoms discriminate against the heavier isotope of silicon ( $^{30}\text{Si}$ ) in favor of the light isotope ( $^{28}\text{Si}$ ). This fractionation leads to BSi that has a lower  $\delta^{30}\text{Si}$  than the DSi source by 1.1 ‰ to 1.5 ‰. In turn, this results in surface waters with low DSi concentrations due to biological removal, and high  $\delta^{30}\text{Si}$  values due to Rayleigh distillation. Conversely, when the BSi dissolves it is with discrimination against the heavier isotope producing dissolved silicon with a  $\delta^{30}\text{Si}$  lower by 0.55 ‰. At the same time, episodes of upwelling occurring throughout the growing season, ocean circulation and mixing, contribute to modify the  $\delta^{30}\text{Si}$  of the dissolved silicon pool in the surface mixed layer, which complicate the use of diatom  $\delta^{30}\text{Si}$  as a proxy for DSi removal during the growing season.

This dissertation aims to better understand the processes driving the Si cycle and the  $\delta^{30}\text{Si}$  signature of water masses in different regions of the ocean. New data of  $\delta^{30}\text{Si}$  of dissolved Si are presented and discussed. These data come from 6 CTD profiles from ANTXXIII/9 campaign (Atlantic and Indian sector of the Southern Ocean), 7 CTD profiles from ANTXXIV/3 (Atlantic sector of the Southern Ocean), and 5 CTD profiles from the campaign MSM10/1 (north Subtropical and Tropical Atlantic Ocean). Samples were purified by ion-exchange chromatography following preconcentration via  $\text{Mg}(\text{OH})_2$  precipitation and extraction of silicon using triethylamine molybdate. Isotopic analyses were carried on a Neptune MC-ICP-MS at medium resolution (Ifremer, Brest).

During this PhD I attempted to understand:

#### ✓ **What processes affect the silica biogeochemical cycle and $\delta^{30}\text{Si}$ in the region of the Kerguelen Plateau**

The key driver of the early autumn decrease in  $\delta^{30}\text{Si}$  appears to be the switch from bloom growth to steady state growth. Secondly, fractionation during dissolution had only a minor effect on the  $\delta^{30}\text{Si}$  of BSi exported throughout the course of the year, implying that seasonal changes in export efficiency strongly influence the  $\delta^{30}\text{Si}$  of BSi accumulating in marine sediments. Finally, the way the mixing between the mixed layer and the winter water is set up (in terms of  $\delta^{30}\text{Si}$ , i.e. constant or variable) is critical to the results of box model simulations of the silica biogeochemical cycle. Altogether, these results suggest that, as a paleoceanographic proxy,  $\delta^{30}\text{Si}$  may more reflect the dominant mode of production of the BSi that is exported (i.e. bloom versus steady state growth) rather than strictly the extent of DSi utilization by diatoms.

#### ✓ **What does the distribution of the $\delta^{30}\text{Si}$ in the deep water masses in the Atlantic Ocean and in the Atlantic sector of the Southern Ocean look like**

The deep and bottom water masses in the Weddell Gyre were homogeneous for DSi concentration and  $\delta^{30}\text{Si}_{\text{DSi}}$  at the time of the sampling. The bottom water masses were characterized by low  $\delta^{30}\text{Si}_{\text{DSi}}$  of 1.1 ‰, slightly lower than the  $\delta^{30}\text{Si}_{\text{DSi}}$  of 1.2 ‰ found in the deep ACC. The influence of NADW on UCDW was observed both in the Drake Passage and at the 0° meridian for the  $\delta^{30}\text{Si}_{\text{DSi}}$ . Our data support the proposed  $\delta^{30}\text{Si}_{\text{DSi}}$  gradient in the deep water masses of high  $\delta^{30}\text{Si}_{\text{DSi}}$  ( $\geq 1.7$  ‰) for NADW in the northern North Atlantic Ocean and the low  $\delta^{30}\text{Si}_{\text{DSi}}$  (1.2 ‰) for the AABW recorded in the Southern Ocean.

## Résumé

### Processus contrôlant la distribution des isotopes du silicium dissous ( $\delta^{30}\text{Si}$ ) dans l'océan Atlantique et Indien.

L'utilisation des isotopes du silicium ( $\delta^{30}\text{Si}$ ) comme proxy paléocéanographique nécessite une bonne connaissance de la répartition et du devenir des isotopes du silicium à travers l'océan. Au cours des dernières années, des efforts considérables ont été faits pour cartographier la composition isotopique du silicium dissous (acide silicique, DSi) et de la silice biogénique (BSi) dans l'océan.

Les diatomées utilisent le DSi pour construire leur frustule fait d'opale (BSi). Durant ce processus, les diatomées discriminent l'isotope lourd de silicium ( $^{30}\text{Si}$ ) en faveur de l'isotope léger ( $^{28}\text{Si}$ ). Ce fractionnement conduit à une BSi qui a un  $\delta^{30}\text{Si}$  inférieur de 1,1 ‰ à 1,5 ‰ par rapport au DSi source. Cela se traduit dans les eaux de surface par de faibles concentrations en DSi en raison de l'utilisation biologique et par des valeurs de  $\delta^{30}\text{Si}$  élevées en raison de la distillation de Rayleigh. Inversement, lorsque la BSi se dissout, il y a une discrimination contre l'isotope lourd et ainsi produit du silicium dissous avec un  $\delta^{30}\text{Si}$  inférieur de 0,55 ‰. Dans le même temps, la circulation océanique et le mélange vertical contribuent à modifier le  $\delta^{30}\text{Si}$  du pool de silicium dissous dans la couche de surface, ce qui complique l'utilisation du  $\delta^{30}\text{Si}$  des diatomées comme proxy pour l'utilisation du DSi durant la saison de croissance.

Cette thèse vise à mieux comprendre les processus qui régissent le cycle du silicium et la signature en  $\delta^{30}\text{Si}$  des masses d'eau dans les différentes régions de l'océan. De nouvelles données de  $\delta^{30}\text{Si}$  de silicium dissous sont présentées et discutées. Ces données proviennent de 6 profils CTD de la campagne ANTXXIII/9 (Atlantique et secteur indien de l'océan Austral), 7 profils CTD de la campagne ANTXXIV/3 (secteur Atlantique de l'océan Austral), et 5 profils CTD de la campagne MSM10/1 (région subtropical et tropical de l'océan Atlantique nord).

Les échantillons ont été purifiés par chromatographie échangeuse d'ions après préconcentration par précipitation de  $\text{Mg}(\text{OH})_2$ , et le silicium est extrait en utilisant du triéthylamine molybdate. Les analyses isotopiques ont été réalisées sur Spectromètre de Masse Multi-Collection à source Plasma (MC-ICP-MS, Naptune) à moyenne résolution (Ifremer, Brest).

Pendant cette thèse j'ai essayé de comprendre :

- ✓ Quels processus affectent le cycle biogéochimique du silicium et le  $\delta^{30}\text{Si}$  dans la région du plateau des Kerguelen ?

Pour cela, un modèle en boîte à été réalisé pour tenter de reproduire le cycle du silicium (concentrations et  $\delta^{30}\text{Si}$ ) de cette région. Le principal facteur de la baisse du  $\delta^{30}\text{Si}$  en début d'automne semble être le passage d'une croissance par efflorescence à une croissance à l'état d'équilibre. Deuxièmement, le fractionnement, lors de la dissolution, a seulement un effet mineur sur le  $\delta^{30}\text{Si}$  de la BSi exportée durant l'année, ce qui implique que les changements saisonniers dans l'efficacité d'exportation influencent fortement le  $\delta^{30}\text{Si}$  de la BSi accumulée dans les sédiments marins. Enfin, la façon dont le mélange entre la couche de mélange et l'eau d'hiver est prit en compte (en termes de  $\delta^{30}\text{Si}$ , soit constant ou variable) est cruciale pour les résultats de simulations de modèle en boîte du cycle biogéochimique du silicium. Finalement, ces résultats suggèrent que, en tant que proxy paléocéanographique le  $\delta^{30}\text{Si}$  refléterait plus le mode dominant de production de la BSi qui est exportée (i.e. bloom par rapport une croissance à l'état d'équilibre), plutôt que le strict degré d'utilisation du DSi par les diatomées.

- ✓ A quoi ressemble la distribution du  $\delta^{30}\text{Si}$  dans les masses d'eau de l'océan Atlantique et dans le secteur Atlantique de l'océan Indien ?



Les masses d'eau de fond et profonde de la gyre de Weddell sont homogènes en termes de concentration en DSi et  $\delta^{30}\text{Si}$  au moment de l'échantillonnage. Les masses d'eau de fond ont été caractérisées par un faible  $\delta^{30}\text{Si}$  de 1,1 ‰, légèrement inférieur au  $\delta^{30}\text{Si}$  de 1,2 ‰ trouvé dans les eaux de fond du courant circumpolaire antarctique (ACC). L'influence de l'eau de fond Nord Atlantique (NADW) par l'eau de fond circumpolaire (UCDW) a été observée à la fois dans le passage de Drake et au niveau du méridien de Greenwich pour le  $\delta^{30}\text{Si}$ . Nos données confirment la présence du gradient de  $\delta^{30}\text{Si}$  dans les masses d'eau profondes ; gradient déjà proposé et décrit par de fort  $\delta^{30}\text{Si}_{\text{DSi}}$  ( $\geq 1,7$  ‰) pour l'eau de fond Nord Atlantique (NADW) dans le nord de l'océan Atlantique Nord et par de faible  $\delta^{30}\text{Si}_{\text{DSi}}$  (1,2 ‰) pour l'eau de fond antarctique (AABW) enregistré dans l'océan Austral.



# Summary

<b>CHAPTER 1 – INTRODUCTION .....</b>	<b>1</b>
I    SILICA CYCLE.....	2
I.1    General.....	2
I.2    The silicon input pathways to the ocean .....	3
I.3    Dissolved silicon and biogenic silica in the oceans .....	5
I.4    Diatoms as conductors of the marine silica cycle .....	7
II   ISOTOPE SYSTEMATICS.....	14
II.1    The silicon isotope system .....	14
II.2    Silicon isotopes in different environments.....	15
<b>CHAPTER 2 – METHODS AND ANALYTICAL TECHNIQUES .....</b>	<b>22</b>
I    SAMPLE PREPARATION .....	23
I.1    Determination of DSi concentration.....	23
I.2    Magnesium induced coprecipitation (MAGIC).....	24
I.3    Tri-ethylamine molybdate coprecipitation (TEA-moly).....	24
I.4    Sample preparation for mass spectrometry.....	25
II   MASS SPECTROMETRY .....	26
II.1    Sample dilution.....	26
II.2    Multi-Collector - Inductive Coupled Plasma Mass Spectrometry.....	27
II.3    Performance of a MC-ICP MS .....	28
II.4    Measurement conditions.....	31
II.5    Data validation .....	32
<b>CHAPTER 3 – EXPLORING INFLUENCES ON THE SILICON ISOTOPIC COMPOSITION OF THE SURFACE OCEAN: A CASE STUDY FROM THE KERGUELEN PLATEAU .....</b>	<b>35</b>
<b>CHAPTER 4 – SILICON ISOTOPIC COMPOSITION (<math>\Delta^{30}\text{Si DSI}</math>) OF WATER MASSES IN THE ATLANTIC OCEAN .....</b>	<b>59</b>
I    AN OVERVIEW OF LARGE SCALE CIRCULATION IN THE ATLANTIC OCEAN .....	61
I.1    The Atlantic Ocean .....	61
I.2    The water masses of the North Atlantic Ocean.....	62
I.3    The Southern Ocean water masses circulation.....	65
II   SILICON ISOTOPIC COMPOSITION ( $\Delta^{30}\text{Si DSI}$ ) OF WATER MASSES IN THE ATLANTIC OCEAN.....	68
II.1    Introduction.....	68
II.2    Materiel and Method .....	70
II.3    Results .....	78
II.4    Discussion .....	85
II.5    Global Atlantic Ocean.....	92
II.6    Conclusion .....	94
<b>CONCLUSIONS AND PERSPECTIVES.....</b>	<b>97</b>
<b>BIBLIOGRAPHY .....</b>	<b>103</b>
<b>APPENDIX.....</b>	<b>114</b>
<b>PARTICIPATION AT CONFERENCES .....</b>	<b>122</b>
<b>CURRICULUM VITAE .....</b>	<b>126</b>





## Figure list

### Chapter 1: Introduction – General context

**Figure 1.1** The steady state biogeochemical cycle of silica (Tréguer and De La Rocha, 2013) (adapted from Tréguer et al. (1995)). The dotted line represents the limit between the estuaries and the ocean. Gray arrows represent fluxes of DSi and black arrows represent fluxes of BSi; all fluxes are in teramoles of silicon per year. Abbreviations:  $FR_{(gross)}$ : gross river inputs,  $FR_{(net)}$ : net river inputs,  $F_{RW}$ : BSi deposits and reverse weathering in estuaries,  $F_{GW}$ : groundwater flux,  $F_A$ : aeolian inputs,  $F_H$ : hydrothermal inputs,  $F_W$ : seafloor weathering inputs,  $FP_{(gross)}$ : BSi gross production,  $F_{D(surface)}$ : flux of DSi recycled in the surface reservoir,  $F_{E(export)}$ : flux of BSi exported toward the deep reservoir,  $F_{D(deep)}$ : flux of DSi recycled in deep waters,  $F_{D(benthic)}$ : flux of DSi recycled at the sediment-water interface,  $F_{S(rain)}$ : flux of BSi that reaches the sediment-water interface,  $F_{upw/ed}$ : flux of DSi transferred from the deep reservoir to the surface mixed layer (upwelling, eddy diffusion),  $F_{B(netdeposit)}$ : net deposit of BSi in coastal and abyssal sediments,  $F_{sp}$ : net sink of BSi in sponges on continental shelves. ....3

**Figure 1.2** Longitudinal section across the entire Atlantic Ocean (top panel) and Pacific Ocean (bottom panel) of the DSi concentration versus depth (eWOCE, Schlitzer, 2000). ....5

**Figure 1.3** Nutrient concentrations (Si, N) from the Southern Ocean to low latitudes. Conceptual diagram depicting the Southern Ocean physical and biological processes that form low-Si\* waters and feed them into the global thermocline. Water flow is depicted on top and the detail of the surface processes at the bottom. CDW: Circumpolar Deep Water, AAIW: Antarctic Intermediate Water, SAMW: Subantarctic Mode Water, APF: Antarctic Polar Front, PFZ: Polar Front Zone, SAF: Subantarctic Front, SAZ: Subantarctic Zone, STF: Subtropical Front, from Sarmiento (2004). ....6

**Figure 1.4** Schematic structure of the diatom cell (center) and diatom cell cycle (shown in cross section). In grey: the protoplast, green line: the plasma membrane. For simplicity, intracellular organelles other than the Silica Deposition Vesicle (SDV) are not shown. Cell cycle: (1) Shortly before cell division the cell wall contains the maximum number of girdle bands, (2) immediately after cytokinesis new biosilica (*red*) is formed in each sibling cell inside a valve SDV (*yellow*), (3) expansion of the valve SDVs with increasing silica deposited, (4) at the final stage of valve SDV development, each SDV contains a fully developed valve, (5) the newly formed valves are deposited in the cleavage furrow on the surface of each protoplast by SDV exocytosis, (6) the sibling cells have separated, (7+8) expansion of the protoplast in interphase requires the synthesis of new silica (*red*) inside girdle band SDVs (*yellow*), each girdle band is synthesized in a separate SDV, and after SDV exocytosis is added to the newly formed valve (hypovalve), (9) after synthesis of the final hypovalve girdle band (pleural band) cell expansion stops, and DNA replication is initiated (Kröger and Poulsen, 2008). ....9

**Figure 1.5** Range of  $\delta^{30}Si$  variations at the surface of the Earth in relation to rock-forming processes [1, water-rock interactions [2], biological processes [3], water reservoirs [4] (Opfergelt and Delmelle, 2012 and references therein). .... 16

**Figure 1.6** Typical profile of  $\delta^{30}Si_{DSi}$  and DSi concentration versus depth in marine environment (data from this PhD). Blue diamonds are  $\delta^{30}Si_{DSi}$  values and orange diamonds are the corresponding DSi concentrations. .... 17

**Figure 1.7** Representation of the Rayleigh distillation model (solid lines) and the Steady state model (dotted lines). f: remaining fraction, blue: DSi, green: BSi and grey: BSi accumulation in the system. 18

**Figure 1.8** Representation of the South Atlantic sediment core RC13-269 (52°38' S, 00°08' W, 2,591 mbsl) for the A)  $\delta^{30}\text{Si}$  evolution versus depth, error bars on  $\delta^{30}\text{Si}$  represent standard error on 2–3 separate measurements, the arrow indicates the Last Glacial Maximum (LGM) and B) BSi against depth. The percentage opal (P. N. Froelich, unpublished data) was determined through extraction into a sodium carbonate solution 32. Modified from De La Rocha et al. (1998). ..... 19

## Chapter 2: Method and analytical techniques

**Figure 2.1** Protocol for DSi precipitation via TEA-moly and extraction ..... 25

**Figure 2.2** A) Neptune (Thermo Fisher Scientific), B) Main parts of the Neptune, the Inductively Coupled Plasma module (ICP Module), the Electrostatic Analyzer module (ESA Module) and the Multi-collector module ([wwz.ifremer.fr/neptune](http://wwz.ifremer.fr/neptune)). ..... 27

**Figure 2.3** Samples measurement of the ratio  $\delta^{29}\text{Si}$  vs.  $\delta^{30}\text{Si}$  for A) ANTXXIII/9 campaign, B) ANTXXIV/3 campaign and C) MSM10/1 campaign, along the fractionation line  $\delta^{30}\text{Si} = 1.93 \cdot \delta^{29}\text{Si}$ . Each session on the MC-ICPMS is represented by a different colour, standard deviation ( $1\sigma$ ). ..... 33

## Chapter 4: The silicon isotopic composition ( $\delta^{30}\text{Si}$ ) of water masses in Atlantic Ocean

**Figure 4.1** The great conveyor belt. Representation of warm surface currents (red), cold deep currents (blue) and bottom currents (purple). Circles: sites of deep water formation, white zones: salinity < 34, dark blue: salinity > 36 psu, (Kuhlbrodt et al., 2007). ..... 61

**Figure 4.2** Map of the Subtropical and Tropical North Atlantic Ocean circulation. The dashed and dotted line represent the Cape Verde Frontal Zone (CVFZ), the North Equatorial Current (NEC), the northern band of the South Equatorial Current (nSEC), the North Equatorial Countercurrent (NECC) and around the Guinea Dome is found the northern NECC (nNECC) as labelled on the plot (Stramma et al., 2005). ..... 63

**Figure 4.3** A schematic view of the map of meridional overturning circulation in the Southern Ocean (Speer et al., 2000; Dong, 2012). SAMW is the surface water, AAIW is the Antarctic Intermediate Water, UCDW is Upper circumpolar Deep Water, NADW is North Atlantic Deep Water, LCDW is Lower Circumpolar Deep Water and AABW is Antarctic Bottom Water. .... 65

**Figure 4.4** Mean solution composition showing concentration (greater than 50%) of all source water types along Section 1 of ANT-XXIII/3 in the Drake Passage. Gray colour represents a mixing of SWTs without major contribution of any SWT (white contours represent neutral density values) (Sudre et al., 2011). ..... 66

**Figure 4.5** Section along the prime meridian in the Southern Ocean and in the Weddell Gyre showing potential temperature ( $\theta(^{\circ}\text{C})$ ) and the generalized locations and movements of various water masses. The region between 40°S and 55°S represents the Antarctic Circumpolar Current (ACC). The region from 55°S to 70°S represents the actual Weddell Gyre. AAIW: Antarctic Intermediate Water, NADW: North Atlantic Deep Water, CDW: Circumpolar Deep Water, AABW: Antarctic Bottom Water, SHALLOW: the shallowest 200m of the water column, WDW: Warm Deep Water, WSDW: Weddell Sea Deep Water and WSBW: Weddell Sea Bottom Water (van Heuven et al., 2011). ..... 67

**Figure 4.6** Sampling locations of the two campaigns used in this study. Green dots indicate stations sampled in the Subtropical and Tropical Atlantic Ocean (MSM10/1 campaign) and red dots indicate stations sampled in the Southern Ocean (ANTXXIV/3 campaign). Stations from which samples were analysed are encircled and numbered (Schlitzer, R., Ocean Data View, <http://odv.awi.de>, 2013)..... 71

**Figure 4.7** Temperature–salinity depth profiles of stations from ANTXXIV/3 campaign. A) Full depth profiles, B) zoom in on stations (146, 189 and 211) in the Weddell Gyre. Modified from Mackensen (2001). ..... 73

**Figure 4.8** Longitudinal transect through Weddell Gyre realized with data from ANTXXIV/3 campaign. Our stations 211 and 189 are indicated by vertical lines. Thin horizontal lines indicate temperature boundaries. Salinity colour maps were created with ODV (Schlitzer, Ocean Data View, <http://odv.awi.de>, 2013) using data from ANTXXIV/3 campaign. ASW: Antarctic Surface Water, MWDW: Modified Warm Deep Water, WDW: Warm Deep Water, WSDW: Weddell Sea Deep Water and WSBW: Weddell Sea Bottom Water. .... 74

**Figure 4.9** Latitudinal transect of Drake Passage realized with data from ANTXXIV/3 campaign. Our stations 248 and 226 are indicated by vertical lines. Thin horizontal lines indicate salinity boundaries. Potential temperature colour maps were created with ODV (Schlitzer, Ocean Data View, <http://odv.awi.de>, 2013) using data from ANTXXIV/3 campaign. SASW: Subantarctic surface Water, SAMW: Subantarctic Mode Water, AAIW: Antarctic Intermediate Water, SPDSW: Southeast Pacific Deep Slope Water, UCDW: Upper Circumpolar Deep Water, LCDW: Lower Circumpolar Deep Water, SPDW: Southeast Pacific Deep Water, WSDW: Weddell Sea Deep Water. .... 75

**Figure 4.10** Latitudinal transect on the 0° meridian realized with data from ANTXXIV/3 campaign. Our stations 106, 115 and 146 are indicated by vertical lines. Thin horizontal lines indicate temperature boundaries. Salinity colour maps were created with ODV (Schlitzer, Ocean Data View, <http://odv.awi.de>, 2013) using data from ANTXXIV/3 campaign. .... 76

**Figure 4.11** Temperature – Salinity diagram for Atlantic Ocean water masses. Coloured lines indicate stations sampled during MSM10/1 campaign: station 1 (green), 2 (red), 3 (pink), 4 (brown), 21 (blue). SACW: South Atlantic Central Water, wNACW and eNACW: western and eastern North Atlantic Central Water, MW: Mediterranean Water, NADW: North Atlantic Deep Water, AABW: Antarctic Bottom Water, AAIW: Antarctic Intermediate Water, WASIW and EASIW: western and eastern Atlantic Modified from Emery (2003). .... 77

**Figure 4.12** Latitudinal transect of the Subtropical and Tropical Atlantic Ocean realized with data from MSM10/1 campaign. Our stations 1, 2, 3, 4 and 21 are indicated by vertical lines. Thin horizontal lines indicate temperature boundaries. Salinity colour map was created with ODV (Schlitzer, Ocean Data View, <http://odv.awi.de>, 2013) using data from MSM10/1 campaign ..... 77

**Figure 4.13** Depth profiles of DS<sub>i</sub> concentration (A, C, E, G, I, K, M, O, Q, S, U, W) and  $\delta^{30}\text{Si}$  (B, D, F, H, J, L, N, P, R, T, V, X) for the Southern Ocean (ANTXXIV/3 campaign, A to N) and for the tropical and subtropical Atlantic Ocean (MSM 10/1, O to X). Stations 226 and 248 were located in the Drake Passage; 248 was part of the Antarctic Circumpolar Current (ACC); 211, 189 and 146 were located in the Weddell Gyre (WG); 146 was at the edge of the WG and the ACC on the 0° meridian; and 106 and 115 were part of the ACC along the 0° meridian. Station 115 (K, L) is on a shallower depth scale (0 – 1000 m) than other stations of the Southern Ocean. Stations 1, 2 and 3 were north of the Cape Verde Frontal Zone (CVFZ), and stations 4 and 21 were south of the front. The depth and DS<sub>i</sub> concentration scales for the subtropical and tropical Atlantic Ocean are smaller than the Southern Ocean..... 79

**Figure 4.14** DSi concentration versus  $\delta^{30}\text{Si}_{\text{DSi}}$  of Upper Circumpolar Deep Water (UCDW) for stations in the Antarctic Circumpolar Current (ACC) and in the Weddell Gyre. (Station 146 was not taken into account for the regression). ..... 82

**Figure 4.15** Deep water masses of the Weddell Gyre showing  $\delta^{30}\text{Si}_{\text{DSi}}$  versus longitude. Station 211 represents the western part of the gyre, 189 the central part and 146 is on the 0° meridian in the Weddell Gyre. WDW: Warm Deep Water, WSDW; Weddell Sea Deep Water and WSBW: Weddell Sea Bottom Water..... 83

**Figure 4.16** Longitudinal transect through the Weddell Gyre realized with data from the ANTXXIV/3 campaign. Our stations 211 and 189 are indicated by vertical lines that represent in the same time the  $\delta^{30}\text{Si}_{\text{DSi}}$  of 1.2 ‰ characteristic of deep water masses value in the Southern Ocean. Grey lines with diamond markers represent  $\delta^{30}\text{Si}_{\text{DSi}}$  profiles. Thin horizontal lines indicate [DSi] boundaries. DSi concentration colour map was created with ODV (Schlitzer, Ocean Data View, <http://odv.awi.de>, 2013) using data from ANTXXIV/3 campaign ..... 86

**Figure 4.17** Depth profiles until only down to 1000 m at station 146 for A) salinity, B) temperature (°C), C) DSi concentration (µM) and D)  $\delta^{30}\text{Si}_{\text{DSi}}$  (‰)..... 86

**Figure 4.18** Latitudinal transect through the Drake Passage realized with data from the ANTXXIV/3 campaign. Our stations 248 and 226 are indicated by vertical lines that represent in the same time the  $\delta^{30}\text{Si}_{\text{DSi}}$  of 1.2 ‰ characteristic of deep water masses value in the Southern Ocean. Grey lines with diamond markers represent  $\delta^{30}\text{Si}_{\text{DSi}}$  profiles. Thin horizontal lines indicate [DSi] boundaries. DSi concentration colour map was created with ODV (Schlitzer, Ocean Data View, <http://odv.awi.de>, 2013) using data from ANTXXIV/3 campaign ..... 87

**Figure 4.19** Latitudinal transect through 0° meridian realized with data from the ANTXXIV/3 campaign. Our stations 106, 115 and 146 are indicated by vertical lines that represent in the same time the  $\delta^{30}\text{Si}_{\text{DSi}}$  of 1.2 ‰ characteristic of deep water masses value in the Southern Ocean. Grey lines with diamond markers represent  $\delta^{30}\text{Si}_{\text{DSi}}$  profiles. Thin horizontal lines indicate [DSi] boundaries. DSi concentration colour map was created with ODV (Schlitzer, Ocean Data View, <http://odv.awi.de>, 2013) using data from ANTXXIV/3 campaign. .... 88

**Figure 4.20** Representation of the A) DSi concentration versus latitude and B)  $\delta^{30}\text{Si}$  versus latitude for data from intermediate and deep water masses of the Atlantic Ocean from the literature for which data for DSi concentration and  $\delta^{30}\text{Si}$  were available (de Souza et al., 2012b; Fripiat et al., 2012), including data from this study. A) Regression line:  $R^2 = 0.80$ ,  $p < 0.0001$  and  $n = 140$ , and B) Regression line:  $R^2 = 0.34$ ,  $p < 0.0001$  and  $n = 140$ . Black diamond: deep water masses, grey diamonds: intermediate water masses, both were used in the calculation of the regression lines .... 93



Table list
------------

**Chapter 2: Method and analytical techniques**

**Table 2.1** Characteristics of the MC-ICPMS Neptune (Ifremer, Brest) used for the silicon isotope measurements..... 29

Appendix list
---------------

**Appendix 1** Data information about samples from Atlantic sector and Indian sector of the Southern Ocean during the campaign ANTXXIV/9..... 115

**Appendix 2** Data information about samples from the Atlantic sector of the Southern Ocean (ANTXXIV/3 campaign, stations 146 to 248) and for samples from the Subtropical and Tropical North Atlantic Ocean (MSM10/1 campaign, stations 1 to 21) used in this thesis ..... 117

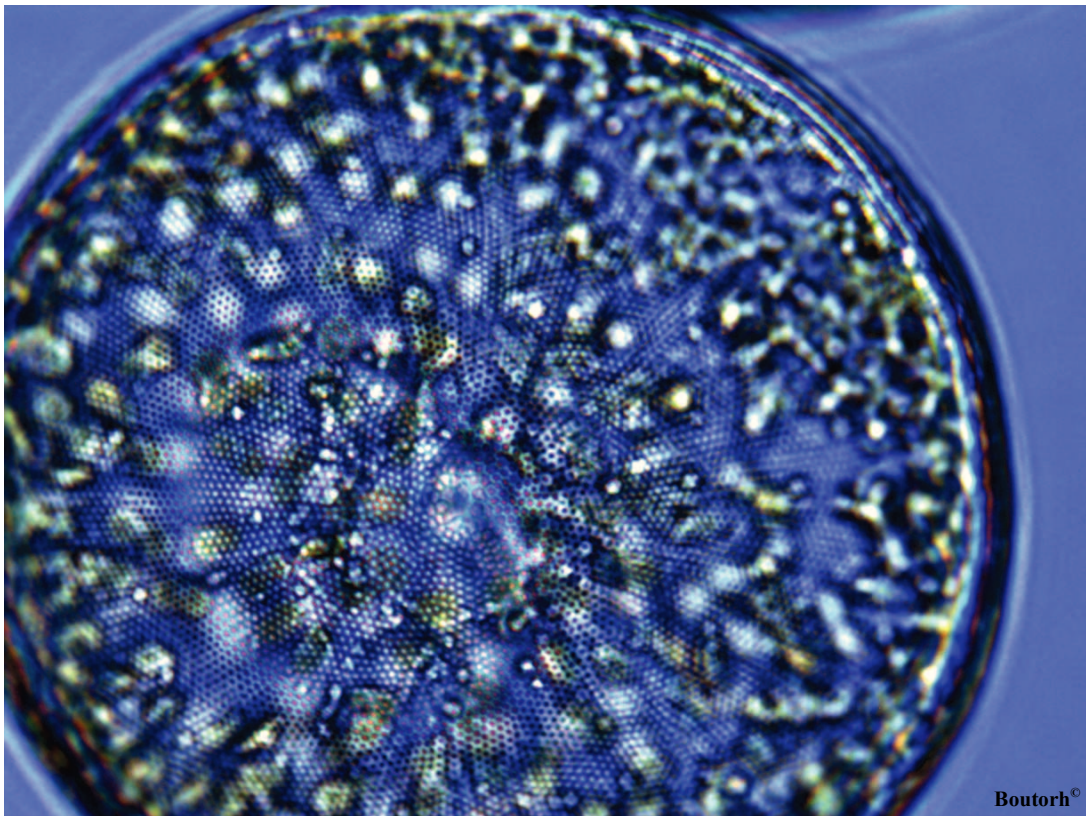


---

# Introduction - General context

## — Chapter 1 —

---



# Chapter 1 – Introduction

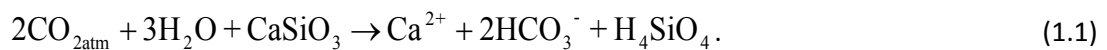
---

## I Silica cycle

### I.1 General

Even if silicon (Si) is the 2<sup>nd</sup> most abundant element of the Earth's crust (Epstein, 1999) it is mainly inaccessible for organisms as it is found in association with oxygen as quartz and silicate minerals (Laruelle et al., 2009). Its participation in terrestrial and marine biogeochemical cycles ultimately results from the weathering of silicate minerals and rocks. The weathering process releases essential nutrients, making them available to aquatic and terrestrial organisms (Ziegler et al., 2005). The release of Si during weathering to yield dissolved silicon (DSi) in soil water, groundwater, river water, and seawater leads in part to the incorporation of Si into biogenic silica (BSi), e.g., phytoliths in land plants (Ziegler et al., 2005; Cardinal et al., 2010; Opfergelt and Delmelle, 2012). The DSi released during weathering may be transported, via rivers and groundwater, to the ocean (Opfergelt and Delmelle, 2012). Some of the Si released through silicate weathering becomes incorporated into clay minerals, but silicon is still such a major element of silicate rocks that dissolved silicon is the dominant nutrient in river waters, and rivers supply roughly 80% of the silicic acid added to the ocean each year (Tréguer et al., 1995; Ziegler et al., 2005; Tréguer and De La Rocha, 2013). Silicon cycling is strongly linked to climate inasmuch that the chemical transformation of silicate rocks into solutes through weathering requires atmospheric CO<sub>2</sub> (Berner et al., 1983; Georg et al., 2007).

The dissolution of silicate minerals converts atmospheric CO<sub>2</sub> into alkalinity (carbonate and bicarbonate ions) as with the following idealized example:



This addition of alkalinity to the ocean, in turn, governs the oceanic capacity to hold dissolved CO<sub>2</sub>. At typical seawater pH (7.5 – 8.4), Si(OH)<sub>4</sub>, the undissociated form of silicic acid, is the most abundant, accounting for 97% of the dissolved silicon, with about 3% of it present as its dissociated anion, SiO(OH)<sub>3</sub><sup>-</sup>. In the long term, the solutes added to the ocean from silicate weathering are removed, for example, via the production of calcium carbonate and biogenic silica (BSi) by plankton such as diatoms, requiring silicon and the removal of these materials to the sediments (Dessert et al., 2003). Eventually these CaCO<sub>3</sub> and SiO<sub>2</sub> sediments will be subducted back into the mantle along with



ocean crust due to plate tectonics and metamorphosed back to  $\text{CO}_2$  and  $\text{CaSiO}_3$  to be emitted again later through volcanism.

## 1.2 The silicon input pathways to the ocean

According to Tréguer and De La Rocha (2013), there are four pathways for the transfer of silicon to ocean estimated to bring to the ocean  $9.4 \pm 4.7 \text{ Tmol-Si yr}^{-1}$  (Fig. 1.1).

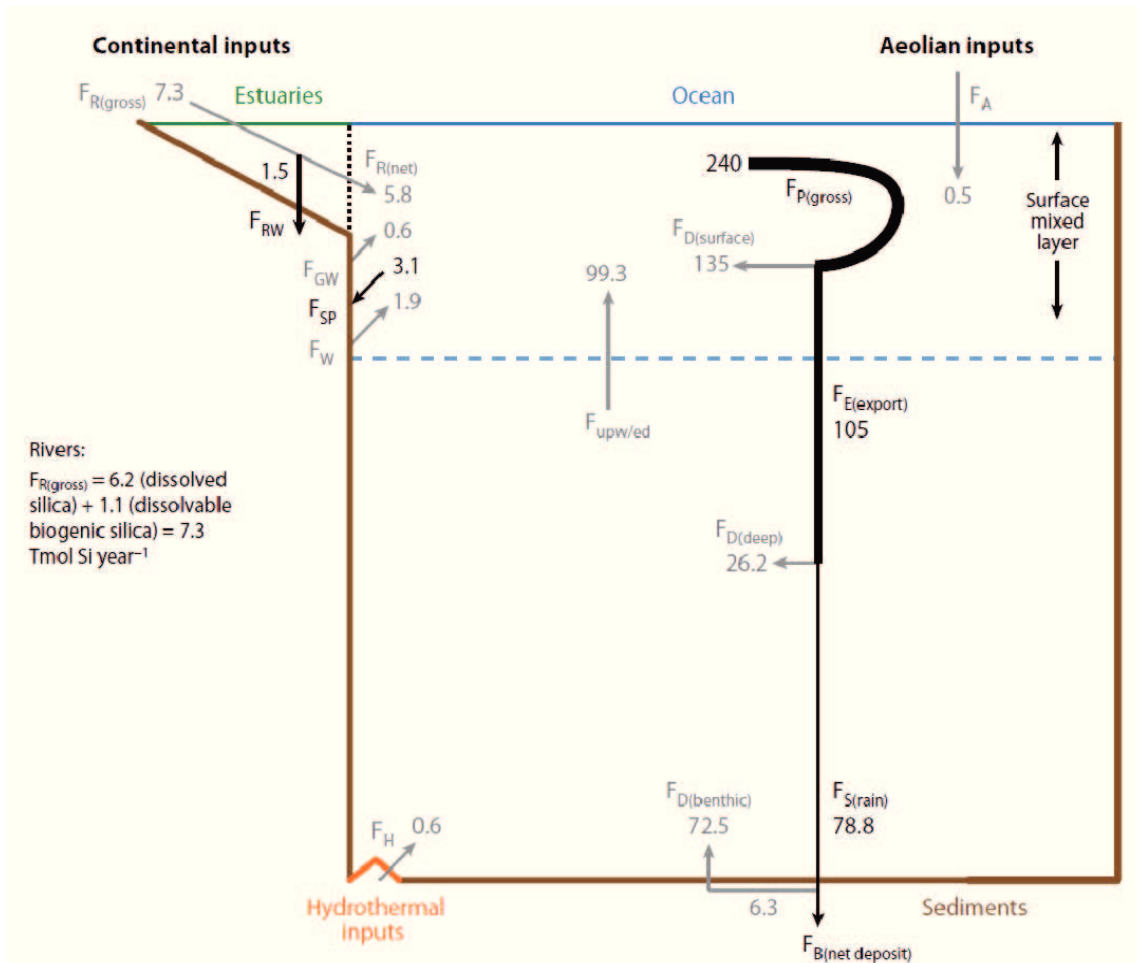


**Figure 1.1** The steady state biogeochemical cycle of silica (Tréguer and De La Rocha, 2013) (adapted from Tréguer et al. (1995)). The dotted line represents the limit between the estuaries and the ocean. Gray arrows represent fluxes of DSi and black arrows represent fluxes of BSi; all fluxes are in teramoles of silicon per year. Abbreviations:  $F_{R(gross)}$ : gross river inputs,  $F_{R(net)}$ : net river inputs,  $F_{RW}$ : BSi deposits and reverse weathering in estuaries,  $F_{GW}$ : groundwater flux,  $F_A$ : aeolian inputs,  $F_H$ : hydrothermal inputs,  $F_W$ : seafloor weathering inputs,  $F_{P(gross)}$ : BSi gross production,  $F_{D(surface)}$ : flux of DSi recycled in the surface reservoir,  $F_{E(export)}$ : flux of BSi exported toward the deep reservoir,  $F_{D(deep)}$ : flux of DSi recycled in deep waters,  $F_{D(benthic)}$ : flux of DSi recycled at the sediment-water interface,  $F_{S(rain)}$ : flux of BSi that reaches the sediment-water interface,  $F_{upw/ed}$ : flux of DSi transferred from the deep reservoir to the surface mixed layer (upwelling, eddy diffusion),  $F_{B(net deposit)}$ : net deposit of BSi in coastal and abyssal sediments,  $F_{SP}$ : net sink of BSi in sponges on continental shelves.

The main sources of Si to the ocean are rivers with an input of  $7.3 \pm 1.8 \text{ Tmol-Si yr}^{-1}$ . Rivers discharge an amount of DSi and easily soluble BSi that, after losses to clay formation (reverse

weathering) in estuarine and nearshore environments, represents 68% of the total inputs of Si to the ocean (Tréguer and De La Rocha, 2013).

The second source of DSi to the ocean comes from the seafloor (ocean crust), accounting for 20% ( $1.9 \pm 0.7 \text{ Tmol-Si yr}^{-1}$ ) of the influx of DSi. Basaltic seafloor weathering at low temperature releases DSi to the ocean. In addition, terrigenous silicates deposited on continental margins may release significant amounts of DSi (Tréguer and De La Rocha, 2013).

Hydrothermalism is the third pathway for DSi leading to an input of  $0.6 \pm 0.4 \text{ Tmol-Si yr}^{-1}$ . This represents high temperature weathering of ocean crust in association with the circulation of fluids through mid-ocean ridges. Cold seawater sinks into fissures in the ocean crust and as it sinks closer to the mid ocean ridge heat source (magma chamber), the water heats up and begins to react with the minerals it is in contact with. This leads to the considerable addition of silicon to these fluids which may then be vented at high temperature, close to the ridge axis, or emitted more diffusely at low temperatures after cooling (and probably losing much of its excess Si) during its percolation back through the ocean crust and overlying sediments. Together, both high and low temperature hydrothermal fluids entering the deep-sea account for 6% of the marine DSi input (Tréguer et al., 1995; Tréguer and De La Rocha, 2013).

Aeolian inputs are the last input of DSi. Lithogenic and biogenic Si (in the form of dust) are deposited on the ocean surface and may release some dissolved Si. Much of this dust comes from the Sahara and Gobi Deserts and yields an estimate of aeolian Si deposited of 2.8 to 4.6  $\text{Tmol-Si yr}^{-1}$  (Tegen and Kohfeld, 2006; Tréguer and De La Rocha, 2013). Dissolution rates vary greatly depending on the type of dust, and not all Si deposited as dust will become available to the phytoplankton; the available (i.e. soluble) fraction is estimated to be  $0.5 \text{ Tmol-Si yr}^{-1}$  (Tréguer et al., 1995; Tréguer and De La Rocha, 2013). These external DSi inputs total  $9.4 \text{ Tmol-Si yr}^{-1}$ , in conjunction with roughly  $99.3 \text{ Tmol-Si yr}^{-1}$  upwelled to the surface ocean from sub-thermocline waters, supporting a net BSi production of  $240 \text{ Tmol-Si yr}^{-1}$  in the surface ocean by diatoms and other silica-secreting organisms. Only 3 % of BSi produced in the oceanic surface water survives to burial in the sediment (DeMaster, 2001).

### I.3 Dissolved silicon and biogenic silica in the oceans

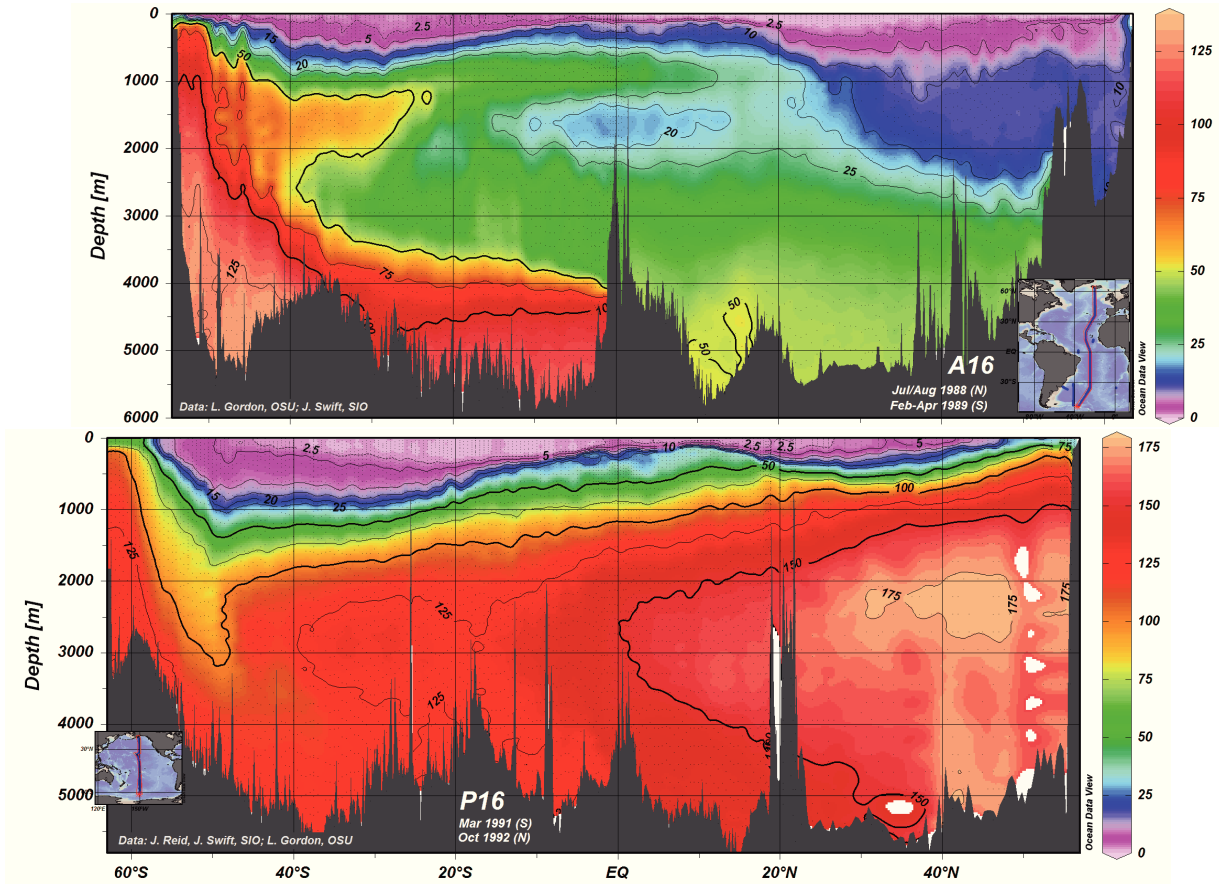


**Figure 1.2** Longitudinal section across the entire Atlantic Ocean (top panel) and Pacific Ocean (bottom panel) of the DSi concentration versus depth (eWOCE, Schlitzer, 2000).

Dissolved silicon is a major limiting nutrient in ocean for silicified organisms such as diatoms, which are a dominant phytoplankton group in the ocean (see section I.4.). Their requirement of DSi for growth (Lewin, 1962; Brzezinski et al., 1990) makes them the main actor of the marine silica cycle. The residence time for silicon in the ocean is estimated between 15 000 and 17 000 years, assuming that the silica cycle is currently at reasonably close to steady state (Tréguer and De La Rocha, 2013).

DSi is unevenly distributed in the ocean in terms of both depth and latitude (Fig 1.2). The typical depth profile shows an increase of the DSi concentration with depth. The surface ocean (euphotic zone) is affected by biological activities leading to a drop in concentration (DeMaster, 2001) to as little as a few  $\mu\text{mol-Si L}^{-1}$  in the equatorial Atlantic and Pacific Oceans (Nelson et al., 1995; Nelson and Brzezinski, 1997). In the deep ocean, DSi concentrations can reach values of  $40 \mu\text{mol-Si L}^{-1}$  in the North Tropical Atlantic Ocean to values as high as  $125 \mu\text{mol-Si L}^{-1}$  in the Atlantic sector of the Southern Ocean and  $180 \mu\text{mol-Si L}^{-1}$  in the North Pacific Ocean (DeMaster, 2001). These high concentrations in the deep ocean water are the consequence of BSi dissolution as it sinks through

the water column en route to the sediments. More than 90% of the biogenic silica is dissolved by inorganic dissolution in the column (DeMaster, 2001). This, coupled with the biological removal in surface waters, leads to a deep DSi concentration which is  $\sim 30$  times higher than the surface.

However there are disparities in the deep ocean regarding the DSi concentration (Fig. 1.2). The deep ocean concentrations are the consequence of the thermohaline circulation, commonly called the Conveyor Belt, allowing for an increase of the DSi concentration during its flow by the constant settling of dissolving siliceous particles.

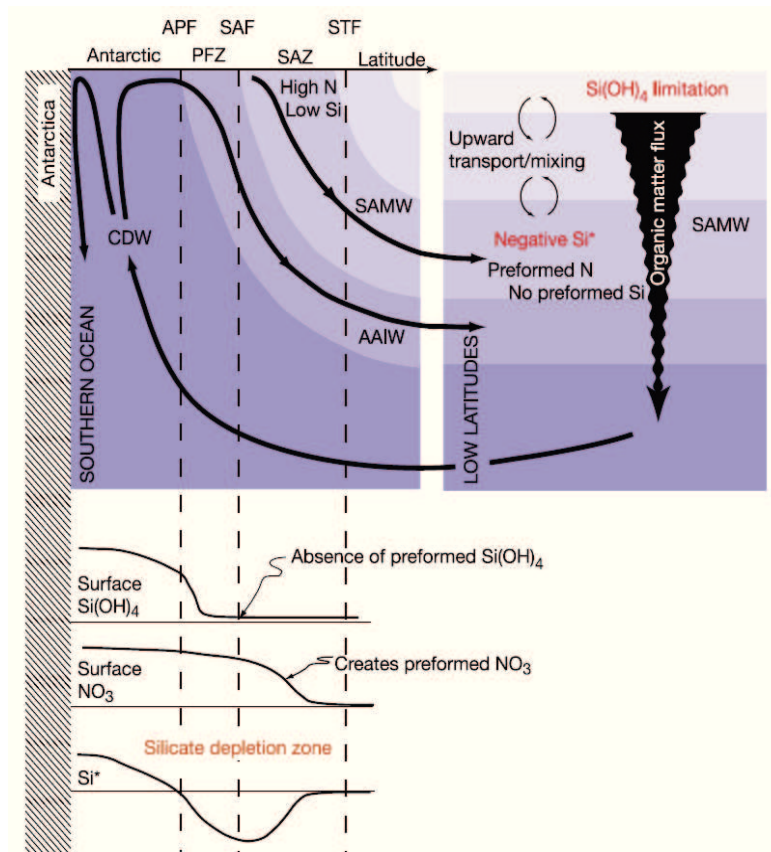


**Figure 1.3** Nutrient concentrations (Si, N) from the Southern Ocean to low latitudes. Conceptual diagram depicting the Southern Ocean physical and biological processes that form low- $\text{Si}^*$  waters and feed them into the global thermocline. Water flow is depicted on top and the detail of the surface processes at the bottom. CDW: Circumpolar Deep Water, AAIW: Antarctic Intermediate Water, SAMW: Subantarctic Mode Water, APF: Antarctic Polar Front, PFZ: Polar Front Zone, SAF: Subantarctic Front, SAZ: Subantarctic Zone, STF: Subtropical Front, from Sarmiento (2004).

The transport of DSi-rich deep and intermediate waters to the surface spurs significant silica production in the regions affected. The region south of the Antarctic Polar Front, in the Antarctic Circumpolar Current (ACC) and near the Marginal Ice Zone, are the regions of the main BSi production (Fig. 1.3) due to the upwelling of deep, nutrient-rich water (Quéguiner et al., 1991; Quéguiner et al., 1997; Brzezinski et al., 2001; Fripiat et al., 2011b). In consequence, another important region for the flow of nutrient in the Atlantic Ocean is the northern part of the ACC. In the

Polar Front zone, the deep water is upwelled to the surface and then flows northward as subantarctic mode water, carrying nutrients to the low latitudes (Sarmiento et al., 2004). Finally the North Pacific Ocean is another region of importance where general upwelling of nutrient-rich water is observed, enriching the surface with high DSi concentrations (Sarmiento et al., 2004).

Opal rich sediments are found in various locations throughout the ocean and at all depths (from the shelf to the abyss) (Ragueneau et al., 2000). However, the Southern Ocean is the main site of opal deposition in the sediments (DeMaster, 1981). For a long time, the idea of this impressive export of biogenic silica was at odds with the idea of the Southern Ocean as a high-nutrient, low-chlorophyll area of modest productivity. Higher rates than expected for BSi production were recorded in the Southern Ocean (from  $1.62 \pm 0.58 \text{ mol-Si m}^{-2} \text{ yr}^{-1}$  to  $3.34 \pm 0.54 \text{ mol-Si m}^{-2} \text{ yr}^{-1}$  (Pondaven et al., 2000)). This resulted in a higher opal rain rate, and thus did not require exceptional preservation efficiency to explain the high rates of BSi accumulation required to maintain the "high opal belt" underlying the Polar Frontal Zone. Compared to the Atlantic Ocean, the Southern Ocean is twice as productive in term of BSi (Pondaven et al., 1998) and 2 – 3 times more productive than the Equatorial Pacific. The opal accumulation rate that leads the Southern Ocean to be the main deposit site for BSi is higher by 12 times, compared to the equatorial Pacific ( $0.016 \text{ mol-Si m}^{-2} \text{ yr}^{-1}$ ), 31 times compare with the mesotrophic northeast Atlantic ( $0.008 \text{ mol-Si m}^{-2} \text{ yr}^{-1}$ ) and by 185 times compared to the oligotrophic Atlantic ( $0.001 \text{ mol-Si m}^{-2} \text{ yr}^{-1}$ ).

The two processes involved in the surface and deep water, and at the surface sediment are production (P) and the dissolution (D) of the BSi (Nelson et al., 1995). These will be discussed in the next section.

## I.4 Diatoms as conductors of the marine silica cycle

Diatoms are major actors of the biogeochemical cycle of silica in ocean. Diatoms are as far as we know the main silica biomineralizing group in the modern ocean; groups such as silicoflagellates, radiolarians and siliceous sponges have a comparatively smaller influence on the silica cycle. Diatoms have an absolute requirement for Si (DeMaster, 2002) and a strong affinity for DSi which means they can maintain high rates of DSi uptake (up to  $0.63 \mu\text{mol-Si cell}^{-1} \text{ d}^{-1}$  in Martin-Jézéquel et al., 2000 and references therein) at even very low concentrations of DSi ( $0.3 - 1.3 \mu\text{M}$  (Dugdale et al., 1995)). Additionally, their silicon requirement is relatively high, with a typical cellular ratio being 0.9:6.6 (mol : mol) Si:C contributing to a more efficient export of BSi compared to organic matter (Brzezinski et al., 2003). This leads to a net production of  $240 \text{ Tmol-Si yr}^{-1}$  in the surface water. In addition Baines et al. (2012) mentioned for the first time the possible role of picocyanobacteria in the silica cycle as they

observed Si accumulation in the cell and that “the water column inventory of silicon in *Synechococcus* can exceed that of diatoms in some cases”.

Diatoms are also important in the biogeochemical cycles of N, P, Fe (Sarhou et al., 2005 and references therein) and have a dominant role in the export production of C (Ragueneau et al., 2000; Sarhou et al., 2005). This is due to the fact that they are numerically quite abundant and often dominate phytoplankton blooms in many aquatic ecosystems (Nelson et al., 1995; De La Rocha et al., 2000; Martin-Jézéquel et al., 2000). They account for up to 75 % of the annual primary production in the Southern Ocean (Nelson et al., 1995). 20% of the CO<sub>2</sub> fixed during photosynthesis is the result of diatoms (Field et al., 1998). Also, very important to note, their heavy silica frustules mean they have faster sinking rates and are removed from the surface much more quickly than non-silicified cells (Smayda, 1970). For this work BSi will refer to diatoms.

#### 1.4.1 BSi production

Diatoms are the main producers of biogenic silica in the marine environment. They are eukaryotic unicellular microalgae requiring dissolved silicon to produce their frustules made of amorphous, hydrated silica (opal, BSi). They have 2 modes of reproduction, a sexual reproduction involving the fusion of gametes and a vegetative mode in which silicon metabolism is strongly linked to cell division (Martin-Jézéquel et al., 2000). Here the focus will be made on the vegetative reproduction that produces an exact replica of the frustule structure at each generation.

The structure of diatoms is an outer cell wall lined internally with a plasma membrane containing the cytoplasm and organelles protected from dissolution by an organic coating. The organic matrix is made up of layers of polysaccharides, lipids and proteins. The cell wall is made of silicon dioxide (SiO<sub>2</sub>) produced through the polymerization of DSi (Martin-Jézéquel et al., 2000). The cell wall consists of 2 valves of slightly different size (Fig. 1.4), separated by a cingulum made itself of girdle bands (Kröger and Poulsen, 2008). The epitheca and hypotheca are the large and the small valve respectively. When the new mature valve is formed, the mother cell forces it out, and the mature valve is protected from dissolution by an organic coating. The creation of a new siliceous valve for the new diatom strongly links silicon metabolism and the cell cycle with restrictions due to the rigidity of the frustule (Kröger and Poulsen, 2008). As observed in figure 1.4 (7 and 8) the distance between the 2 valves increases for the new valve formation, and to avoid a gap within the cell wall the girdle bands synthesis is necessary.

The diatom cell cycle is divided in 4 phases (like every eukaryotic cell) named G1, S, G2 and M. The S phase represents the DNA replication phase, M corresponds to the mitosis and the cell division period and G1 and G2 are the gap phases during which the cell growth occurs (Martin-Jézéquel et al.,

2000; Claquin et al., 2006). During the cell cycle, two common features to all diatoms species were observed resulting in non-continuous silicon uptake during the cell growth. There is a predominant arrest point at the G2/M boundary and another one at the G1/S boundary associated with new valve formation (Martin-Jézéquel et al., 2000). The latest can be indicative of DNA synthesis being silicon dependent but it was not proved yet and could be a way for the diatom to estimate the external Si concentration and to discern if the cell division can be completed.

Compared to nitrogen or phosphorus, the internal pool of silicon is not sufficient to support the entire division cell, therefore diatoms require Si uptake from their environment to complete their division. The Si uptake appears to regulate the DSi pool in the cell and the thickness of the frustule (Claquin et al., 2006).

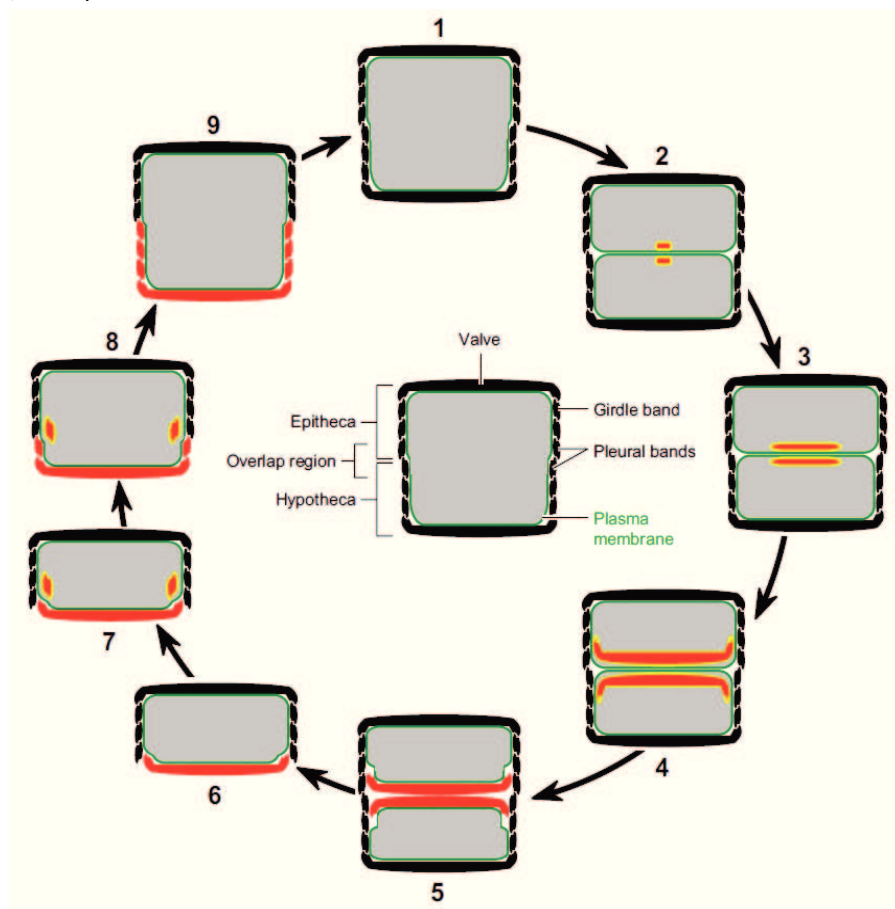


**Figure 1.4** Schematic structure of the diatom cell (center) and diatom cell cycle (shown in cross section). In grey: the protoplast, green line: the plasma membrane. For simplicity, intracellular organelles other than the Silica Deposition Vesicle (SDV) are not shown. Cell cycle: (1) Shortly before cell division the cell wall contains the maximum number of girdle bands, (2) immediately after cytokinesis new biosilica (red) is formed in each sibling cell inside a valve SDV (yellow), (3) expansion of the valve SDVs with increasing silica deposited, (4) at the final stage of valve SDV development, each SDV contains a fully developed valve, (5) the newly formed valves are deposited in the cleavage furrow on the surface of each protoplast by SDV exocytosis, (6) the sibling cells have separated, (7+8) expansion of the protoplast in interphase requires the synthesis of new silica (red) inside girdle band SDVs (yellow), each girdle band is synthesized in a separate SDV, and after SDV exocytosis is added to the newly formed valve (hypovalve), (9) after synthesis of the final hypovalve girdle band (pleural band) cell expansion stops, and DNA replication is initiated (Kröger and Poulsen, 2008).

Four DSi fluxes have been identified as important in diatoms that link the metabolism and the Si cycle. There are the influx and the efflux of DSi from outside into the cell and inversely, the incorporation flux that allows the growth cell by BSi formation and the dissolution flux at the opposite that converts the BSi into DSi (Milligan et al., 2004). Here we will focus on the polymerisation and depolymerisation of the DSi.

#### 1.4.2 Uptake and BSi production processes in diatom

Silicon uptake was demonstrated to occur as active transport (Paasche, 1973; Martin-Jézéquel et al., 2000 and references therein). The silicon forms available for diatom are the silicic acid at 97% ( $\text{Si}(\text{OH})_4$ ) and the remaining  $\text{SiO}(\text{OH})_3^-$  and the DSi influx in diatom is sodium dependent. Bhattacharyya and Volcani (1980) observed in *Nitzschia alba* that Si and  $\text{Na}^+$  transport is driven by the  $\text{Na}^+$  gradient across the membrane. An advantage for diatoms, that can explain their dominance in blooms, is the fact that DSi uptake is not dependant of photosynthesis energy but only from respiratory energy (Claquin et al., 2006). There are 2 pools of Si to differentiate, the intracellular silicon pool (by silicon uptake) required for silicification and the silica deposition pool (by silicon mineralization) necessary for cell division and growth (Ragueneau et al., 2000). These 2 phenomena can be coupled as in *Chaetoceros gracilis*, where DSi uptake and BSi mineralization occur at the same time, or uncoupled as for *Thalassiosira weissflogii*, depending on the species and influences the internal silicon pool (Ragueneau et al., 2000).

Silicon is transported across the plasmalemma, through the cytoplasm to reach the silicon deposit vesicle (SDV) which is located at the polymerization site (Martin-Jézéquel et al., 2000). The DSi uptake is regulated by silica transporter genes (SITs) (Hildebrand, 2008) and the deposit is regulated by proteins called silaffins (Kröger and Poulsen, 2008 and references therein). The SDV is bounded by a membrane called the silicalemma that contains an acidic environment favourable for DSi polymerisation. Proteins, cytoskeleton and some cellular components are also involved in this transformation.

The intracellular pool was observed to be in soluble form despite being at concentration supersaturated with respect to silica. Presumably some organic silicon-binding component makes this possible (Martin-Jézéquel et al., 2000 and references therein). This pool can vary depending on the species and depending on the cell stage. During cell wall synthesis, which occurs in all cycles stages G2 and M, a greater quantity of silicon will be required than can be provided by the internal pool.

Depending on DSi concentration around the cell, three modes of DSi uptake have been identified. Surge uptake consists of a rapid increase of intracellular silicon concentrations after



starvation as it is a replenishment mode. Externally controlled DSi uptake happens when the extracellular silicon concentration becomes very low and represents submaximal Si uptake rates. Finally the internally controlled uptake is regulated by use of Si in the cell, depending on the rate of Si deposit in the cell wall (Martin-Jézéquel et al., 2000).

Silicon uptake and cell division for natural assemblage or cell culture under silicon-limited conditions are well described by the following equations:

$$V = \frac{V_{\max} \cdot [Si(OH)_4]}{K_s + [Si(OH)_4]}, \quad \text{Michaelis-Menten kinetics of nutrient uptake} \quad (1.2)$$

$$\mu = \frac{\mu_{\max} \cdot [Si(OH)_4]}{K_{\mu} + [Si(OH)_4]}, \quad \text{Monod law of nutrient limited growth} \quad (1.3)$$

where  $V_{\max}$  and  $\mu_{\max}$  represent the maximum rate of uptake and division at non-limiting Si concentrations,  $K_s$  is the Si concentration at  $0.5 V_{\max}$  and  $K_{\mu}$  is the silicon concentration that limits  $\mu$  to  $0.5 \mu_{\max}$  (Martin-Jézéquel et al., 2000; Ragueneau et al., 2000; Claquin et al., 2006). The DSi uptake and BSi production are directly affected by environmental and physiological conditions (Passow et al., 2011) and so influence the values of  $K_s$  and  $V_{\max}$ . It has been reported that values for  $K_s$  and  $V_{\max}$  can evolve during the cell cycle. Low affinity and low capacity (high  $K_s$  and low  $V_{\max}$ ) were observed for Si uptake by *Navicula pelliculosa* before frustule deposition but the opposite during the deposition of BSi. The explanation advanced for the  $K_s$  decrease is higher affinity transporters and for the increase of  $V_{\max}$  it is a bigger number of transporters or a better efficiency of these latter in the plasma membrane (Martin-Jézéquel et al., 2000 and references therein).

Environmental conditions will have an effect on the growth rate of diatoms, mainly through co-limitation. For example Brzezinski et al. (2008) demonstrated that addition of iron in the environment significantly increases Si uptake by  $87 \pm 59 \%$ , but that addition of Fe and Si increases the uptake up to  $172 \pm 43 \%$ . This study revealed a co-limitation Fe - Si. Another co-limitation, between Fe and light was highlighted by Sunda and Huntsman (1997). This study revealed that in low light environments, diatoms are more iron limited, these conditions stimulate the development of small cells.

A decoupling exists between silicon metabolism and photosynthesis that is species dependent (Ragueneau et al., 2000). In 1955 Lewin indicated that the energy needed for silicification comes from aerobic respiration. Energy is required for silicon transport but there is not really a need of energy for biogenic silica mineralization, outside of what is necessary to create the organic matrix that guides polymerization of the silica (literature review in Martin-Jézéquel et al., 2000). For example, Sullivan (1986), described that after an increase in respiration with a period of silicon

transport, cells have enough energy to sustain biomineralization of the new valve. This decoupling between silicification and photosynthesis could explain why Si uptake and deposit can happen in the dark (Martin-Jézéquel et al., 2000). And knowing that carbon and nitrogen uptake are directly dependent on photosynthetic energy while silicon is dependent on the respiration of general cellular stores of energy, this can explain diatom dominance in phytoplankton blooms. Indeed, under less favourable conditions (i.e. water column mixing following a storm even) that could deepen the Mixed Layer, and so increase the depth at which they can “stay” (limit of the euphotic zone) they are more adapted to growth. Moreover diatoms have higher growth rates than dinoflagellates explaining why they bloom.

The advantages of having a frustule still remain unclear but some hypotheses are made. One major hypothesis is the protective role of the frustule against grazing by zooplankton. It was confirmed that because of the huge pressure needed to break the frustules, this is a good protection and that could explain the success of diatoms by decreasing their mortality rate (Hamm et al., 2003; Smetacek et al., 2004). Other assumptions are made about a possible role as an ultraviolet filter (Davidson et al., 1994), as a photonic crystal (Fuhrmann et al., 2004) or as ballast to control the position of diatom cells in the water column (Villareal, 1988). According to (Raven, 1983) there is less cost in creating a cell wall made of BSi rather than organic carbon. And lately, the role of polymerized silica as a buffer for the carbonic anhydrase (catalyser of the reaction between  $\text{HCO}_3^-$  and  $\text{CO}_2$ ) was demonstrated by Milligan and Morel (2002).

#### 1.4.3 Silicon dissolution and export

The second process affecting silicon in the marine environment is the dissolution of biogenic silica between a few hundred meters from the surface (Passow et al., 2003) and to the sediments (Van Cappellen et al., 2002). The dissolution (at neutral pH) is due to nucleophilic attack of water molecules that breaks Si-O-Si bonds found at the surface of the frustules (Loucaides and Behrends, 2008). The BSi dissolution rate determines the fraction of silica recycled in the euphotic zone that contributes to the gross amount of silicic acid that is available for diatom growth each year. The fraction recycled at depth (Passow et al., 2003) controls silicon recycling in the oceans (Van Cappellen et al., 2002) versus its burial in deep sea sediments and export from the ocean. Recycling and export of silicon are linked to areas of significant diatom productivity. The residence time of the BSi in the surface layer depends on the sinking speed and the dissolution rate. Seasonality, food web structure and aggregate formation are the main processes that will impact the export of silica (Ragueneau et al., 2000). According to Nelson et al. (1995), 50 to 60 % of the marine BSi produced dissolves in the euphotic zone and less than 3 % is buried in the sediment (DeMaster, 2001). But the export rates are

generally low due to the high BSi solubility ( $> 1000 \mu\text{mol-Si L}^{-1}$ ) and the undersaturated conditions of the ocean (surface  $< 50 \mu\text{M DSi}$ , deep  $< 180 \mu\text{M DSi}$ ) (Tréguer et al., 1995; Passow et al., 2003).

Frustules of living diatoms are protected from dissolution by an organic coating that isolates the cell from the slightly basic pH of seawater. In living diatoms the dissolution rate is minimal ( $0.2$  to  $0.3 \% \text{ d}^{-1}$ ) unless bacteria have colonized the cells (Bidle and Azam, 1999). Dissolution begins when diatoms die, as bacteria start to degrade this protection around the frustules letting the BSi underneath come into contact with seawater resulting in high dissolution rates of BSi in the upper ocean (Passow et al., 2003). Hurd and Birdwhistell (1983) described the specific dissolution rate  $V_{\text{diss}}$  ( $\text{h}^{-1}$ ) of the BSi as follow:

$$V_{\text{diss}} = k \cdot ([\text{Si}(\text{OH})_4]_{\text{sat}} - [\text{Si}(\text{OH})_4]) \cdot A_{\text{sp}}, \quad (1.4)$$

where  $k$  is a constant ( $\text{cm h}^{-1}$ ),  $\text{Si}(\text{OH})_{4\text{sat}}$  is opal solubility ( $\text{mol cm}^{-3}$ ),  $\text{Si}(\text{OH})_4$  is the ambient DSi concentration ( $\text{mol cm}^{-3}$ ) and  $A_{\text{sp}}$  is the specific surface area of opal present ( $\text{cm}^2 \text{ mol}^{-1}$ ). This equation allows us to better understand the conditions affecting the dissolution rate in the ocean, for example allowing us to discern that the lowest dissolution rates occur in the Antarctic between  $-1.5^\circ\text{C}$  and  $+6^\circ\text{C}$  and the highest dissolution rates occur in coastal waters between  $+14^\circ\text{C}$  to  $+22^\circ\text{C}$ . These observations led to the conclusion that the temperature of the surface layer plays an important role in the dissolution rate observed in different regions.

From experiments a list of physical and chemical processes that modify dissolution has been made. An increase of the temperature or pH will have increased the dissolution rate, while silica with a greater aluminium content or otherwise impurity will inversely decrease the dissolution rate. A pH increase leads to a deprotonation of Si-OH groups at the surface, facilitating then the Si-O-Si bounds to be broken (Loucaides and Behrends, 2008). The composition of the cell medium, the morphology and the structure of the frustule more than the surface area (Martin-Jézéquel et al., 2000) and the silica's age will as well influence dissolution (Van Cappellen et al., 2002 and references therein).

Food web structure impacts recycling and export of BSi by grazers that feed on diatoms. Grazing by heterotrophic dinoflagellates will remove all organic matter from the frustules, leaving them exposed to seawater, and so increase the dissolution rate of the silica. Grazing by crustaceans like copepods will have two different effects. The first effect is to break the frustules into smaller pieces in surface waters, inhibiting their export from the surface (Ragueneau et al., 2006). The second is to export BSi via fecal pellets (Beucher et al., 2004), contributing to the export of the silica to the deep ocean. Diatoms may also sediment as aggregates. Aggregation can play a protection role if there is

little exchange between the aggregate and the surrounding seawater. Or it can acts as a stimulation of dissolution if there is considerable bacterial activity in the aggregate (Passow et al., 2003).

#### I.4.4 BSi as a proxy

We have just seen that diatoms are the main actor of the silica cycle, that the DSi concentration influences diatom growth and that 3% of the BSi produced in surface waters reaches the seafloor. There has been strong interest in using the BSi that accumulates in the sediment to somehow reconstruct the productivity of the past ocean. De La Rocha et al. (1997) suggested that the silicon isotopic composition of this silica might serve as a robust proxy for the extent of utilization of DSi by diatoms. They showed that diatoms fractionate Si isotopes in favour of the light isotope ( $^{28}\text{Si}$ ) when they take up DSi to produce BSi, leading to BSi lower by  $1.1 \pm 0.4 \text{ ‰}$  compared to the DSi source. This fractionation was not observed to vary with temperature (in the range 12 – 22 °C) nor among the three species of diatoms tested. However this year Sutton et al. (2013) revealed fractionation during BSi production being species dependant. The extremes values obtained were for two Southern Ocean diatoms, *Fragilariopsis kerguelensis* and *Chaetoceros brevis* that expressed fractionation of  $-0.54 \text{ ‰}$  and  $-2.09 \text{ ‰}$ . The previous value defined by De La Rocha et al. (1997) is in the range of these values. In 2009 Demarest et al. observed fractionation again in favour of the light isotope during BSi dissolution leading to the production of DSi lighter by  $0.55 \text{ ‰}$  compare to the BSi.

## II Isotope systematics

### II.1 The silicon isotope system

Atoms of the same element, with the same number of protons (Z) and electrons but with different numbers of neutrons (N) are called isotopes. Because they do not have the same number of neutrons, all isotopes of an element have a different atomic masse (m). The atomic mass variations of an element leads to small differences in chemical and physical properties, known as isotope effects (Hoefs, 1996). Stable isotopes are defined as nuclides with low atomic mass and with a stability achieved when the number of protons and neutrons are approximately equal. The process resulting in variation of abundance of isotopes is called fractionation. Processes that induce isotopic fractionation cause differences in the ratios of the different isotopes of an element between two substances or between two phases of a substance.

Hoefs (1996) highlighted the existence of two types of mass-dependent fractionation laws. There is kinetic isotopic fractionation that results from motions and unidirectional reactions, and

equilibrium isotopic fractionation that results from isotope exchange between chemical substances or two phases, and that is bidirectional. The extent of mass dependent fractionation by a kinetic isotope effect is very slightly different from that of an equilibrium isotope effect, allowing the two to be distinguished in a set of extremely precisely measured samples. The resulting slope of the silicon isotopic composition of samples on a three isotope plot (i.e.  $\delta^{29}\text{Si}$  versus  $\delta^{30}\text{Si}$ ) is either 1.93 or 1.96, corresponding to kinetic or equilibrium isotope fractionation respectively (Young et al., 2002).

Silicon has three natural stable isotopes,  $^{28}\text{Si}$ ,  $^{29}\text{Si}$  and  $^{30}\text{Si}$ , for which the relative abundance is respectively 92.22 %, 4.69 % and 3.09 %. There is also a radioactive isotope  $^{32}\text{Si}$  with a half life of  $140 \pm 6$  years. The relative mass difference between the heaviest and the lightest isotopes ( $^{30}\text{Si}/^{28}\text{Si} = 7$  and  $^{29}\text{Si}/^{28}\text{Si} = 3.6$ ) indicate that large mass-dependent fractionations are to be expected (Engström, 2009). The isotope ratio variations are expressed as  $\delta^{29}\text{Si}$  or  $\delta^{30}\text{Si}$  as follows:

$$\delta^x \text{Si} = \left[ \frac{\left( \frac{^x \text{Si}}{^{28} \text{Si}} \right)_{\text{sample}}}{\left( \frac{^x \text{Si}}{^{28} \text{Si}} \right)_{\text{std}}} - 1 \right] \cdot 1000 \text{‰}, \quad (1.5)$$

where x corresponds to  $^{29}\text{Si}$  or  $^{30}\text{Si}$ . The standard (*std*) commonly used is the international Si standard NBS28 (RM8546).

The measurement of silicon isotopes is interesting due to silicon abundance, for example, silica represents ~ 60 % of the dry weight of diatoms (Sicko-Goad et al., 1984). Moreover, in the Southern Ocean, an ocean of importance for the distribution of nutrients in the ocean, the seafloor is rich in opal and poor in carbonate. Douthitt (1982) made the first observation of a difference in the natural abundance of Si isotopes in diatoms compared to igneous rock.

## II.2 Silicon isotopes in different environments

Variations in silicon isotopes offer a means to track processes involving silicon utilisation and fractionation. The weak valence of silicon ( $4^+$ ) is bound with O and the non-existence of a gaseous phase leads to little isotopic fractionation on Earth. The four domains in which silicon fractionation is involved are rock-forming, water-rock interactions, biological processes and water reservoirs. I will focus on the water-rock interactions, rivers and oceanic biological processes that are more relevant for this study.

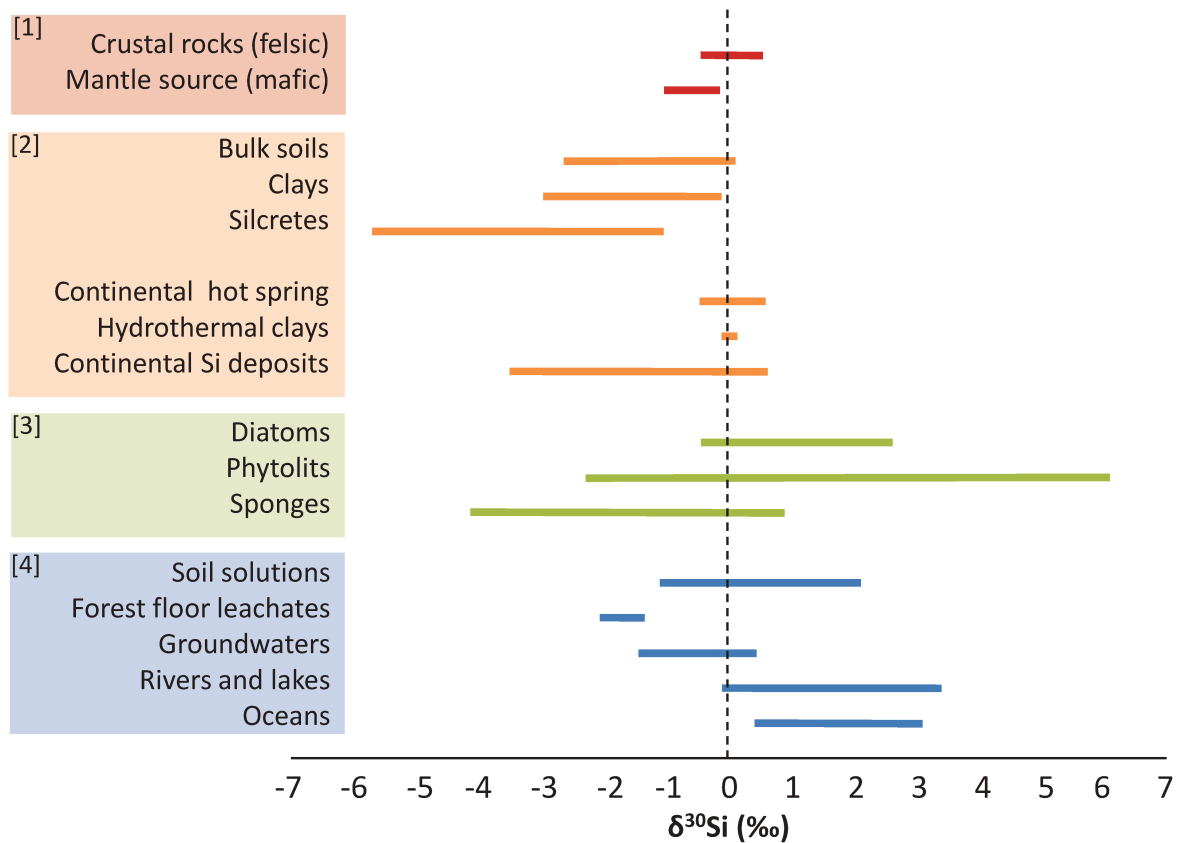


**Figure 1.5** Range of  $\delta^{30}\text{Si}$  variations at the surface of the Earth in relation to rock-forming processes [1], water-rock interactions [2], biological processes [3], water reservoirs [4] (Opfergelt and Delmelle, 2012 and references therein).

Silicate rock weathering serves as the ultimate source of silicon to rivers and the oceans and to biological processes. On Earth values of  $\delta^{30}\text{Si}$  range from  $-5.70\text{‰}$  for silcretes (Basile-Doelsch et al., 2005) to  $+6.10\text{‰}$  for rice grains (Ding et al., 2005) (Fig 1.5). Processes that influence weathering are the age of the soil/mineral that determine the time of the reaction, the lithology that affects the rocks solubility, the climate and vegetation that increase the weathering reaction, and finally the erosion that contributed to the chemical weathering (Opfergelt and Delmelle, 2012).

Igneous rocks have a  $\delta^{30}\text{Si}_{\text{DSi}}$  around  $-0.34\text{‰}$  and rock weathering processes lead to two products, DSi with a higher  $\delta^{30}\text{Si}$  due to mineral dissolution and clay formation with a lower  $\delta^{30}\text{Si}$ . Compared to igneous rocks, rivers and lakes are enriched in  $^{30}\text{Si}$  relative to  $^{28}\text{Si}$  with a large range varying from  $-0.10\text{‰}$  to  $+3.40\text{‰}$  (Fig. 1.5). This large range is in part linked with the biological processes occurring in water. The isotopic fractionation by diatoms when they take up DSi leads to high values of  $\delta^{30}\text{Si}$  in ocean surface waters, for example (De La Rocha et al., 2000). Two phenomena happen in fresh water; (1) in surface water diatoms take up DSi which lead to a higher surface water  $\delta^{30}\text{Si}$  and (2) the formation of clay lead to a lower  $\delta^{30}\text{Si}$  DSi.

In the oceans, gradients are observed for  $\delta^{30}\text{Si}_{\text{DSi}}$  mainly due to biological activities, and due to BSi dissolution and the circulation and mixing of water masses. Because diatoms that are in the euphotic zone take up DSi to build their frustules, a gradient with depth is observed with  $\delta^{30}\text{Si}_{\text{DSi}}$  decreasing with depth as DSi concentrations increase. The highest marine values of  $\delta^{30}\text{Si}_{\text{DSi}}$  are found in surface waters with a maximum value of + 3.10 ‰ recorded by Varela et al. (2004) in the Pacific sector of the Southern Ocean. For the deep water (> 2000 m) average values are + 1.20 ‰ for the Antarctic Circumpolar Current (Fripiat et al., 2011a) and + 1.25 ‰ for the deep water of equatorial Pacific Ocean and Pacific sector of the Southern Ocean (de Souza et al., 2012a). A typical silicon isotopic profile is presented in figure 1.6.

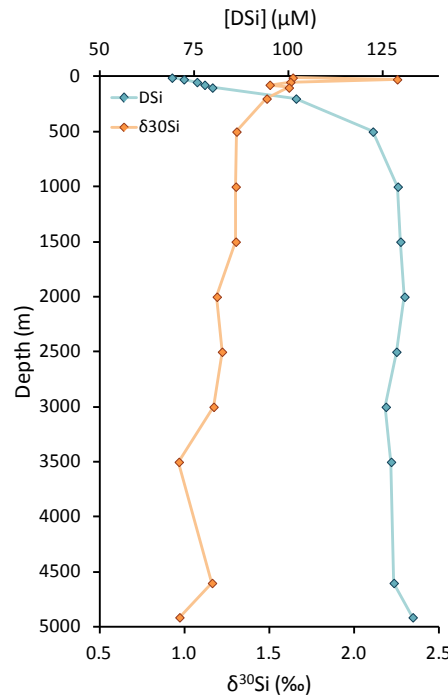


**Figure 1.6** Typical profile of  $\delta^{30}\text{Si}_{\text{DSi}}$  and DSi concentration versus depth in marine environment (data from this PhD). Blue diamonds are  $\delta^{30}\text{Si}_{\text{DSi}}$  values and orange diamonds are the corresponding DSi concentrations.

To estimate the fractionation between the DSi used and the resulting BSi by diatom based on the evolution of silicon isotopes in surface waters during DSi drawdown, either of the two simple models can be used. The fact that these models only work during times of net nutrient drawdown is a key point, as this makes them unsuitable for use at other times. Not all production of biomass in the ocean occurs during times of net nutrient removal (i.e. there are times when net production of biomass occurs but does not exceed daily inputs of nutrients to the euphotic zone through upwelling or mixing).

The Rayleigh distillation (or closed system) model (Fig. 1.7, eq. 1.6) (De La Rocha et al., 1997; Sigman et al., 1999) assumes a single input of nutrient to the surface at the beginning of the growing

season, that the reservoir is well mixed and that the BSi produced does not subsequently dissolve or exchange isotopes with the remaining DSi reservoir:

$$\delta^{30}\text{Si}_{\text{DSi}} = \delta^{30}\text{Si}_{\text{DSi initial}} + \varepsilon \cdot \ln\left(\frac{[\text{DSi}]_{\text{measured}}}{[\text{DSi}]_{\text{initial}}}\right) \quad (1.6)$$

It is characterized by an exponential enrichment of DSi reservoir through time with BSi formation and accumulation of the product formed.

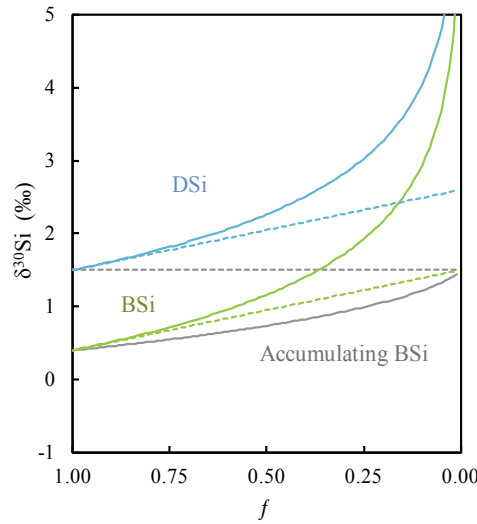


**Figure 1.7** Representation of the Rayleigh distillation model (solid lines) and the Steady state model (dotted lines). *f*: remaining fraction, blue: DSi, green: BSi and grey: BSi accumulation in the system.

The second model is the Continuous input model (or open model) (eq. 1.7) (Sigman et al., 1999). This model hypothesizes a continuous input of DSi to the surface over the growing season. DSi is partially consumed and the residual fraction exported:

$$\delta^{30}\text{Si}_{\text{DSi}} = \delta^{30}\text{Si}_{\text{DSi initial}} - \varepsilon \cdot \left(1 - \left(\frac{[\text{DSi}]_{\text{measured}}}{[\text{DSi}]_{\text{initial}}}\right)\right) \quad (1.7)$$

BSi deposits in the sediment have an important role in helping us to determine the patterns and controls over past climate. Diatoms make an important contribution to primary production in the Southern Ocean and because primary production is CO<sub>2</sub> consuming, there is a great interest of using opal in the sediment to reconstruct diatom productivity in relation to past climate. A reconstruction based only on the rate of sediment deposition is complicated by the fact that 50 % of the BSi produced is dissolved in the first hundred meters and ocean circulation leads to the deposition of BSi not necessarily in the area of its production. To counteract that, De La Rocha et al., (1998) used the silicon isotopic composition of the BSi as a proxy. This suggested that during the Last Glacial Maximum (Fig. 1.8 arrow) the extent of DSi utilisation was smaller than today (and coincided with reduced rates of opal accumulation on the seafloor). The opposite was true for the Holocene. A study



of Brzezinski et al. (2002) confirmed these results and suggested that, due to a higher iron concentration compared to the present day, surface water recorded a DSi excess and a depletion of  $\text{NO}_3^-$ .

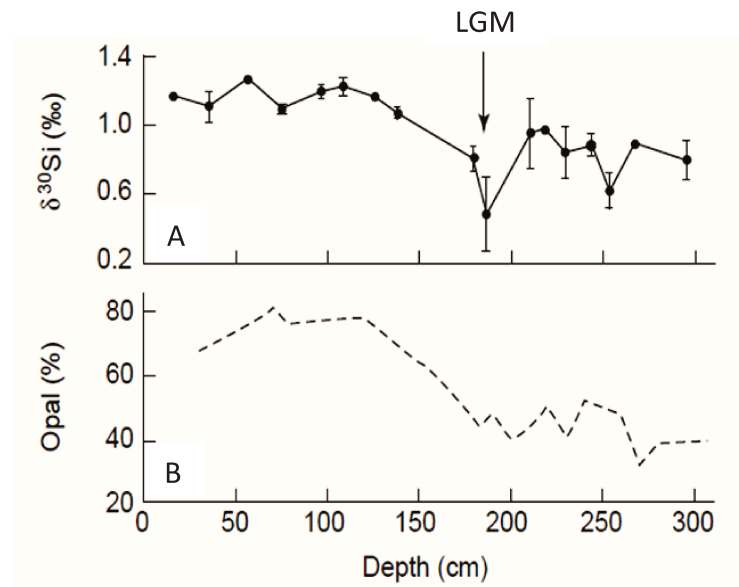


**Figure 1.8** Representation of the South Atlantic sediment core RC13-269 (52°38' S, 00°08' W, 2,591 mbsl) for the A)  $\delta^{30}\text{Si}$  evolution versus depth, error bars on  $\delta^{30}\text{Si}$  represent standard error on 2–3 separate measurements, the arrow indicates the Last Glacial Maximum (LGM) and B) BSi against depth. The percentage opal (P. N. Froelich, unpublished data) was determined through extraction into a sodium carbonate solution 32. Modified from De La Rocha et al. (1998).

The subject of my dissertation is the study of the silicon biogeochemical cycle in the Indian sector of the Southern Ocean, and in the Atlantic Ocean, using natural silicon stable isotope abundances ( $\delta^{30}\text{Si}$ ). The two main objectives of this dissertation:

- ✓ To study the processes affecting the cycling of silicon isotopes on the Kerguelen Plateau. For this purpose, new data profiles (from ANTXXIII/9 campaign) of the  $\delta^{30}\text{Si}$  of dissolved Si are presented for the Kerguelen Plateau. Additionally, a new model was developed in order to evaluate – on a seasonal time scale - the relative influence of biological and physical processes on the isotopic composition ( $\delta^{30}\text{Si}$ ) of dissolved Si and biogenic silica in the region of the Kerguelen Plateau.
- ✓ To understand the distribution of silicon isotopes in the Atlantic Ocean, from the northern North Atlantic Ocean to the Atlantic sector for the Southern Ocean. The data profiles presented are the first for the Weddell Gyre covering different areas of the gyre. Also, profiles from the Drake Passage and the 0° meridian (some stations being in the Antarctic Circumpolar Current) for the Southern Ocean (from ANTXXIV/3 campaign) were measured as well as profiles close to the Cape Verde Islands (from MSM10/1 campaign). Together and with Atlantic Ocean data from the literature I tried to track the deep and intermediate Atlantic Ocean circulation and its silicon isotopic composition.

Altogether, this thesis is composed of 5 chapters. The introduction chapter gives background that helps to place the data chapters into a broader context. The 2<sup>nd</sup> chapter describes the methods used for the collection and analyses of samples. Chapter 3 is the publication “Exploring interacting influences on the silicon isotopic composition of the surface ocean: a case study from the Kerguelen Plateau”. The 4<sup>th</sup> chapter is composed of a first part that is a general overview of the intermediate and deep circulation in the Atlantic Ocean. This is a background followed by the second part which describes the silicon isotopes data in the Atlantic Ocean, as part of the GEOTRACES Zero and Drake transects, the ANTXXIV/3 campaign and the MSM10/1 campaign. This thesis ends with general conclusions as the 5<sup>th</sup> chapter.

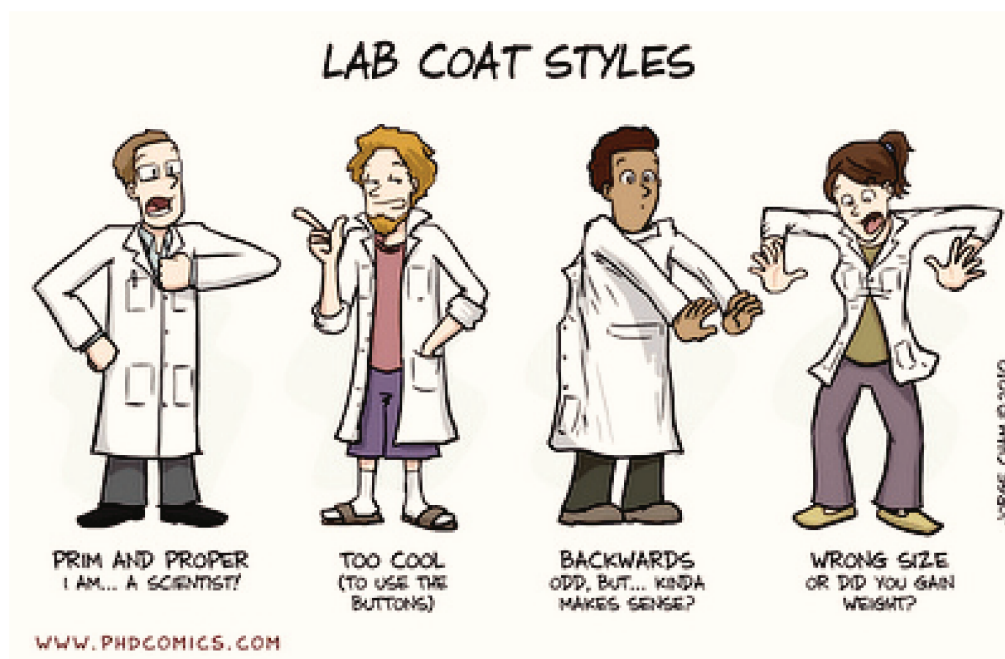


---

# Methods and analytical techniques

## — Chapter 2 —

---



# Chapter 2 – Methods and analytical techniques

---

This chapter presents the steps used in the preparation of samples detailed in the following chapters and the measurement of isotope ratios with the multi-collector inductive coupled plasma mass spectrometer (MC-ICP-MS) Neptune (Thermo Fisher Scientific). The initial collection of samples in the field is detailed in the chapter specific to each oceanographic campaign.

## I Sample preparation

### I.1 Determination of DSi concentration

The first step in the preparation of samples for mass spectrometry was the determination of the dissolved silicon (DSi) concentration of the samples. The well known interaction between silicic acid and molybdate was used to determine the concentrations colorimetrically with a spectrophotometer (Shimadzu UV-1700) following the formation of a complex of silicomolybdate ( $\text{H}_4\text{SiMo}_{12}\text{O}_{40}$ ) and its reduction to create a blue solution (Strickland and Parsons, 1972). This technique allows only the dissolved, monomeric form of silica and straight-chain polymers of relatively short length to react with molybdate. However, even polymers at low DSi concentrations are not a problem for DSi concentration determination due to the fact they are “probably unreactive”, as described by the authors.

The ammonium molybdate ( $(\text{NH}_4)_6\text{Mo}_7\text{O}_{24} \cdot 4\text{H}_2\text{O}$ ) reagent was prepared with concentrated HCl and stored in a polyethylene bottle. The reducing agent was a mix of metol-sulphite ( $\text{Na}_2\text{SO}_3 + (\text{C}_7\text{H}_{10}\text{NO})_2\text{SO}_4$ ), sulphuric acid ( $\text{H}_2\text{SO}_4$ ) and saturated oxalic acid ( $\text{C}_2\text{H}_2\text{O}_4$ ) stored in polyethylene bottles. For a sample 2 mL metol-sulfite + 1.6 mL Milli-Q water + 1.2 mL of 50%  $\text{H}_2\text{SO}_4$  + 1.2 mL of saturated oxalic acid are needed. All acids used are analytical grade and diluted with Milli-Q water ( $18.2 \text{ M}\Omega \text{ cm}^{-1}$ ).

For the standard curve a minimum of 7 concentrations were used in clean polyethylene bottles ranging from  $0 \mu\text{mol-Si L}^{-1}$  (blank) to  $140 \mu\text{mol-Si L}^{-1}$  ( $133 \mu\text{mol-Si L}^{-1}$  was the maximum concentration measured) covering the DSi concentration range of samples. Artificial seawater prepared according to Strickland and Parsons (1972) was used to match our samples, and the silica standard used was silicon hexafluoride ( $\text{SiF}_6^{2-}$ ).

The blank was prepared by mixing the reducing agent with artificial seawater. Straight after that addition the reagent is poured and mixed. The standard solutions and samples were prepared by

adding the reagent to the sample, and ten minutes later the reducing agent was added to the reagent plus sample and mixed in the bottles. Approximately three hours is needed for the reaction to stabilise before the measurements are performed at a wave length ( $\lambda$ ) of 810 nm.

## I.2 Magnesium induced coprecipitation (MAGIC)

The samples were preconcentrated according to an adapted brucite coprecipitation (MAGIC) technique developed by Karl and Tien (1992). The principle is to add sodium hydroxide (NaOH) to a seawater sample to reach a  $\text{pH} \geq 10$  which will induce the precipitation of the brucite ( $\text{Mg}(\text{OH})_2$ ) and many solutes including DSi. To initiate the precipitation, 2 % volume of 1 M NaOH is added to the samples and mixed. Another centrifugation was performed one hour later and the precipitates from the two centrifugations are added to the same sample and dissolved in concentrated HCl for recovery of DSi. This was found necessary for complete recovery (i.e. 97.93 %) and quantitative extraction of DSi from seawater.

## I.3 Tri-ethylamine molybdate coprecipitation (TEA-moly)

DSi quantitatively reacts with the molybdate ion at acidic pHs, allowing a DSi extraction from seawater and purification via precipitation of the silicomolybdate ion, as triethylamine silicomolybdate (DeFritas et al., 1991; De La Rocha et al., 1996). This method permits quantitative recovery of silicon even for samples with low concentration (10  $\mu\text{M}$ ). Quantitative recovery is very important to avoid silicon fractionation during silicon extraction that can occur if an isotope is preferentially removed compared to other silicon isotopes. Following the protocols of De La Rocha et al. (1996), the prepared reagent stands for seven days in a dark polyethylene bottle to let the trace amounts of silicon in the water and/or reagents to precipitate as triethylamine silicomolybdate. The reagent is prepared by mixing ammonium molybdate ( $(\text{NH}_4)_6\text{Mo}_7\text{O}_{24} \cdot 4\text{H}_2\text{O}$ ) and tri-ethylamine hydrochloride ( $(\text{C}_2\text{H}_5)_3\text{N} \cdot \text{HCl}$ ). When the trace amounts of silicon have precipitated, the reagent is filtered through a 0.4  $\mu\text{m}$  polycarbonate filter immediately prior to use (Fig. 2.1). For each 100 mL of water sample, 60 mL of reagent was added.

The coprecipitation reaction occurs in two steps. Firstly, monomeric  $\text{Si}(\text{OH})_4$  reacts with molybdate to form silicomolybdic acid ( $\text{H}_4\text{SiO}_4 \cdot 12\text{MoO}_3$ ), and then silicomolybdate reacts with triethylamine to form an insoluble, yellow complex, triethylamine silicomolybdate ( $((\text{CH}_3\text{CH}_2)_3\text{NH})_4\text{SiMo}_{12}\text{O}_{40} \cdot 4\text{H}_2\text{O}$ ). The pH must be acidic (between 1 and 4) and the DSi concentration must be  $> 3 \mu\text{M}$ -Si for the reaction to proceed rapidly and quantitatively. Once the complex is formed, the sample is given 24 h for complete reaction before filtration through a 0.4  $\mu\text{m}$

polycarbonate filter and rinsed carefully with a very small amount of Milli-Q water (or diluted reagent) to remove any seasalts. The filter is then put in a platinum (Pt) crucible for combustion to form  $\text{SiO}_2$ . A first combustion at  $400^\circ\text{C}$  for 3 h is necessary to remove organic matter (i.e. the triethylamine), and a second at  $1000^\circ\text{C}$  for 10 h is needed to sublime the molybdenum, leaving behind a normally clean, white  $\text{SiO}_2$ .

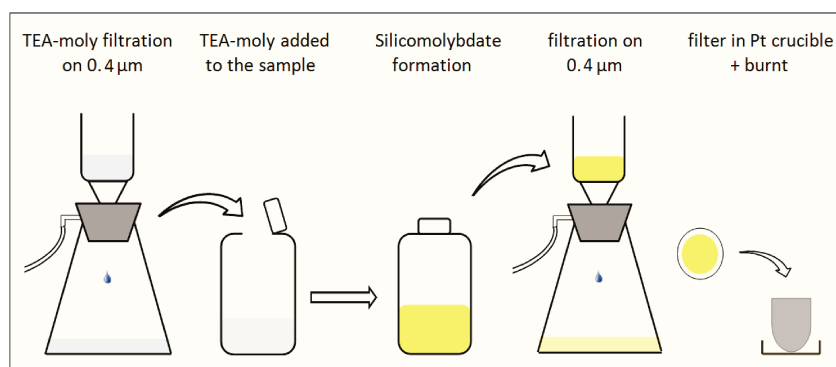


**Figure 2.1 Protocol for DSi precipitation via TEA-moly and extraction.**

For some of the samples something in the water (maybe some colloidal matter) had blocked the filters leading to bad recoveries, by adding material on the filter. This had further participated to the recovery of non-pure silica fractions after the combustion step for some samples, maybe due to some salt, and so too small silica samples. However, for most of the samples the silica concentration was high enough for analysis.

The  $\text{SiO}_2$  sample is weighed in an acid-cleaned Eppendorf microcentrifuge tube using a microbalance. Then, in a class 1000 clean lab at Ifremer (Brest, France), concentrated hydrochloric acid (HF, 22.6 M, suprapur Merck) was added to dissolve  $\text{SiO}_2$ . A sufficient volume of HF is added to attain a Si:HF molar ratio of 1:98 to ensure the formation of  $\text{SiF}_6^{2-}$  instead of  $\text{SiF}_4$  (gas), which would result in a loss of the sample. Samples were allowed to dissolve for several days, even though they were entirely dissolved within a few hours given the weakly crystalline structure of the  $\text{SiO}_2$  formed during the combustion (De La Rocha et al., 1996).

## I.4 Sample preparation for mass spectrometry

Despite the purification of our samples via the TEA-moly method, a second purification step was needed before applying isotope analyses by multicollector inductively coupled plasma - mass spectrometer (MC-ICP-MS) where even trace quantities of contaminants can adversely affect the measurement of isotope ratios. We separated silicon from these potential remaining contaminants through ion exchange chromatography carried out in a laminar flow extraction hood in a class 1000

clean lab. Acids used were all suprapur (Merck) and were diluted with Milli-Q water. The dissolution with HF charges the silicon negatively (anion) as  $\text{SiF}_6^{2-}$ , and therefore, an AG 1-X8 strong base anion exchange resin (BioRad or Eichrom) was used. This resin is a polymer of fixed ion as  $\text{N-CH}_2\text{N-(CH}_3)_3$  linked with an ion that is mobile (e.g.,  $\text{Cl}^-$ ). The particle size of the resin used was 100 200 mesh (150 – 75  $\mu\text{m}$ ). The resin beds of  $\sim 1.8$  mL were placed in acid-cleaned columns of 2 mL (Eichrom) and held in place by a frit at the bottom and at the top of the resin bed.

The resin is first washed using Milli-Q water and then preconditioned with 15 mL of 2 M NaOH. 7.7 mL of sample, containing 4  $\mu\text{mol-Si}$  and having a HF concentration of 52 mM, is loaded into the column. The ions of  $\text{SiF}_6^{2-}$  are retained on the resin, displacing the  $\text{OH}^-$  carried by NaOH. The sample matrix (including potential contaminants) is eluted using Milli-Q water followed by a solution of 95 mM HCl + 23 mM HF and another of 23 mM HF. To elute the Si from the column, two 10 mL aliquots of 0.14 M  $\text{HNO}_3$  + 5.6 mM were used, with the second being collected as it contains all of the Si loaded onto the column (i.e.,  $99.34 \pm 0.20$  %). The concentration of purified Si in the eluent was thus 11.2 ppm of Si. During each session, a blank of 52 mM HF was run on a column that is silica clean at  $99.62 \pm 0.16$  %. A minimum of one silica standard was also run on one column during each session. The silica standard commonly used is the NBS28 (RM8546), a quartz sand sample supplied by the National Institute of Standards and Technology (NIST). Another silica standard used was a 99.995 % pure silica sample (Alfa Aesar) adopted as the working standard (De La Rocha, 2002). Samples, blanks and standards were stored in acid-cleaned polypropylene centrifuge tubes (VWR) in the clean lab until analysis on the mass spectrometer.

## II Mass Spectrometry

The mass spectrometry method is the most effective way to determine atomic and molecular masses and isotope abundance of a sample. In a mass spectrometer the sample is converted into an ionised, gaseous state, and charged molecules or charged atoms are separated according to their mass to charge ( $m/z$ ) ratio, and their relative abundance is recorded.

### II.1 Sample dilution

As mentioned in the chapter 1, silicon has three natural stable isotopes,  $^{28}\text{Si}$ ,  $^{29}\text{Si}$  and  $^{30}\text{Si}$ , for which the relative abundance is respectively 92.22 %, 4.69 % and 3.09 %. The silica samples are diluted from 1.5 to 2.5 ppm to obtain a signal of  $\sim 10$  V on the mass 28, at medium resolution. The samples and standards were matched for silicon and acid concentrations to obtain the same signal. A sample-standard bracketing technique was used, that required identical solutions to avoid a matrix-



effect that could bias the isotopic ratio measurement (Cardinal et al., 2003). The samples and standards are “spiked” with an external element, which is chosen according to its mass being as close as possible to the targeted element (See section II.3.2.). For silicon ( $^{28}\text{Si}$ ,  $^{29}\text{Si}$  and  $^{30}\text{Si}$ ) the most suitable element is magnesium due to its isotopes  $^{24}\text{Mg}$ ,  $^{25}\text{Mg}$  and  $^{26}\text{Mg}$ . We used a pure mono-elementary Mg solution (Cardinal et al., 2003).

## II.2 Multi-Collector - Inductive Coupled Plasma Mass Spectrometry

The Neptune (Thermo Fisher Scientific, Fig. 2.2 A) is a double-focusing mass spectrometer used for the analyses at Ifremer (Brest, France). It is divided in three main parts, the inductively coupled plasma module (ICP), the electrostatic analyser module (ESA) and the multi-collector module (Fig. 2.2 B).

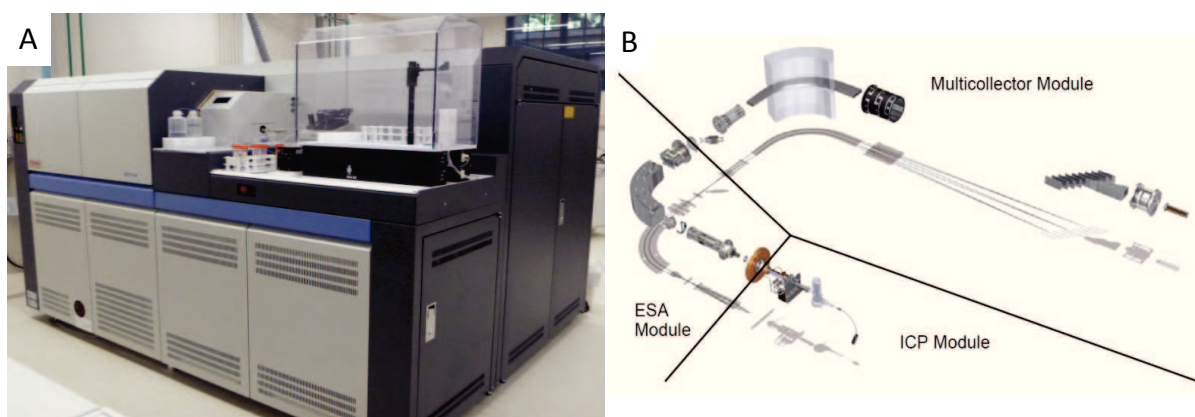


**Figure 2.2 A) Neptune (Thermo Fisher Scientific), B) Main parts of the Neptune, the Inductively Coupled Plasma module (ICP Module), the Electrostatic Analyzer module (ESA Module) and the Multi-collector module ([wwz.ifremer.fr/Neptune](http://wwz.ifremer.fr/Neptune)).**

The ICP module is composed of the inlet system and the plasma where the sample is ionised. The inlet system conveys the liquid sample via aspiration from the sample vial, generally positioned in an auto-sampling rack, into the nebulizer, where the sample is transformed into a fine aerosol by argon (Ar) gas flowing through the nebulizer. In general, this mist enters in the spray chamber that prevents large droplets from passing through to the plasma. However, during this study a desolvating nebulizer (for earlier measurement (samples from ANTXXIII/9) the Apex was used, and for later measurements (ANTXXIV/3 and MSM10/1) the Aridus II) to minimise the transfer of all liquid to the plasma. Carried along by a flow of Ar gas, the sample reaches the torch where it is injected into the plasma and ionised. The Ar plasma is maintained by a coupling coil which transmits a specific radio frequency to the heated Ar gas which is ignited by a spark. The plasma is extremely hot, especially towards its core, and the sample is ionised upon contact with it.

The ESA module is the interface region that focuses and accelerates ions from the plasma at atmospheric pressure into a  $10^{-6}$  Torr pressure mass spectrometer. The aim is to reduce ion dispersion by filtering the speed and energy of the ions transmitted and to accelerate them through the system. This helps to obtain a peak shape with a flat top needed for precise, accurate, and stable measurements of isotope abundance ratios. For that, immediately after ionisation of the sample in the plasma, the ions go through a sampler cone which blocks all ions except for those travelling with a directly forward trajectory at the centre of the plasma. After passing through the small orifice of the sampler cone, the ions spread out and are subsampled again a few centimetres later by the skimmer cone, which is steeper and has a smaller orifice. Again, only the ions at the centre of the ion beam pass through the skimmer cone. This allows a uniform ion beam and a decrease in pressure moving in to the high vacuum area of the mass spectrometer. Through the lens system that is downstream of the cones, the vacuum starts to improve and the ions begin to accelerate towards the Faraday detectors due to the electrical field established in the mass spectrometer. When the ion beam reaches the electrostatic sector, the ions are diverted according to their energy to the magnetic sector. The electrostatic sector is composed of two curved plates with direct current voltages that have opposite polarity, attracting oppositely charged ions thus creating ion aversion. The ion beam is focused and deflected with a  $90^\circ$  angle and an intermediate slit at the end of the ESA acts as an energetic filter allowing only ions with a narrow range of kinetic energy to pass.

The multi-collector module is where the mass separation and detection of ions take place. This consists of the magnetic sector that separates ions into beams characterised by their mass to charge value. After the magnetic field each separated ion beams is collected by one of the eight available Faradays cups, four on the low mass side (L4, L3, L2, and L1) of a fixed central cup (C), and four on the high mass side of the central cup (H1, H2, H3 and H4). For Si masses 28, 29 and 30, the cups used are L2, C and H2. Ions landing in a cup are transformed into an electrical impulse which is amplified to give an ion current proportional to the isotope abundance.

### II.3 Performance of a MC-ICP MS

There are potentially three types of errors/problems that can occur during analyses of silicon isotopes when using the mass spectrometer: (1) interferences with the masses of interest (28, 29 and 30 in this study), (2) overestimation of sample peak intensities due to high blank concentrations, and (3) isotopic fractionation at the interface part of the machine (De La Rocha, 2002; Cardinal et al., 2003; Engström et al., 2006).

Three procedure blanks are used for correction for each run on the Neptune. A procedure blank has the same composition and concentration of acid as the sample and standard, and goes through

the same chemistry, but contains no silicon. It is a blank for the column chemistry. An average of three procedure blanks are measured for each silicon isotope and used to correct measurements on the mass spectrometer by subtracting the blank average from the isotope value measured. The operating conditions of the Neptune are described in Table 2.1

**Table 2.1 Characteristics of the MC-ICPMS Neptune (Ifremer, Brest) used for the silicon isotopes measurements.**

Parameter	Running conditions
resolution	Medium (6317.33 amu)
sensitivity	~6 V ppm <sup>-1</sup>
plasma mode	dry plasma
forward power	1200 W
accelerating voltage	10 kV
cool gas	15.5 L min <sup>-1</sup>
auxiliary gas	0.8 L min <sup>-1</sup>
sample gas	1 L min <sup>-1</sup>
sampler cone	standard Ni cone
skimmer cone	standard Ni cone
desolvator <sub>1</sub>	Apex (ESI)
desolvator <sub>2</sub>	Aridius II
nebulizer	60 µL min <sup>-1</sup> PFA microconcentric

### II.3.1 Mass interferences

The interferences due to nickel (<sup>58</sup>Ni<sup>2+</sup>, <sup>60</sup>Ni<sup>2+</sup>) and iron (<sup>56</sup>Fe<sup>2+</sup>, <sup>58</sup>Fe<sup>2+</sup>) are eliminated by the column chromatography chemistry because they can create interferences by forming doubly charged ions located at the same *m/z* values as silicon isotopes (Engström et al., 2006). Isobaric interferences such as from compounds containing carbon, nitrogen and/or oxygen and hydrides (<sup>28</sup>SiH<sup>+</sup> and <sup>29</sup>SiH<sup>+</sup>), that are an unavoidable by-product of ionisation in a plasma, are avoided by the resolution performance of the Neptune (Engström et al., 2006). The resolution of the machine is its ability to separate masses at the entrance slit and can be set to low, medium or high. Improvement of the resolution allows a better separation of the masses but leads to a decrease in the signal, and therefore, the medium resolution was the best compromise for our analyses. The resolving power (resolution: *R*) for a multi-collector mass spectrometer is calculated according to Weyer and Schwieters (2003) as follows:

$$R = \frac{m}{\Delta m}, \quad (2.1)$$

where *m* is the mass of the isotope (30 for silicon) and  $\Delta m$  is the difference between 5 and 95% of the mass intensity signal. An average *R* of 6317.33 atomic mass unit (amu) was obtained at medium resolution during this study.

The remaining interferences with the  $^{14}\text{N}_2$  and the  $^{14}\text{N}^{16}\text{O}$  are negligible for the 28 and 29 masses, but not for the 30 due to the high magnitude of the signal (De La Rocha, 2002). For high precision and to measure the  $^{30}\text{Si}/^{28}\text{Si}$  ratio a flat top peak is required. As it was not the case, high resolution was used to better identify the interferences. The interference of  $^{28}\text{Si}$  is on the right end side of the peak and negligible for  $^{29}\text{Si}$  (interference signal compared to isotope signal), and therefore,  $^{29}\text{Si}$  is used to detect the centre peak and to configure the cup for analyses.

### II.3.2 Mass bias

Mass bias occurs when the heavy isotope is discriminate (mass discrimination effects) during the transmission of the isotopes through the mass spectrometer on their way to the detector. It is the main difficulty that needs to be overcome for the measurement of accurate isotopes ratios. The mass bias in plasma mass spectrometers is much greater than in conventional gas source isotope ratio mass spectrometers mainly because the skimmer cone focuses heavier isotopes preferentially into the ion beam over the lighter isotopes which due to their lighter mass are more easily deflected. To correct for mass bias we used two methods, the external mass bias correction (Cardinal et al., 2003) and the standard-sample-standard-bracketing (Hoefs, 1996).

The external correction requires measuring the isotope ratio of an element of known isotopic composition and with a mass as close as possible to the targeted element, assuming that within this narrow mass range, the bias of the MC-ICP-MS is independent of the elemental species (Platzner et al., 1997). From the deviation of the measured ratio from the known a simple mass difference calculation may be carried out to obtain the magnitude of the mass bias. For silicon the external correction is applied using magnesium ( $^{25}\text{Mg}$  and  $^{26}\text{Mg}$ ) as follows:

$$\left(\frac{^{30}\text{Si}}{^{28}\text{Si}}\right)_{\text{corr}} = \left(\frac{^{30}\text{Si}}{^{28}\text{Si}}\right)_{\text{meas}} \times \left(\frac{^{30}\text{Si}_{\text{AM}}}{^{28}\text{Si}_{\text{AM}}}\right)^{\epsilon_{\text{Mg}}} \quad (2.2)$$

where  $(^{30}\text{Si}/^{28}\text{Si})_{\text{corr}}$  (the corrected ratio of  $^{30}\text{Si}$  to  $^{28}\text{Si}$ ) is calculated,  $(^{30}\text{Si}/^{28}\text{Si})_{\text{meas}}$  is the measured ratio of  $^{30}\text{Si}$  to  $^{28}\text{Si}$ , and  $^{30}\text{Si}_{\text{AM}}$  and  $^{28}\text{Si}_{\text{AM}}$  are the atomic masses of  $^{30}\text{Si}$  and  $^{28}\text{Si}$ .  $\epsilon_{\text{Mg}}$  is calculated from the beam intensities at Mg masses 25 and 26 as follows (Cardinal et al., 2003):

$$\epsilon_{\text{Mg}} = \ln \left[ \frac{\left(\frac{^{25}\text{Mg}}{^{26}\text{Mg}}\right)_{\text{nat}}}{\left(\frac{^{25}\text{Mg}}{^{26}\text{Mg}}\right)_{\text{meas}}} \right] \div \ln \left[ \frac{^{25}\text{Mg}_{\text{AM}}}{^{26}\text{Mg}_{\text{AM}}} \right] \quad (2.3)$$

where  $(^{25}\text{Mg}/^{26}\text{Mg})_{nat}$  is the ratio expected based on the natural abundances of the isotopes,  $(^{25}\text{Mg}/^{26}\text{Mg})_{meas}$  is the ratio measured, and  $^{25}\text{Mg}_{AM}$  and  $^{26}\text{Mg}_{AM}$  are the atomic masses of  $^{25}\text{Mg}$  and  $^{26}\text{Mg}$ .

We applied the sample-standard bracketing that leads to three series of measurements for the standard with in between two measurements of a sample. As the standard is compared to the sample during all analyses, and as the mass bias affects the sample and the standard in the same way, the correction by the standard between each sample measurement allows for the calculation of a corrected value of the sample. This led to the calculation of the isotopic ratio of a sample as follows:

$$\delta^{30}\text{Si}_x = \left[ \frac{\left( \frac{^{30}\text{Si}}{^{28}\text{Si}} \right)_x}{\left( \frac{^{30}\text{Si}}{^{28}\text{Si}} \right)_{std}} - 1 \right] \cdot 1000 \quad (2.4)$$

$$\delta^{30}\text{Si} = \frac{(\delta^{30}\text{Si}_1 + \delta^{30}\text{Si}_2 + \delta^{30}\text{Si}_3)}{3} \quad (2.5)$$

where  $x$  denotes the sample, and  $std$  the standard.

## II.4 Measurement conditions

For each run the mass spectrometer is calibrated using a silicon standard, the NBS28 or a working standard to give the best signal on the  $^{28}\text{Si}$  at medium resolution. This signal is obtained by moving the torch to the best position. The signal was decreased by 20% to make it more stable during the run when using the Apex. The isotopic values of the ANTXXIII/9 campaign's samples are the average of thirty measurements of twenty three seconds per sample using the Apex. It was decreased to twenty-five measurements of fourteen seconds for the campaigns ANTXXIV/3 and MSM 10/1 using the Aridus II. As previously mentioned, standards are measured after every sample with the standard bracketing technique. After each measurement a blank solution was used to rinse the system and prevent a memory effect.

The precision on individual measurements of  $\delta^{30}\text{Si}$  was typically  $\pm 0.04 \text{ ‰}$  for the dataset of the campaign ATNXXIV/3 and  $\pm 0.07 \text{ ‰}$  for the campaigns ANTXXIII/9 and MSM10/1 ( $1 \sigma$  standard deviation). The long term precision (also  $1 \sigma$  SD) for the procedure (i.e. including the column chemistry) was  $\pm 0.07 \text{ ‰}$ . Backgrounds and procedural blanks were both less than 1 % of the sample signal. For the runs where the background was higher than the 1 % a corrected value was calculated by subtracting the blank. Measured values fell along the expected kinetic mass dependent fractionation line calculated as follows (De La Rocha, 2002):

$$\delta^{30}\text{Si} = \delta^{29}\text{Si} \cdot \left(\frac{29}{30}\right) \cdot \frac{(30-28)}{(29-28)} = \delta^{29}\text{Si} \cdot 1.93 \quad (2.6)$$

## II.5 Data validation

Three main parameters were assessed during data validation. The first parameter that is useful for selecting data is the ratio of the signal of the sample measured on the  $^{28}\text{Si}$  compared to the signal of the  $^{28}\text{Si}$  from the standard (sample: standard ratio). A value of one means that the concentrations of both are the same, allowing us to keep the sample. Samples with a ratio greater than 80 % were excluded because if the sample is too far from the standard it is impossible to certify that it went through the same mass fractionation, or whether the drift of the machine affected it to the same extent.

The second parameter assessed was the sample to standard ratio of the  $\epsilon_{\text{Mg}}$  that allows for the tracking of the mass fractionation of the machine. To have a value that can be properly corrected for mass bias it has to be the same Mg value as the standard and with the same intensity. Therefore, we rejected samples with an intensity ratio below 80 % and a  $\epsilon_{\text{Mg}}$  ratio that deviated from 1 by more than 0.1 %.

The final parameter assessed was the value of the  $^{30}\text{Si}/^{29}\text{Si}$  ratio. There are two mass fractionation isotope laws in nature, the kinetic and the equilibrium (Young et al., 2002). The kinetic effect is the fact of incomplete and unidirectional movement of molecules or isotopes, while the equilibrium effect is an exchange reaction between two phases of a compound taking into account isotopic mass (Hoefs, 1996; Engström et al., 2006). The kinetic law is expressed as  $\delta^{30}\text{Si} = 1.93 \cdot \delta^{29}\text{Si}$  and the equilibrium law is written  $\delta^{30}\text{Si} = 1.96 \cdot \delta^{29}\text{Si}$ . The robustness of the data is verified doing a plot of the  $\delta^{29}\text{Si}$  values against the  $\delta^{30}\text{Si}$ , and comparing them with the mass-fractionation theoretical line. Presented here are our values of  $\delta^{29}\text{Si}$  versus  $\delta^{30}\text{Si}$  for the three campaigns (Fig. 2.3).

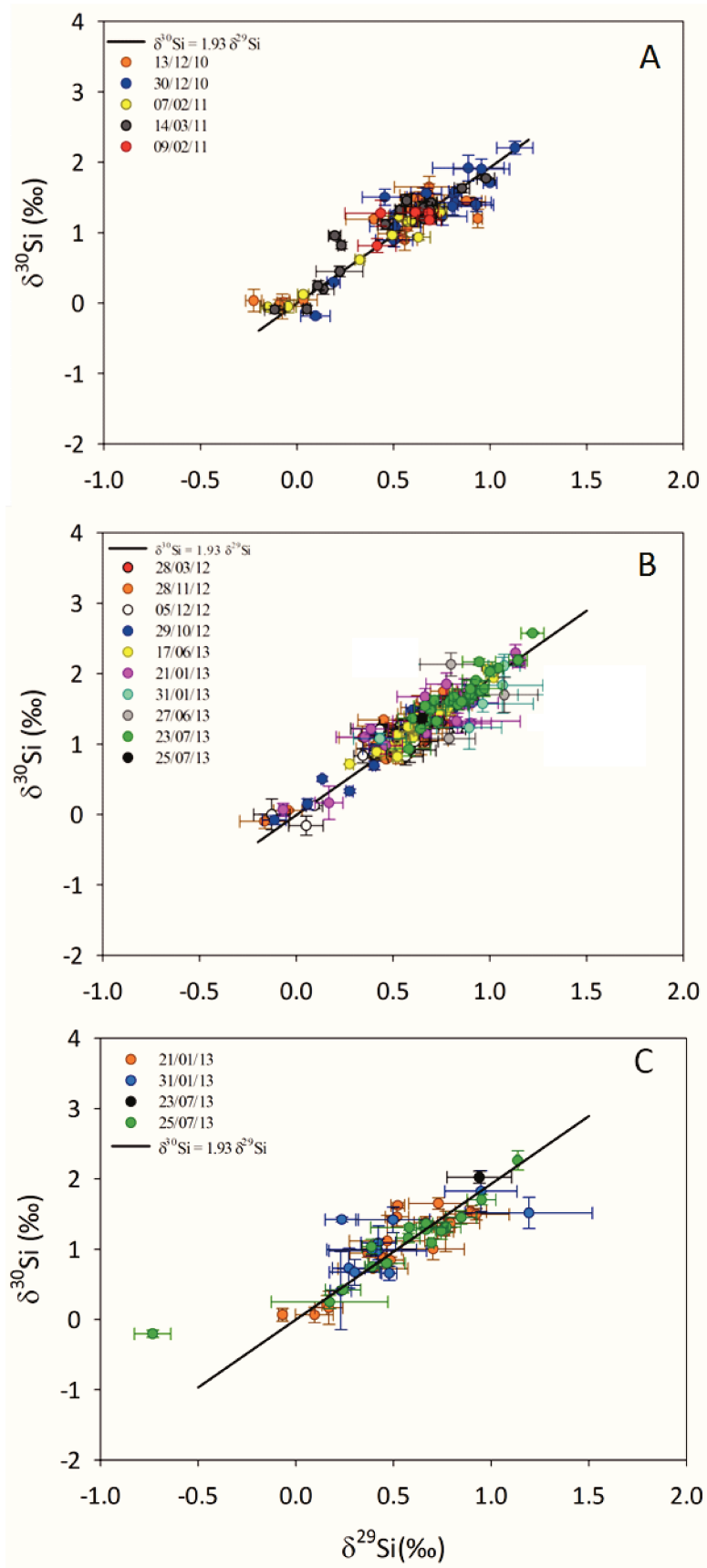


Figure 2.3 Samples measurement of the ratio  $\delta^{29}\text{Si}$  vs.  $\delta^{30}\text{Si}$  for A) ANTXXIII/9 campaign, B) ANTXXIV/3 campaign and C) MSM10/1 campaign, along the fractionation line  $\delta^{30}\text{Si} = 1.93 \cdot \delta^{29}\text{Si}$ . Each session on the MC-ICPMS is represented by a different colour, standard deviation ( $1 \sigma$ ).



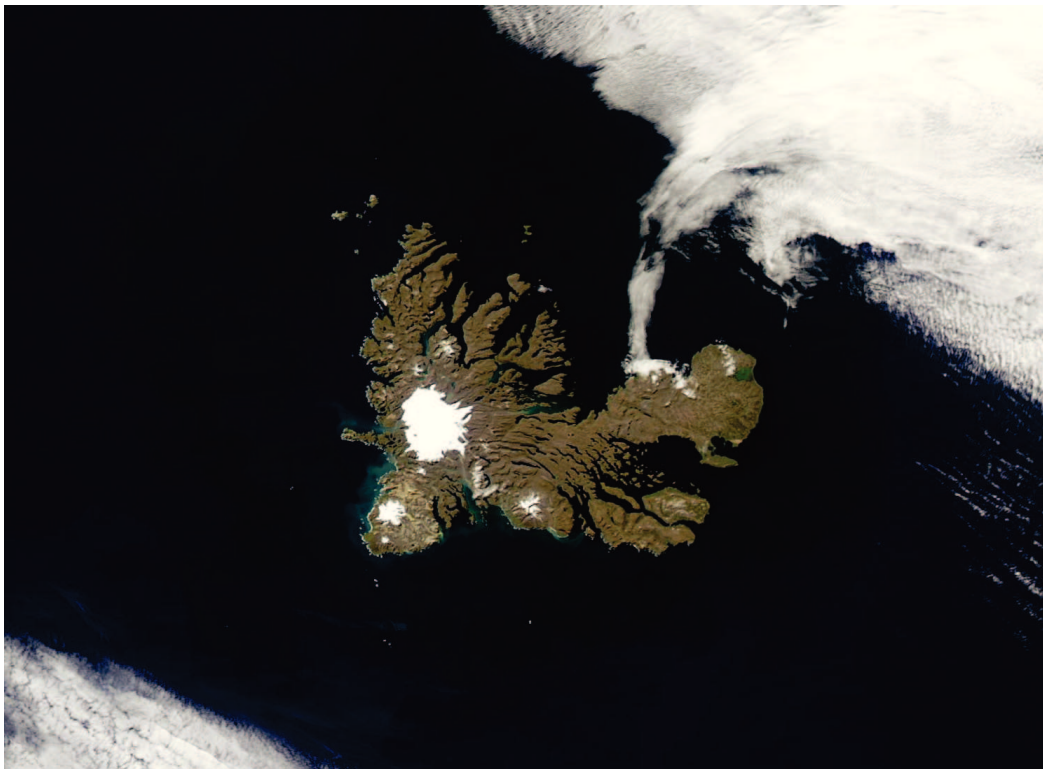


---

# Exploring interacting influences on the silicon isotopic composition of the surface ocean: a case study from the Kerguelen Plateau

## — Chapter 3 —

---



# Chapter 3 – Exploring influences on the silicon isotopic composition of the surface ocean: A case study from the Kerguelen Plateau

---

N. Coffineau<sup>1</sup>, C.L. De La Rocha<sup>1</sup> and P. Pondaven<sup>1</sup>

[1] {CNRS UMR 6539, Institut Universitaire Européen de la Mer, Université de Bretagne Occidentale, Plouzané, France}

Correspondence to: N. Coffineau ([Nathalie.Coffineau@univ-brest.fr](mailto:Nathalie.Coffineau@univ-brest.fr))



# Exploring interacting influences on the silicon isotopic composition of the surface ocean: a case study from the Kerguelen Plateau

N. Coffineau, C. L. De La Rocha, and P. Pondaven

Institut Universitaire Européen de la Mer, CNRS UMR6539, Université de Bretagne Occidentale, Plouzané, France

Correspondence to: N. Coffineau (nathalie.coffineau@univ-brest.fr)

Received: 28 June 2013 – Published in Biogeosciences Discuss.: 10 July 2013

Revised: 30 November 2013 – Accepted: 21 January 2014 – Published: 12 March 2014

**Abstract.** This study presents six new water column profiles of the silicon isotopic composition ( $\delta^{30}\text{Si}$ ) of dissolved silicon (DSi) from the Atlantic and Indian sectors of the Southern Ocean and a variable depth box model of silica cycling in the mixed layer that was constructed to illuminate the evolution of surface ocean  $\delta^{30}\text{Si}$  over the full course of a year. In keeping with previous observations,  $\delta^{30}\text{Si}$  values ranged from +1.9 to +2.4‰ in the mixed layer (ML), +1.2 to +1.7‰ in Winter Water (WW), and +0.9 to +1.4‰ in Circumpolar Deep Water (CDW). These data also confirmed the occurrence of diminished values for ML  $\delta^{30}\text{Si}$  at low DSi concentrations in early austral autumn on the Kerguelen Plateau. The box model was used to investigate whether these low, post-growing season values of  $\delta^{30}\text{Si}$  were related to input of DSi to the ML from basalt weathering, biogenic silica dissolution (with or without isotopic fractionation), the onset of winter mixing, or some combination of the three. Basalt weathering and fractionation during biogenic silica dissolution could both lower ML  $\delta^{30}\text{Si}$  below what would be expected from the extent of biological uptake of DSi. However, the key driver of the early autumn decrease in  $\delta^{30}\text{Si}$  appears to be the switch from bloom growth (with net removal of DSi and net accumulation of biogenic silica (BSi) biomass) to steady state growth (when slow but continuing production of BSi prevented significant net increase in DSi concentrations with diffusive input of DSi from WW but not decrease in ML  $\delta^{30}\text{Si}$  towards WW values). Model results also indicated that fractionation during dissolution has only a negligible effect on the  $\delta^{30}\text{Si}$  of BSi exported throughout the course of the year. However, seasonal changes in export efficiency (e.g. favouring the export of bloom BSi versus the export of BSi produced during other times of the year) should strongly influence the  $\delta^{30}\text{Si}$  of BSi accumulating in marine sediments.

Finally, the choice for the parameterisation of the mixing between the ML and the WW in terms of  $\delta^{30}\text{Si}$  (i.e. constant or allowed to vary with the seasonal migration of the thermocline) is critical to take into account in box model simulations of the silica biogeochemical cycle. Altogether, these results suggest that as a paleoceanographic proxy,  $\delta^{30}\text{Si}$  may more reflect the dominant mode of production of the BSi that is exported (i.e. bloom versus steady state growth) rather than strictly the extent of DSi utilisation by diatoms.

## 1 Introduction

Diatoms, which are phytoplankton that produce frustules of amorphous, hydrated silica (opal), fractionate silicon isotopes when they take up dissolved silicon (DSi) and use it to produce this biogenic silica (BSi). This results in BSi with a silicon isotopic composition ( $\delta^{30}\text{Si}$ ) roughly  $-1.1$ ‰ lower relative to its DSi source and marine surface waters with  $\delta^{30}\text{Si}_{\text{DSi}}$  values that generally increase as DSi is increasingly removed by diatoms (De La Rocha et al., 1997, 2000, 2011; Milligan et al., 2004; Varela et al., 2004; Cardinal et al., 2005; Beucher et al., 2008, 2011; Fripiat et al., 2011b; Fripiat et al., 2011c; de Brauwere et al., 2012; de Souza et al., 2012a). A pure relationship between the biological removal and the isotopic composition of DSi is, however, complicated by input of DSi to the surface ocean through vertical mixing (and the episodic versus continuous nature of this input relative to the biological uptake of DSi), the dissolution of BSi (a process which may have an isotopic fractionation of  $-0.55$ ‰ associated with it; Demarest et al., 2009), and, in relevant regions, the weathering of lithogenic silica such as basalt (Fripiat et al., 2011b, c; Oelkers et al., 2011).

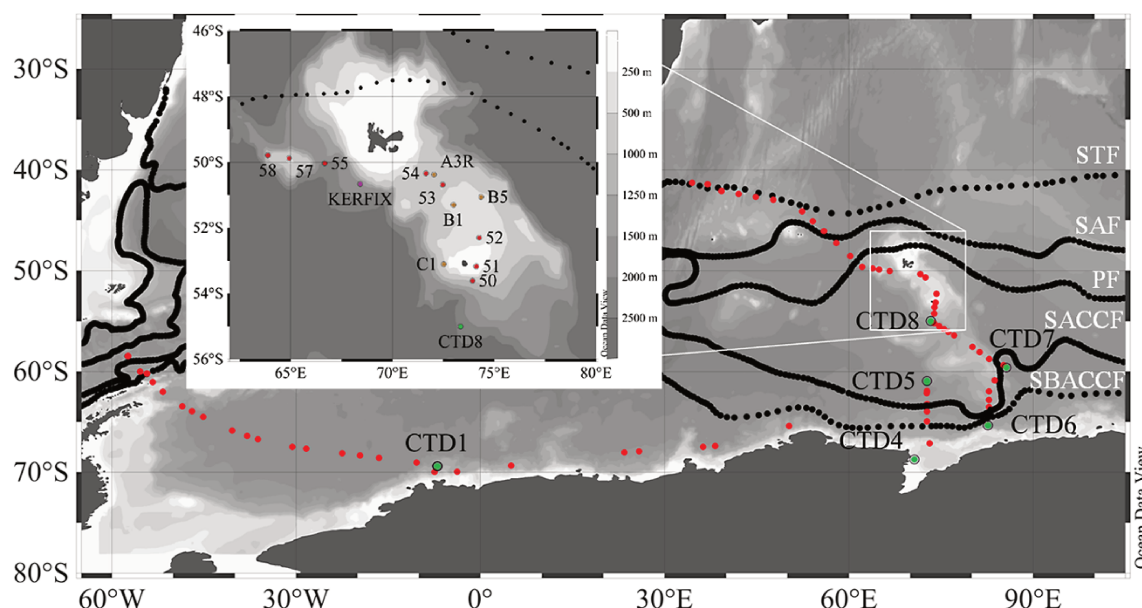


**Fig. 1.** Map of the study area in the Atlantic and Indian sectors of the Southern Ocean. Red dots are surface water samples from De La Rocha et al. (2011) and green dots represent the CTD stations from this study. The inset shows the area from the north of Kerguelen Island to the south of Heard Island to show the Kerguelen Plateau in more detail. Stations numbered A3R, B1, B5 and C1 are KEOPS stations from Fripiat et al. (2011b), the KERFIX time series site is from Jeandel et al. (1998), stations numbered from 50 to 55 are surface samples from De La Rocha et al. (2011), and CTDs from 1 to 8 are from this study. Black lines represent the Subtropical Front (STF), the Subantarctic Front (SAF), the Polar Front (PF), the Southern Antarctic Circumpolar Current Front (SACCF), and the Southern Boundary of the Antarctic Circumpolar Current Front (SBACCF) of the Antarctic Circumpolar Current.

One of the places where the distribution of silicon isotopes has been most intensely investigated is the Southern Ocean, which, in addition to being one of the major high nutrient, low chlorophyll (HNLC) regions of the ocean, is an ocean with a strong and dynamic silica cycle. Among the Southern Ocean's key features is the Antarctic Circumpolar Current (ACC) that connects the Indian, Atlantic, and Pacific ocean basins (Orsi et al., 1995). This strong circumpolar flow is diverted in places by submarine topography and this is particularly the case for the Kerguelen Plateau (Fig. 1) (Orsi et al., 1995; Cunningham, 2005; Park et al., 2008). The Kerguelen Plateau is a large igneous province (LIP) in the Indian sector of the Southern Ocean that acts as a barrier to the circumpolar flow of the ACC, forcing 2/3 of the flow to pass along the northern escarpment of the plateau, which lies to the north of Kerguelen Island, and the remaining third to flow through the Fawn Trough, which lies to the south of Heard Island (Park et al., 1993; Mongin et al., 2008; Roquet et al., 2009). Thus, despite being in the midst of the ACC, the relatively shallow region between Kerguelen Island and Heard Island represents a zone of weak eastward circulation (Park et al., 1998b; McCartney and Donohue, 2007; Roquet et al., 2009), with the potential for a high degree of nutrient recycling (due to its retention of water and particulates) and of input of material from the subaerial and submarine weathering of basalt. These factors, along with natural iron fertilization on the plateau (Blain et al., 2007), allow considerable

biological nutrient removal and buildup of standing stocks of chlorophyll and BSi to occur in this area during phytoplankton blooms relative to the surrounding open ocean waters of the ACC (De La Rocha et al., 2011; Fripiat et al., 2011b).

Interestingly, in this region between Kerguelen Island and Heard Island, the  $\delta^{30}\text{Si}$  of DSi in surface waters (depths of 10–50 m) at low concentrations of DSi is high (+2.4 to +2.7‰ at 2 to 12  $\mu\text{M}$ ) in late January/early February (about six weeks into austral summer) (Fripiat et al., 2011b). This is as expected from a high degree of biological removal of DSi, but by the end of March (early austral autumn) this is no longer the case (De La Rocha et al., 2011). At this point, at concentrations of DSi which are still low (4 to 17  $\mu\text{M}$ ), surface water  $\delta^{30}\text{Si}$  clusters around +1.8‰ (De La Rocha et al., 2011), suggesting that some process has lowered surface water  $\delta^{30}\text{Si}$  without notably increasing DSi concentrations. This early autumn decrease in  $\delta^{30}\text{Si}$  could represent the beginning of seasonal mixing of Winter Water (whose  $\delta^{30}\text{Si}$  ranges between +1.2 and +2.2‰ (Fripiat et al., 2011b)) into the surface mixed layer on the plateau. Alternatively, the DSi pool in the mixed layer in early autumn, when DSi concentrations are low, could contain a maximal proportion of DSi from basalt weathering (which could have a  $\delta^{30}\text{Si}$  of anywhere from −1.0 to +1.5‰ (Ziegler et al., 2005; Georg et al., 2007b), based on studies of the subaerial weathering of basalt). Lastly, the early autumn DSi pool could also or instead contain a significantly high proportion of DSi that was

dissolved from sinking BSi, which would also act to lower its  $\delta^{30}\text{Si}$ .

To examine these possibilities, we constructed a biogeochemical model of silica and silicon isotope cycling in the region. In this model, phytoplankton growth rates are controlled by the availability of light (i.e. depending on day length and mixed layer depth) and DSi concentrations. DSi is input to the mixed layer by deepening of the mixed layer depth and, in some simulations, from basalt weathering. The DSi incorporated into BSi that does not dissolve within the mixed layer is exported from it through sinking. This model differs considerably from the models recently presented by de Brauwere et al. (2012) and Fripiat et al. (2012) by being driven by changes in mixed layer depth and day length and by incorporating basalt as a potential source of DSi. This model can be used to track the size and  $\delta^{30}\text{Si}$  of dissolved and biogenic silica pools throughout the year and to follow the  $\delta^{30}\text{Si}$  values related to bloom versus steady state phytoplankton growth and silica production, surface ocean stratification versus mixing, and the dissolution of BSi and/or basalt.

## 2 Material and methods

### 2.1 Data sampling and analyses

During the ANTXXIII/9 campaign that took place in the Southern Ocean in February–April 2007, samples for silicon isotopes ( $\delta^{30}\text{Si}$ ) were collected from six depth profiles (Fig. 1) along the edge of the ice shelf in the Atlantic and Indian sectors of the Southern Ocean and on the Kerguelen Plateau (see De La Rocha et al. (2011) for more details of the cruise). Water samples from the Niskin bottle rosette were filtered through 0.6  $\mu\text{m}$  polycarbonate filters and then stored at room temperature in acid-cleaned LDPE bottles. The dissolved silicon concentrations of these never-frozen samples were measured colorimetrically with a spectrophotometer (Shimadzu UV-1700) following the formation and reduction of silicomolybdate (Strickland and Parsons, 1972).

The first step in the isotopic analysis of the DSi was its extraction as triethylamine silicomolybdate and then combustion to form  $\text{SiO}_2$  (De La Rocha et al., 1996). This silica was dissolved in 40% HF at an F:Si ratio of 100 mol mol<sup>-1</sup>, ensuring enough of an excess of F to form  $\text{SiF}_6^{2-}$  ions rather than  $\text{SiF}_4$  gas. The silicon was further purified via anion exchange chromatography following Engström et al. (2006), as detailed in De La Rocha et al. (2011). In brief, samples of 4  $\mu\text{mol}$  Si in 52 mM HF were loaded onto columns of AG 1-X8 resin (100–200 mesh, Eichrom) preconditioned with 2 M NaOH. Any contaminants remaining after the initial extraction and combustion were eluted using a solution of 95 mM HCl + 23 mM HF. Purified Si was then eluted with a solution of 0.14 M  $\text{HNO}_3$  + 5.6 mM HF. All acids used were Suprapur (Merck) and were diluted using MilliQ water (18.2 M $\Omega$  cm<sup>-1</sup>).

Purified samples were diluted to 2 ppm Si and doped with 0.1 ppm Mg and measurement of silicon isotope ratios was carried out in Brest, France on a Neptune MC-ICP-MS (Thermo Scientific) (see Table 1 for operating conditions). Values of  $^{30}\text{Si}/^{28}\text{Si}$  and  $^{29}\text{Si}/^{28}\text{Si}$  were initially corrected for instrumental mass bias using Mg correction (Cardinal et al., 2003), for example:

$$\left(\frac{^{30}\text{Si}}{^{28}\text{Si}}\right)_{\text{corr}} = \left(\frac{^{30}\text{Si}}{^{28}\text{Si}}\right)_{\text{meas}} \times \left(\frac{^{30}\text{Si}_{\text{AM}}}{^{28}\text{Si}_{\text{AM}}}\right)^{\varepsilon_{\text{Mg}}}, \quad (1)$$

where  $(^{30}\text{Si}/^{28}\text{Si})_{\text{corr}}$  (the corrected ratio of  $^{30}\text{Si}$  to  $^{28}\text{Si}$ ) is calculated from  $(^{30}\text{Si}/^{28}\text{Si})_{\text{meas}}$  (the measured ratio of  $^{30}\text{Si}$  to  $^{28}\text{Si}$ ),  $^{30}\text{Si}_{\text{AM}}$  and  $^{28}\text{Si}_{\text{AM}}$  (the atomic masses of  $^{30}\text{Si}$  to  $^{28}\text{Si}$ ), and  $\varepsilon_{\text{Mg}}$ , which has been calculated from the beam intensities at mass 25 and 26:

$$\varepsilon_{\text{Mg}} = \ln \left[ \frac{^{25}\text{Mg}_A / ^{26}\text{Mg}_A}{\left(\frac{^{25}\text{Mg}}{^{26}\text{Mg}}\right)_{\text{meas}}} \right] \div \ln \left[ \frac{^{25}\text{Mg}_{\text{AM}}}{^{26}\text{Mg}_{\text{AM}}} \right], \quad (2)$$

where  $^{25}\text{Mg}_A / ^{26}\text{Mg}_A$  is the ratio expected based on the known natural abundances of the isotopes,  $(^{25}\text{Mg} / ^{26}\text{Mg})_{\text{meas}}$  is the ratio that was measured, and  $^{25}\text{Mg}_{\text{AM}}$  and  $^{26}\text{Mg}_{\text{AM}}$  are the atomic masses of  $^{25}\text{Mg}$  and  $^{26}\text{Mg}$ .

Measurements of samples occurred between measurements of the standard NBS28, with each reported value consisting of three full measurements of a standard and two full measurements of a sample, with the values reported as  $\delta^{30}\text{Si}$ :

$$\delta^{30}\text{Si} = \frac{R_{\text{sam}} - R_{\text{std}}}{R_{\text{std}}} \times 10^3, \quad (3)$$

where  $R_{\text{sam}}$  is the Mg-corrected sample  $^{30}\text{Si}/^{28}\text{Si}$  and  $R_{\text{std}}$  the Mg-corrected ratio for NBS28.

The precision on individual measurements of  $\delta^{30}\text{Si}$  was typically  $\pm 0.04\%$  ( $1\sigma$  standard deviation). The long-term precision (also  $1\sigma$  SD) for the procedure (i.e. including the column chemistry) was  $\pm 0.07\%$ . Backgrounds and procedural blanks were both less than 1 % of the sample signal. Measured values fell along the expected mass-dependent fractionation line  $\delta^{30}\text{Si} = (\delta^{29}\text{Si})1.93$ .

### 2.2 Model

To better appreciate the processes controlling the behaviour of  $\delta^{30}\text{Si}$  on the Kerguelen Plateau, we built a one-box model of the silica cycle in the surface mixed layer in this area, as described in detail in the following sections. Among other things, this model takes into consideration seasonal variation in the depth of the mixed layer using techniques developed in previous modelling studies (Evans and Parslow, 1985; Fasham et al., 1990; Platt et al., 2003). As such, the model was parameterised in part by using data from the slightly off-plateau KERFIX time series site, and the model results were

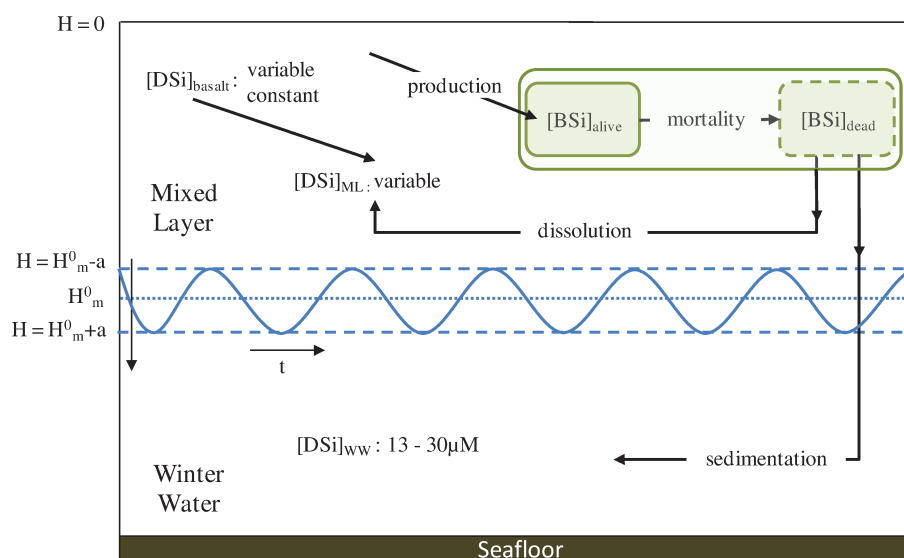


**Fig. 2.** Schematic representation of the box model, adapted from Platt et al. (2003). Dissolved silicon in the mixed layer ( $DSi_{ML}$ ) is supplied by the Winter Water (WW) through mixing, by the dissolution of non-living diatoms ( $BSi_D$ ) in the mixed layer (ML), and, in some runs, by the weathering of basalt ( $DSi_{bst}$ ).  $DSi_{bst}$  can be null, a constant, or variable input to the ML.  $DSi_{ML}$  is converted to living biomass ( $BSi_A$ ) during diatom growth.  $BSi_D$  is produced by mortality of  $BSi_A$ .  $BSi_D$  is exported by sedimentation and by mixing process, while  $BSi_A$  is not allowed to sink. Concentrations of  $BSi_A$  and  $BSi_D$  can be diluted by mixing and losses can be incurred by deepening of the ML. The ML depth ( $H_m$ ) throughout the year is based on KERFIX data (Jeandel et al., 1998) following a time step  $t$  of  $0.05 \text{ d}^{-1}$ .

**Table 1.** Operating conditions for the Neptune MC-ICP-MS.

Resolution	Medium
Sensitivity	$\sim 6 \text{ V ppm}^{-1}$
Forward power	1200 W
Accelerating voltage	10 kV
Cool gas	$15.5 \text{ L min}^{-1}$
Auxiliary gas	$0.8 \text{ L min}^{-1}$
Sample gas	$1 \text{ L min}^{-1}$
Sampler cone	Standard Ni cone
Skimmer cone	Standard Ni cone
Desolvator	Apex (ESI)
Nebulizer	$60 \mu\text{L min}^{-1}$
	PFA microconcentric

compared to data from KERFIX and from stations located in different areas of the plateau in order to assess whether or not the model was behaving in a realistic manner. The purpose of this modelling exercise was thus not to obtain an exact match with the Kerguelen Plateau data, but to create a reasonably realistic model of silica cycling that could be used to explore the effects of different processes on the cycling of silicon isotopes.

### 2.2.1 Model structure

We used a simple box model to simulate the main features of the seasonal variations in DSi and BSi observed in the gen-

eral vicinity of the Kerguelen Plateau. The model consisted of 1 variable depth box (Fig. 2), the mixed layer (ML), which is the sunlit (euphotic) zone where phytoplankton grow. The model was forced using the observed climatology of (1) the ML depth, (2) the concentration of DSi below the ML, and (3) the light intensity at the surface around the KERFIX time series station located at the edge of the Kerguelen Plateau ( $50^\circ 40' \text{ S}$ ,  $68^\circ 25' \text{ E}$ ) (Jeandel et al., 1998; Park et al., 1998a; Fasham et al., 2006). This station sits at the “upstream” side of the plateau where water depths are  $> 1500 \text{ m}$  and is thus not a true “on plateau” location, but the KERFIX data set is the only 5-year, fairly continuous, seasonally resolved data set available for this area and provides a reasonable basis from which to explore the seasonal dynamics that control the changes in the  $\delta^{30}\text{Si}$  of DSi and BSi in surface waters. The small intrinsic time step ( $0.05 \text{ d}^{-1}$ ) utilised in the modelling allows consideration of the model as if all processes (mixing, production, dissolution, etc) occurred concurrently. For each simulation, the model was run from 1 July (austral winter) until 30 June. Model spin-up was attained after the 3rd year; the results given in this paper are from year 6 of each model run.

Following Fasham et al. (1990), the ML was considered biologically homogeneous. The depth of the ML varied from 72 to 215 m, depending on the time of year, in accordance with the data from KERFIX (Jeandel et al., 1998). The deepening of the mixed layer via convective overturning in autumn diluted the ML diatom biomass and replenished the surface box with DSi (whose concentration decreased during



spring and summer because it was used for diatom growth). Conversely, when the mixed layer shoaled, there was no dilution of biomass and nutrient input to the ML occurred only through diffusion. BSi was produced only in the ML and was not returned from WW to the surface box via mixing. The concentration of DSi in the WW added to the ML was allowed to vary through the seasons based on DSi data from KERFIX. The isotopic composition ( $\delta^{30}\text{Si}$ ) of the WW, however, was fixed at 1.60 ‰, representing an average between values from the KEOPS data set ( $1.80 \pm 0.24$  ‰ (Fripiat et al., 2011b)) and  $+1.40 \pm 0.04$  ‰ from CTD 8 (see results).

For the sake of simplicity and because the concentrations of the other macronutrients are never low enough in this region to be limiting to phytoplankton growth (Jacques, 1983; Sommer, 1986), DSi was the only nutrient represented in this model. In addition, the diatoms (in the form of biogenic silica, BSi) were the only phytoplankton represented as they are the main group influencing the silica cycle in the modern day ocean (Jeandel et al., 1998; Tréguer and De La Rocha, 2013).

BSi production in the ML was governed by the concentration of living BSi, the DSi concentration, and the availability of light (which depended on day length and ML depth). BSi was lost from the ML through both sinking (export) or dissolution back to DSi in the ML. Thus changes in the concentrations of DSi and BSi in the ML were controlled by a combination of physical processes (mixing, BSi dissolution, and BSi sinking) and biological processes (DSi uptake, BSi production, and diatom mortality).

## 2.2.2 Model equations

### Equations for change in concentrations of DSi and BSi

Temporal changes in the concentrations of DSi and biogenic silica ( $\text{BSi}_A$  for living diatoms,  $\text{BSi}_D$  for dead diatoms) are written:

$$\frac{d\text{DSi}}{dt} = M_{\text{bst}} + M_{\text{WW}}^{\text{DSi}} - P + D, \quad (4)$$

$$\frac{d\text{BSi}_A}{dt} = -M_{\text{WW}}^{\text{BSi}_A} + P - M_t, \quad (5)$$

$$\frac{d\text{BSi}_D}{dt} = -M_{\text{WW}}^{\text{BSi}_D} + M_t - D - E. \quad (6)$$

In Eq. (4),  $M_{\text{bst}}$  ( $\mu\text{mol-Si L}^{-1}$ ) is the quantity of DSi input from the basalt weathering. Basalt input is zero, constant, or variable depending on the run. The constant input ( $0.001103 \mu\text{mol L}^{-1}$  per time step) sums to an amount equivalent to 10 % of the yearly total DSi input from the WW while the variable input is a quantity equal to 10 % of the WW input at each time step. In all equations,  $M_{\text{WW}}$  is the mixing of DSi or BSi between the WW and the ML (through diffusion and entrainment). In Eqs. (4) and (5)  $P$  is the production of BSi in the ML, and  $D$  is BSi dissolution. Finally, in Eqs. (5) and (6),  $M_t$  is the amount of dead diatom biomass

and  $E$  is the quantity of dead diatom biomass exported out of the ML. Each of these processes is described below.

Mixing ( $M_{\text{WW}}$ ) is parameterised in the same manner for  $\text{BSi}_A$  and  $\text{BSi}_D$  according to (Evans and Parslow, 1985; Fasham et al., 1990). For DSi, this term is written as

$$M_{\text{WW}}^{\text{DSi}} = \left( (\text{DSi}_{\text{WW}t} - \text{DSi}_{\text{ML}t-1}) \times \left( \frac{m}{H_{t-1}} + \frac{\max\left(\left(\frac{H_{t-1}-H_t}{dt}\right), 0\right)}{H_{t-1}} \right) \right), \quad (7)$$

where  $\text{DSi}_{\text{WW}}$  and  $\text{DSi}_{\text{ML}}$  are, respectively, the DSi concentrations in the Winter Water and mixed layer,  $m$  is the mixing coefficient (in units of  $\text{m d}^{-1}$ ),  $H$  is the depth, in m, of the mixed layer at time  $t$  (d), and  $(\text{DSi}_{\text{WW}} - \text{DSi}_{\text{ML}})$  is the gradient of concentration at the base of ML (Evans and Parslow, 1985; Fasham et al., 1990). This equation takes into account vertical mixing at the boundary between the two water masses and the motile and non-motile entities (Evans and Parslow, 1985; Fasham et al., 1990). This results in an increased concentration of DSi due to vertical mixing in the ML when mixed layer depth deepens, and in input of DSi to the ML from diffusive mixing only when the mixed layer depth shoals (Platt et al., 2003). In the model, the depth of the mixed layer ( $H$ ) at each time  $t$  is calculated by interpolating monthly averaged data from the KERFIX time series station (Jeandel et al., 1998; Park et al., 1998a; Fasham et al., 2006). Similarly, seasonal variations of the DSi concentration in the Winter Water ( $\text{DSi}_{\text{WW}}$ ) are calculated using monthly averaged data from KERFIX ([http://www.obs-vlfr.fr/cd\\_rom\\_dmtt/kfx\\_main.htm](http://www.obs-vlfr.fr/cd_rom_dmtt/kfx_main.htm)). The mixing of BSi is handled in exactly the same way as DSi (see Eq. 5), although the concentration of BSi in the WW is assumed to be  $0 \mu\text{mol L}^{-1}$ , so that BSi is not entrained into the ML from WW during mixing.

The second process ( $P$ ,  $\mu\text{mol-Si L}^{-1} \text{d}^{-1}$ ) represents the diatom growth rate, or the production of  $\text{BSi}_A$ . It is written as

$$P = \mu_{\text{max}} \times \left[ \frac{\text{DSi}}{\text{DSi} + K_{\text{Si}}} \times \left( 1 - \left( \exp\left(\frac{-\varphi P \times I_{H,t}}{\mu_{\text{max}}}\right) \right) \right) \right] \times \text{BSi}_A \quad (8)$$

In this equation, the diatom growth rate is governed by the availability of DSi and light by a multiplicative limitation term (Paasche, 1973). The maximal growth rate is  $\mu_{\text{max}}$  ( $\text{d}^{-1}$ ) and  $K_{\text{Si}}$  ( $\mu\text{mol L}^{-1}$ ) is the half-saturation constant for silicon uptake.

The  $\mu_{\text{max}}$  of  $1.5 \text{ d}^{-1}$  and the  $K_{\text{Si}}$  of  $4 \mu\text{M}$  were selected according to Sarthou et al. (2005, and references therein) as typical values for the maximal growth rate of diatoms and for the half-saturation constant associated with diatom uptake of silicic acid. These values can be, of course, quite different depending on the diatom species and physiological condition. For example,  $K_{\text{Si}}$  values may range from relatively low to values high enough to hold diatoms in a state of chronic growth rate limitation by silicic acid (Brzezinski and Nelson, 1996).  $K_{\text{Si}}$  values recently measured by Mosseri

et al. (2008) for large diatoms  $> 10 \mu\text{m}$  on the Kerguelen Plateau were as high as 4 to  $57 \mu\text{M}$ , although non-linear uptake behaviour at high DSi concentrations and some scatter in the data at lower concentrations yielded considerable uncertainties in the curve fits used to generate the  $K_{\text{Si}}$  values. In light of this, we tested the sensitivity of the model to these coefficients (see results sections).

The second part of the equation accounts for light limitation, with  $\bar{I}_H$ ,  $\text{W m}^{-2}$  being the mean intensity of light in the mixed layer and  $\varphi_P$  ( $\text{d}^{-1} (\text{W m}^{-2})^{-1}$ ) being the affinity of the phytoplankton for light (Platt and Jassby, 1976). The mean light intensity at time  $t$  is calculated using the Beer Lambert law of light extinction:

$$\bar{I}_{H,t} = \frac{1}{H_t} \int_{z=0}^{z=H_t} I_{0,t} \exp(-K_{\text{PAR},t} z) dz, \quad (9)$$

which gives:

$$\bar{I}_{H,t} = \left( \frac{I_{0,t}}{H_t} \right) \times \left( \frac{1 - \exp(-K_{\text{PAR},t} \times H_t)}{K_{\text{PAR},t}} \right). \quad (10)$$

In Eqs. (9) and (10),  $H_t$  is the depth of the mixed layer (m),  $I_{0,t}$  is the photosynthetically available radiation (PAR) at the surface of the ocean (in  $\text{W m}^{-2}$ ), and  $K_{\text{PAR},t}$  ( $\text{m}^{-1}$ ) is the extinction coefficient for PAR.

A climatology of the mean daily PAR at the surface of the ocean,  $I_{0,t}$  was built using predicted downward solar radiation from the European Centre for Meteorological Weather Forecast (ECMWF, in Fasham et al., 2006)

$$I_{0,t} = \frac{(130 + 20)}{2} + 55 \times \sin\left(2 \times \pi \times \frac{t}{365} + 243\right). \quad (11)$$

In Eq. (10),  $K_{\text{PAR},t}$  was calculated using the formulation of Nelson and Smith (1991):

$$K_{\text{PAR},t} = 0.04 + 0.0088 \times \text{Chl}_{a,t} + 0.054 \times \text{Chl}_{a,t}^{2/3}. \quad (12)$$

In the model, the biomass of chlorophyll a,  $\text{Chl}_{a,t}$ , was calculated from the BSi concentration using the molar ratios Si : N of 4 : 1 (a typical value for the Southern Ocean (Pondaven et al., 1998), especially given the heavy silicification of diatoms like *Fragilariopsis kerguelensis*) and C : N of 106 : 16 (the Redfield ratio), and a mass ratio of C : Chlorophyll of 80 : 1 (Chan, 1980) as follows:

$$\text{Chl}_{a,t} = \text{BSi}_A \times \frac{\text{C}}{\text{Si}} \times 12 \times \frac{\text{Chl}_a}{\text{C}}. \quad (13)$$

Si : N and C : N values are quite variable in nature, especially under conditions of silicon, light, and iron limitation. Use of different values would have the ultimate effect of either increasing or decreasing the phytoplankton growth rate, depending on the values used.

The last parameter of Eq. (4),  $D$  ( $\mu\text{mol-Si L}^{-1} \text{d}^{-1}$ ), accounts for dissolution of BSi. In the model, only dead diatoms ( $\text{BSi}_D$ ) are allowed to dissolve. It is calculated following Nugraha et al. (2012). The fraction of BSi dissolved in

the ML,  $\overline{\text{SR}}$ , depends on two parameters, the specific remineralisation rate of detritus ( $\tau$ ,  $\text{d}^{-1}$ ) and the sinking velocity of particles ( $V$ ,  $\text{m d}^{-1}$ ). The dissolution rate chosen, following Demarest et al. (2009), was  $0.035 \text{ d}^{-1}$ , a value which was observed for surface samples during the early stage of BSi dissolution (the first 0–10 % of dissolution of the biogenic silica). This value sits within the range of the in vivo dissolution rates measured in the Southern Ocean, being close to  $0.04 \text{ d}^{-1}$ , the minimum dissolution rate measured by Beucher et al. (2004) in the Pacific sector, but generally higher than the rates of 0.01 to  $0.04 \text{ d}^{-1}$  measured by Nelson and Gordon (1982) in austral spring in the ACC of the Pacific sector of the Southern Ocean. In the box model, we derived estimates of  $\overline{\text{SR}}$  using the following relationships:

$$\overline{\text{SR}} = \frac{1}{H_t} \int_{z=0}^{z=H_t} \left( 1 - e^{-\tau x \left( \frac{H_t - z}{V} \right)} \right) p(z) dz, \quad (14)$$

where  $H$  is the depth of the surface layer and  $p(z)$  is a probability distribution for particles in the water column. For simplicity, we assumed that BSi was homogeneously distributed between  $z = 0$  and  $z = H$ . Integration of this equation between  $z = 0$  and  $z = H$  yielded

$$\overline{\text{SR}} = 1 - \left( 1 - e^{-\frac{\tau H}{V}} \right) \frac{V}{\tau H}. \quad (15)$$

The sinking velocity  $V$  is calculated as follows:

$$V = V_{\min} + \frac{V_{\max}}{1 + \left( \frac{\text{BSi}_{T,t-1}}{\beta} \right)^{-2}}, \quad (16)$$

with  $V_{\min}$  and  $V_{\max}$  being the minimum and the maximum sinking velocities allowed (in  $\text{m d}^{-1}$ );  $\beta$  is the BSi concentration ( $\mu\text{mol-Si L}^{-1}$ ) value at the inflexion point of this function, i.e. the concentration above which the sinking rate increases rapidly from its minimum value ( $1 \text{ m d}^{-1}$ ) and converges to the maximum sinking velocity ( $20 \text{ m d}^{-1}$ ). The choice of the minimum and maximum sinking velocity was made based on the sinking speeds of individual cells versus aggregates  $> 0.5 \text{ mm}$  (marine snow). According to Smayda (1970), individual cells will generally sink slowly, e.g.  $\sim 1 \text{ m d}^{-1}$ , while aggregates, being larger, sink faster, some more than  $100 \text{ m d}^{-1}$  (Alldredge and Gotschalk, 1988). We have set the upper limit here at  $20 \text{ m d}^{-1}$ . Thus:

$$D = \overline{\text{SR}} \times M_t. \quad (17)$$

The mortality term of living diatoms ( $\text{BSi}_A$ ) is written as

$$M_t = \left( g \times \frac{\text{BSi}_A}{(\text{BSi}_A + 0.1)} \times \text{BSi}_A \right), \quad (18)$$

with  $g$  being the mortality rate of diatoms ( $\text{d}^{-1}$ ). As higher trophic levels (i.e. zooplankton) are not explicitly included in



**Table 2.** Parameter values used in the model.

Symbol	Parameter	Unit	Value
$\mu_{\max}$	Maximum growth rate of phytoplankton	$\text{d}^{-1}$	1.5 <sup>a</sup>
$K_{\text{Si}}$	Half-saturation constant for Si-limited growth	$\mu\text{mol L}^{-1}$	3.9
$m$	Mixing coefficient between ML and WW	$\text{m d}^{-1}$	H/50
$g$	Mortality rate of phytoplankton	$\text{d}^{-1}$	0.192 <sup>b</sup>
$\tau$	BSi dissolution rate	$\text{d}^{-1}$	0.035 <sup>c</sup>
$V_{\min}$	Minimal sinking speed	$\text{m d}^{-1}$	1
$V_{\max}$	Maximal sinking speed	$\text{m d}^{-1}$	20
$\delta^{30}\text{Si}_{\text{bst}}$	Isotopic composition of DSi released during basalt weathering	‰	$-1.00 + 1.80^{\text{d}}$
$\delta^{30}\text{Si}_{\text{WW}}$	Isotopic composition of DSi from the WW	‰	1.60

<sup>a</sup> Sarthou et al. (2005); <sup>b</sup> Tyrrell (1999); <sup>c</sup> Demarest (2009); <sup>d</sup> Douthitt (1982); Ziegler et al. (2005); and Georg et al. (2007b)

**Table 3.** Abbreviations and subscripts used in the model equations.

Variables	Abbreviation	Units
DSi winter water	DSi <sub>WW</sub>	$\mu\text{mol L}^{-1}$
DSi mixed layer	DSi <sub>ML</sub>	
DSi total	DSi <sub>T</sub>	
DSi basalt	DSi <sub>bst</sub>	
BSi dead diatom	BSi <sub>D</sub>	
BSi alive diatom	BSi <sub>A</sub>	Dimensionless
BSi total	BSi <sub>T</sub>	
After mixing process	m	
After production	p	
After death	d	
After dissolution	ds	
After sinking	s	

the model, a quadratic formulation was used to parameterise grazing on diatoms (see for example Steele and Henderson, 1995). The grazing term selected was  $0.20 \text{ d}^{-1}$  (i.e. 70/365) (Tyrrell, 1999; Nugraha et al., 2012).

The final term in Eq. (6),  $E$  ( $\mu\text{mol-Si L}^{-1} \text{ d}^{-1}$ ), describes the loss of dead diatoms due to sinking out of the mixed layer.

$$E = \frac{V_t}{H_t} \times \text{BSi}_D \quad (19)$$

The parameter values utilised in the modelling are given in Table 2.

### Equations for change in the isotopic composition of DSi and BSi

In the model, the ratio ( $R$ ) of silicon isotopes ( $^{30}\text{Si}/^{28}\text{Si}$ ) of DSi and BSi was calculated based on mass balance and by isotopic fractionation during processes for which this is known to be important. For example, the change in the  $^{30}\text{Si}/^{28}\text{Si}$  of DSi of the ML with time is influenced by mixing with the WW, removal of DSi for BSi production, the

dissolution of BSi, and in a subset of model runs, input from the subaerial and/or submarine weathering of basalt:

$$\frac{d\text{RDSi}}{dt} = \frac{(([\text{DSi}]_{\text{bst}} \times \text{RDSi}_{\text{bst}}) + ([\text{DSi}]_m \times \text{RDSi}_m) - ([\text{DSi}]_p \times \text{RDSi}_p) + ([\text{DSi}]_{\text{ds}} \times \text{RDSi}_{\text{ds}}))}{[\text{DSi}_T]} \quad (20)$$

It was difficult to ascribe a precise value for the silicon isotope ratio produced through basalt weathering ( $\text{RDSi}_{\text{bst}}$ ) because to date there has been no study of isotope fractionation during the submarine weathering of basalt. Several studies have noted the typical  $\delta^{30}\text{Si}$  of basalt itself of  $-0.29$  to  $-0.50$  ‰ (Ziegler et al., 2005; Georg et al., 2007b; Abraham et al., 2008; Bern et al., 2010; Opfergelt and Delmelle, 2012; Pogge von Strandmann et al., 2012). Other studies provide data on the  $\delta^{30}\text{Si}$  of DSi produced during the subaerial weathering of basalt, yielding values ranging from  $-1.0$  to  $+0.4$  ‰. We have thus tested a range of values for the  $\delta^{30}\text{Si}$  of DSi from basalt weathering from  $-1.0$  to  $+0.7$  ‰ (Ziegler et al., 2005; Georg et al., 2007a, b; Pogge von Strandmann et al., 2012).

Likewise, the change in the isotopic ratio of live BSi ( $\text{BSi}_A$ ) over time represented a mixture of old and newly produced  $\text{BSi}_A$  (see Table 3 for abbreviation):

$$\frac{d\text{RBSi}_A}{dt} = \frac{([\text{BSi}_A]_p \times \text{RBSi}_{Ap})}{[\text{BSi}_A]_T} \quad (21)$$

Similarly, the change in the  $^{30}\text{Si}/^{28}\text{Si}$  of dead diatoms ( $\text{BSi}_D$ ) with time represents mass balance between inputs due to BSi production by live diatoms and to output due to the death of live diatoms and the dissolution of BSi:

$$\frac{d\text{RBSi}_D}{dt} = \frac{(([\text{BSi}_D]_p \times \text{RBSi}_{Dp}) + ([\text{BSi}_D]_d \times \text{RBSi}_{Dd}) - ([\text{BSi}_D]_{\text{ds}} \times \text{RBSi}_{Dds}))}{[\text{BSi}_D]_T} \quad (22)$$

Isotope fractionation occurred during the production of live BSi from DSi and during the dissolution of non-living BSi. Isotope fractionation during BSi production within each time step was calculated following Rayleigh distillation. Although given the very small time step used, the DSi reservoir

was never depleted by more than 1.4 ‰ during one time step (i.e. the inclusion of Rayleigh distillation in the calculation had an insignificant effect on the model outcome):

$$\text{RBSi}_A = \text{RDSi}_m \times \frac{(1 - f^{\alpha_p})}{(1 - f)}, \quad (23)$$

where  $f$  is the remaining fraction and  $\alpha_p$  is the isotopic fractionation factor of 0.9988 during biogenic silica production (De La Rocha et al., 1997).

Likewise, fractionation during the dissolution of non-living BSi occurred, producing new DSi and altering the isotopic composition of the dead BSi pool as follows:

$$\text{RDSi} = \text{RBSi}_{Dd} \times \frac{(1 - f^{\alpha_d})}{(1 - f)}, \quad (24)$$

with  $\alpha_d$  the isotopic fractionation factor for biogenic silica dissolution set at either 1 (no fractionation) or 0.9995 (Demarest et al., 2009), depending on the run.

### 3 Results and discussion

#### 3.1 Concentration and $\delta^{30}\text{Si}$ of DSi and BSi on the Kerguelen Plateau and at the Antarctic Divergence

As expected, DSi concentrations in Southern Ocean surface waters increased southwards, ranging from 11  $\mu\text{M}$  in the surface layer at CTD8 located on the edge of the Kerguelen Plateau to 56  $\mu\text{M}$  at CTD1 in the Antarctic Divergence in the Atlantic sector of the Southern Ocean (Fig. 3a) (Dafner and Mordasova, 1994; Brzezinski et al., 2001; Varela et al., 2004; De La Rocha et al., 2011). As also expected based on previous studies (Brzezinski et al., 2001; Varela et al., 2004; Cardinal et al., 2005; Fripiat et al., 2011c), the isotopic composition of DSi ( $\delta^{30}\text{Si}_{\text{DSi}}$ ) generally increased with decreasing DSi concentration, both at the surface (Fig. 4), and with depth in the water column (Fig. 3b), reflecting the effects of biological discrimination against the heavier isotopes during DSi uptake and/or BSi production.

The data from the CTD profiles can be pooled into three categories: DSi concentrations between 0 and 45  $\mu\text{M}$  (the surface mixed layer), DSi concentrations between 45 and 90  $\mu\text{M}$  (WW), and DSi concentrations > 90  $\mu\text{M}$  (Circumpolar Deep Water, CDW). The  $\delta^{30}\text{Si}_{\text{DSi}}$  of the surface layer ranged between +1.90 ‰ and +2.39 ‰, the  $\delta^{30}\text{Si}_{\text{DSi}}$  of WW ranged from +1.20 ‰ to +1.65 ‰, and the  $\delta^{30}\text{Si}_{\text{DSi}}$  of CDW varied from +0.92 ‰ to +1.44 ‰, all in accordance with previous observations (De La Rocha et al., 2011; Fripiat et al., 2011b).

The  $\delta^{30}\text{Si}$  of surface water on the Kerguelen Plateau, between Kerguelen and Heard islands, has been observed to decrease from values of +2.7 to +2.0 ‰ at DSi concentrations of 2 to 20  $\mu\text{M}$  in late January/early February (austral summer) (Fripiat et al., 2011b) to around +1.8 ‰ at the end of March (early austral autumn) at DSi concentrations that are essentially equivalent (4–17  $\mu\text{M}$ ) (samples 51–53 and 58

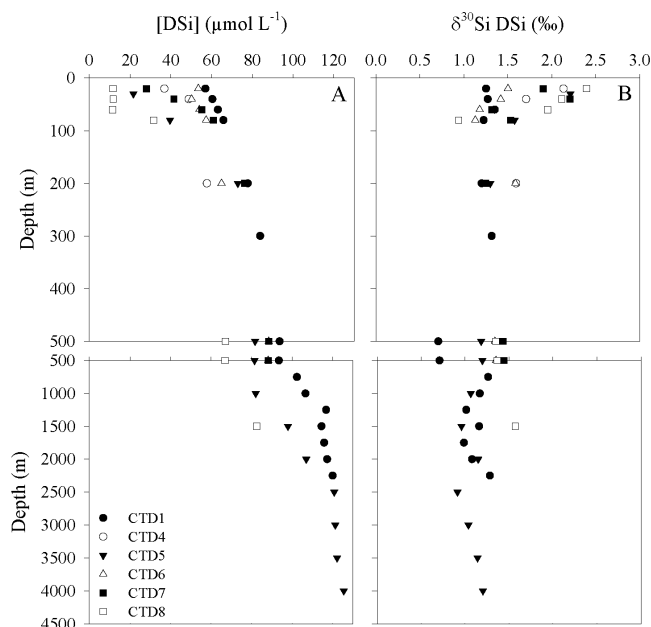


**Fig. 3.** Profiles of (A) DSi concentration data versus depth and (B)  $\delta^{30}\text{Si}_{\text{DSi}}$  versus depth from the CTD stations.

in (De La Rocha et al., 2011)). This is not, however, true for the surface water samples taken at the same time just outside of the relatively shallow area (< 1000 m) between Kerguelen and Heard islands (surface transect samples 43–50 in De La Rocha et al., 2011) or at the edge of the plateau (surface values from CTD8 where the seafloor was at 2100 m). These  $\delta^{30}\text{Si}$  values remain relatively high, around +2.3 to +2.5 ‰, at DSi concentrations ranging from 10 to 25  $\mu\text{M}$ . Together, these data are suggestive of a process which has lowered the surface water  $\delta^{30}\text{Si}$  without notably increasing DSi concentrations in the shallow, restricted circulation region of the Kerguelen Plateau and without lowering the  $\delta^{30}\text{Si}$  of DSi in surrounding surface waters more open to exchange with the waters of the Antarctic Circumpolar Current (ACC).

At the same time, the plot of  $\delta^{30}\text{Si}$  of DSi versus DSi concentration for all the Southern Ocean samples (Fig. 4) suggests that in general, the  $\delta^{30}\text{Si}$  values of DSi at concentrations below 20  $\mu\text{M}$  are somewhat variable and depressed. Isotope fractionation during DSi removal should result in values of  $\delta^{30}\text{Si}$  of DSi upwards of +2.5 ‰ or +3.0 ‰ at these low concentrations, based on either open system (continuous input) or closed system (single input) models for the evolution of  $\delta^{30}\text{Si}$  in the surface layer during the net growth of diatoms (De La Rocha et al., 1997; Varela et al., 2004). Instead, many  $\delta^{30}\text{Si}$  values from the Southern Ocean at DSi concentrations < 20  $\mu\text{M}$  fall between +1.5 ‰ and +2.5 ‰ (Fig. 4). While many of these values are the low values from the shallow region of the Kerguelen Plateau in March, not all of them are, suggesting that whatever process is at work, it is not unique to this somewhat special region. For example, data

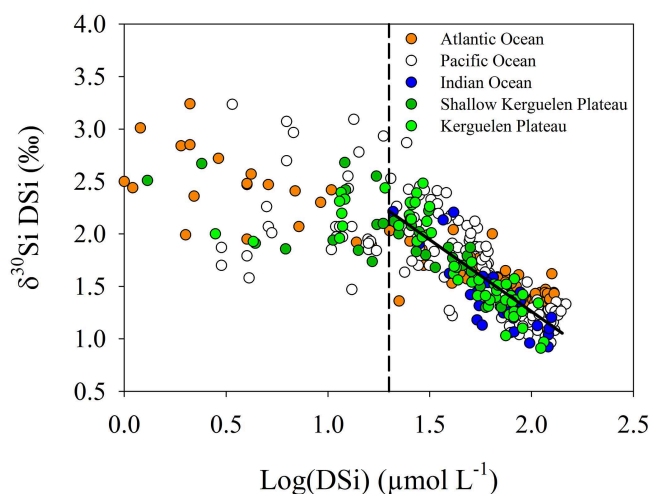


**Fig. 4.** The  $\delta^{30}\text{Si}$  DSi versus the  $\text{Log}(\text{DSi})$  of samples from the Southern Ocean from the Atlantic sector and the Indian sector (this study and De La Rocha et al., 2011; Fripiat et al., 2011a; de Souza et al., 2012b), the Kerguelen Plateau (De La Rocha et al., 2011; Fripiat et al., 2011b), and the Pacific sector (Varela et al., 2004; Cardinal et al., 2005; Cardinal et al., 2007). The dotted line occurs at a DSi concentration of  $20\text{ }\mu\text{M}$  and the solid line is the regression line for the data, except for the samples from the Kerguelen Plateau and from Cardinal et al. (2005), which are outliers ( $y_0 = -1.37x + 4.00$ ,  $R^2_{\text{adjusted}} = 0.64$  for  $p < 0.001$ ).

from the Antarctic Circumpolar Current (ACC) south of Tasmania (Cardinal et al., 2005) also have relatively low  $\delta^{30}\text{Si}$  values of  $+1.4$  to  $+2.3$  ‰ at DSi concentrations as low as  $1.8$  to  $18\text{ }\mu\text{M}$ .

There are at least three possible explanations for the low values of  $\delta^{30}\text{Si}$  of DSi observed.

First DSi input from basalt weathering on the LIP that is the Kerguelen Plateau may be reducing the surface water  $\delta^{30}\text{Si}$  values in the shallow region from the high post-diatom bloom values reported by Fripiat et al. (2011b). These authors observed some low  $\delta^{30}\text{Si}$  values (around  $+1.90$  ‰ for DSi at  $10$  to  $50\text{ m}$ ) very close to Heard Island, prompting them to suggest that basalt weathering would add DSi with a low  $\delta^{30}\text{Si}$ , decreasing the average surface water value. Assuming the  $\delta^{30}\text{Si}$  of basalt of  $-0.3$  to  $-0.4$  ‰ (Douthitt, 1982; Ding et al., 1996; Ziegler et al., 2005; Georg et al., 2007a; Georg et al., 2007b; Savage et al., 2011) and no fractionation during weathering, Fripiat et al. (2011b) estimated that  $10 \pm 5\%$  of the DSi would have had to come from basalt dissolution to explain the low  $\delta^{30}\text{Si}$  values near Heard Island. Data from isotopes of other elements (e.g. Nd) support this estimate (Jeandel et al., 2011; Oelkers et al., 2011), assuming their congruent release with Si during the submarine and/or subaerial weathering of basalt (an assumption that is unlikely to be true).

Another possibility is that the progressively more important recycling of silicon later in the growing season (and ex-

port of BSi with a slightly elevated  $\delta^{30}\text{Si}$ , due to fractionation during dissolution (Demarest et al., 2009)) causes the drop in  $\delta^{30}\text{Si}$  of DSi in these surface waters without increasing the DSi concentration. In the model of de Brauwere et al. (2012), because BSi production continues after the peak of the bloom, the post-peak of BSi should parallel the  $\delta^{30}\text{Si}$  of DSi (Fig. 8b), as in our model (Fig. 6). However, the  $\delta^{30}\text{Si}$  of BSi remains flat even as the  $\delta^{30}\text{Si}$  of DSi in the de Brauwere et al. (2012) model declines. This most likely reflects the increasing importance of dissolution in their model at this time to the point where the D:P ratios exceed 1. Thus in their model, the  $\delta^{30}\text{Si}$  of BSi becomes increasingly similar to that of DSi because fractionation during dissolution prevents a decline in the  $\delta^{30}\text{Si}$  of BSi in their model.

Lastly, the downward shift in  $\delta^{30}\text{Si}$  of DSi at low concentrations of DSi may be seasonal in nature, related to input of lower  $\delta^{30}\text{Si}$  of DSi from WW at the beginning of autumn occurring with no notable increase in ML DSi concentrations because of the continued, albeit minimal due to light limitation, production of BSi.

We have used the box model approach to evaluate each of the three hypotheses mentioned above.

## 3.2 The basic behaviour of the model

### 3.2.1 The predicted seasonal Si cycle around the Kerguelen Plateau

As mentioned previously (see Sect. 2.2), the goal of the modelling was not specifically to reproduce the results from the KERFIX time series site or from the plateau depth profile and surface sampling stations, but to simulate a system that was behaving similarly enough to this general region to investigate the processes controlling the behaviour of silicon isotopes in the mixed layer throughout the course of the year. Our first benchmark for the model was for it to represent the main features of the annual silica cycle in the Southern Ocean in the general region around the Kerguelen Plateau, since that is where the input parameters and data for comparison with the model output come from. Figure 5 shows that the model indeed does a reasonable job of simulating an annual silica cycle typical of the Kerguelen Plateau and environs.

The annual maximum DSi concentration in the model ML ( $24.5\text{ }\mu\text{M}$ ) and the yearly minimum in the model BSi concentration ( $1.19\text{ }\mu\text{mol L}^{-1}$ ) occurred in spring (September) associated with the annual maximal mixed layer depth ( $216\text{ m}$ ) (Fig. 5), as expected. Although the 5-year average KERFIX DSi concentrations ( $15.77 \pm 2.95\text{ }\mu\text{M}$ ) and BSi concentrations ( $0.29 \pm 0.10\text{ }\mu\text{mol L}^{-1}$ ) at this time are slightly lower, the differences are not alarming. The model successfully produced a spring bloom of phytoplankton, although by occurring in spring (November) and resulting in a maximal concentration of BSi of  $4.90\text{ }\mu\text{mol L}^{-1}$ , it was earlier and larger than the bloom observed at the KERFIX site (which typically attained BSi concentrations around  $1.0\text{ }\mu\text{mol L}^{-1}$ ). The

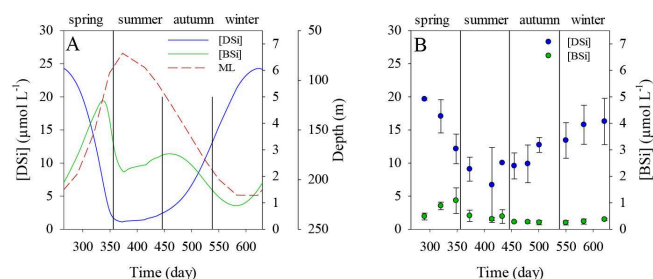


**Fig. 5.** Seasonal evolution of (A) modelled concentrations of dissolved silicon (DSi) and biogenic silica (BSi) shown alongside the mixed layer depth (ML) of the model and (B) monthly averaged DSi and BSi from the KERFIX data set (Jeandel et al., 1998).

model also produced a second bloom in early autumn (April), as expected from the onset of the seasonal deepening of the ML. This autumn bloom resulted in BSi concentrations of  $2.86 \mu\text{mol L}^{-1}$ .

Exact values for the modelled concentrations of DSi and BSi are sensitive to the values selected for DSi uptake kinetics and BSi dissolution rates, and the parameterisations of diatom mortality and BSi sinking. We certainly could have tuned these models to yield more perfectly matching results, but decided against this. The similarity obtained between modelled and measured values is good enough to use the model to consider the processes contributing to the day-to-day values of  $\delta^{30}\text{Si}$  in the ML.

The ratio of BSi dissolution to production (D : P) varied throughout the year in the model (Fig. 7a), ranging from a maximum of 0.64 in winter to a minimum of 0.19 in summer as diatom growth rates increased. This falls well within the range observed over various timescales (daily to annual) in the Southern Ocean (Tréguer and De La Rocha, 2013), with values  $< 0.3$  taken to reflect conditions during blooms (when rapid net production of BSi occurs) and the annual average D : P (0.37) falling close to the roughly expected value of 0.5.

The ratio between DSi uptake and supply also varied throughout the year, driven mostly by change in BSi production rates. Rates of BSi production (and therefore DSi uptake) peaked during the spring bloom, the time when the rate of DSi supply due to mixing was relatively low (Fig. 7c), resulting in high DSi uptake to supply ratios. The ratio of uptake and supply was lowest in early winter, not because of a high rate of DSi supply (by this time the ML had finished deepening and DSi concentrations were already close between the ML and the WW, resulting in little net modelled change in ML DSi concentration), but due to very low rates of BSi production (Fig. 7b). Over the course of the model year, the DSi uptake to supply ratio ranged from 0.5 to 7.

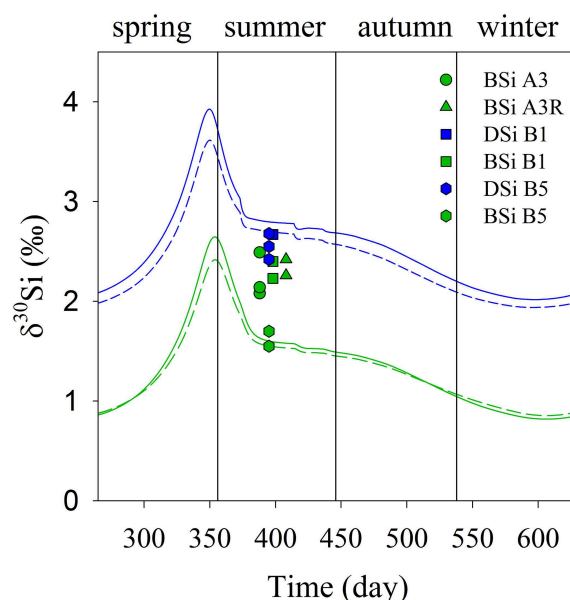


**Fig. 6.** Annual evolution of  $\delta^{30}\text{Si}_{\text{DSi}}$  and  $\delta^{30}\text{Si}_{\text{BSi}}$  in the model. Blue represents DSi and green represents BSi. Solid lines represent the initial run without fractionation during BSi dissolution and dotted lines are the simulation with fractionation during BSi dissolution. Data points are from KEOPS (Fripiat et al., 2011b).

### 3.2.2 Model simulation without fractionation during BSi dissolution, and no input from basalt

During the basic run of the model (no fractionation during BSi dissolution and no input from basalt), the  $\delta^{30}\text{Si}$  of DSi and BSi increased during spring growth to reach maximal values by the end of spring (from  $+2.0$  to  $+3.7$ ‰ for DSi and from  $+0.8$  to  $+2.6$ ‰ for BSi) (Fig. 6). These values steeply decreased during summer and continued to decline through autumn (from  $+2.6$  to  $+2.2$ ‰ for DSi and from  $+1.5$  to  $+1.0$ ‰, for BSi), while DSi concentrations increased and BSi concentrations decreased due to a combination of mixing of DSi up into the ML and light limitation of phytoplankton growth.

If this basic model represents the sum total of the processes influencing the isotopic composition and cycling of DSi and BSi, several conclusions may be drawn.

The first is that there is a period of time, specifically during summer stratification, when the DSi concentration in the ML is at its annual minimum and relatively constant, but the  $\delta^{30}\text{Si}$  of the DSi is decreasing over time (Fig. 6b). This is due to diffusive input of low  $\delta^{30}\text{Si}$  DSi from WW into the ML, which brings down the average  $\delta^{30}\text{Si}$  of DSi in the ML. At the same time, Si-limited growth of diatoms is able to maintain the DSi concentration at a minimum determined by the DSi uptake kinetics of the diatom species present. Despite gross production of BSi at this time, BSi concentrations increased only slightly (from  $0.30$  to  $0.42 \mu\text{mol L}^{-1} \text{d}^{-1}$ ), due to losses to sinking and dissolution that are nearly as great as

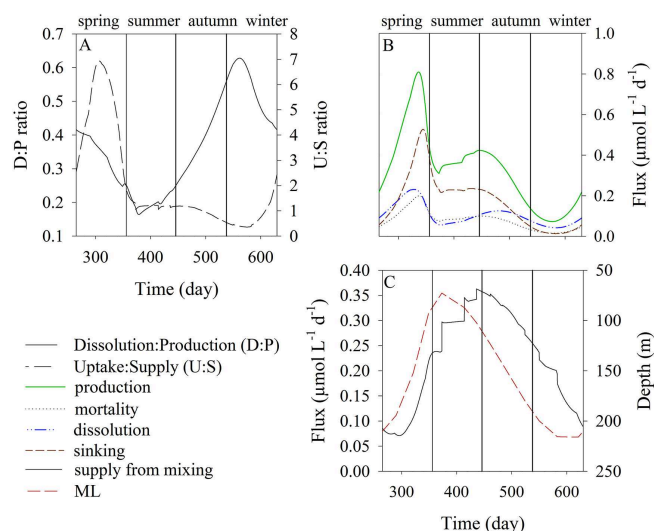


**Fig. 7.** Evolution of the main fluxes and ratios in the basic model run (with neither basalt input nor fractionation during biogenic silica dissolution); (A) variation of the ratio of Dissolution to Production and of the Uptake to Supply ratio during the year; (B) evolution of production, mortality, dissolution and sedimentation fluxes; (C) evolution of the DSi supply and the ML depth throughout the year.

the gains due to production. Thus the input of low  $\delta^{30}\text{Si}$  DSi from WW coupled with the export of BSi with a  $\delta^{30}\text{Si}$  lower than the  $\delta^{30}\text{Si}$  of the ML DSi drives down the  $\delta^{30}\text{Si}$  of the DSi without any increase in DSi concentrations. This alone would explain the lower  $\delta^{30}\text{Si}$  for ML DSi observed in early autumn by De La Rocha et al. (2011) compared to those in the middle of summer by Fripiat et al. (2011b). In principle then, neither basalt dissolution nor fractionation during BSi dissolution is necessary to attain this result.

The second thing to note is that in all likelihood, none of the published studies have sampled the Kerguelen Plateau, or anywhere else in the Atlantic and Indian sectors of the Southern Ocean, early enough in the growing season to capture the highest possible values for  $\delta^{30}\text{Si}$  in the mixed layer.

### 3.2.3 Model run including fractionation during biogenic silica dissolution

In some of the model runs, fractionation during BSi dissolution was allowed to occur with a fractionation ( $\epsilon$ ) of  $-0.55\text{‰}$ . At the full extent of expression of the fractionation, this would produce DSi with a  $\delta^{30}\text{Si}$  that was  $-0.55\text{‰}$  compared to the BSi being dissolved. This fractionation resulted in a diminishment of the  $\delta^{30}\text{Si}$  of DSi in the model by roughly  $0.2\text{‰}$  throughout the entire year (Fig. 7). Such fractionation during dissolution should lower the  $\delta^{30}\text{Si}$  of DSi recycled in the ML, while slightly increasing the  $\delta^{30}\text{Si}$  of BSi exported. Thus discrimination against the heavier isotopes during dissolution will pump Si of slightly higher  $\delta^{30}\text{Si}$

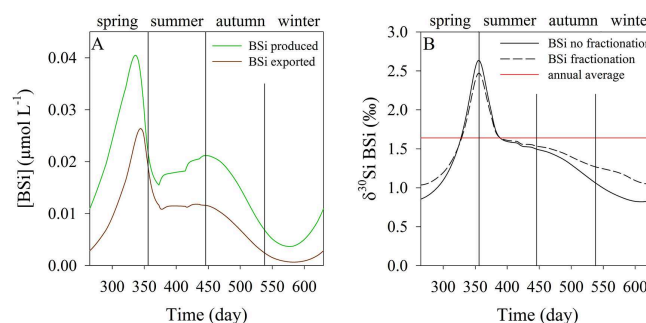


**Fig. 8.** (A) Annual evolution of the BSi production and the exported BSi outside of the ML, and (B) annual behaviour of the  $\delta^{30}\text{Si}$  of the BSi exported outside of the ML (on the sediment) from the initial run (without fractionation during BSi dissolution) and from the run with fractionation during dissolution. The red line represents the mass-weighted average value of the  $\delta^{30}\text{Si}$  of the BSi exported for the runs with and without fractionation during BSi dissolution ( $1.64$  and  $1.65\text{‰}$ , respectively).

out of the ML, while causing the retention of Si with slightly lower  $\delta^{30}\text{Si}$ .

In contrast, the effect of fractionation during dissolution on the  $\delta^{30}\text{Si}$  of BSi did not occur evenly throughout the year, but was largely confined to the higher  $\delta^{30}\text{Si}$  values associated with the seasonal phytoplankton bloom. The bloom values were as much as  $0.2\text{‰}$  lower than they were without fractionation during dissolution, while the low  $\delta^{30}\text{Si}$  values associated with wintertime BSi were identical to those in the simulations without fractionation during BSi dissolution (Fig. 6). The overall result is a damping of the annual range of  $\delta^{30}\text{Si}$  of BSi.

The damping of the yearly range in  $\delta^{30}\text{Si}$  of ML BSi with fractionation during BSi dissolution is a key result, but for the moment it should be taken cautiously. Note, for example, that the winter values for the  $\delta^{30}\text{Si}$  of DSi in all the different simulations (Fig. 6) did not converge on the WW value of  $1.6\text{‰}$ . In part this can be blamed on BSi production which occurs throughout the year and thus always consumes some DSi (Fig. 7a and b), elevating the surface water values of  $\delta^{30}\text{Si}$ , even in winter. By itself, this is both reasonable and realistic; phytoplankton growth may slow to a crawl during winter, but it does not cease entirely. However, the failure of the  $\delta^{30}\text{Si}$  values for DSi in winter to drop all the way down to the WW value may also be partly an artefact of the modelling. In winter in the model, gross input of DSi into the ML is relatively low because the model tracks net input which decreases over the course of the winter as the DSi concentration of the WW and the ML become similar. In the real world, while there would also be little net input of DSi into the ML at this time, exchange of DSi between the ML and the large pool of WW would still occur vigorously, and the winter ML values of  $\delta^{30}\text{Si}$  of DSi in the real world are thus probably closer to the WW values than they are in the model.

Fractionation during dissolution also affected the  $\delta^{30}\text{Si}$  of BSi exported from the ML, decreasing it by 0.2 ‰ during the bloom period but increasing it by 0.3 ‰ during winter (Fig. 8b). Despite this, it did not have a significant effect on the yearly average  $\delta^{30}\text{Si}$  of BSi exported from the ML. The annual average value of exported BSi was +1.64 ‰ in the absence of fractionation during dissolution and +1.65 ‰ with fractionation during dissolution, values that are both very close to the +1.60 ‰ value of DSi input to the ML from WW (Fig. 8b).

The efficiency of BSi export (BSi exported divided by BSi produced) was not controlled in the model, but varied throughout the year due to changes in the mixed layer depth, BSi concentration, and the sinking velocity of the BSi. In reality, the controls on export efficiency are not well understood, but include the compositions and abundances of the phytoplankton and zooplankton communities, the food web structure, the episodic versus continuous nature of primary production, and concentrations of sticky exopolymers that enable the formation of large, rapidly sinking particles through aggregation. In short, it is likely that export efficiency varies considerably from one time of the year to another. Therefore, given the large annual range in the  $\delta^{30}\text{Si}$  of BSi (Fig. 6), the exact  $\delta^{30}\text{Si}$  of BSi exported and accumulating in the sediments must be strongly influenced by the variations in BSi export efficiency throughout the year. For example, if BSi produced during the spring bloom (representing maximal  $\delta^{30}\text{Si}$  values) is preferentially exported to sediments relative to BSi produced during other times of the year (representing lower  $\delta^{30}\text{Si}$ ), the sedimentary record of  $\delta^{30}\text{Si}$  will be higher than if winter BSi was preferentially exported, or if there was no variation in export efficiency throughout the year. This strongly implies that interpretation of paleoceanographic records of  $\delta^{30}\text{Si}$  would be improved by understanding the extent to which the sedimentary record serves as a yearly integrated signal or that biased towards one season or another.

Records of the diatom species composition of Southern Ocean sediments show that over time, different types of diatoms (produced at different times of the year) accumulate in the sediments. For example, in some cores from the Antarctic Polar Frontal Region, heavily silicified (and strongly resistant to dissolution) winter resting stages of *Eucampia antarctica* can represent half of the diatom frustules present at the Last Glacial Maximum (perhaps not coincidentally the time of lowest recorded  $\delta^{30}\text{Si}$  values (e.g. De La Rocha et al., 1998; Brzezinski et al., 2002)), while in other cores and at other times these winter stages are numerically never more than 10 % of the diatom frustules present (Des Combes et al., 2008).

### 3.2.4 Model runs including basalt weathering

One set of simulations was run, both with and without fractionation during BSi dissolution, but with DSi input into the

ML from basalt weathering. This was done in two ways. In the first, or “constant basalt input” scenario, a small and constant amount of DSi from basalt was input directly to the ML at each time step to simulate input from weathering on Kerguelen and Heard islands and in shallower areas (seafloor < 250 mbsl) of the Kerguelen Plateau. Over the course of the year, this basalt input was equivalent to 10 % of the total input from mixing, in accordance with Fripiat et al. (2011a). In the “variable basalt input scenario”, the  $\delta^{30}\text{Si}$  of WW input to the ML was set to reflect a maximum of 10 % contribution from basalt weathering at each time step and was therefore linked to the ML depth evolution.

Values for the  $\delta^{30}\text{Si}$  of the basalt DSi from −1.0 ‰ to +1.8 ‰ were tested, spanning most of the range of values known for DSi solutions produced during basalt weathering on land (Ziegler et al., 2005; Georg et al., 2007b; Pogge von Strandmann et al., 2012). For example, DSi with  $\delta^{30}\text{Si}$  values ranging from −1.1 to +2.0 ‰ have been reported for soil solutions and rivers associated with basalt weathering in Hawaii (Ziegler et al., 2005), while a range of values from −0.08 ‰ to +1.51 ‰ has been reported for DSi in Icelandic rivers, also a product of basalt weathering (Georg et al., 2007b).

Unfortunately, there have been no studies addressing the  $\delta^{30}\text{Si}$  of DSi produced during the submarine weathering of basalt. While inputs of Si from basalt weathering on the islands must certainly occur, given that only a small portion of the Kerguelen Plateau resides above sea level, it is likely that much of the basalt-derived DSi in the region is released during submarine weathering. Because a significant fraction of the Si released during submarine dissolution of basalt will become incorporated into clay minerals like smectite, it is inappropriate to use instead the average  $\delta^{30}\text{Si}$  of basalt of −0.35 ‰. Isotope fractionation during clay formation will cause the  $\delta^{30}\text{Si}$  of the DSi that is released to seawater to be different than the basalt, just as is seen with the weathering of basalt on land.

Because the WW input to the ML in the model has a  $\delta^{30}\text{Si}$  of +1.6 ‰ and the highest value tested for the basalt-derived DSi was +1.8 ‰, the general effect of adding basalt-derived DSi at either a constant daily rate or a variable rate linked to changes in the ML depth was to lower the  $\delta^{30}\text{Si}$  of DSi and, consequently, of BSi in the ML (Fig. 9). Likewise, the lower the  $\delta^{30}\text{Si}$  of the basalt-derived DSi, the greater the diminishment of ML  $\delta^{30}\text{Si}$ . Thus the hypothesis that basalt-derived DSi could be driving down the  $\delta^{30}\text{Si}$  of DSi in the ML on the Kerguelen Plateau is not contradicted by tests covering most of the range of possible  $\delta^{30}\text{Si}$  for basalt-derived DSi.

Although the lowering effect persisted throughout the year, the strongest diminishment in ML  $\delta^{30}\text{Si}$  occurred during the period of greatest net BSi production (spring), resulting in much lower annual maximum values of  $\delta^{30}\text{Si}$  for ML DSi (and subsequently BSi) than would have occurred otherwise (Fig. 9). Essentially, input of basalt-derived DSi with its low  $\delta^{30}\text{Si}$  values worked against the effects of fractionation



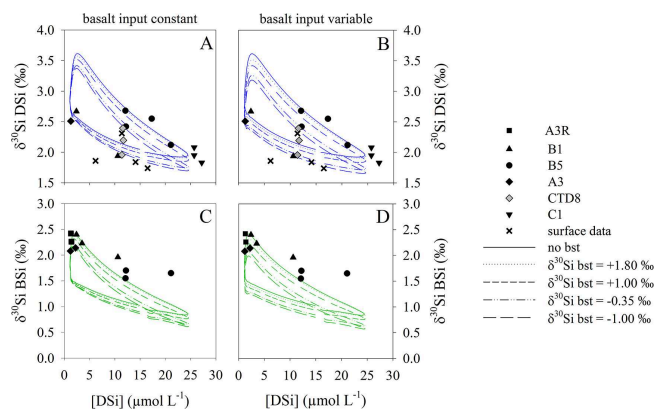


**Fig. 9.** Isotopic composition output versus DSi concentration for model runs with a constant basalt input (panels **A** and **C**) and with a variable basalt input (panels **B** and **D**). Panels **(A)** and **(B)** show  $\delta^{30}\text{Si}_{\text{DSi}}$  and panels **(C)** and **(D)** show  $\delta^{30}\text{Si}_{\text{BSi}}$ . The surface data are from De La Rocha et al. (2011), stations A3R, B1, B5, A3, and C1 are from KEOPS (Fripiat et al., 2011b) and CTD8 is from this study.

during BSi production. In contrast, the effect of the basalt-derived DSi was minor during the middle of summer when BSi production declined due to nutrient limitation and the ML values of  $\delta^{30}\text{Si}$  approached the  $\delta^{30}\text{Si}$  of the inputs as a whole.

Unfortunately, this modelling cannot be used to constrain the possible range of values for basalt-derived DSi on the Kerguelen Plateau. However, it is worth noting that when the  $\delta^{30}\text{Si}$  of basalt-derived DSi is set to  $-1.0\text{‰}$ , the model output yields its best match with the  $\delta^{30}\text{Si}$  data from Kerguelen Plateau stations A3 and B1 (Fig. 9), which are the KEOPS campaign stations identified as best representing the plateau locality. Studies directly addressing the release and isotopic composition of DSi during basalt weathering (subaerial and submarine) on the Kerguelen Plateau are however necessary to confirm this.

### 3.3 Sensitivity analysis

The parameters that are important for the behaviour of the model in terms of the silicon concentration are the maximum diatom growth rate ( $\mu_{\text{max}}$ ), the mortality rate of the diatoms, the dissolution rate of the BSi, and the half-saturation constant ( $K_{\text{Si}}$ ) for DSi uptake by the diatoms. In terms of directly affecting silicon isotopes, the  $\delta^{30}\text{Si}$  input to the mixed layer through mixing, and the fractionation factors for BSi production ( $\varepsilon_{\text{prod}}$ ) and dissolution ( $\varepsilon_{\text{diss}}$ ) are key.

We tested the sensitivity of the model to these different parameters by calculating a sensitivity index (SI), as follows:

$$\text{SI} = \frac{1}{t} \sum_{t=1}^{t=n} \frac{\left( \sqrt{(X_{\text{std}} - X_{\text{var}})^2} \right)}{X_{\text{std}}}, \quad (25)$$

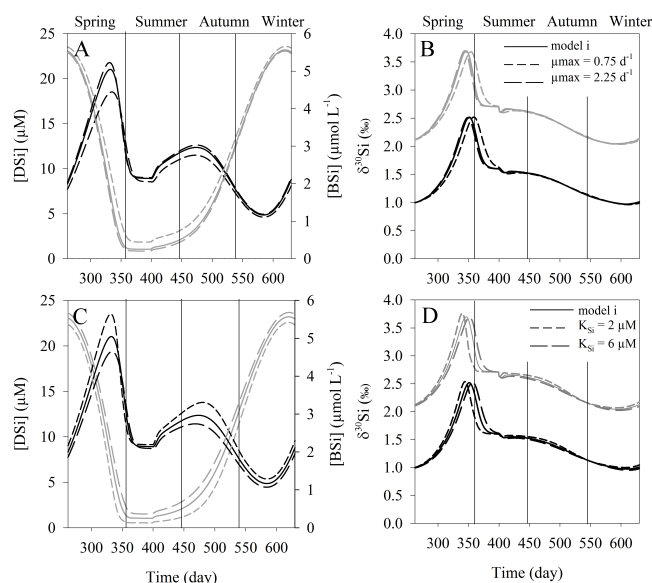


**Fig. 10.** **(A)** DSi and BSi concentrations with time for model runs with  $\mu_{\text{max}}$  values  $\pm 50\%$  of the initial value ( $\mu_{\text{max}} = 1.5 \text{ d}^{-1}$ ), **(C)** DSi and BSi concentrations with time for model runs with  $K_{\text{Si}}$  values  $\pm 50\%$  of the initial value ( $K_{\text{Si}} = 4 \mu\text{mol-Si}$ ), and **(B)** and **(D)**  $\delta^{30}\text{Si}$  of DSi and BSi versus time for the model runs where  $\mu_{\text{max}}$  **(B)** and  $K_{\text{Si}}$  **(D)** were tested. Black: BSi, grey: DSi, solid line: initial run, dashed lines: values tested.

where  $X_{\text{std}}$  is the initial model solution for the variable  $X$  (DSi or BSi and concentration or  $\delta^{30}\text{Si}$ ),  $X_{\text{var}}$  is the model solution for a given variation, and  $t$  is the time. The SI generally varies between zero and one, with values of one indicating a 100 % change in the model output (Table 4).

The sensitivity was tested in one of two ways: by varying the parameters used in the initial modelling by  $\pm 50\%$  or by testing with values of interest taken from the literature.

The maximum growth rate ( $\mu_{\text{max}}$  ( $\text{d}^{-1}$ )) was fixed in the initial modelling at  $1.5 \text{ d}^{-1}$  (solid line in Fig. 10a and b). Increasing this value by 50 % had only a limited effect on concentrations of DSi and BSi throughout the year (Fig. 10a), with what effect there is to be seen (generally less than  $1 \mu\text{mol L}^{-1}$  difference) confined to the summer (Table 4). Decreasing the value of  $\mu_{\text{max}}$  by 50 % (Fig. 10a) drives a slightly larger change in the concentrations, up to about  $2.5 \mu\text{mol L}^{-1}$ , with the largest effect again observed during summer. The SI values associated with these tests for  $\mu_{\text{max}} \pm 50\%$  ranged from a low of 0.009 in the winter  $-50\%$  case to a high of 0.754 in the summer, again for the  $-50\%$  case (Table 4). In both cases, the timing and general pattern of DSi drawdown in spring and recovery in autumn and winter as well as peaks in BSi biomass in spring and autumn remain unchanged.

The effect on the  $\delta^{30}\text{Si}$  of DSi and BSi of changes to  $\mu_{\text{max}}$  is a change in the timing of the peak at the end of spring (Fig. 10b). The effect is really observable for a decrease in

**Table 4.** Sensitivity index (SI) per season for coefficients tested; SI varies from 0 (0 %) to 1 (100 %).

			Spring	Summer	Autumn	Winter
$\mu_{\max}$	0.75	[DSi]	0.259	0.735	0.238	0.026
		$\delta^{30}\text{Si}$ DSi	0.032	0.036	0.002	0.005
		[BSi]	0.096	0.055	0.068	0.050
		$\delta^{30}\text{Si}$ BSi	0.044	0.059	0.004	0.011
	2.25	[DSi]	0.069	0.178	0.067	0.009
		$\delta^{30}\text{Si}$ DSi	0.013	0.007	0.001	0.001
		[BSi]	0.032	0.014	0.021	0.017
		$\delta^{30}\text{Si}$ BSi	0.016	0.013	0.002	0.002
KSi	2	[DSi]	0.203	0.476	0.296	0.048
		$\delta^{30}\text{Si}$ DSi	0.041	0.019	0.012	0.003
		[BSi]	0.091	0.043	0.118	0.092
		$\delta^{30}\text{Si}$ BSi	0.046	0.041	0.021	0.006
	6	[DSi]	0.177	0.449	0.223	0.035
		$\delta^{30}\text{Si}$ DSi	0.024	0.025	0.008	0.001
		[BSi]	0.067	0.038	0.082	0.073
		$\delta^{30}\text{Si}$ BSi	0.034	0.041	0.014	0.003
Mortality rate	0.096	[DSi]	0.314	0.291	0.245	0.092
		$\delta^{30}\text{Si}$ DSi	0.093	0.016	0.020	0.025
		[BSi]	0.294	0.175	0.279	0.422
		$\delta^{30}\text{Si}$ BSi	0.130	0.037	0.034	0.041
	0.288	[DSi]	0.250	0.255	0.175	0.048
		$\delta^{30}\text{Si}$ DSi	0.049	0.024	0.012	0.012
		[BSi]	0.153	0.080	0.138	0.180
		$\delta^{30}\text{Si}$ BSi	0.071	0.040	0.020	0.016
Dissolution rate	0.023	[DSi]	0.011	0.004	0.007	0.005
		$\delta^{30}\text{Si}$ DSi	0.007	0.001	0.003	0.005
		[BSi]	0.006	0.001	0.003	0.013
		$\delta^{30}\text{Si}$ BSi	0.007	0.001	0.001	0.002
	0.2	[DSi]	0.334	0.182	0.218	0.094
		$\delta^{30}\text{Si}$ DSi	0.129	0.036	0.068	0.068
		[BSi]	0.141	0.061	0.076	0.214
		$\delta^{30}\text{Si}$ BSi	0.126	0.032	0.052	0.048
$\delta^{30}\text{Si}$ WW	1.4 ‰	[DSi]	0.000	0.000	0.000	0.000
		$\delta^{30}\text{Si}$ DSi	0.074	0.074	0.083	0.096
		[BSi]	0.000	0.000	0.000	0.000
		$\delta^{30}\text{Si}$ BSi	0.137	0.121	0.147	0.195
	1.8 ‰	[DSi]	0.000	0.000	0.000	0.000
		$\delta^{30}\text{Si}$ DSi	0.074	0.074	0.083	0.096
		[BSi]	0.000	0.000	0.000	0.000
		$\delta^{30}\text{Si}$ BSi	0.137	0.121	0.147	0.195
Fractionation	$\varepsilon_{\text{prod}} = -0.54$	[DSi]	0.000	0.000	0.000	0.000
		$\delta^{30}\text{Si}$ DSi	0.213	0.210	0.175	0.121
		[BSi]	0.000	0.000	0.000	0.000
		$\delta^{30}\text{Si}$ BSi	0.150	0.036	0.089	0.290
	$\varepsilon_{\text{prod}} = -2.09$	[DSi]	0.000	0.000	0.000	0.000
		$\delta^{30}\text{Si}$ DSi	0.377	0.372	0.310	0.214
		[BSi]	0.000	0.000	0.000	0.000
		$\delta^{30}\text{Si}$ BSi	0.265	0.063	0.157	0.513



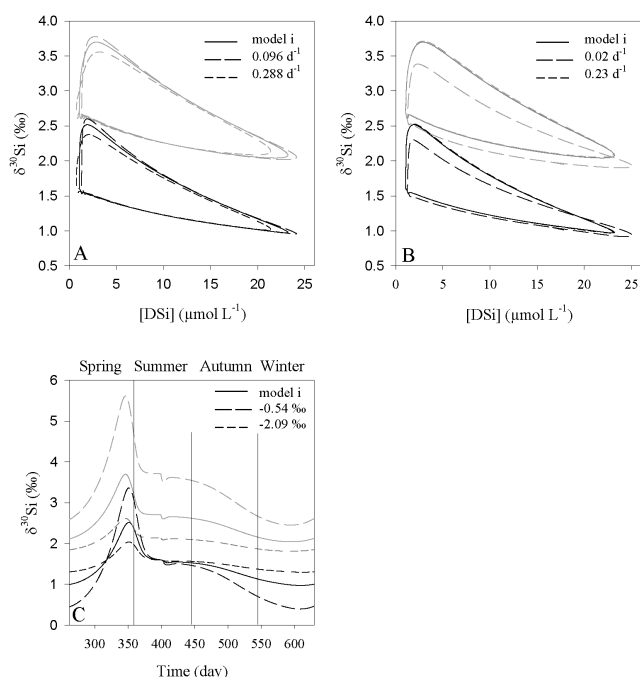


**Fig. 11.** Influence of the different (A) mortality rates on the  $\delta^{30}\text{Si}$  of DSi and BSi versus DSi concentration, (B) dissolution rates on the  $\delta^{30}\text{Si}$  of DSi and BSi versus DSi concentration and (C) variation of the  $\delta^{30}\text{Si}$  DSi and BSi versus time for different  $\varepsilon_{\text{prod}}$ . Black: BSi, grey: DSi, solid line: initial run, dashed lines: values tested.

$\mu_{\text{max}}$  by 50 %, something which leads to a roughly 15-day delay in the peaks of  $\delta^{30}\text{Si}$  in DSi and BSi. An increase of 50 % has little effect (Table 4).

The half-saturation constant for silicon uptake ( $K_{\text{Si}}$  ( $\mu\text{mol-Si L}^{-1}$ )) controls the affinity of diatoms for DSi uptake in the model and was initially fixed at  $4 \mu\text{mol-Si L}^{-1}$  (Fig. 10c and d), based on values from the literature. Decreasing  $K_{\text{Si}}$  to  $2 \mu\text{M}$  (the parameter minus 50 % sensitivity test) allowed diatoms to take up DSi at maximal rates at lower DSi concentrations than when the  $K_{\text{Si}}$  was set to  $6 \mu\text{M}$  (the parameter plus 50 %). The result was, predictably, higher standing stocks of BSi during the spring and autumn blooms for the lower half-saturation constant, and lower standing stocks of BSi during the spring and autumn blooms for the higher half-saturation constant. Again, the overall effects are not huge, never more than about  $3 \mu\text{mol L}^{-1}$  relative to the runs with the initial  $K_{\text{Si}}$  value, and normally much less than this (Fig. 10c). In this case the maximal effect on DSi was 0.476 (SI) in summer at  $K_{\text{Si}} - 50 \%$  (Table 4). For BSi, the maximum SI was 0.118 and in autumn. For  $\delta^{30}\text{Si}$ , the impact is always less than 10 % (SI < 0.082) (Table 4). The  $\delta^{30}\text{Si}$  of DSi and BSi are sensitive to the variation in  $K_{\text{Si}}$  to a similar extent (Fig. 10d). A decrease of 50 % of  $K_{\text{Si}}$  ( $2 \mu\text{M}$ ) leads to an earlier increase in the  $\delta^{30}\text{Si}$  for both DSi and BSi. An increase for  $K_{\text{Si}}$  of  $6 \mu\text{M}$  had the opposite effect and to a similar extent, with maximal values of  $\delta^{30}\text{Si}$  observed slightly later.

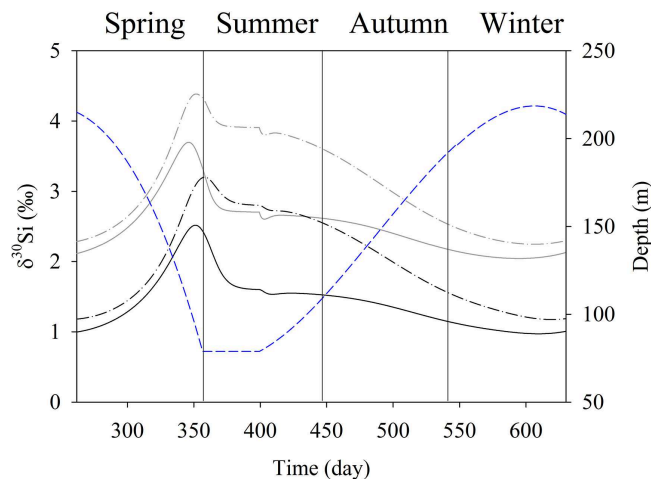


**Fig. 12.** Evolution of  $\delta^{30}\text{Si}$  for DSi (grey lines) and BSi (black lines) versus time for the initial model run (solid lines) and for the model run where  $\delta^{30}\text{Si}_{\text{WW}}$  is allowed to vary with the ML depth (blue dashed lines).

The mortality rate is another important parameter in the model, especially because it is linked to dissolution in that only dead diatoms are allowed to dissolve. The sensitivity of the model to this parameter was also tested for values  $\pm 50 \%$  of the initially assigned value of  $0.192 \text{ d}^{-1}$ . In Table 4 we can see that the mortality influences both DSi concentration and the  $\delta^{30}\text{Si}$  of both BSi and DSi mainly at the lowest and highest DSi concentrations. It affects BSi concentrations also (Fig. 11a). These two periods of greatest influence correspond to the ends of winter and summer. A 50 % increase in the mortality rate leads to higher values of the  $\delta^{30}\text{Si}$  of DSi and BSi just before the end of summer (i.e. just before DSi concentrations cease decreasing) as well as slightly higher minimal values of DSi concentration in late summer and a higher peak concentration of DSi in the mixed layer in winter. A smaller range of DSi concentrations and  $\delta^{30}\text{Si}$  values is observed for a 50 % decrease in mortality rate.

To test the sensitivity of the model to the dissolution rate, instead of using values  $\pm 50 \%$  of the value ultimately used in the modelling, specific values were selected from the literature. At the upper extreme, a dissolution rate of  $0.23 \text{ d}^{-1}$  was used corresponding to the estimated average BSi dissolution rate in the surface ocean (Van Cappellen et al., 2002). For the model it represents a variation of +657 %. At the lower extreme, a dissolution rate of  $0.02 \text{ d}^{-1}$  was used, representing the average dissolution rate in the Antarctic Circumpolar Current (Van Cappellen et al., 2002) and equalling a value equal to 57 % of that ultimately used in the modelling. Decreasing the dissolution rate ( $T_{\text{diss}}$ ) to  $0.02 \text{ d}^{-1}$  had virtually no impact; the results are essentially identical to the “normal” run (Fig. 11b), suggesting that minimal dissolution occurs in the “normal” run of the model. Use of the higher value of  $0.23 \text{ d}^{-1}$  has, however, a significant effect, resulting in an

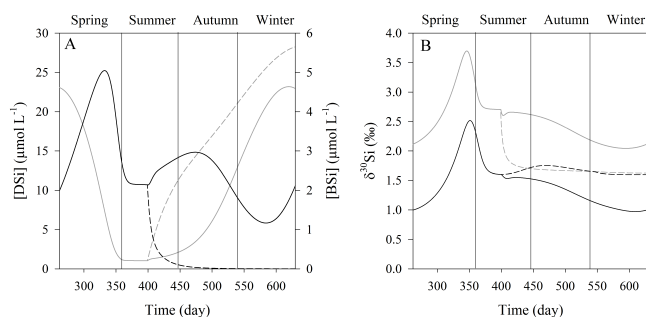


**Fig. 13.** Model run with no post-bloom BSi production. (A) DSi and BSi concentrations and (B) the  $\delta^{30}\text{Si}$  of DSi and BSi. BSi is black, DSi is grey. The solid line represents the initial run and dotted lines represent the run where BSi production is halted at the end of net nutrient drawdown.

increase in the DSi concentration as well as a decrease in the range of  $\delta^{30}\text{Si}$  for both DSi and BSi. This behaviour is expected because dissolution will increase the amount of BSi dissolved and because dissolution enriches the DSi with the lighter isotope ( $^{28}\text{Si}$ ) due to the lower  $\delta^{30}\text{Si}$  value of the BSi compared to the DSi in the ML.

In the model, we used a fractionation of  $-1.1\text{‰}$  during BSi production, as it is the average value observed for diatoms in culture (De La Rocha et al., 1997), in low-latitude upwelling zones (De La Rocha et al., 2000), and very close to the average value determined for diatoms in the Antarctic Circumpolar Current (Fripiat et al., 2011b). However, although initial reports suggested that this fractionation factor was relatively invariant from species to species, according to Sutton et al. (2013) the fractionation during BSi production is in fact species dependent, varying from at least  $-0.54\text{‰}$  for *Fragilariopsis kerguelensis* up to  $-2.09\text{‰}$  for *Chaetoceros brevis*, both of which are Southern Ocean diatoms. For that reason we decided to test these two values in our model sensitivity tests (Fig. 11c). An increase in the extent of the discrimination against the heavier isotope (the  $\epsilon_{\text{prod}}$  of  $-2.09\text{‰}$ ) resulted in a significantly higher spring bloom maximum in  $\delta^{30}\text{Si}$  in both DSi and BSi (Fig. 11c). Likewise, the use of the lesser fractionation (the  $\epsilon_{\text{prod}}$  of  $-0.54\text{‰}$ ) resulted in significantly diminished spring bloom maxima in  $\delta^{30}\text{Si}$  and a much lesser and much less variable difference between the  $\delta^{30}\text{Si}$  of DSi and BSi throughout the year (Table 4).

The shift in diatom community composition during the spring bloom on the Kerguelen Plateau (e.g. as reported by Armand et al., 2008) could be influencing the  $\delta^{30}\text{Si}$  of DSi and BSi. Succession from *Chaetoceros brevis* to *Eucampia antarctica* has been observed and these species may fractionate silicon isotopes to differing degrees (e.g.  $\epsilon_{\text{prod}}$  is the unusually strong  $-2.09\text{‰}$  for *Chaetoceros brevis* (Sutton et al., 2003) compared to values closer to  $-1\text{‰}$  for many other diatom species). Further modelling efforts might take into account variation of the fractionation factor associated with the

probable pattern of succession. First, however, it would be useful to quantify isotope fractionation for all the main diatom species of the spring bloom in this region.

The choice of the constant value for the  $\delta^{30}\text{Si}$  mixed into the ML was set at the Winter Water value of  $1.6\text{‰}$ . To see the influence of this value, two runs were undertaken where this  $\delta^{30}\text{Si}$  was instead set at  $1.4\text{‰}$  or  $1.8\text{‰}$  ( $\pm 12.5\%$  of the initial value). The resulting effects were to shift the  $\delta^{30}\text{Si}$  values (for BSi and DSi) versus DSi up or down by a few tenths of a permil. As expected, there was no influence on the DSi or BSi concentration (Table 4).

### 3.3.1 Model behaviour for a varying Winter Water $\delta^{30}\text{Si}$

To evaluate how changes in the  $\delta^{30}\text{Si}$  of the mixing source can influence the predictions of  $\delta^{30}\text{Si}$  in the dissolved and particulate silicon pools in the mixed layer, we decided to test a varying  $\delta^{30}\text{Si}$  input related to changes in the depth of the mixed layer throughout the year (Fig. 12).

In our box model, the depth of the boundary between the surface mixed layer and the deep reservoir changes seasonally. In consequence, both the DSi concentration and the  $\delta^{30}\text{Si}$  in the source water below this boundary (DSi<sub>0</sub> and  $\delta^{30}\text{Si}_{\text{WW}}$ ) are expected to change seasonally as well. However, in the initial model simulation, only DSi<sub>0</sub> changes seasonally (see Sect. 2.2.1).

To estimate how  $\delta^{30}\text{Si}_{\text{WW}}$  (the  $\delta^{30}\text{Si}$  of the mixing input) might change seasonally, the value was calculated as:

$$\delta^{30}\text{Si}_{\text{WW}} = 7.077343 - 0.4867 \times [\text{DSi}]_{\text{WW}} + 0.0156 \times [\text{DSi}]_{\text{WW}}^2 - 0.0002 \times [\text{DSi}]_{\text{WW}}^3 \quad (26)$$

In this equation, the lowest  $\delta^{30}\text{Si}$  ( $1.6\text{‰}$ ) is assigned to the highest DSi concentration (representing true WW mixed in at the time when the ML is deepest). The maximal  $\delta^{30}\text{Si}$  ( $2.58\text{‰}$ ) is tied to the lowest DSi concentration, which is the input at the time when the upper water column is most stratified and the ML is the shallowest. This improvement in the model leads to  $\delta^{30}\text{Si}_{\text{WW}}$  that varies from  $1.58\text{‰}$  when the ML is the deepest (and the DSi input comes from the true WW present at the deepest depth of winter mixing) up to values up to  $2.80\text{‰}$  at the shallowest ML depth when the water directly below the thermocline is a relic of the ML at the previous time step.

Run this way, the model yields values of  $\delta^{30}\text{Si}$  for DSi and BSi that are higher during most of the year than in the initial (constant  $\delta^{30}\text{Si}_{\text{WW}}$ ) run. The overall trend is the same for the  $\delta^{30}\text{Si}$  evolution, but the major difference is visible from the end of spring until winter, when the initial decrease in the  $\delta^{30}\text{Si}$  at the end of the bloom is less sharp for both DSi and BSi. Another thing to note is that the peak for both DSi and BSi in the new version of the model is almost  $0.6\text{‰}$  higher. As explained above, in the new run the  $\delta^{30}\text{Si}_{\text{WW}}$  increases from  $1.58$  to  $2.80\text{‰}$  as the ML shoals, and this acts to increase the ML  $\delta^{30}\text{Si}$  at some times of the year. The slower

decrease in ML  $\delta^{30}\text{Si}$  as the ML deepens is due to the same processes, but in reverse (as the ML deepens, the  $\delta^{30}\text{Si}_{\text{WW}}$  decreases towards the true WW value).

Although allowing  $\delta^{30}\text{Si}_{\text{WW}}$  to vary like this is more realistic than holding it to a constant value, the KEOPS data from Fripiat et al. (2011b) make a better match with the results when the model is run holding  $\delta^{30}\text{Si}_{\text{WW}}$  constant. This may suggest that on the Kerguelen Plateau, DSi from the WW at the deepest depth of winter mixing of the surface layer plays a strong role as a source of DSi to the ML even in late spring and summer. However, the significant differences between the two model runs highlight the importance of considering seasonal variations in both the DSi concentration and its  $\delta^{30}\text{Si}$  being mixed into the ML, even when working with something as simple as a box model.

### 3.3.2 Behaviour of the model when BSi production in winter is prohibited

To demonstrate the effect of the low levels of BSi production that occur during non-bloom periods of the year (i.e. times of no net decrease in the DSi concentration of the ML) in the model (Sect. 3.2.3), a simulation was performed with BSi production set to zero starting from the time that net draw-down of DSi concentrations ceased at the beginning of summer (Fig. 13).

When BSi production ceased, DSi concentrations increased and the BSi concentration moved quickly towards zero (Fig. 13a). In turn,  $\delta^{30}\text{Si}_{\text{DSi}}$  declined, converging towards the  $\delta^{30}\text{Si}$  value of the input WW (1.6‰) still being added to it (Fig. 13b). The  $\delta^{30}\text{Si}_{\text{BSi}}$  remaining in the ML showed a slight increase as the dissolution and sinking of “dead” BSi (and continuing mortality of the “live” BSi) diminished the amount of BSi in the ML. All told, the model reacted in an expected way to the cessation of BSi production during the “non-bloom” period, underscoring the point that BSi production does indeed continue throughout the seemingly “non-productive” times of the year, just at rates equal to or lower than those of DSi input to the ML.

## 4 Conclusions

The results from the variable mixed layer depth model of silica and silicon isotope cycling presented here offer insight into the behaviour of silicon isotopes in the general vicinity of the Kerguelen Plateau and, more importantly, into the interpretation of marine silicon isotope data in general. For example, the model illustrated that the decline in  $\delta^{30}\text{Si}$  of DSi observed between summer and early autumn in this area, decoupled from notable change in DSi concentrations (De La Rocha et al., 2011; Fripiat et al., 2011b), could be ascribed to a shift from bloom-dominated growth (BSi production by diatoms vastly outpacing DSi supply to the ML via mixing) to steady state growth (BSi production by diatoms keeping

almost perfect pace with the supply of DSi to the ML via diffusion). Such a decrease in  $\delta^{30}\text{Si}$  of ML DSi is likely to occur (without notable net change in DSi concentrations) with the stratification that follows the seasonal phytoplankton bloom in coastal margins, upwelling zones, and in general any locality featuring episodic phytoplankton blooms. This may in turn suggest that the  $\delta^{30}\text{Si}$  of diatom silica as a paleoceanographic proxy (De La Rocha et al., 1998; Brzezinski et al., 2002; Crosta et al., 2007) may more strongly reflect the dominant mode of production (higher  $\delta^{30}\text{Si}$  = bloom growth, lower  $\delta^{30}\text{Si}$  = steady state growth) rather than reflect the extent of removal of DSi for BSi production.

Fractionation during the dissolution of BSi had a visible effect in the model, lowering the  $\delta^{30}\text{Si}$  of DSi in the ML by about 0.2‰ throughout the duration of the year, and diminishing the yearly range of  $\delta^{30}\text{Si}$  of BSi (by reducing the maximum  $\delta^{30}\text{Si}$  value attained at the peak of bloom growth), also by roughly 0.2‰. In this case for the Kerguelen Plateau, this represented a 13 % reduction in the amplitude of the seasonal  $\delta^{30}\text{Si}$  signal in BSi in the water column. However, fractionation during dissolution has a negligible effect on the annual average  $\delta^{30}\text{Si}$  of BSi exported from the mixed layer. Nevertheless, if only the bloom silica accumulates in the sediments, the extent of the DSi removal associated with the bloom would be underestimated because of the overall decrease in the  $\delta^{30}\text{Si}$  of ML DSi and the potential damping of the full seasonal signal in the  $\delta^{30}\text{Si}$  of BSi due to fractionation during dissolution. Thus the effects of fractionation during dissolution may need to be considered for correct interpretation of paleoceanographic reconstructions based on  $\delta^{30}\text{Si}$ . However, even without fractionation during dissolution, season variations in BSi export efficiency should have a significant impact on the  $\delta^{30}\text{Si}$  of BSi accumulating in sediments.

The model results also suggest that the input of DSi from basalt weathering on the Kerguelen Plateau could have a significant influence over ML  $\delta^{30}\text{Si}$ , provided that the  $\delta^{30}\text{Si}$  of this released DSi is low enough relative to that of waters mixing into the ML. However, this topic requires direct investigation of the amount and isotopic composition of DSi added by this process, as the isotopic composition is not necessarily directly equivalent to that of the basalt (weathering involves processes of dissolution as well as the formation of Si-containing secondary minerals).

Finally, the model run tested with  $\delta^{30}\text{Si}_{\text{WW}}$  allowed to vary throughout the year suggests that it is important to consider seasonal variations in the  $\delta^{30}\text{Si}$  input to the ML as the upper ocean stratifies, cutting the ML off from the deeper sources of DSi tapped during winter mixing.

**Acknowledgements.** We thank E. Ponzevera and Y. Germain for technical support and two anonymous reviewers for comments. This work was supported by LEFE/CYBER grants SiMS and SiBRED to CDLR and by student funding from Region Bretagne.

Edited by: A. Shemesh

## References

- Abraham, K., Opfergelt, S., Fripiat, F., Cavagna, A.-J., De Jong, J. T. M., Foley, S. F., André, L., and Cardinal, D.:  $\delta^{30}\text{Si}$  and  $\delta^{29}\text{Si}$  determinations on USGS BHVO-1 and BHVO-2 reference materials with a new configuration on a Nu Plasma Multi-Collector ICP-MS, *Geostand. Geoanal. Res.*, 32, 193–202, 2008.
- Allredge, A. L., and Gotschalk, C.: In situ settling behavior of marine snow, DTIC Document, 1988.
- Bern, C. R., Brzezinski, M. A., Beucher, C., Ziegler, K., and Chadwick, O. A.: Weathering, dust, and biocycling effects on soil silicon isotope ratios, *Geochim. Cosmochim. Acta.*, 74, 876–889, 2010.
- Beucher, C., Tréguer, P., Hapette, A.-M., Corvaisier, R., Metzl, N., and Pichon, J.-J.: Intense summer Si-recycling in the surface Southern Ocean, *Geophys. Res. Lett.*, 31, L09305, doi:10.1029/2003gl018998, 2004.
- Beucher, C. P., Brzezinski, M. A., and Jones, J. L.: Sources and biological fractionation of silicon isotopes in the Eastern Equatorial Pacific, *Geochim. Cosmochim. Acta*, 72, 3063–3073, 2008.
- Beucher, C. P., Brzezinski, M. A., and Jones, J. L.: Mechanisms controlling silicon isotope distribution in the Eastern Equatorial Pacific, *Geochim. Cosmochim. Acta*, 75, 4286–4294, 2011.
- Blain, S., Queguiner, B., Armand, L., Belviso, S., Bombled, B., Bopp, L., Bowie, A., Brunet, C., Brussaard, C., Carlotti, F., Christaki, U., Corbiere, A., Durand, I., Ebersbach, F., Fuda, J.-L., Garcia, N., Gerringa, L., Griffiths, B., Guigue, C., Guillermin, C., Jacquet, S., Jeandel, C., Laan, P., Lefevre, D., Lo Monaco, C., Malits, A., Mosseri, J., Obernosterer, I., Park, Y.-H., Picheral, M., Pondaven, P., Remenyi, T., Sandroni, V., Sarthou, G., Savoye, N., Scouarnec, L., Souhaut, M., Thuiller, D., Timmermans, K., Trull, T., Uitz, J., van Beek, P., Veldhuis, M., Vincent, D., Viollier, E., Vong, L., and Wagener, T.: Effect of natural iron fertilization on carbon sequestration in the Southern Ocean, *Nature*, 446, 1070–1074, 2007.
- Brzezinski, M. A. and Nelson, D. M.: Chronic substrate limitation of silicic acid uptake rates in the western Sargasso Sea, *Deep-Sea Res. II*, 43, 437–453, 1996.
- Brzezinski, M. A., Nelson, D. M., Franck, V. M., and Sigmon, D. E.: Silicon dynamics within an intense open-ocean diatom bloom in the Pacific sector of the Southern Ocean, *Deep-Sea Res. II*, 48, 3997–4018, 2001.
- Brzezinski, M. A., Pride, C. J., Franck, V. M., Sigman, D. M., Sarmiento, J. L., Matsumoto, K., Gruber, N., Rau, G. H., and Coale, K. H.: A switch from  $\text{Si}(\text{OH})_4$  to  $\text{NO}_3$  depletion in the glacial Southern Ocean, *Geophys. Res. Lett.*, 29, 12, doi:10.1029/2001GL014349, 2002.
- Cardinal, D., Alleman, L. Y., de Jong, J., Ziegler, K., and Andre, L.: Isotopic composition of silicon measured by multicollector plasma source mass spectrometry in dry plasma mode, *J. Anal. Atom. Spectrom.*, 18, 213–218, 2003.
- Cardinal, D., Alleman, L. Y., Dehairs, F., Savoye, N., Trull, T. W., and Andre, L.: Relevance of silicon isotopes to Si-nutrient utilization and Si-source assessment in Antarctic waters, *Global Biogeochem. Cy.*, 19, GB2007, doi:10.1029/2004GB002364, 2005.
- Cardinal, D., Savoye, N., Trull, T. W., Dehairs, F., Kopczynska, E. E., Fripiat, F., Tison, J.-L., and André, L.: Silicon isotopes in spring Southern Ocean diatoms: Large zonal changes despite homogeneity among size fractions, *Mar. Chem.*, 106, 46–62, 2007.
- Chan, A. T.: Comparative physiological study of marine diatoms and dinoflagellates in relation to irradiance and cell-size. 2. Relationship between photosynthesis, growth, and carbon:chlorophyll a ratio., *J. Phycol.*, 16, 428–432, 1980.
- Crosta, X., Beucher, C., Pahnke, K., and Brzezinski, M. A.: Silicic acid leakage from the Southern Ocean: Opposing effects of nutrient uptake and oceanic circulation, *Geophys. Res. Lett.*, 34, L13601, doi:10.1029/2006GL029083, 2007.
- Cunningham, C. M.: Southern Ocean circulation, *Arch. Nat. Hist.*, 32, 265–280, 2005.
- Dafner, E. V. and Mordasova, N. V.: Influence of biotic factors on the hydrochemical structure of surface water in the Polar Frontal Zone of the Atlantic Antarctic, *Mar. Chem.*, 45, 137–148, 1994.
- de Brauwere, A., Fripiat, F., Cardinal, D., Cavagna, A.-J., De Ridder, F., André, L., and Elskens, M.: Isotopic model of oceanic silicon cycling: The Kerguelen Plateau case study, *Deep-Sea Res. I*, 70, 42–59, 2012.
- De La Rocha, C. L., Brzezinski, M. A., and DeNiro, M. J.: Purification, recovery, and laser-driven fluorination of silicon from dissolved and particulate silica for the measurement of natural stable isotope abundances, *Anal. Chem.*, 68, 3746–3750, 1996.
- De La Rocha, C. L., Brzezinski, M. A., and DeNiro, M. J.: Fractionation of silicon isotopes by marine diatoms during biogenic silica formation, *Geochim. Cosmochim. Acta*, 61, 5051–5056, 1997.
- De La Rocha, C. L., Brzezinski, M. A., DeNiro, M. J., and Shemesh, A.: Silicon-isotope composition of diatoms as an indicator of past oceanic change, *Nature*, 395, 680–683, 1998.
- De La Rocha, C. L., Brzezinski, M. A., and DeNiro, M. J.: A first look at the distribution of the stable isotopes of silicon in natural waters, *Geochim. Cosmochim. Acta.*, 64, 2467–2477, 2000.
- De La Rocha, C. L., Bescont, P., Croguennoc, A., and Ponzevera, E.: The silicon isotopic composition of surface waters in the Atlantic and Indian sectors of the Southern Ocean, *Geochim. Cosmochim. Acta.*, 75, 5283–5295, 2011.
- Demarest, M. S., Brzezinski, M. A., and Beucher, C. P.: Fractionation of silicon isotopes during biogenic silica dissolution, *Geochim. Cosmochim. Acta.*, 73, 5572–5583, 2009.
- de Souza, G. F., Reynolds, B. C., Johnson, G. C., Bullister, J. L., and Bourdon, B.: Silicon stable isotope distribution traces Southern Ocean export of Si to the eastern South Pacific thermocline, *Biogeosciences*, 9, 4199–4213, doi:10.5194/bg-9-4199-2012, 2012a.
- de Souza, G. F., Reynolds, B. C., Rickli, J., Frank, M., Saito, M. A., Gerringa, L. J. A., and Bourdon, B.: Southern Ocean control of silicon stable isotope distribution in the deep Atlantic Ocean, *Global Biogeochem. Cy.*, 26, GB2035, doi:10.1029/2011gb004141, 2012b.
- Ding, T., Tang, L., Wan, D., Li, Y., Li, J., Song, H., Liu, Z., and Yao, X.: Silicon isotope geochemistry, Geological Publishing House, Beijing, China, 125 pp., 1996.

- Douthitt, C. B.: The geochemistry of the stable isotopes of silicon, *Geochim. Cosmochim. Acta.*, 46, 1449–1458, 1982.
- Engström, E., Rodushkin, I., Baxter, D. C., and Öhlander, B.: Chromatographic purification for the determination of dissolved silicon isotopic compositions in natural waters by high-resolution multicollector inductively coupled plasma mass spectrometry, *Anal. Chem.*, 78, 250–257, 2006.
- Evans, G. T. and Parslow, J. S.: A model of annual plankton cycles, *Biol. Oceanogr.*, 3, 327–347, 1985.
- Fasham, M. J. R., Ducklow, H. W., and McKelvie, S. M.: A nitrogen-based model of plankton dynamics in the oceanic mixed layer, *J. Mar. Res.*, 48, 591–639, 1990.
- Fasham, M. J. R., Flynn, K. J., Pondaven, P., Anderson, T. R., and Boyd, P. W.: Development of a robust marine ecosystem model to predict the role of iron in biogeochemical cycles: A comparison of results for iron-replete and iron-limited areas, and the SOIREE iron-enrichment experiment, *Deep-Sea Res. I*, 53, 333–366, 2006.
- Fripiat, F., Cavagna, A. J., Dehairs, F., Speich, S., Andre, L., and Cardinal, D.: Silicon pool dynamics and biogenic silica export in the Southern Ocean inferred from Si-isotopes, *Ocean Sci.*, 7, 533–547, 2011a, <http://www.ocean-sci.net/7/533/2011/>.
- Fripiat, F., Cavagna, A. J., Savoye, N., Dehairs, F., André, L., and Cardinal, D.: Isotopic constraints on the Si-biogeochemical cycle of the Antarctic Zone in the Kerguelen area (KEOPS), *Mar. Chem.*, 123, 11–22, 2011b.
- Fripiat, F., Leblanc, K., Elskens, M., Cavagna, A. J., Armand, L., Andre, L., Dehairs, F., and Cardinal, D.: Efficient silicon recycling in summer in both the Polar Frontal and Subantarctic Zones of the Southern Ocean, *Mar. Ecol. Prog. Ser.*, 435, 47–61, 2011c.
- Fripiat, F., Cavagna, A.-J., Dehairs, F., de Brauwere, A., André, L., and Cardinal, D.: Processes controlling the Si-isotopic composition in the Southern Ocean and application for paleoceanography, *Biogeosciences*, 9, 2443–2457, doi:10.5194/bg-9-2443-2012, 2012.
- Georg, R. B., Halliday, A. N., Schauble, E. A., and Reynolds, B. C.: Silicon in the Earth's core, *Nature*, 447, 1102–1106, 2007a.
- Georg, R. B., Reynolds, B. C., West, A. J., Burton, K. W., and Halliday, A. N.: Silicon isotope variations accompanying basalt weathering in Iceland, *Earth Planet. Sci. Lett.*, 261, 476–490, 2007b.
- Jacot Des Combes, H., Esper, O., De La Rocha, C. L., Abellmann, A., Gersonde, R., Yam, R., and Shemesh, A.: Diatom  $\delta^{13}\text{C}$ ,  $\delta^{15}\text{N}$ , and C/N since the Last Glacial Maximum in the Southern Ocean: Potential impact of species composition, *Paleoceanography*, 23, PA4209, doi:10.1029/2008PA001589, 2008.
- Jacques, G.: Some ecophysiological aspects of the Antarctic phytoplankton, *Polar Biol.*, 2, 27–33, 1983.
- Jeandel, C., Ruiz-Pino, D., Gjata, E., Poisson, A., Brunet, C., Charriaud, E., Dehairs, F., Delille, D., Fiala, M., Fravallo, C., Miquel, J. C., Park, Y. H., Pondaven, P., Quéguiner, B., Razouls, S., Shauer, B., and Tréguer, P.: KERFIX, a time-series station in the Southern Ocean: a presentation, *J. Mar. Syst.*, 17, 555–569, 1998.
- Jeandel, C., Peucker-Ehrenbrink, B., Jones, M. T., Pearce, C. R., Oelkers, E. H., Godderis, Lacan, F., Aumont, O., and Arsouze, T.: Ocean margins: The missing term in oceanic element budgets?, *Trans. Am. Geophys. Union*, 92, 217–218, 2011.
- McCartney, M. S. and Donohue, K. A.: A deep cyclonic gyre in the Australian–Antarctic Basin, *Prog. Oceanogr.*, 75, 675–750, 2007.
- Milligan, A. J., Varela, D. E., Brzezinski, M. A., and Morel, F. M. M.: Dynamics of silicon metabolism and silicon isotopic discrimination in a marine diatom as a function of  $p\text{CO}_2$ , *Limnol. Oceanogr.*, 49, 322–329, 2004.
- Mongin, M., Molina, E., and Trull, T. W.: Seasonality and scale of the Kerguelen plateau phytoplankton bloom: A remote sensing and modeling analysis of the influence of natural iron fertilization in the Southern Ocean, *Deep-Sea Res. II*, 55, 880–892, 2008.
- Nelson, D. M. and Gordon, L. I.: Production and pelagic dissolution of biogenic silica in the Southern Ocean, *Geochim. Cosmochim. Acta.*, 46, 491–501, 1982.
- Nelson, D. M. and Smith, W. O.: Sverdrup revisited : critical depths, maximum chlorophyll levels, and the control of Southern Ocean productivity by the irradiance-mixing regime, *Limnol. Oceanogr.*, 36, 1650–1661, 1991.
- Nugraha, A., Pondaven, P., and Tréguer, P.: Influence of consumer-driven nutrient recycling on primary production and the distribution of N and P in the ocean, *Biogeosciences*, 7, 1285–1305, doi:10.5194/bg-7-1285-2010, 2010.
- Oelkers, E. H., Gislason, S. R., Eiriksdottir, E. S., Jones, M. T., Pearce, C. R., and Jeandel, C.: The role of riverine particulate material on the global cycles of the elements, *Appl. Geochem.*, 26, 365–369, 2011.
- Opfergelt, S. and Delmelle, P.: Silicon isotopes and continental weathering processes: Assessing controls on Si transfer to the ocean, *C. R. Geosci.*, 344, 723–738, 2012.
- Orsi, A. H., Whitworth III, T., and Nowlin Jr, W. D.: On the meridional extent and fronts of the Antarctic Circumpolar Current, *Deep-Sea Res. I*, 42, 641–673, 1995.
- Paasche, E.: Silicon and the ecology of marine plankton diatoms, II. Silicate-uptake kinetics in five diatom species, *Mar. Biol.*, 19, 262–269, 1973.
- Park, Y.-H., Gamberoni, L., and Charriaud, E.: Frontal structure, water masses, and circulation in the Crozet Basin, *J. Geophys. Res.-Oceans*, 98, 12361–12385, 1993.
- Park, Y.-H., Charriaud, E., and Fieux, M.: Thermohaline structure of the Antarctic Surface Water/Winter Water in the Indian sector of the Southern Ocean, *J. Mar. Syst.*, 17, 5–23, 1998a.
- Park, Y.-H., Roquet, F., Durand, I., and Fuda, J.-L.: Large-scale circulation over and around the Northern Kerguelen Plateau, *Deep-Sea Res. II*, 55, 566–581, 1998b.
- Park, Y.-H., Fuda, J.-L., Durand, I., and Naveira Garabato, A. C.: Internal tides and vertical mixing over the Kerguelen Plateau, *Deep-Sea Res. II*, 582–593, 2008.
- Platt, T. and Jassby, A. D.: The relationship between photosynthesis and light for natural assemblages of coastal marine phytoplankton, *J. Phycol.*, 12, 421–430, 1976.
- Platt, T., Sathyendranath, S., Edwards, A. M., Broomhead, D. S., and Ulloa, O.: Nitrate supply and demand in the mixed layer of the ocean, *Mar. Ecol. Prog. Ser.*, 254, 3–9, 2003.
- Pogge von Strandmann, P. A. E., Opfergelt, S., Lai, Y.-J., Sigfússon, B., Gislason, S. R., and Burton, K. W.: Lithium, magnesium and silicon isotope behaviour accompanying weathering in a basaltic soil and pore water profile in Iceland, *Earth Planet. Sci. Lett.*, 339/340, 11–23, 2012.

- Pondaven, P., Fravallo, C., Ruiz-Pino, D., Tréguer, P., Quéguiner, B., and Jeandel, C.: Modelling the silica pump in the Permanently Open Ocean Zone of the Southern Ocean, *J. Mar. Syst.*, 17, 587–619, 1998.
- Roquet, F., Park, Y.-H., Guinet, C., Bailleul, F., and Charrassin, J.-B.: Observations of the Fawn Trough Current over the Kerguelen Plateau from instrumented elephant seals, *J. Mar. Syst.*, 78, 377–393, 2009.
- Sarthou, G., Timmermans, K. R., Blain, S., and Tréguer, P.: Growth physiology and fate of diatoms in the ocean: a review, *J. Sea Res.*, 53, 25–42, 2005.
- Savage, P. S., Georg, R. B., Williams, H. M., Burton, K. W., and Halliday, A. N.: Silicon isotope fractionation during magmatic differentiation, *Geochim. Cosmochim. Acta*, 75, 6124–6139, 2011.
- Smayda, T. J.: The suspension and sinking of phytoplankton in the sea, *Oceanogr. Mar. Biol. Ann. Rev.*, 8, 353–414, 1970.
- Sommer, U.: Nitrate- and silicate-competition among antarctic phytoplankton, *Mar. Biol.*, 91, 345–351, 1986.
- Steele, J. H. and Henderson, E. W.: Predation control of plankton demography, *ICES J. Mar. Sci.*, 52, 565–573, 1995.
- Strickland, J. D. H. and Parsons, T. R.: A practical handbook of seawater analysis, Fish. Res. Board Can., Ottawa, 310 pp., 1972.
- Sutton, J. N., Varela, D. E., Brzezinski, M. A., and Beucher, C. P.: Species-dependent silicon isotope fractionation by marine diatoms, *Geochim. Cosmochim. Acta*, 104, 300–309, 2013.
- Tréguer, P. J. and De La Rocha, C. L.: The World Ocean Silica Cycle, *Ann. Rev. Mar. Sci.*, 5, 477–501, 2013.
- Tyrrell, T.: The relative influences of nitrogen and phosphorus on oceanic primary production, *Nature*, 400, 525–531, 1999.
- Van Cappellen, P., Dixit, S., and Van Beusekom, J.: Biogenic silica dissolution in the oceans: Reconciling experimental and field-based dissolution rates, 4, American Geophysical Union, Washington, DC, Etats-Unis, 2002.
- Varela, D. E., Pride, C. J., and Brzezinski, M. A.: Biological fractionation of silicon isotopes in Southern Ocean surface waters, *Global Biogeochem. Cy.*, 18, GB1047, doi:10.1029/2003gb002140, 2004.
- Ziegler, K., Chadwick, O. A., Brzezinski, M. A., and Kelly, E. F.: Natural variations of  $\delta^{30}\text{Si}$  ratios during progressive basalt weathering, Hawaiian Islands, *Geochim. Cosmochim. Acta.*, 69, 4597–4610, 2005.

## Appendix

**Table A1.** Data for water samples from ANTXXIII/9.

Station	Date	Latitude	Longitude	Depth (m)	[DSi] ( $\mu\text{M}$ )	$\delta^{30}\text{Si} \pm \sigma$ (‰)	Location
CTD1	02/11/07	69°24.03' S	7°0.12' W	20	57	1.63 $\pm$ 0.06	Weddell Gyre
CTD1	02/11/07	69°24.03' S	7°0.12' W	40	60.4	1.65 $\pm$ 0.10	
CTD1	02/11/07	69°24.03' S	7°0.12' W	60	63.1	1.33 $\pm$ 0.03	
CTD1	02/11/07	69°24.03' S	7°0.12' W	80	65.8	1.23 $\pm$ 0.08	
CTD1	02/11/07	69°24.03' S	7°0.12' W	200	77.8	1.21 $\pm$ 0.07	
CTD1	02/11/07	69°24.03' S	7°0.12' W	300	83.9	1.33 $\pm$ 0.06	
CTD1	02/11/07	69°24.03' S	7°0.12' W	500	93.4	0.71 $\pm$ 0.05	
CTD1	02/11/07	69°24.03' S	7°0.12' W	750	102.3	1.26 $\pm$ 0.08	
CTD1	02/11/07	69°24.03' S	7°0.12' W	1000	106.5	1.17 $\pm$ 0.03	
CTD1	02/11/07	69°24.03' S	7°0.12' W	1250	116.7	1.01 $\pm$ 0.10	
CTD1	02/11/07	69°24.03' S	7°0.12' W	1500	114.4	1.18 $\pm$ 0.04	
CTD1	02/11/07	69°24.03' S	7°0.12' W	1750	115.7	0.99 $\pm$ 0.07	
CTD1	02/11/07	69°24.03' S	7°0.12' W	2000	117.2	1.08 $\pm$ 0.06	
CTD1	02/11/07	69°24.03' S	7°0.12' W	2250	119.9	1.30 $\pm$ 0.01	
CTD4	02/24/07	68°43.34' S	70°40.66' E	20	36.8	2.13 $\pm$ 0.02	Prydz Bay
CTD4	02/24/07	68°43.34' S	70°40.66' E	40	48.8	1.71 $\pm$ 0.02	
CTD4	02/24/07	68°43.34' S	70°40.66' E	60	52.8	–	
CTD4	02/24/07	68°43.34' S	70°40.66' E	80	55.3	–	
CTD4	02/24/07	68°43.34' S	70°40.66' E	200	57.7	1.60 $\pm$ 0.02	
CTD4	02/24/07	68°43.34' S	70°40.66' E	500	58.7	–	
CTD6	03/21/07	65°20.98' S	82°39.48' E	20	53.5	1.44 $\pm$ 0.04	Prydz Bay
CTD6	03/21/07	65°20.98' S	82°39.48' E	40	50.2	1.42 $\pm$ 0.04	
CTD6	03/21/07	65°20.98' S	82°39.48' E	60	54	1.18 $\pm$ 0.06	
CTD6	03/21/07	65°20.98' S	82°39.48' E	80	57.3	1.13 $\pm$ 0.05	
CTD6	03/21/07	65°20.98' S	82°39.48' E	200	64.9	1.59 $\pm$ 0.03	
CTD6	03/21/07	65°20.98' S	82°39.48' E	500	88.1	1.35 $\pm$ 0.07	
CTD5	03/02/07	60°56.97' S	72°43.30' E	30	20.2	2.21 $\pm$ 0.08	Antarctic Circumpolar Current
CTD5	03/02/07	60°56.97' S	72°43.30' E	40	21.6		
CTD5	03/02/07	60°56.97' S	72°43.30' E	60	37.5	–	
CTD5	03/02/07	60°56.97' S	72°43.30' E	80	39.6	1.62 $\pm$ 0.06	
CTD5	03/02/07	60°56.97' S	72°43.30' E	200	72.9	1.25 $\pm$ 0.03	
CTD5	03/02/07	60°56.97' S	72°43.30' E	500	81.4	1.20 $\pm$ 0.04	
CTD5	03/02/07	60°56.97' S	72°43.30' E	1000	82	1.07 $\pm$ 0.03	
CTD5	03/02/07	60°56.97' S	72°43.30' E	1500	97.9	0.96 $\pm$ 0.05	
CTD5	03/02/07	60°56.97' S	72°43.30' E	2000	106.9	1.12 $\pm$ 0.06	
CTD5	03/02/07	60°56.97' S	72°43.30' E	2500	120.7	0.92 $\pm$ 0.07	
CTD5	03/02/07	60°56.97' S	72°43.30' E	3000	121.2	1.04 $\pm$ 0.05	
CTD5	03/02/07	60°56.97' S	72°43.30' E	3500	122.1	1.10 $\pm$ 0.05	
CTD5	03/02/07	60°56.97' S	72°43.30' E	4000	125.4	1.20 $\pm$ 0.09	
CTD7	03/24/07	59°37.25' S	85°40.52' E	20	28.1	1.90 $\pm$ 0.15	South of Antarctic Circumpolar Current
CTD7	03/24/07	59°37.25' S	85°40.52' E	40	41.5	2.21 $\pm$ 0.09	
CTD7	03/24/07	59°37.25' S	85°40.52' E	60	55.3	1.32 $\pm$ 0.06	
CTD7	03/24/07	59°37.25' S	85°40.52' E	80	60.9	1.53 $\pm$ 0.07	
CTD7	03/24/07	59°37.25' S	85°40.52' E	200	76.2	1.25 $\pm$ 0.05	
CTD7	03/24/07	59°37.25' S	85°40.52' E	500	88.1	1.44 $\pm$ 0.02	
CTD7	03/24/07	59°37.25' S	85°40.52' E	1000	94.2	–	
CTD7	03/24/07	59°37.25' S	85°40.52' E	1500	117.3	–	
CTD7	03/24/07	59°37.25' S	85°40.52' E	2000	120.8	–	
CTD7	03/24/07	59°37.25' S	85°40.52' E	2500	118.5	–	
CTD7	03/24/07	59°37.25' S	85°40.52' E	3000	118.1	–	
CTD7	03/24/07	59°37.25' S	85°40.52' E	3500	119.6	–	
CTD8	03/26/07	55°0.30' S	73°19.98' E	20	11.6	2.39 $\pm$ 0.06	Kerguelen Plateau
CTD8	03/26/07	55°0.30' S	73°19.98' E	40	11.7	2.20 $\pm$ 0.07	
CTD8	03/26/07	55°0.30' S	73°19.98' E	60	11.4	1.99 $\pm$ 0.03	
CTD8	03/26/07	55°0.30' S	73°19.98' E	80	31.5	0.94 $\pm$ 0.02	
CTD8	03/26/07	55°0.30' S	73°19.98' E	500	66.8	1.40 $\pm$ 0.04	
CTD8	03/26/07	55°0.30' S	73°19.98' E	1500	82.4	1.57 $\pm$ 0.02	





---

# The silicon isotopic composition ( $\delta^{30}\text{Si}_{\text{DSi}}$ ) of water masses in the Atlantic Ocean

— Chapter 4 —

---



# Chapter 4 – Silicon isotopic composition ( $\delta^{30}\text{Si}_{\text{DSi}}$ ) of water masses in the Atlantic Ocean

---

This study focuses on silicon isotopic composition ( $\delta^{30}\text{Si}_{\text{DSi}}$ ) and concentration of dissolved silicon at different locations in the Atlantic Ocean (Subtropical and Tropical Atlantic Ocean and Atlantic sector of the Southern Ocean). As water masses, such as the North Atlantic Deep Water (NADW), can travel very long distances from their source area, their characteristics (T, S, [DSi],...) can be modified from those observed at the initial location. So it is of importance to understand where water masses form, which other waters mix in, how they flow and what their boundaries are in order to make sense of the  $\delta^{30}\text{Si}_{\text{DSi}}$  values observed.

Surface waters are imprinted by biological activity in the euphotic zone resulting in specific DSi concentrations and  $\delta^{30}\text{Si}_{\text{DSi}}$ . With depth, these values change as we move into intermediate and then to bottom water masses, ending with high DSi concentrations and low  $\delta^{30}\text{Si}_{\text{DSi}}$  in bottom water resulting from biogenic silica dissolution and exchange between water masses. Physical events such as upwelling and downwelling also contribute to the observed distributions of DSi and silicon isotopes by raising intermediate water to surface or by bringing down surface water to deep Ocean. Riverine discharge can as well modify surface water characteristics.

In a first part of this chapter I will present an overview of large scale circulation in the Atlantic Ocean and in a second part I will present new DSi concentration and  $\delta^{30}\text{Si}_{\text{DSi}}$  data from the tropical and subtropical Atlantic Ocean and from the Atlantic sector of the Southern Ocean. I will attempt to better understand the behavior of the Weddell Gyre in terms of DSi concentration and  $\delta^{30}\text{Si}_{\text{DSi}}$  of deep water masses and the origin of the tropical Atlantic Ocean values around Cape Verde Island.

# I An overview of large scale circulation in the Atlantic Ocean

## I.1 The Atlantic Ocean

The Atlantic Ocean is the 2<sup>nd</sup> largest ocean basin in area with its 106.000.000 km<sup>2</sup> that separates the American continent from the Euro-African continent. The Atlantic Ocean is bounded by the Arctic Ocean on its northern side and at around 60°S by the Southern Ocean on its southern side. The Drake Passage separates the Pacific Ocean from the Atlantic Ocean in the Southwest and the eastern limit is the 20°E meridian south of Cape Agulhas (South Africa) that separates the Atlantic Ocean from the Indian Ocean.

The North Atlantic Ocean is a key ocean for the global thermohaline circulation, also known as the great conveyor belt (Fig. 4.1). Surface waters from the South Atlantic Ocean flow northward to the pole. During its flow toward the North Atlantic it undergoes temperature loss due to ocean - air exchange leading to water surface cooling that results in its densification. This water becomes dense enough to sink in the northern North Atlantic Ocean, leading to the formation of North Atlantic Deep Water (NADW) that initiates the thermohaline circulation. In the Atlantic sector of the Southern Ocean, in the Weddell Sea, surface waters cool down and sink along the continental shelf that guides the formation of the Antarctic Bottom Water (AABW) that will flow in the deep ocean, below NADW.

According to Emery and Meincke (1986), surface and central water masses are defined as residing above 500 m, intermediate water as occurring between 500 – 1000 m and the deep water as being situated below 1000 m. A water mass is defined by a range of temperature ( $\theta$ ), salinity ( $S$ ), and density ( $\sigma$ ) values characteristic of the forming-region, these characteristics being eroded during the flow by interactions with other water masses.

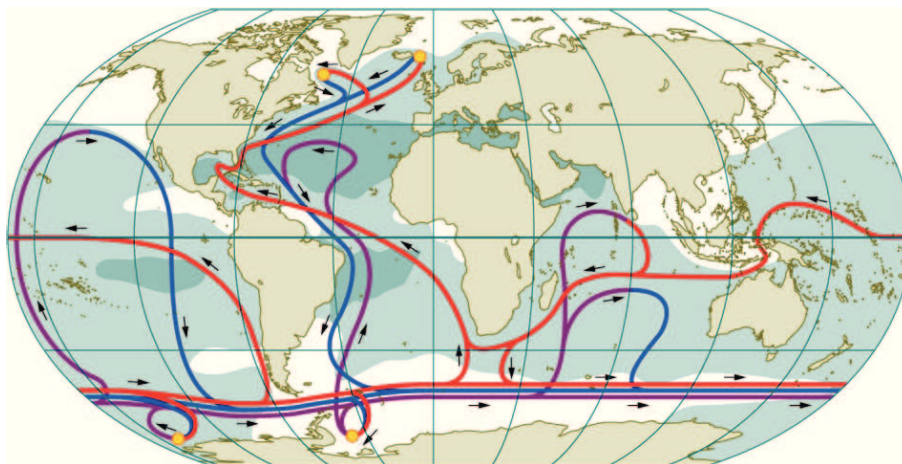


**Figure 4.1 The great conveyor belt. Representation of warm surface currents (red), cold deep currents (blue) and bottom currents (purple). Circles: sites of deep water formation, white zones: salinity < 34, dark blue: salinity > 36 psu, (Kuhlbrodt et al., 2007).**

## I.2 The water masses of the North Atlantic Ocean

The Tropical Atlantic Ocean falls between 20°N and 20°S and the Subtropical Atlantic Ocean is found at higher latitudes between 40°N and 40°S. The description will focus on of the Subtropical and Tropical Atlantic Ocean around the Cape Verde Island, where the samples from MSM10/1 campaign were collected.

### I.2.1 Central and intermediate water masses

#### I.2.1.1 Central Water masses

A main feature of the Tropical Atlantic Ocean is the coastal upwelling off Senegal, bringing to surface cold and nutrient rich subsurface water (Bory et al., 2001). This upwelling is active mainly from end of November to mid-March (Stramma and Schott, 1999). Its influence is mainly restricted to coastal areas but can be observed to a limited extent further offshore. The second characteristic is the Cape Verde Frontal Zone (CVFZ) that serves as a border between two different water masses, namely North Atlantic Central Water (NACW) and the South Atlantic Central Water (SACW) (Stramma and Schott, 1999) located north of Cape Verde Island (Fig 4.2).

North of the front is the North Equatorial Current (NEC) that flows in the southwest Atlantic along the front as a sinking zone. South of the CVFZ, the North Equatorial Counter Current (NECC) flows north-eastward and at ~ 9°N flows back in the western Atlantic along the CVFZ. Opposite to the subduction of the north part of the front, the Guinea Dome is an upwelling zone. At intermediate depths (400 – 600 m), the CVFZ is the boundary between North Atlantic Central Water (NACW) and South Atlantic Central Water (SACW).

The central water masses in the Atlantic Ocean are the North Atlantic Central Water (NACW) and the South Atlantic Central Water (SACW). These water masses form by the subduction of water from the Mixed Layer in winter by Ekman pumping in the subtropical convergence zone and the advection of water along isopycnal surfaces (Sprintall and Tomczak, 1993). According to Emery (2003) central water can be separated into three water masses. In the North Atlantic Ocean is found the western North Atlantic Central Water (wNACW,  $35 < S < 36.7$  and  $7 < \theta < 20$  °C) formed at 60 – 30°W and 40 – 50°N. The 2<sup>nd</sup> water mass is the Eastern North Atlantic Central Water (eNACW,  $35.2 < S < 36.7$  and  $8 < \theta < 18$  °C) formed from 60° – 40°N close to Europe. In the South Atlantic only the South Atlantic Central Water (SACW,  $34.3 < S < 35.8$  and  $5 < \theta < 18$  °C) is found (Arhan et al., 1994) formed on the southern edge of the subtropical front in the Southern Ocean.

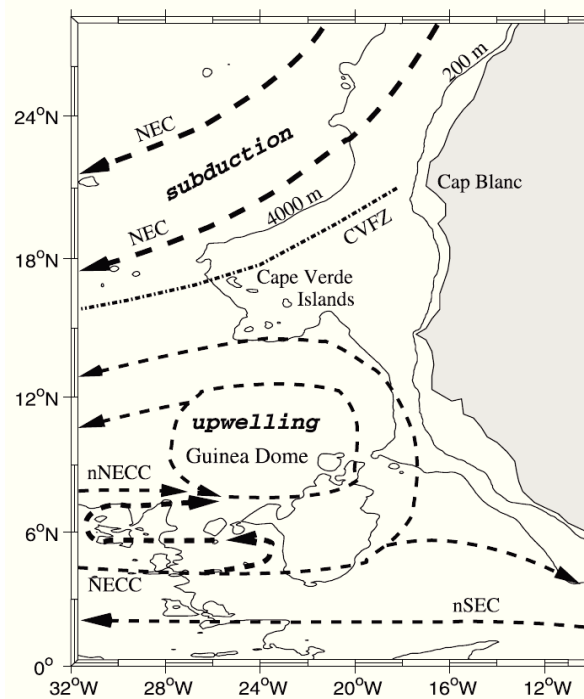


**Figure 4.2 Map of the Subtropical and Tropical North Atlantic Ocean circulation. The dashed and dotted lines represent the Cape Verde Frontal Zone (CVFZ), the North Equatorial Current (NEC), the northern band of the South Equatorial Current (nSEC), the North Equatorial Countercurrent (NECC) and around the Guinea Dome is found the northern NECC (nNECC) as labelled on the plot (Stramma et al., 2005).**

According to Bory et al. (2001), a second frontal zone exists at 22 – 24°N that serves as a boundary between intermediate water masses Mediterranean Water (MW) and Antarctic Intermediate Water (AAIW) in the South, at 800 – 1000m. The front location is as well an area where the NADW overflows the AABW, due to greater density of the latter.

#### 1.2.1.2 Intermediate Water masses

The flow of intermediate water in both the North and the South Atlantic Ocean is generally toward the equator. In the North Atlantic, two intermediate water masses are found, Arctic Intermediate Water (AIW) and Antarctic Intermediate Water (AAIW).

The southward flow is composed of AIW and Mediterranean Outflow Water (MOW). The AIW ( $34.7 < S < 34.8$  and  $-1.5 < \theta < 3$  °C) coming from the Arctic domain flows south out of the Labrador Sea to 50°N and then flows north in the direction of the Greenland Sea. The MOW ( $35.0 < S < 36.2$  and  $2.6 < \theta < 11$  °C) flows northeast to Ireland and then flows south-westward to 30°N on the west side of the Atlantic Ocean to finally propagate until the Greenland Sea where it meets the AIW.

The second intermediate water, AAIW ( $33.8 < S < 34.8$  and  $2 < \theta < 6$  °C), comes from the Southern Ocean. The first branch flows northward to propagate across the equator until ~30°N along the American continent in a gyre circulation and the second branch flows longitudinally to the Indian

Ocean at  $\sim 50^{\circ}\text{S}$  (Schmitz, 1996). AAIW is the layer found above the NADW in a major part of the Atlantic Ocean.

The AIW is formed in the northern North Atlantic by subduction of water coming from the Labrador Sea and from the Iceland Sea.

### 1.2.2 The deep water masses of the Atlantic Ocean

The general flow of the deep water masses in the Atlantic Ocean is latitudinal (North – South). North Atlantic Deep Water (NADW,  $34.8 < S < 35.0$  and  $1.50 < \theta < 4.0^{\circ}\text{C}$ ) formed in the northern North Atlantic flows southward along the western side of the Atlantic Ocean as far as  $50^{\circ}\text{S}$ .

In the South Atlantic Ocean, Antarctic Bottom Water (AABW,  $34.6 < S < 34.7$  and  $-0.8 < \theta < 2.0^{\circ}\text{C}$ ), the deep water of the Southern Ocean, flows north as far as  $\sim 35^{\circ}\text{S}$ . NADW and AABW first meet in the tropical Atlantic Ocean where the NADW is displaced to flow above the AABW.

The sites of first NADW identification (where the NADW is formed) are located in the North Atlantic Ocean at  $\sim 60^{\circ}\text{N}$  (Morozov et al., 2010). This water mass is found at depths below 1500 m (Emery and Meincke, 1986). The formation of NADW involves three major components: Labrador Sea Water (LSW), Iceland-Scotland Overflow Water (ISOW), and Denmark Strait Overflow Water (DSOW) (Frew et al., 2000).

Mediterranean Outflow Water (MOW) and subsurface water from the Southern Ocean can contribute to NADW formation (Smethie and Fine, 2001; Morozov et al., 2010). There are three layers of NADW depending on the water source. Lower NADW results from a mix of Antarctic Bottom Water (AABW), DSOW and intermediate water. Middle NADW comes from a mix of AABW, ISOW and intermediate water. This Middle NADW does not exist south of  $25^{\circ}\text{S}$ . Upper NADW is formed by a mixture of LSW and MOW in the Deep Western Boundary Current and cannot be distinguished from INADW beyond  $25^{\circ}\text{S}$ .

NADW propagates southward along the western coast of the basin. At the equator, NADW enters in the eastern basin at  $\sim 20^{\circ}\text{W}$ . In the South Atlantic Ocean, at about  $\sim 40^{\circ}\text{S}$ , the main flow is divided into 2 branches, one follows the main flow from the north and the second flows latitudinally to the eastern basin. The eastern branch reaches  $\sim 60^{\circ}\text{S}$  then flows eastward to the Indian Ocean.

Another deep water mass called the North East Atlantic Deep Water (NEADW) is formed, by mixing the ISOW and the water masses in the area by a recirculation cell of the subpolar gyre (McCartney, 1992; Lacan, 2002). This water mass has a salinity maximum and oxygen minimum at  $27.85$  (Lacan, 2002) and flows in the north Atlantic subpolar gyre.

### 1.3 The Southern Ocean water masses circulation

The Southern Ocean is found at about 60°S (between 55°S to 75°S) divided by 5 fronts: the Subtropical Front (STF), Subantarctic Front (SAF), the Polar Front (PF), the Subantarctic Circumpolar Front (SACCF) and the Southern Boundary (Fig. 4.3). The SAF and PF characterise the Antarctic Circumpolar Current (Emery, 1977; Whitworth III, 1980) that dominates the Southern Ocean circulation (Orsi et al., 1995; van Wijk et al., 2010). By flowing eastward unbroken around Antarctica, the ACC (Orsi et al., 1995) connects the 3 sectors (Atlantic, Pacific and Indian) and main oceans together carrying over and mixing water masses and properties from one ocean basin to another (Cunningham, 2005).

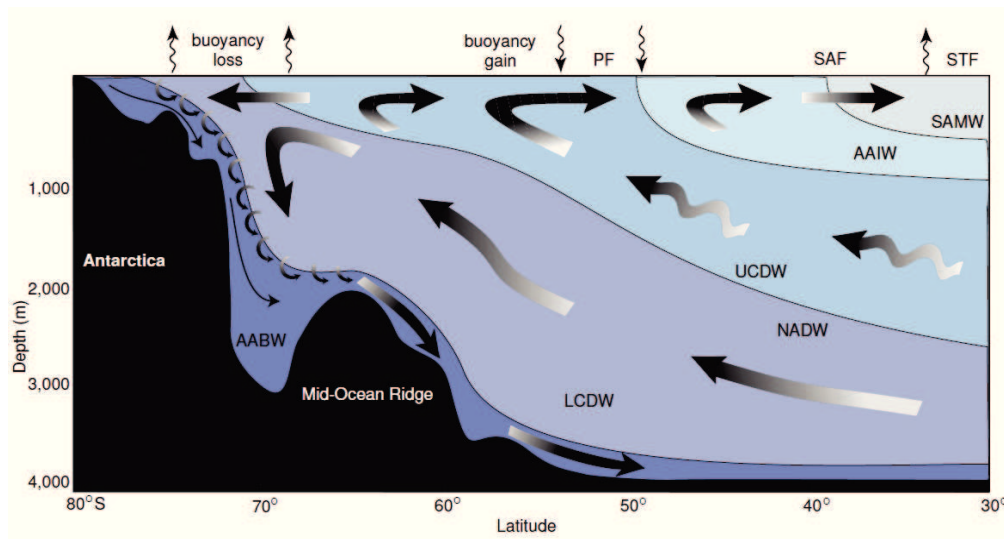


**Figure 4.3** A schematic view of the map of meridional overturning circulation in the Southern Ocean (Speer et al., 2000; Dong, 2012). SAMW is the surface water, AAIW is the Antarctic Intermediate Water, UCDW is Upper Circumpolar Deep Water, NADW is North Atlantic Deep Water, LCDW is Lower Circumpolar Deep Water and AABW is Antarctic Bottom Water.

Three special areas will be describe in term of circulation and water masses formation, that are the Drake Passage that connect the Pacific and the Atlantic Ocean, Weddell Gyre in the Atlantic sector of the Southern Ocean and the Kerguelen Plateau in the Indian sector of the Southern Ocean.

#### 1.3.1 The Drake Passage

The Drake Passage is located between Antarctic Peninsula and the South Scotia ridge (the southern limit) and the northern limit is South America. It is the narrowest part (700 km) on the Antarctic Circumpolar Current (ACC) flow where the distance between the fronts are minimum and the passage is also shallower than the surrounding basins. The water flow through the Drake Passage is driven by the ridge system that deflects the ACC flow to the north (Provost et al., 2011). Due to that the passage is considered as a choke point for the ACC flow. A characteristic of the water masses in the Drake Passage is the depth difference between north and south of the Polar Front (Fig. 4.4).



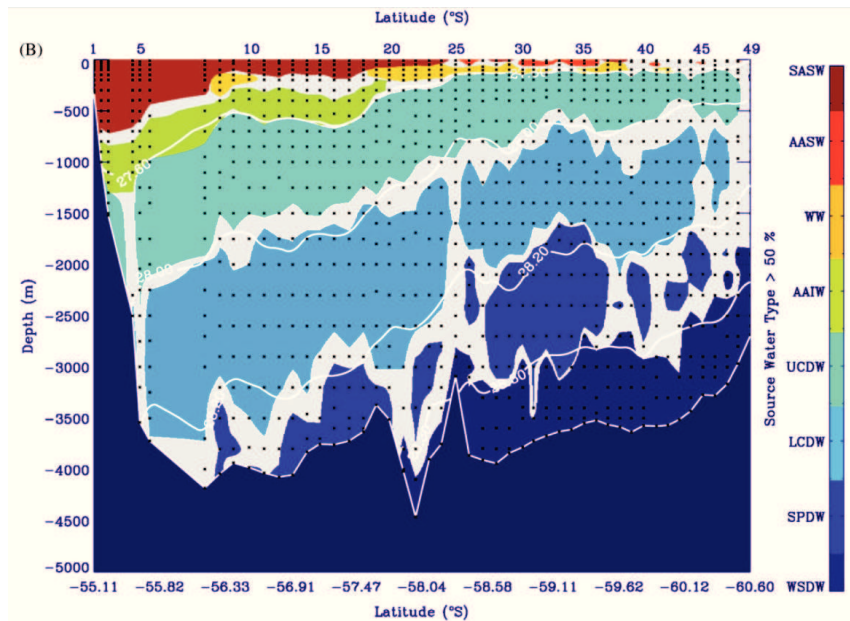


**Figure 4.4** Mean solution composition showing concentration (greater than 50%) of all source water types along Section 1 of ANT-XXIII/3 in the Drake Passage. Gray color represents a mixing of SWTs without major contribution of any SWT (white contours represent neutral density values) (Sudre et al., 2011).

#### I.3.1.1 Intermediate water mass

The intermediate water mass found in the Drake Passage is Antarctic Intermediate Water (AAIW). There are several hypotheses linked to AAIW formation and the most recent one is from Sloyan and Rintoul (2001). These authors described AAIW formation between the Subpolar Front and the Subantarctic Zone by a modification of Antarctic Surface Water (ASW). The ASW then detaches from the cyclonic meanders of the Subantarctic Front to flow northward then the surface water moves from the surface to the intermediate layer (Morozov et al., 2010). The AAIW formed flows northward in a gyre circulation. A second gyre is centered on the equator. A debate on how far AAIW is transported to the north is still topical but according to Perez et al. (2001) it can be traced until the Canary archipelago.

#### I.3.1.2 Deep water masses

In the Drake Passage, the 2 main water masses are Upper Circumpolar Deep Water (UCDW,  $34.4 < S < 34.7$  and  $1.50\text{ }^{\circ}\text{C} < \theta$ ) and Lower Circumpolar Deep Water (LCDW,  $\sigma = 27.8\text{ kg m}^{-3}$ ) (Well et al., 2003), found below the intermediate water (Fig. 4.4). UCDW is formed in the Pacific and Indian Ocean and LCDW is formed at the northern periphery of the ACC in the Atlantic Ocean. UCDW is formed by mixing of Indian Ocean Deep Water (IODW) and Pacific Deep Water (PDW) while LCDW is formed by the mix of North Atlantic Deep Water with deep ACC water masses (Orsi et al., 1995; Morozov et al., 2010).



Other deep water masses from the Pacific Ocean are found in the Drake Passage. Southeast Pacific Deep Water (SPDW) and Southeast Pacific Deep Slope Water (SPDSW) (Well et al., 2003) come from the deep Pacific Ocean and the southward flow along the continental slope of the west coast of South America that is an exit source for Pacific water.

### 1.3.2 The Weddell Gyre

The Weddell Gyre is located in the Southern Ocean between the Antarctic Peninsula on to the western side, Antarctica to the south and the Antarctic Circumpolar Current (ACC) in the north and east. The ACC influences the gyre circulation that circulates clockwise (van Heuven et al., 2011).

Warm Deep Water (WDW,  $34.64 < S < 34.72$  and  $0 < \theta < 0.8$  °C) found in the Weddell Gyre comes from the eastern part of the gyre as a slope current and flows northeast (Fig. 4.5). Weddell Sea Deep Water (WSDW,  $34.45 < S < 34.64$  and  $-1.20 < \theta < 0.20$  °C) found below WDW comes from the southeast of the Weddell Gyre and flows in the same direction as WDW (Huhn et al., 2013). Weddell Sea Bottom Water (WSBW,  $34.64 < S < 34.68$  and  $-1.40 < \theta < -0.70$  °C) formed close to the Antarctic shelves south and southwest of the gyre, propagates north-eastward in the Weddell Gyre.

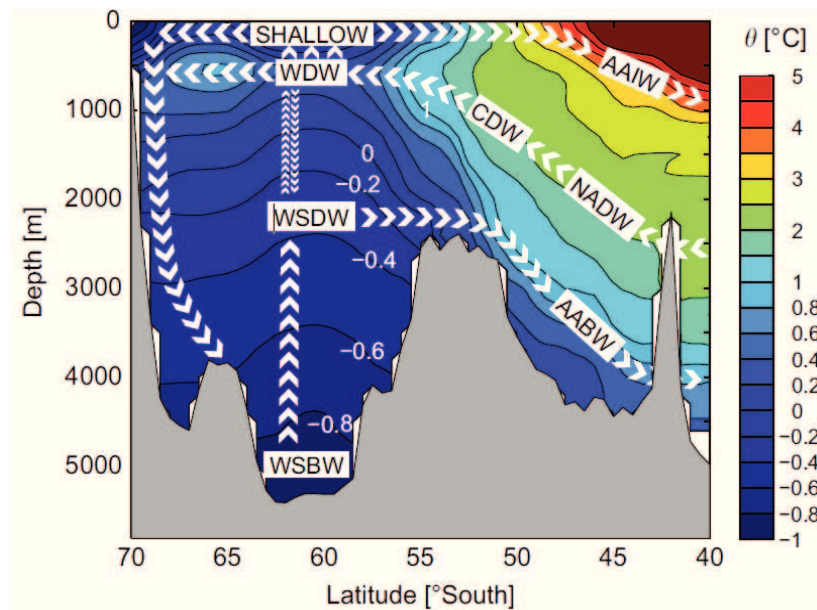


**Figure 4.5** Section along the prime meridian in the Southern Ocean and in the Weddell Gyre showing potential temperature ( $\theta$ (°C)) and the generalized locations and movements of various water masses. The region between 40°S and 55°S represents the Antarctic Circumpolar Current (ACC). The region from 55°S to 70°S represents the actual Weddell Gyre. AAIW: Antarctic Intermediate Water, NADW: North Atlantic Deep Water, CDW: Circumpolar Deep Water, AABW: Antarctic Bottom Water, SHALLOW: the shallowest 200m of the water column, WDW: Warm Deep Water, WSDW: Weddell Sea Deep Water and WSBW: Weddell Sea Bottom Water (van Heuven et al., 2011).

Warm Deep Water is formed by entry of Lower Circumpolar Deep Water (LCDW) from the ACC into the gyre where it mixes with surface and shelf waters (Mackensen, 2001). WSDW, the main

water mass in the gyre, is found under the WDW. This water mass is mainly formed by large scale mix of the WDW with Weddell Sea Bottom Water.

A small fraction of WSDW is formed by a mix between surface water and WDW (Fahrbach et al., 2011). WSBW is formed in the south and west of the Weddell Basin by the flow of the dense shelf water and then flows eastward by the northern circulation. In the Weddell Sea two types of WSBW may be distinguished, depending on the formation area. WSBWb is the result of the WSBW formation at the seabed of the basin near Filchner-Ronne Ice Shelf, while the WSBWs is on the Antarctic Peninsula formed in the western side of the gyre at the ice shelves (Huhn et al., 2013).

Antarctic Bottom Water (AABW) is mainly formed in the Weddell Gyre (60–65 % (Morozov et al., 2010)) in the southern Ocean. Its formation occurs by a mix of Shelf Water and CDW near the shelf break. The AABW propagates in the Atlantic Ocean by the eastern slope of the Mid-Atlantic Ridge and reaches low northern latitudes in a modified water mass that plays a role in the production of North Atlantic Deep Water (NADW). AABW flows eastward but does not flow in a circumpolar fashion around Antarctica due to its high density. The relatively shallow depth of the Drake Passage is considered as a topographic barrier to its dense flow.

## II Silicon isotopic composition ( $\delta^{30}\text{Si}$ DSi) of water masses in the Atlantic Ocean

### II.1 Introduction

The silica cycle of the Atlantic Ocean is poorly studied (see for example (Mosseri et al., 2005)), especially in terms of silicon isotopes, due to its relatively minor contribution to the global BSi production (up to 10 %, Sarmiento et al. (2007)), compared to 60 % from the Southern Ocean. However, the Atlantic Ocean forms a major part of the understanding of the silica cycle due to the formation of deep water masses and their circulation through this ocean. The formation of these deep water masses is the main driver of the Meridional Overturning Circulation (MOC) that redistributes nutrients, including silicon, to the world's oceans through physical and biological processes.

As previously mentioned in the chapter 1, diatoms take up dissolved silicon (DSi), favouring the light isotope ( $^{28}\text{Si}$ ), when they build their frustules which are composed of biogenic silica (BSi). This fractionation leads to BSi with a silicon isotopic composition ( $\delta^{30}\text{Si}$ ) that is generally around 1.1 ‰ lower than the DSi source (De La Rocha et al., 1997), although, there may be some variability

between diatom species in the extent of fractionation (Sutton et al., 2013). Conversely, the dissolution of the frustules fractionates silicon isotopes, discriminating against the heavier isotopes, with the  $\delta^{30}\text{Si}$  of the DSi that is liberated being 0.55 ‰ lower than the BSi source (Demarest et al., 2009). The resulting diatom influence over the silicon isotopic composition of seawater is reflected by high  $\delta^{30}\text{Si}_{\text{DSi}}$  values in the surface water, associated with DSi concentrations significantly lower than that of the deeper, upwelling waters. Deep waters have high DSi concentration due to the accumulation of DSi coming from dissolution of sinking BSi, resulting in relatively low  $\delta^{30}\text{Si}_{\text{DSi}}$  values in older deep waters (De La Rocha et al., 1997; De La Rocha et al., 2000; Milligan et al., 2004; Varela et al., 2004; Cardinal et al., 2005; Beucher et al., 2008, 2011; De La Rocha et al., 2011; Fripiat et al., 2011a; Fripiat et al., 2011b; de Brauwere et al., 2012; de Souza et al., 2012a).

The two main deep water masses in the Atlantic Ocean are formed at opposite ends of the basin (at high northern and southern latitudes) and then flow in opposite directions to fill the entire Atlantic Ocean basin. In the southern Atlantic, this deep water mass is Antarctic Bottom Water (AABW), which flows northward after forming in the Southern Ocean. The northern water mass is North Atlantic Deep Water (NADW), and it flows southward (Orsi et al., 1999). These two water masses of very different origin carry specific characteristics of their original location and interact along their flow paths, controlling the  $\delta^{30}\text{Si}_{\text{DSi}}$  and DSi concentration in the deep Atlantic (de Souza et al., 2012b). One consequence of this is a meridional  $\delta^{30}\text{Si}_{\text{DSi}}$  gradient observed in the deep and intermediate water going from  $\delta^{30}\text{Si}_{\text{DSi}}$  of  $\sim +1.75$  ‰ in fairly young deep waters in the northern North Atlantic to  $\sim +1.20$  ‰ in the southern South Atlantic (de Souza et al., 2012b).

To better understand the  $\delta^{30}\text{Si}_{\text{DSi}}$  and concentrations of DSi at low latitudes, it is necessary to understand deep water mass circulation and  $\delta^{30}\text{Si}_{\text{DSi}}$  properties of these water masses. By increasing the knowledge of the  $\delta^{30}\text{Si}$  of DSi in deep and intermediate waters in the Atlantic Ocean, we may be able to separate mixing processes from input sources of DSi, such as sinking BSi, in terms of their influence on the isotopes along deep water flow paths. It will also help us to differentiate the influence of external sources, such as rivers, along ocean margins.

In this study, silicon isotope data from water masses of the Atlantic Sector of the Southern Ocean collected during a GEOTRACES campaign, Zero and Drake (ANTXXIV/3) are presented. This dataset includes the first set of  $\delta^{30}\text{Si}_{\text{DSi}}$  values for water column profiles of the Weddell Gyre in the Southern Ocean (Atlantic Sector) and will allow the characterization of DSi concentrations and  $\delta^{30}\text{Si}_{\text{DSi}}$  of the deep water masses that recirculate in the gyre. For the Southern Ocean new data from the Drake Passage and on the  $0^\circ$  meridian are presented. In addition, we present new data from the tropical and subtropical near the Cape Verde Island in the North Atlantic Ocean (MSM10/1

campaign). The  $\delta^{30}\text{Si}_{\text{DSi}}$  data from the literature and these datasets will help us track the deep and intermediate Atlantic Ocean circulation and characterize its isotopic composition.

## II.2 Materiel and Method

### II.2.1 Sample analysis

Water samples were collected for the analysis of the silicon isotope composition ( $\delta^{30}\text{Si}$ ) of dissolved silicon during two campaigns (Fig. 4.6). The Zero and Drake campaign (ANTXXIV/3) sampled the Southern Ocean from the 6<sup>th</sup> of February to the 10<sup>th</sup> of April 2008. The campaign track began at Punta Arenas (Chile), crossed the Drake Passage and the Weddell Gyre, and traversed up the prime meridian before finally reaching Cape Town (South Africa). The tropical and subtropical Atlantic Ocean was sampled during the MSM10/1 campaign. The vessel RV Merian started from Ponta Delgada (Azores) on the 10<sup>th</sup> of October 2008, cruised along the west coast of Africa between 23°W and 30°W to sample the oxygen minimum zone until 4°S and ended up in Mindelo (Cape Verde) on December 12, 2008.

Seven depth profiles were collected in the Southern Ocean (Drake Passage, Weddell Gyre and Antarctic Circumpolar Current) and five more were sampled in the Oxygen Minimum Zone (north and south of the Cape Verde Frontal Zone). The samples were collected using a Niskin bottle rosette, were filtered through 0.6  $\mu\text{m}$  polycarbonate filters and stored at room temperature in acid-cleaned low-density polyethylene (LDPE) bottles. The dissolved silicon concentrations of these never-frozen samples were measured colorimetrically with a spectrophotometer (Shimadzu UV-1700) following the formation and reduction of silicomolybdate (Strickland and Parsons, 1972).

During the isotopic analysis, the DSi was extracted as triethylamine silicomolybdate, and combusted to form  $\text{SiO}_2$  (De La Rocha et al., 1996). This purified silica was dissolved in 40% hydrogen fluoride (HF) at a F:Si ratio of 100 mol:mol, ensuring enough of an excess of fluorine (F) to form *silicon hexafluoride* ( $\text{SiF}_6^{2-}$ ) (for more details see chapter. 2).

The silicon was further purified via anion exchange chromatography following Engström et al. (2006) as detailed in chapter 2. In brief, samples of 4  $\mu\text{mol}$  Si in 52 mM HF were loaded onto columns of AG 1-X8 resin (100– 200 mesh, (150 – 75  $\mu\text{m}$ ), Eichrom) preconditioned with 2 M NaOH. Contaminants remaining after the initial extraction and combustion were eluted using a solution of 95 mM HCl + 23 mM HF. Purified Si was then eluted with a solution of 0.14 M  $\text{HNO}_3$  + 5.6 mM HF. All acids (Suprapur, Merck) were diluted using MilliQ water (18.2  $\text{M}\Omega\text{ cm}^{-1}$ ).

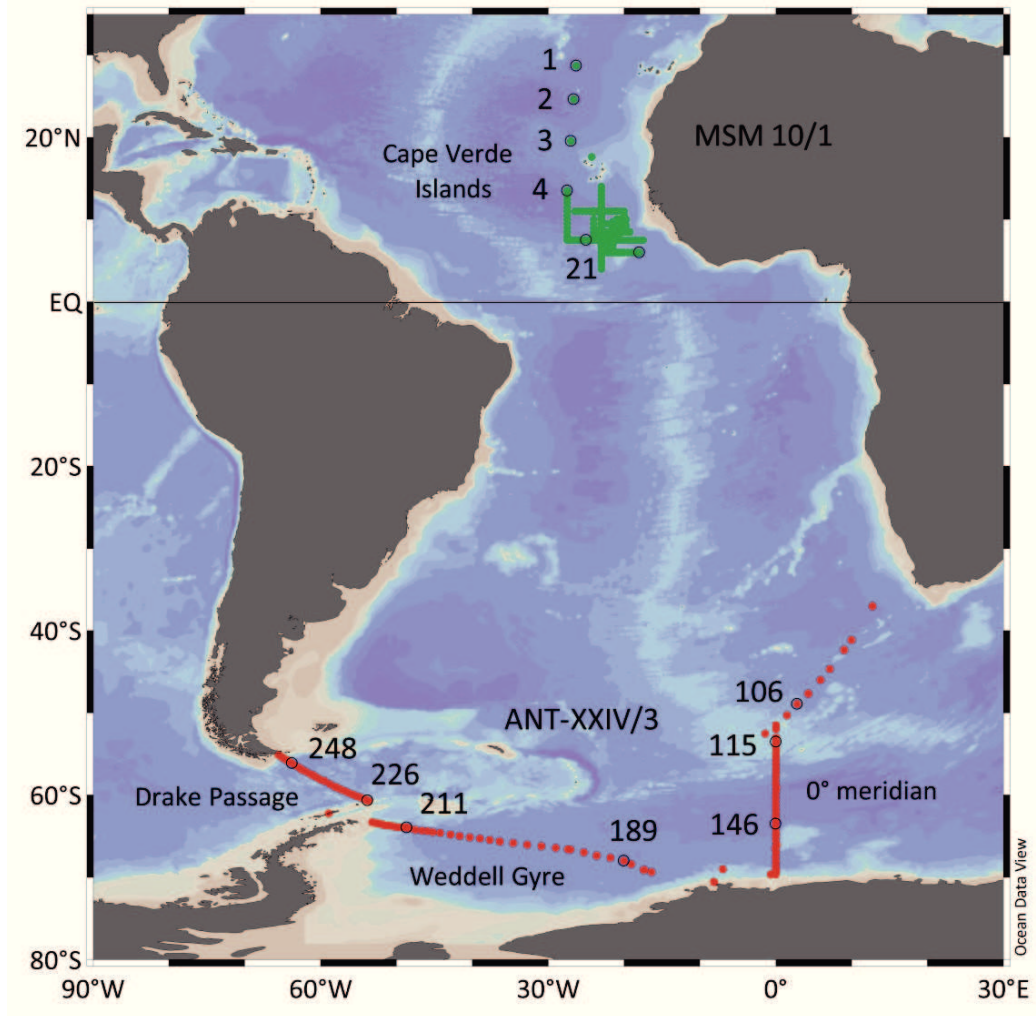


Figure 4.6 Sampling locations of the two campaigns used in this study. Green dots indicate stations sampled in the Subtropical and Tropical Atlantic Ocean (MSM10/1 campaign) and red dots indicate stations sampled in the Southern Ocean (ANTXXIV/3 campaign). Stations from which samples were analysed are encircled and numbered (Schlitzer, R., Ocean Data View, <http://odv.awi.de>, 2013).

Purified samples were diluted to 2 ppm Si and doped with 0.1 ppm Mg. The measurement of silicon isotope ratios was carried out in Brest, France on a Neptune MC-ICP-MS (Thermo Scientific) (see Table 2.1 chapter 2 for operating conditions). Values of  $^{30}\text{Si}/^{28}\text{Si}$  and  $^{29}\text{Si}/^{28}\text{Si}$  were corrected for instrumental mass bias using Mg-correction (Cardinal et al., 2003), for example:

$$\left(\frac{^{30}\text{Si}}{^{28}\text{Si}}\right)_{\text{corr}} = \left(\frac{^{30}\text{Si}}{^{28}\text{Si}}\right)_{\text{meas}} \times \left(\frac{^{30}\text{Si}_{\text{AM}}}{^{28}\text{Si}_{\text{AM}}}\right)^{\epsilon_{\text{Mg}}} \quad (4.1)$$

where  $(^{30}\text{Si}/^{28}\text{Si})_{\text{corr}}$  (the corrected ratio of  $^{30}\text{Si}$  to  $^{28}\text{Si}$ ) is calculated from  $(^{30}\text{Si}/^{28}\text{Si})_{\text{meas}}$  (the measured ratio of  $^{30}\text{Si}$  to  $^{28}\text{Si}$ ),  $^{30}\text{Si}_{\text{AM}}$  and  $^{28}\text{Si}_{\text{AM}}$  (the atomic masses of  $^{30}\text{Si}$  to  $^{28}\text{Si}$ ), and  $\epsilon_{\text{Mg}}$ , which was calculated from the beam intensities at masses of 25 and 26:

$$\varepsilon_{Mg} = \ln \left[ \frac{\frac{{}^{25}Mg_A}{{}^{26}Mg_A}}{\left( \frac{{}^{25}Mg}{{}^{26}Mg} \right)_{meas}} \right] \div \ln \left[ \frac{{}^{25}Mg_{AM}}{{}^{26}Mg_{AM}} \right] \quad (4.2)$$

where  ${}^{25}Mg_A/{}^{26}Mg_A$  is the ratio expected based on the known natural abundances of the magnesium isotopes,  $({}^{25}Mg/{}^{26}Mg)_{meas}$  is the ratio that was measured, and  ${}^{25}Mg_{AM}$  and  ${}^{26}Mg_{AM}$  are the atomic masses of  ${}^{25}Mg$  and  ${}^{26}Mg$ . Analyses where the measured  $\varepsilon_{Mg}$  values of the sample measurement did not agree to within a thousandth of a percent with those of the bracketing standards were excluded.

Measurements of samples occurred between NBS28 standard measurements, with each reported value consisting of three full measurements of a standard and two full measurements of a sample, with the values reported as  $\delta^{30}Si$ :

$$\delta^{30}Si = \frac{R_{sam} - R_{std}}{R_{std}} \times 10^3 \quad (4.3)$$

where  $R_{sam}$  is the Mg-corrected sample of  ${}^{30}Si/{}^{28}Si$ , and  $R_{std}$  the mg-corrected ratio for NBS28.

The precision on individual measurements of  $\delta^{30}Si$  was typically  $\pm 0.04$  ‰ (1 $\sigma$  standard deviation). The long term precision (also 1  $\sigma$  SD) for the procedure (i.e. including the column chemistry) was  $\pm 0.07$  ‰. Backgrounds and procedural blanks were both less than 1% of the sample signal. Measured values fell along the expected mass dependent fractionation line  $\delta^{30}Si = 1.93 \cdot \delta^{29}Si$ .

## II.2.2 Water masses identification

### II.2.2.1 The Southern Ocean

#### II.2.2.1.1 The Weddell Gyre

As mentioned in chapter 4, the Weddell Gyre is one of the main gyre of the Southern Ocean with Ross gyre maintained between the Antarctic continent and the Antarctic Circumpolar Current (ACC). The boundary between the ACC and the Weddell Gyre is according to Orsi et al. (1995) the southern limit of the Upper Circumpolar Deep Water (UCDW) and according to Park et al. (2001) this boundary is the 1.5°C isotherm of Lower Circumpolar Deep Water (LCDW). Three stations analysed represented distinctive parts of the gyre. Station 211 was on the western part of the Weddell Sea close to the Larsen Ice Shelf, station 189 represents the southern part of the gyre, and station 146, located on the 0° meridian, and sampled the eastern side of the gyre (Fig. 4.6). The water masses at these stations were identified using a temperature-salinity (T-S) diagram (Fig. 4.7).

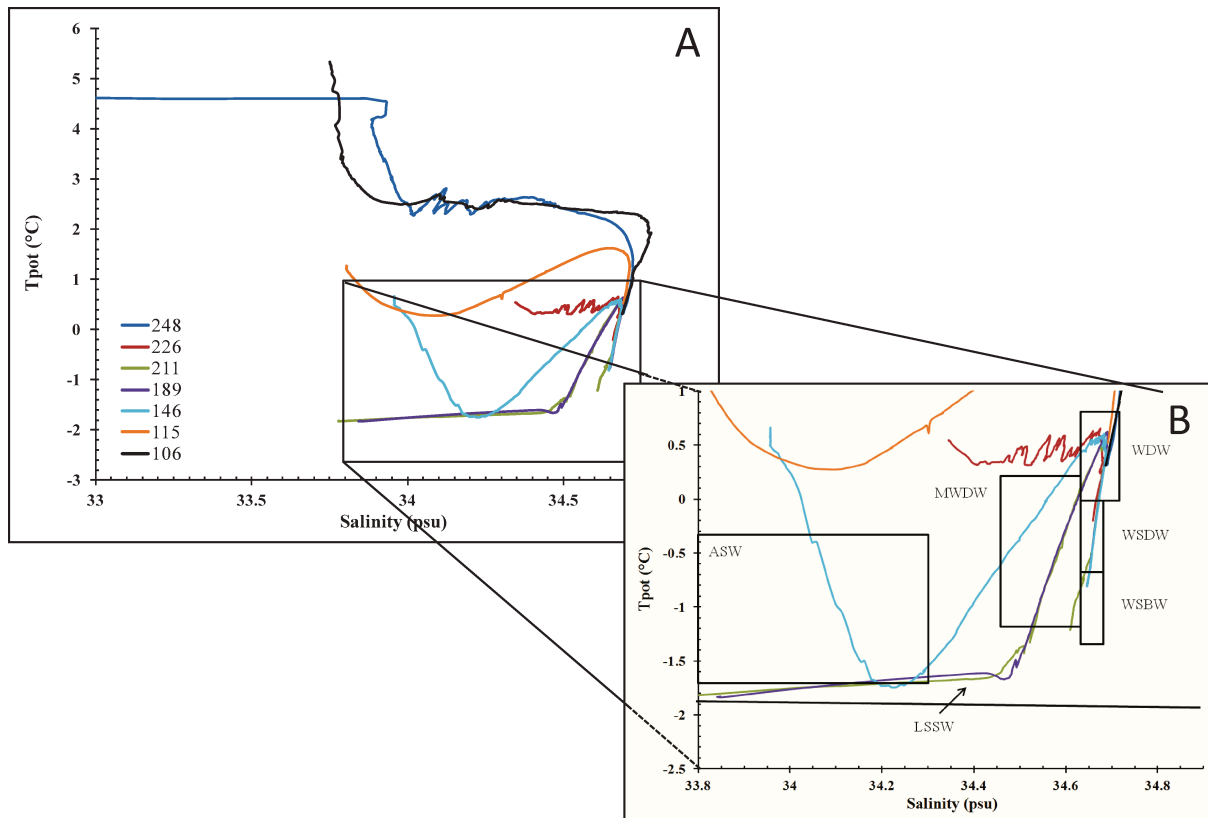


**Figure 4.7** Temperature–salinity depth profiles of stations from ANTXXIV/3 campaign. A) Full depth profiles, B) zoom in our stations (146, 189 and 211) in the Weddell Gyre. Modified from Mackensen (2001).

The water masses found at station 146 were Antarctic Surface Water (AASW) from the surface until 100 m, UCDW from 100 m to 200 m, and Warm Deep Water (WDW) until 1500 m depth (Fig. 4.8). Weddell Sea Deep Water (WSDW) was below WDW until 4000 m where it was displaced by Weddell Sea Bottom Water (WSBW). Station 189 was inside the gyre and exhibited almost the same water masses at the same depths, except that instead of UCDW there was Modified Warm Deep Water (MWDW) because between stations 146 and 189, UCDW disappears and MWDW appears as described at the boundary of the gyre. Station 211 on the western side of the gyre shows the same profile as station 189, with WSBW recorded below 3500 m (Fig. 4.8). This implies that even stations located on opposite sides of the gyre sampled similar water masses.

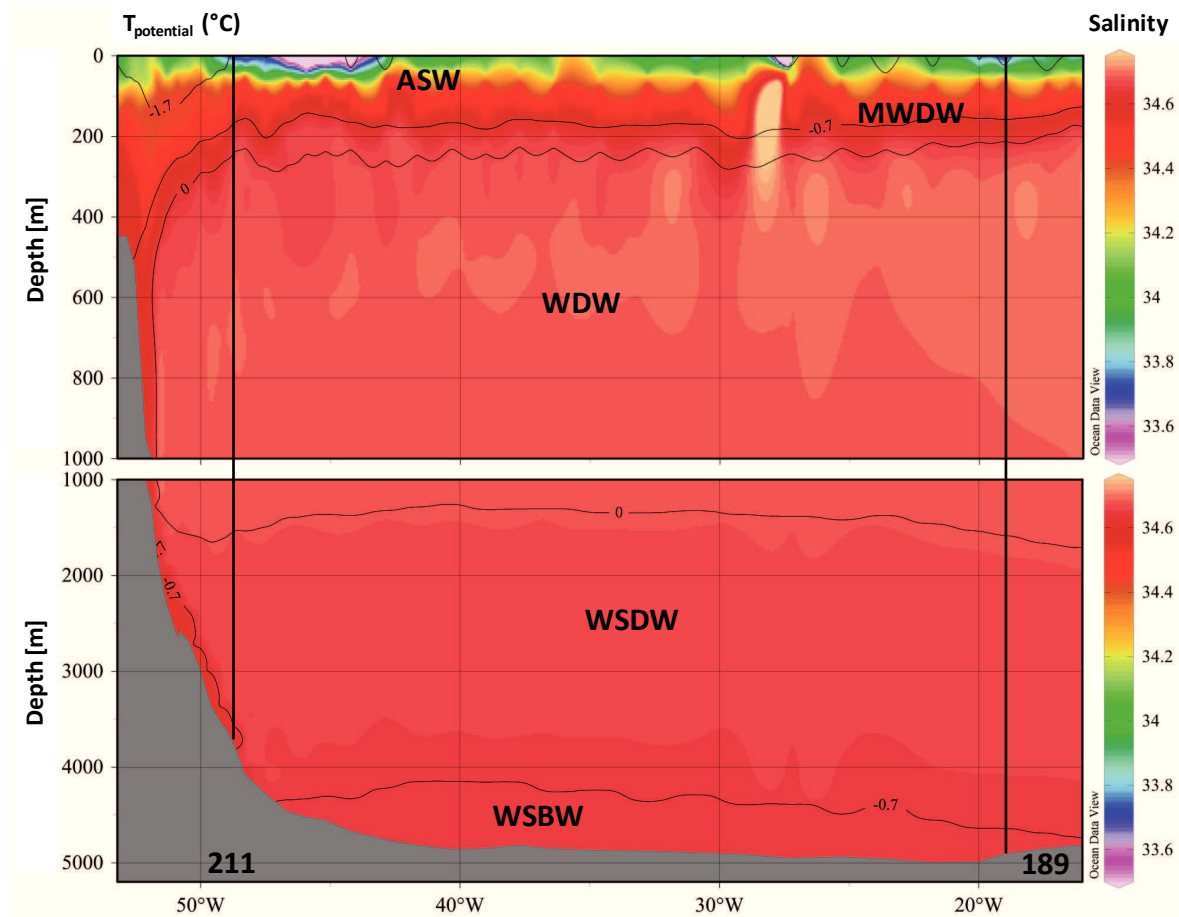


**Figure 4.8** Longitudinal transect through Weddell Gyre realized with data from ANTXXIV/3 campaign. Our stations 211 and 189 are indicated by vertical lines. Thin horizontal lines indicate temperature boundaries. Salinity colour maps were created with ODV (Schlitzer, Ocean Data View, <http://odv.awi.de>, 2013) using data from ANTXXIV/3 campaign. ASW: Antarctic Surface Water, MWDW: Modified Warm Deep Water, WDW: Warm Deep Water, WSDW: Weddell Sea Deep Water and WSBW: Weddell Sea Bottom Water.

### ***The Drake Passage***

The Drake Passage connects the Pacific Ocean and Atlantic Ocean and is the narrowest section of the Antarctic Circumpolar Current (ACC), serving to focus the current. Due to this characteristic, the Drake Passage is an area of strong jets, eddies and meanders that act in part on the mixing of water masses (Sudre et al., 2011). The latitudinal section (Fig. 4.9) reveals shoaling of the deep water masses. The Antarctic Polar Front (PF), which was located around 57.3°S during the cruise, limits the flow of Subantarctic Surface Water (SASW) and Antarctic intermediate water (AAIW) toward the south and AASW toward the north. South of 60.4°S, the southern limit of the ACC, an inflow of water from the Weddell Gyre was observed (pink/purple water mass on Fig. 4.9). However, the two prevailing water masses in the Drake Passage are LCDW and UCDW (Well et al., 2003).

North of the Polar Front at station 248, the surface water (upper 150 m) consisted of SASW. Winter Water (WW) was found between 150 and 270 m at above the AAIW, which was recorded as deep as 800 m. The deep water masses were SPDSW, found between 800 and 1700 m, and UCDW



and LCDW, found respectively at 1700 – 2500 m and 2500 – 3600 m. The deepest water mass was SPDW, which was found below 3600 m. The water masses observed at station 226 south of the Southern Boundary were AASW, found as deep as 500 m, LCDW recorded between 500 and 1500 m, and WSDW flowing from the Weddell Sea below 1500 m.

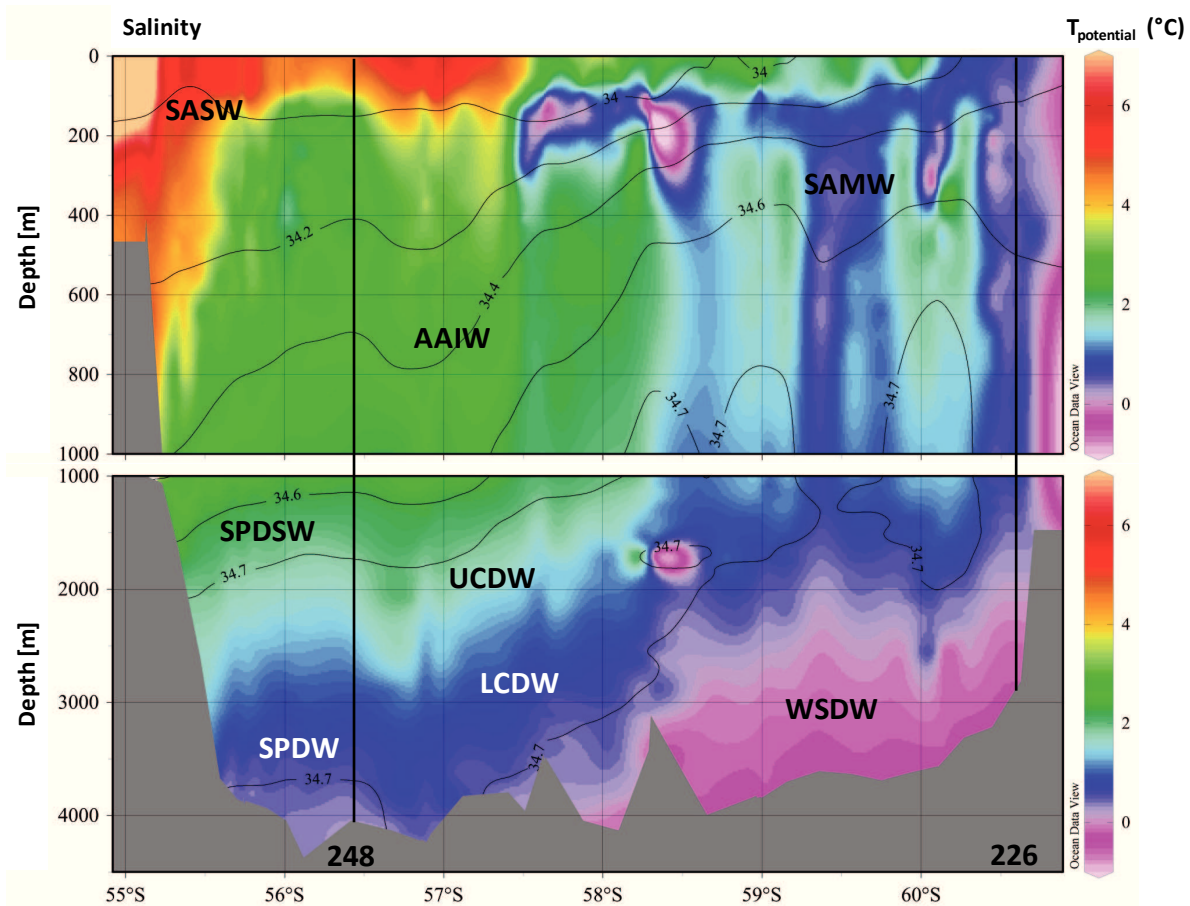


**Figure 4.9** Latitudinal transect of Drake Passage realized with data from ANTXXIV/3 campaign. Our stations 248 and 226 are indicated by vertical lines. Thin horizontal lines indicate salinity boundaries. Potential temperature colour maps were created with ODV (Schlitzer, Ocean Data View, <http://odv.awi.de>, 2013) using data from ANTXXIV/3 campaign. SASW: Subantarctic surface Water, SAMW: Subantarctic Mode Water, AAIW: Antarctic Intermediate Water, SPDSW: Southeast Pacific Deep Slope Water, UCDW: Upper Circumpolar Deep Water, LCDW: Lower Circumpolar Deep Water, SPDW: Southeast Pacific Deep Water, WSDW: Weddell Sea Deep Water.

### ***The Antarctic Circumpolar Current (ACC)***

The ACC is the only major circumpolar current and it connects three major oceans, the Atlantic, Indian and Pacific Oceans. At station 106, located north of the Antarctic Polar Front, Subantarctic Surface Water (SSW) was detected until 200 m, then AAIW until 300 m (Fig. 4.10), and UCDW until 1000 m. Below this the influence of the NADW on the LCDW layer until 2500 m was observed, followed by a layer of about 500 m of only LCDW. The deepest water mass at this station was WDW. Water masses observed at the station south of the Polar Front (115) were similar to those at station 106, except that the layers were shallower, the surface layer consisted of the AASW and the UCDW

had a greater influence than at station 106. The influence of the Polar Front was less prominent along the prime meridian than in the Drake Passage, although, the latitudinal southward flow to the surface was observed again (Fig. 4.10). The Antarctic Polar Front was located at around 49.6°S on the 0° meridian.

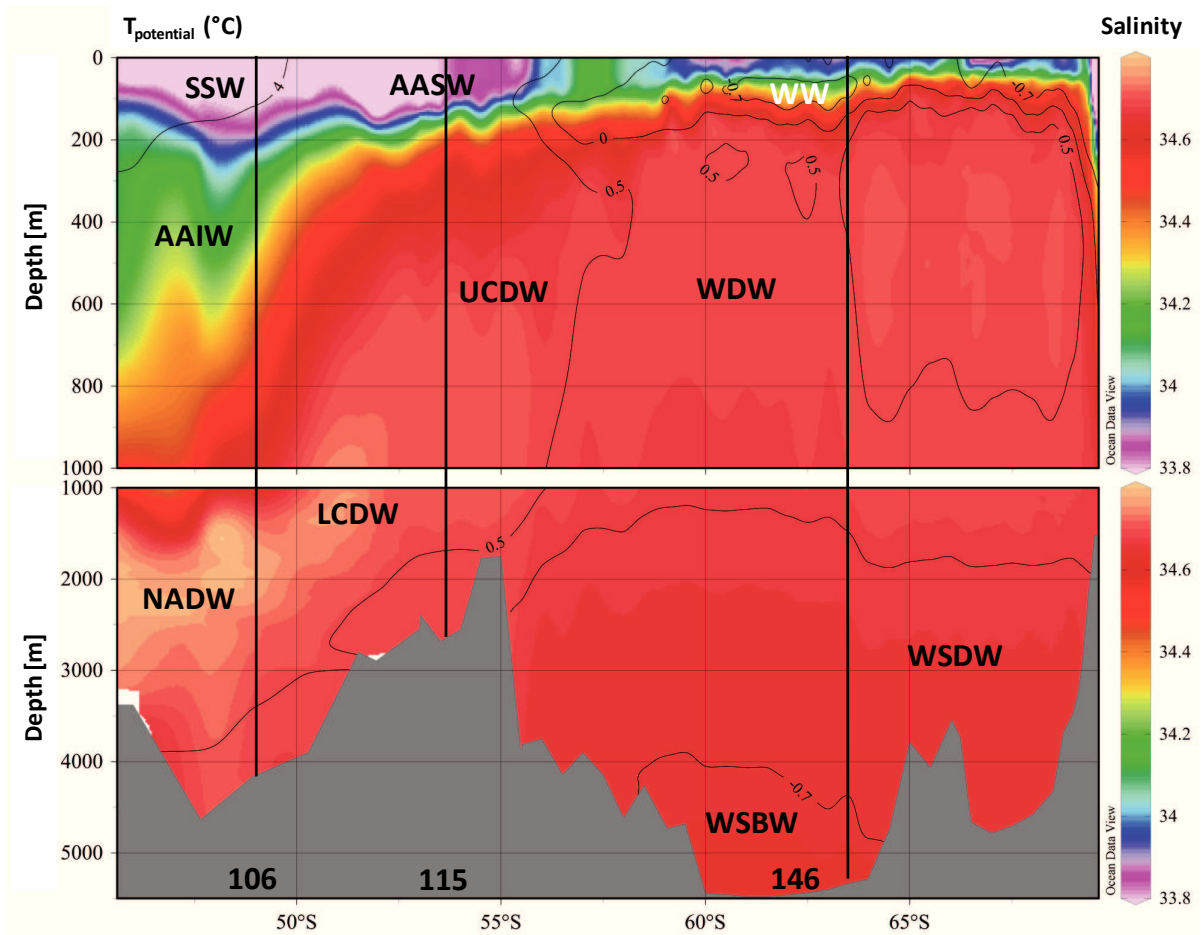


**Figure 4.10** Latitudinal transect on the 0° meridian realized with data from ANTXXIV/3 campaign. Our stations 106, 115 and 146 are indicated by vertical lines. Thin horizontal lines indicate temperature boundaries. Salinity colour maps were created with ODV (Schlitzer, Ocean Data View, <http://odv.awi.de>, 2013) using data from ANTXXIV/3 campaign.

### II.2.3 The Subtropical and Tropical North Atlantic Ocean

The area sampled in the Subtropical and Tropical North Atlantic Ocean is characterized by coastal upwelling around of Cape Verde Island that leads to a frontal zone from 19 – 20°N at 20°W to 15 – 17°N at 30°W and a split in the intermediate water (Stramma and Schott, 1999). The front is strongly marked, with various water masses with vastly different sites of origin on either side. Stations 1 and 2 were in the subtropical region and the other three were in the tropical Atlantic Ocean (Fig. 4.6). Station 1, 2 and 3 were located north of the Cape Verde Frontal Zone (CVFZ), while stations 4 and 21 were south of the CVZF. The water masses were identified using a TS diagram (Fig. 4.11).

Stations 1, 2 and 3 have similar depth profiles with Salinity Maximum Water (MSW) found from the surface until 200 – 300 m, with the deeper western North Atlantic Central Water (wNACW) found between 200 m and 600 m (station 2) or 700 m (station 3). wNACW was between 200 and 1700 m at station 1 (Fig. 4.7). Under this central water flows the intermediate water mass Atlantic Subarctic Intermediate Water (ASIW) (Stramma and Schott, 1999), which is the deepest water mass found at stations north of the Cape Verde Frontal Zone. Stations 4 and 21 have different profiles to the other stations, with the South Atlantic Central Water (SACW) extending from the surface down to 600 and 1300 m at stations 21 and 4, respectively. Below the central water at station 21, AAIW was found between 600 m and 1100 m, with NADW below this. AAIW and NADW were not recorded below NACW at station 4.

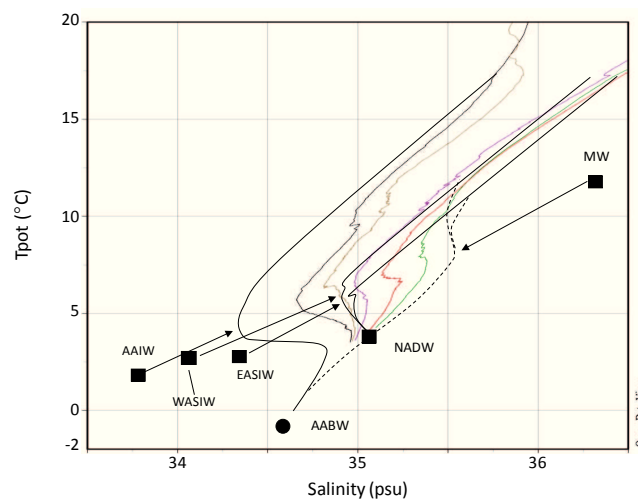


**Figure 4.11** Temperature – Salinity diagram for Atlantic Ocean water masses. Coloured lines indicate stations sampled during MSM10/1 campaign: station 1 (green), 2 (red), 3 (pink), 4 (brown), 21 (blue). SACW: South Atlantic Central Water, wNACW and eNACW: western and eastern North Atlantic Central Water, MW: Mediterranean Water, NADW: North Atlantic Deep Water, AABW: Antarctic Bottom Water, AAIW: Antarctic Intermediate Water, WASIW and EASIW: western and eastern Atlantic Modified from Emery (2003).

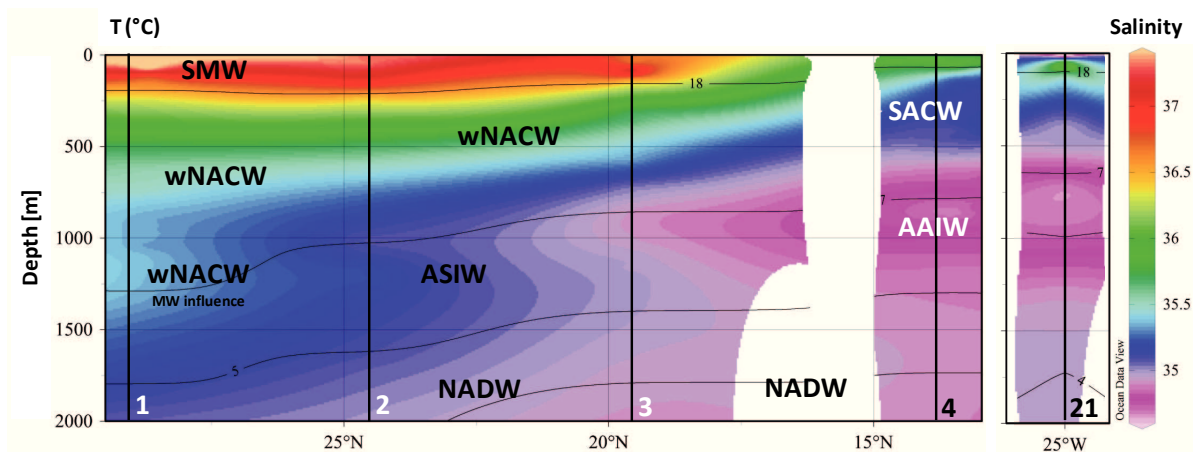


**Figure 4.12** Latitudinal transect of the Subtropical and Tropical Atlantic Ocean realized with data from MSM10/1 campaign. Our stations 1, 2, 3, 4 and 21 are indicated by vertical lines. Thin horizontal lines indicate temperature boundaries. Salinity colour map was created with ODV (Schlitzer, Ocean Data View, <http://odv.awi.de>, 2013) using data from MSM10/1 campaign.

## II.3 Results

### II.3.1 General observations

Our data come from the Atlantic sector of the Southern Ocean and the Subtropical and Tropical North Atlantic Ocean. Typical depth profiles for the DSi concentrations at our twelve stations show a increase in DSi concentration with depth (Fig. 4.13) as entirely expected. The highest DSi concentrations were detected in the Southern Ocean, where surface water (< 100 m) DSi concentrations ranged between 6.43  $\mu\text{M}$  (minimum concentration at station 106, ACC) and 90.47  $\mu\text{M}$  (maximal concentration at station 211, Weddell Gyre) (Fig. 4.13 A) compared to an average of 3.64  $\mu\text{M}$  in the North Atlantic equatorial samples.

DSi concentrations were relatively invariable from 1000 m for all Southern Ocean stations (Fig. 4.13: A, C, E, G, I, K, M), except for station 211 where the concentration decreased below 3547 m (Fig. 4.13: E). Conversely, DSi concentrations varied below 1000 m at stations from the Subtropical and Tropical North Atlantic Ocean (Fig. 4.13: O, Q, S, U, W). At depth, DSi concentrations reach 100 - 130  $\mu\text{M}$  in the Southern Ocean, compare to only 28  $\mu\text{M}$  in the North Atlantic Ocean (Appendix 2).

$\delta^{30}\text{Si}$  values in surface water (< 100 m) ranged from 1.3 ‰ (station 115, Fig. 4.13 L) to 2.3 ‰ (station 146, 0° meridian in Weddell Gyre, Fig. 4.13 B) in the Southern Ocean. Unfortunately, due to the low concentrations and insufficient sample sizes, minimal data are available for the equatorial North Atlantic Ocean in our dataset.

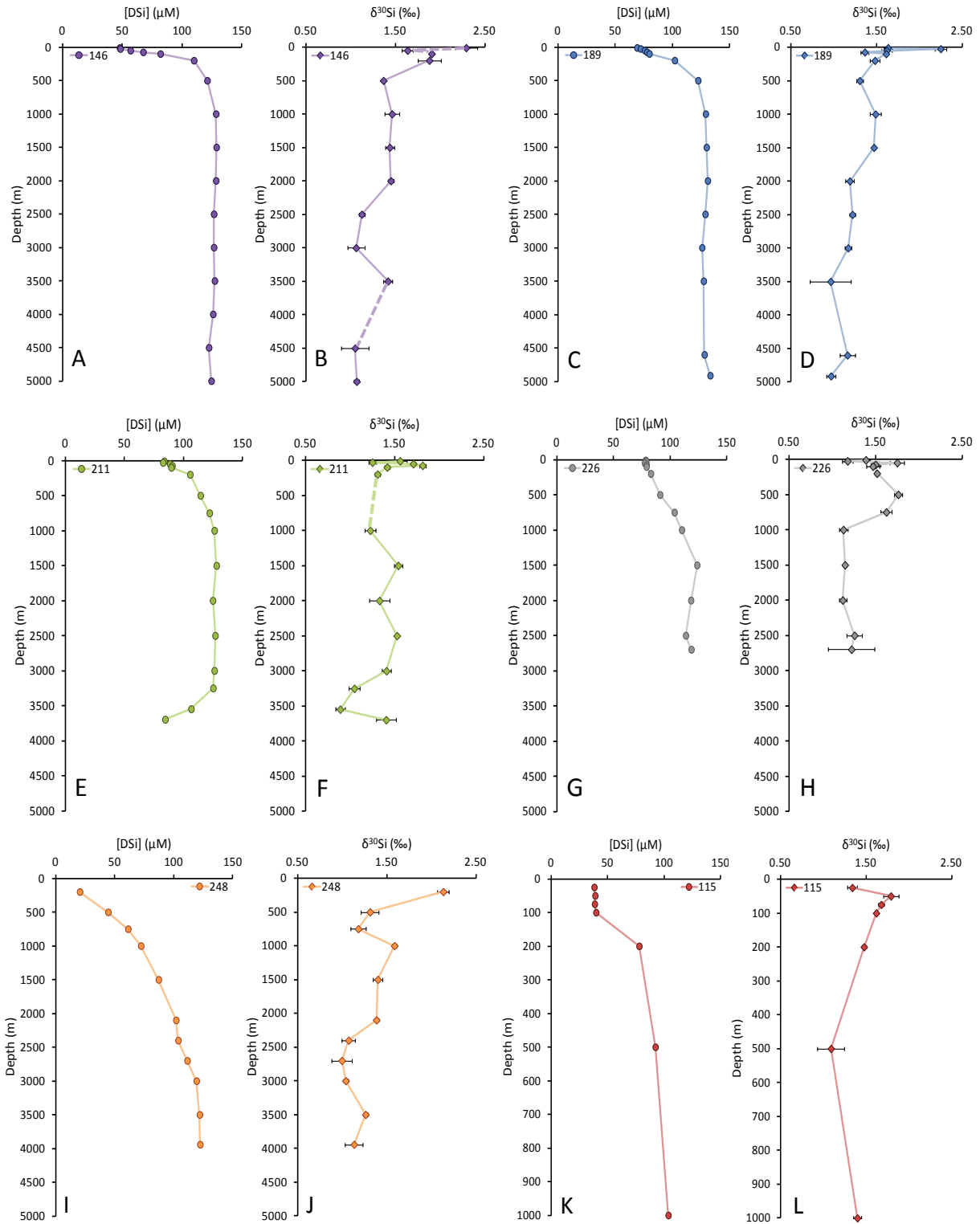


**Figure 4.13** Depth profiles of DSi concentration (A, C, E, G, I, K, M, O, Q, S, U, W) and  $\delta^{30}\text{Si}$  (B, D, F, H, J, L, N, P, R, T, V, X) for the Southern Ocean (ANTXXIV/3 campaign, A to N) and for the tropical and subtropical Atlantic Ocean (MSM 10/1, O to X). Stations 226 and 248 were located in the Drake Passage; 248 was part of the Antarctic Circumpolar Current (ACC); 211, 189 and 146 were located in the Weddell Gyre (WG); 146 was at the edge of the WG and the ACC on the  $0^\circ$  meridian; and 106 and 115 were part of the ACC along the  $0^\circ$  meridian. Station 115 (K, L) is on a shallower depth scale (0 – 1000 m) than other stations of the Southern Ocean. Stations 1, 2 and 3 were north of the Cape Verde Frontal Zone (CVFZ), and stations 4 and 21 were south of the front. The depth and DSi concentration scales for the subtropical and tropical Atlantic Ocean are smaller than the Southern Ocean. Continued overleaf.

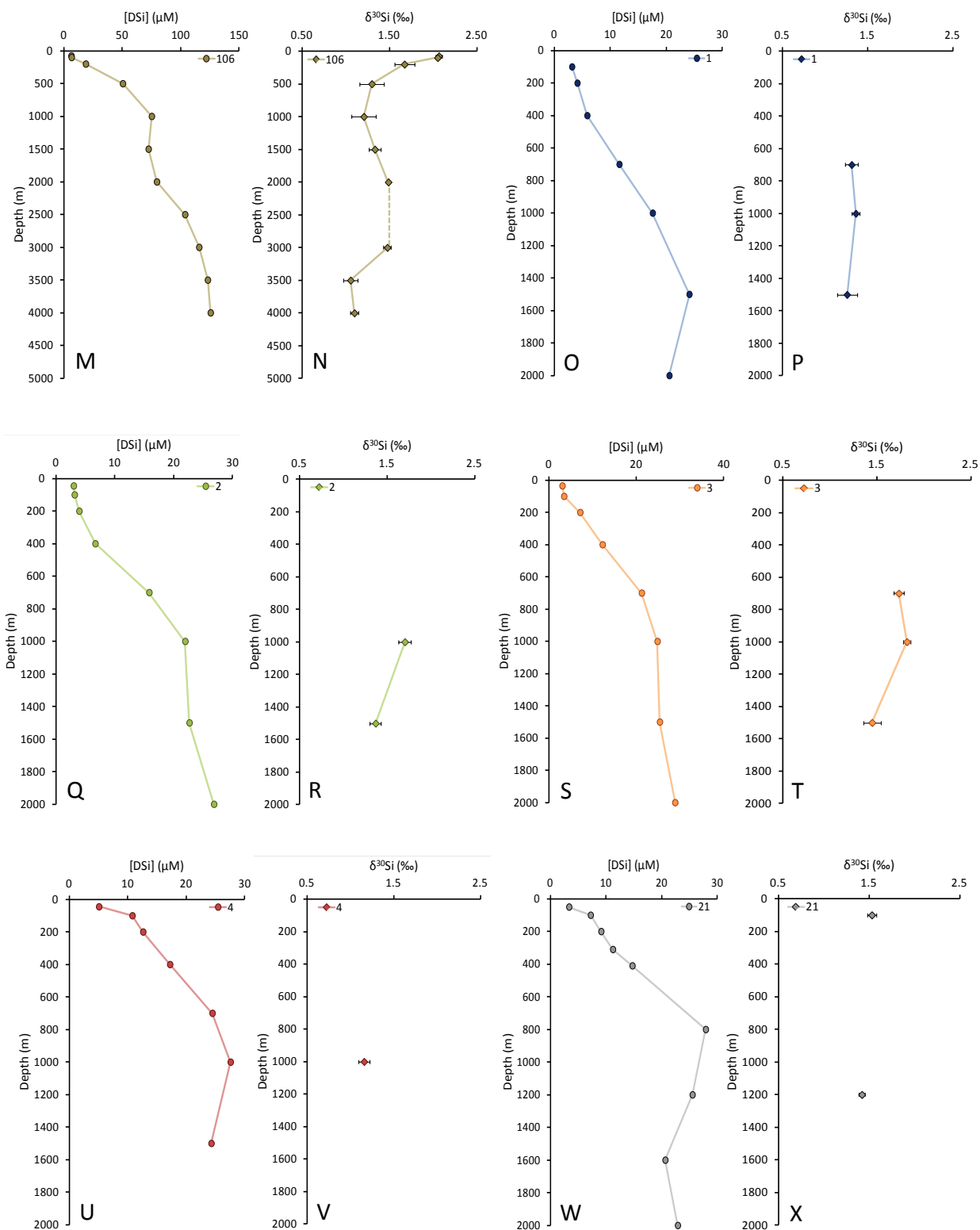


Figure 4.13

## II.3.2 Water mass profiles in the Southern Ocean

### II.3.2.1 The surface water

A surface gradient for DSi concentrations was recorded in the Weddell Gyre from the eastern inflow region of the Weddell Gyre with higher DSi concentrations (station 146, Fig. 4.13 A) to the western side of the gyre, with lower DSi concentrations (station 211, Fig. 4.13 E). A similar trend was observed for  $\delta^{30}\text{Si}_{\text{DSi}}$  values, with average ( $\pm$  standard deviation) surface water  $\delta^{30}\text{Si}_{\text{DSi}}$  values of  $1.94 \pm 0.07$  ‰ detected at stations 146 and 189 (Fig. 4.13 B and D) and  $1.41 \pm 0.06$  ‰ at station 211 (Fig. 4.13 F). Station 226, located on the Antarctic Peninsula, outside the Weddell Gyre, had an average DSi concentration of 79  $\mu\text{M}$  and average  $\delta^{30}\text{Si}_{\text{DSi}}$  value of  $1.29 \pm 0.06$  ‰ (Fig. 4.13 G, H).

Low Salinity Shelf Water (LSSW) was only found at station 189 and 211 (50 - 75 m) (Fig. 4.8), with on average  $\delta^{30}\text{Si}_{\text{DSi}}$  slightly lower at station 189 ( $1.49 \pm 0.05$  ‰) than at station 211 ( $1.76 \pm 0.02$  ‰).

Station 211, located on the western side of the gyre, was sampled in autumn and exhibited lower  $\delta^{30}\text{Si}_{\text{DSi}}$  values and higher DSi concentrations than stations 146 and 189, which were sampled in mid-summer.

The surface water of the ACC on the  $0^\circ$  meridian was strongly marked by the Antarctic Polar Front (Fig. 4.10) evidenced by higher average DSi concentrations south of the Polar Front (39  $\mu\text{M}$  and  $\delta^{30}\text{Si}_{\text{DSi}}$  of  $1.61 \pm 0.07$  ‰, station 115) compared to at station 106 (DSi concentration of 7  $\mu\text{M}$  and  $\delta^{30}\text{Si}_{\text{DSi}}$  of  $2.06 \pm 0.03$  ‰) (Fig. 4.13).

### II.3.2.2 Antarctic Intermediate water (AAIW)

AAIW was detected in the ACC at stations 106 and 115 along the  $0^\circ$  meridian and station 248 in the Drake Passage (Fig. 4.9 and Fig. 4.10). The water mass was found at different depth depending on the station, going as shallow as 200 m (stations 106 and 115) to as deep as 500 – 750 m at station 248 (appendix 2).

DSi concentrations were greatest at station 248 (87  $\mu\text{M}$ ), compared to stations 106 (19  $\mu\text{M}$ ) and 115 (78  $\mu\text{M}$ ). With this increase in DSi concentrations a decrease in the average  $\delta^{30}\text{Si}_{\text{DSi}}$  values of  $1.67 \pm 0.12$  ‰ (station 106),  $1.48 \pm 0.03$  ‰ (station 115) and  $1.25 \pm 0.10$  ‰ (station 248) was observed.

### II.3.2.3 Upper Circumpolar Deep Water (UCDW)

UCDW was detected at various depths in the ACC until the limit with the Weddell Gyre (station 146). UCDW was recorded at 200 m (station 146), 500 m (stations 106 and 115), and as deep as 2100 m (station 248). The DSi concentrations of UCDW were higher south of the Polar Front (109  $\mu\text{M}$ , station 146; 92  $\mu\text{M}$ , station 115), compared to north of the front (50 – 73  $\mu\text{M}$ , station 106). The

shallow UCDW at station 146 had a  $\delta^{30}\text{Si}_{\text{DSi}}$  of 1.88 ‰, which is high compared to other stations for which UCDW  $\delta^{30}\text{Si}_{\text{DSi}}$  was between 1.10 – 1.30 ‰ (appendix 2).

A northward DSi concentration gradient was observed between station 115 (93  $\mu\text{M}$ ) and station 106 (50 – 75  $\mu\text{M}$ ) on either side of the PF, and  $\delta^{30}\text{Si}_{\text{DSi}}$  values of UCDW for station 106 are higher than at station 115,  $1.28 \pm 0.12$  ‰ and  $1.09 \pm 0.16$  ‰ respectively (Fig. 4.14).

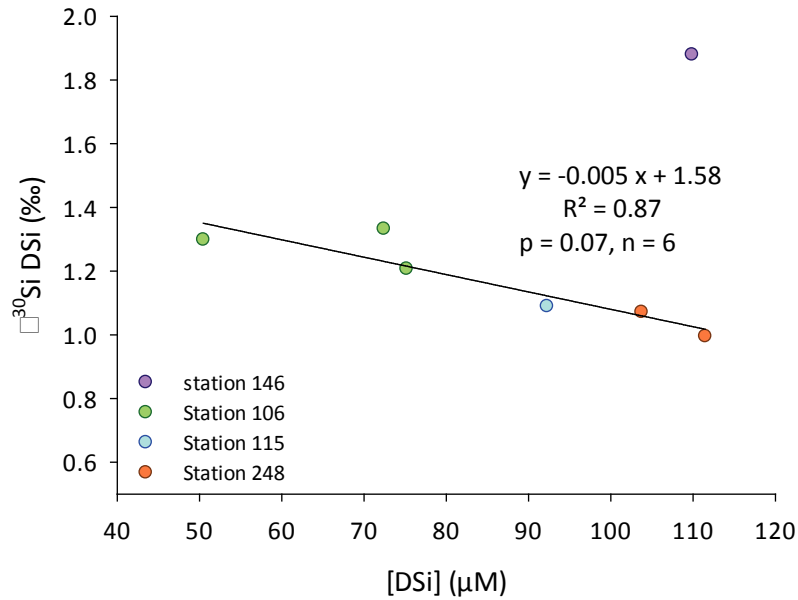


**Figure 4.14 DSi concentration versus  $\delta^{30}\text{Si}_{\text{DSi}}$  of Upper Circumpolar Deep Water (UCDW) for stations in the Antarctic Circumpolar Current (ACC) and in the Weddell Gyre. (Station 146 was not taken into account for the regression).**

At station 248 in the Drake Passage, variable  $\delta^{30}\text{Si}_{\text{DSi}}$  values were detected between 2100 m and 2700 m ( $1.38 \pm 0.03$  ‰ to  $1.00 \pm 0.11$  ‰, respectively), at DSi concentrations between 103  $\mu\text{M}$  and 111  $\mu\text{M}$  (Fig. 4.13). The higher  $\delta^{30}\text{Si}_{\text{DSi}}$  of  $1.38 \pm 0.03$  ‰ was detected in the top of the UCDW layer, just below the Southeast Pacific Deep Slope Water (SPDSW) coming from the Pacific Ocean, with a  $\delta^{30}\text{Si}_{\text{DSi}}$  value of 1.4 ‰ at 1500 m.

A decrease in  $\delta^{30}\text{Si}_{\text{DSi}}$  and an increase in DSi concentration was observed in the UCDW from stations at the  $0^\circ$  meridian to stations in the Drake Passage (Fig. 4.14), except in the shallow UCDW at station 146.

#### II.3.2.4 Lower Circumpolar Deep Water (LCDW)

LCDW was present in the ACC in the Drake Passage and at the  $0^\circ$  meridian. This water mass contained high DSi concentrations, with concentrations of 119  $\mu\text{M}$  recorded at station 248 and between 91 and 124  $\mu\text{M}$  (between 500 and 1500 m) at station 226. Station 106, on the  $0^\circ$  meridian, contained DSi concentrations of 103  $\mu\text{M}$  and between 80 and 116  $\mu\text{M}$  (between 2000 m and 3000 m) (Fig. 4.13).



$\delta^{30}\text{Si}_{\text{DSi}}$  values were highly variable between stations, ranging from  $1.04 \pm 0.03$  ‰ at station 248 (3000 m) to  $1.40 \pm 0.05$  ‰ and  $1.49 \pm 0.06$  ‰ at station 115 (1000 m) and 106 (2000 m to 3000 m), respectively. Station 226 (on the Antarctic Peninsula) showed large variation in  $\delta^{30}\text{Si}_{\text{DSi}}$  with depth, revealing two layers, an upper layer (500 – 750 m) with a high average value of  $1.69 \pm 0.05$  ‰ and a lower layer (1000– 1500 m) with a lower average value of  $1.14 \pm 0.04$  ‰ at 1500 m. Station 248, north of the PF in the Drake Passage, presented a typical deep value for the Southern Ocean, with  $\delta^{30}\text{Si}_{\text{DSi}}$  of  $1.04 \pm 0.04$  ‰ and a DSi concentration of 120  $\mu\text{M}$ .

#### II.3.2.5 The deep water masses (WDW, WSDW, WSBW and AABW)

##### **Warm Deep Water (WDW)**

WDW originates as LCDW that enters in the Weddell Gyre, coming from the ACC, and station 146 was at the boundary between the ACC and the gyre. WDW was detected at stations 146, 189 and 211 in the Weddell Gyre. The DSi concentrations varied between 106  $\mu\text{M}$  and 130  $\mu\text{M}$  (from the top to the bottom of the water mass layer at the stations), with an average  $\delta^{30}\text{Si}_{\text{DSi}}$  of  $1.42 \pm 0.05$  ‰,  $1.35 \pm 0.04$  ‰ and  $1.36 \pm 0.04$  ‰ for stations 146, 189 and 211, respectively. The  $\delta^{30}\text{Si}_{\text{DSi}}$  values were essentially homogenous through the gyre stations (Fig. 4.15).

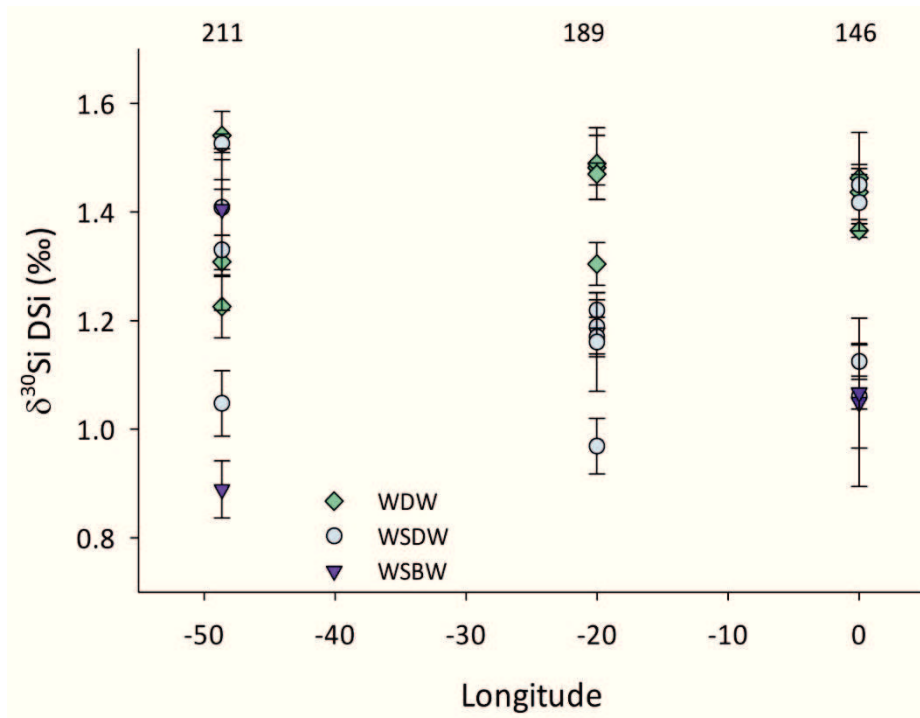


Figure 4.15 Deep water masses of the Weddell Gyre showing  $\delta^{30}\text{Si}_{\text{DSi}}$  (standard deviation  $1\sigma$ ) versus longitude. Station 211 represents the western part of the gyre, 189 the centra part and 146 is on the  $0^\circ$  meridian in the Weddell Gyre. WDW: Warm Deep Water, WSDW; Weddell Sea Deep Water and WSBW: Weddell Sea Bottom Water.

##### **Weddell Sea Deep Water (WSDW)**

For stations 146, 189 and 211, DSi concentrations recorded in the WSDW varied from 126  $\mu\text{M}$  to 128  $\mu\text{M}$  (station 146), from 127  $\mu\text{M}$  to 131  $\mu\text{M}$  (station 189), and was 125  $\mu\text{M}$  at station 211. At station 226 in the Scotia Ridge System, WSDW was recorded between 2000 m to 2699 m, with an average DSi concentration of 116  $\mu\text{M}$  and an average  $\delta^{30}\text{Si}_{\text{DSi}}$  value of  $1.2 \pm 0.13 \text{ ‰}$  (Fig. 4.9 and Fig. 4.13).

In the Weddell Gyre an increase in  $\delta^{30}\text{Si}_{\text{DSi}}$  from the eastern station 146 ( $1.03 \pm 0.13 \text{ ‰}$ ) to the western station 211 ( $1.42 \pm 0.06 \text{ ‰}$ ) was observed, with station 189 being intermediate ( $1.14 \pm 0.10 \text{ ‰}$ ). However, due to the overlapping standard deviations at stations 146 and 189 these stations are in the same range of  $\delta^{30}\text{Si}_{\text{DSi}}$  (Fig. 4.15).

### ***Weddell Sea Bottom Water (WSBW) and Antarctic Bottom Water (AABW)***

WSBW was encountered in the Weddell Gyre at stations 146 and 189, and AABW was observed at stations 106. AABW is a part of the WSBW that flows out of the gyre.

DSi concentrations recorded in the AABW seemed to be slightly lower (ranging between 123–125  $\mu\text{M}$ ) compared to those in the WSBW (ranging from 123–133  $\mu\text{M}$ ), however,  $\delta^{30}\text{Si}_{\text{DSi}}$  values of these two water masses were the same, with a deep water mass average of  $1.07 \pm 0.08 \text{ ‰}$ .

### **II.3.3 The water masses in the subtropical and tropical North Atlantic Ocean** ***Atlantic Central Water (ACW), Atlantic Subarctic Intermediate Water (ASIW), and Antarctic Intermediate Water (AAIW)***

At station 1, north of the Cape Verde Frontal Zone (CVFZ) in the subtropical region, the central water sampled was western North Atlantic Central Water (wNACW) with DSi concentrations ranging from 12 to 24  $\mu\text{M}$  and  $\delta^{30}\text{Si}_{\text{DSi}}$  values of  $1.31 \pm 0.08 \text{ ‰}$  (Fig. 4.12 and Fig. 4.13).

SACW was observed at stations 4 and 21, south of the CVFZ, as deep as 1000 m at station 4 and at 400 m at station 21. A higher concentration of DSi was detected at station 4 (25  $\mu\text{M}$ ) than at station 21 (7  $\mu\text{M}$ ), the opposite trend was observed for  $\delta^{30}\text{Si}_{\text{DSi}}$  values, with station 21 ( $1.53 \pm 0.05 \text{ ‰}$ ) greater than station 4 ( $1.16 \pm 0.07 \text{ ‰}$ ) (Fig. 4.13).

ASIW was only observed north of the CVFZ at stations 1, 2 and 3. The concentration of DSi was 21  $\mu\text{M}$  (2000 m) at station 1, varied from 22 to 27  $\mu\text{M}$  at station 2 (1000 – 2000 m) and was the greatest at station 3 (ranging from 21  $\mu\text{M}$  to 29  $\mu\text{M}$  at 700 – 2000 m). The  $\delta^{30}\text{Si}_{\text{DSi}}$  values were variable between stations and with depth, with  $1.53 \pm 0.08 \text{ ‰}$  at station 1,  $1.37 - 1.73 \text{ ‰}$  at station 2, and station 3 showing an increase in  $\delta^{30}\text{Si}_{\text{DSi}}$  with depth from  $1.73 \text{ ‰}$  at 700 m to  $2.02 \text{ ‰}$  at 2000 m.

AAIW was only observed at station 21 in the tropical Atlantic Ocean and had a DSi concentration of 26  $\mu\text{M}$  and a  $\delta^{30}\text{Si}_{\text{DSi}}$  value of  $1.42 \pm 0.03 \text{ ‰}$ . This  $\delta^{30}\text{Si}_{\text{DSi}}$  value is comparable to the one recorded at station 115 south of the PF ( $1.48 \pm 0.03 \text{ ‰}$ ). Additionally, these  $\delta^{30}\text{Si}_{\text{DSi}}$  values were lower than those recorded at station 106 ( $1.67 \pm 0.12 \text{ ‰}$ , AAIW north of the PF,  $0^\circ$  meridian) and higher than those at station 248 ( $1.25 \pm 0.09 \text{ ‰}$ , AAIW north of the PF, Drake Passage) (Fig. 4.13).

## II.4 Discussion

### II.4.1 Surface water

Seasonal variations of  $\delta^{30}\text{Si}$  are linked to factors such as the Mixed Layer depth, light, mixing events and other factors (see chapter 3 for detailed explanations about the seasonal variation of the  $\delta^{30}\text{Si}$  values).

The biological activity usually results in low DSi concentrations and high  $\delta^{30}\text{Si}$  values in the surface water layer ( $< 100 \text{ m}$ ) compared to the rest of the water column (De La Rocha et al., 1997). Diatoms discriminate against the heavier isotope ( $^{30}\text{Si}$ ) when they take up silicon, leading to a decrease in the DSi concentration and an increase of the  $\delta^{30}\text{Si}$  value in surface. High  $\delta^{30}\text{Si}$  values and low DSi concentrations were observed during this study during periods of net nutrient drawdown.

#### II.4.1.1 Weddell Gyre

In the surface water layer of the Weddell Gyre a DSi concentration gradient was observed from high concentrations at station 211 (western part of the gyre) to lower concentrations at 146 (eastern part) (Fig. 4.19). The  $\delta^{30}\text{Si}_{\text{DSi}}$  follows the opposite trend, with higher values found on the eastern side, suggesting the presence of biological activity during or just prior the campaign. The lower  $\delta^{30}\text{Si}_{\text{DSi}}$  and the higher DSi concentrations recorded in autumn at station 211 may be attributed to a breakdown in stratification and input of deeper DSi with lower  $\delta^{30}\text{Si}_{\text{DSi}}$ .

At least two mechanisms can be put forward to explain the differences in DSi concentration and  $\delta^{30}\text{Si}$  between stations 146, 189 and 211 in the surface waters. First, at stations 189 and 211, this could be linked to the shelf water coming from the Larsen Ice Shelf (close to station 211) and the Filchner-Ronne Ice shelf (close to station 189) (Huhn et al., 2013). Second, this could be linked to differences between stations regarding the magnitude of the BSi production during the productive period, which in turn will impact the magnitude of the changes in  $\delta^{30}\text{Si}$ . The magnitude of the BSi production can be estimated from differences of DSi concentrations between the surface ML and the depth of the temperature minimum - which keeps track of conditions prevailing during the preceding winter (Pondaven et al., 2000). At station 146 for example, the temperature minimum is found at 75

m (Fig. 4.17), with a DSi concentration of 68  $\mu\text{M}$ , compared to 48  $\mu\text{M}$  at the surface. This yields to a net diatom consumption of 20  $\mu\text{M}$ -Si during the productive period, and a concomitant increase of the  $\delta^{30}\text{Si}$  from  $\sim 1.8$  ‰ (at the depth of the temperature minimum, i.e. winter conditions) to 2.29 ‰ in late summer (Fig 4.17).

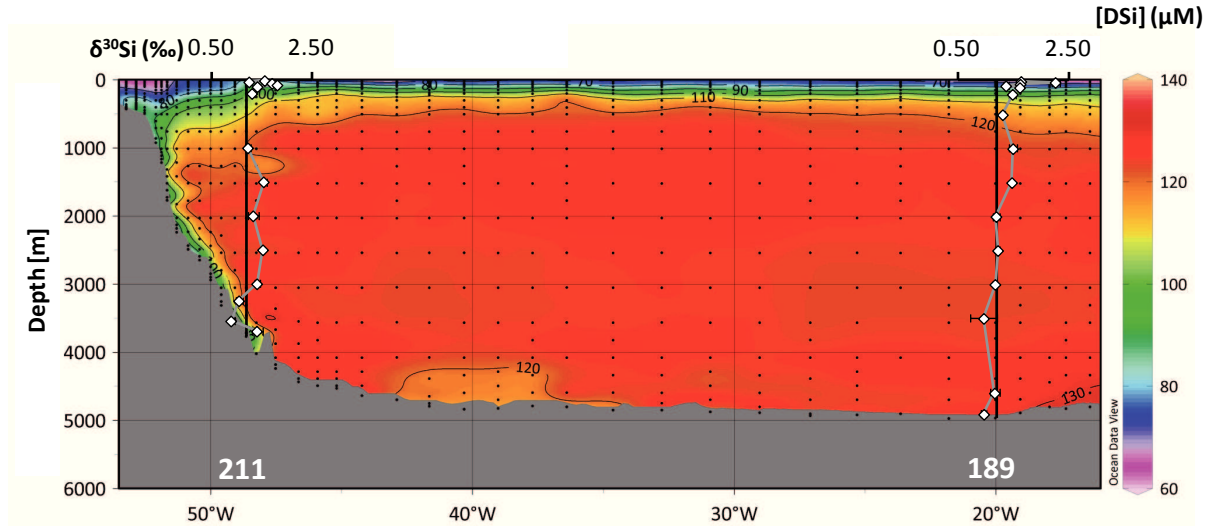


**Figure 4.16** Longitudinal transect through the Weddell Gyre realized with data from the ANTXXIV/3 campaign. Our stations 211 and 189 are indicated by vertical lines that represent in the same time the  $\delta^{30}\text{Si}_{\text{DSi}}$  of 1.2 ‰ characteristic of deep water masses value in the Southern Ocean. Grey lines with diamond markers represent  $\delta^{30}\text{Si}_{\text{DSi}}$  profiles. Thin horizontal lines indicate [DSi] boundaries. DSi concentration colour map was created with ODV (Schlitzer, Ocean Data View, <http://odv.awi.de>, 2013) using data from ANTXXIV/3 campaign.

### Antarctic Circumpolar Current (ACC)

The observed gradient in DSi concentration in surface water in the ACC was in agreement with previous studies that recorded a gradient in the Polar Front Zone (Varela et al., 2004; Cardinal et al., 2007) at other locations in the Southern Ocean (e.g. the Pacific Sector).

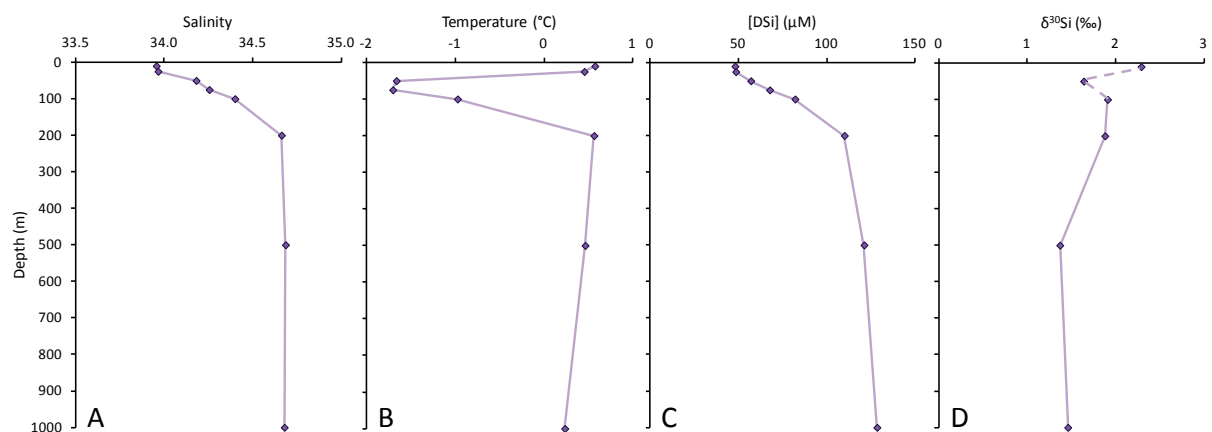


**Figure 4.17** Depth profiles until only down to 1000 m at station 146 for A) salinity, B) temperature ( $^{\circ}\text{C}$ ), C) DSi concentration ( $\mu\text{M}$ ) and D)  $\delta^{30}\text{Si}_{\text{DSi}}$  (‰).

## 0° meridian

An algal bloom occurred in December 2008 along the 0° meridian between the Subantarctic Front (~56°S) and the Polar Front (~50°S) from 10°W to 10°E and had moved south to reach 70°S in February 2008 (Rutgers van der Loeff et al., 2011). The northern station (106), north of the Polar Front, was sampled in mid-February (the latter half of summer). Consequently, the data from this station should represent the post-bloom regime, with high  $\delta^{30}\text{Si}_{\text{DSi}}$  values (2.07 – 1.67 ‰, < 200 m) and low DSi concentrations (6 – 19  $\mu\text{M}$ ). This would suggest that the surface water was approximately two months old, which is in the age range of surface water sampled in the western Weddell Sea by Hoppema et al. (2000). Station 115 was located in the low algal abundance area (54°S – 59°S) (Rutgers van der Loeff et al., 2011), which is in agreement with the DSi concentration and  $\delta^{30}\text{Si}_{\text{DSi}}$  values recorded in the surface water during the present study. The southernmost station on the 0° meridian (146) was still in the bloom, something which may explain the low DSi concentrations and the high  $\delta^{30}\text{Si}_{\text{DSi}}$  values observed. This is supported by Rutgers van der Loeff et al. (2011) who recorded high  $^{234}\text{Th}$  export indicating high production in this area.

## Drake Passage

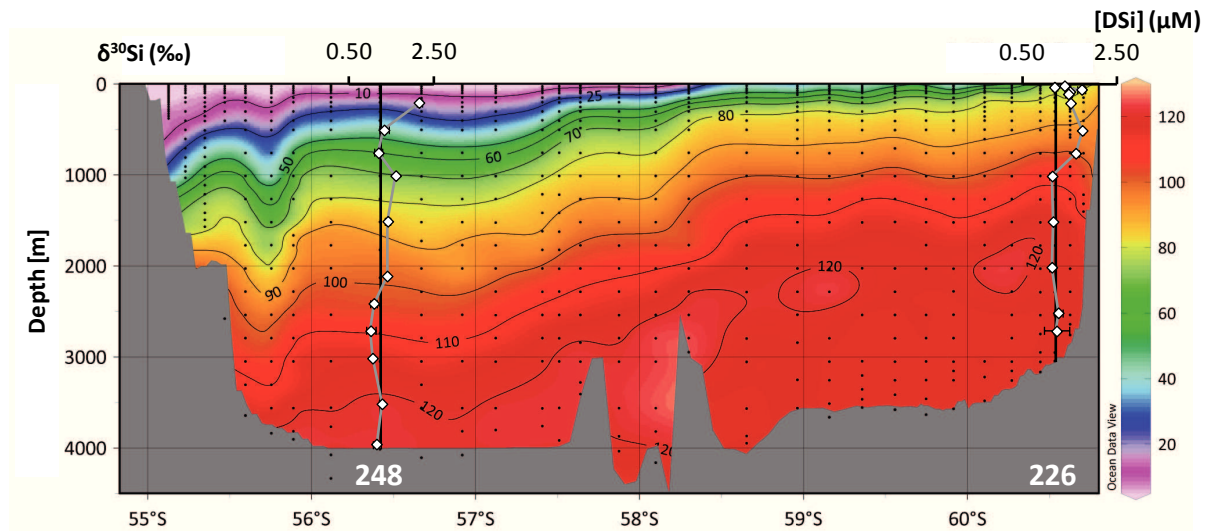


**Figure 4.18** Latitudinal transect through the Drake Passage realized with data from the ANTXXIV/3 campaign. Our stations 248 and 226 are indicated by vertical lines that represent in the same time the  $\delta^{30}\text{Si}_{\text{DSi}}$  of 1.2 ‰ characteristic of deep water masses value in the Southern Ocean. Grey lines with diamond markers represent  $\delta^{30}\text{Si}_{\text{DSi}}$  profiles. Thin horizontal lines indicate [DSi] boundaries. DSi concentration colour map was created with ODV (Schlitzer, Ocean Data View, <http://odv.awi.de>, 2013) using data from ANTXXIV/3 campaign.

The two stations located in the Drake Passage represented different condition in term of phytoplankton activity recorded in autumn. Station 226 was located south of the Southern Boundary of the ACC, north of the area considered as the region of production (Rutgers van der Loeff et al., 2011). The high DSi concentration in the surface water at station 226 (< 100 m, 78  $\mu\text{M}$ ) can be

attributed to the upwelling of subsurface water flowing southward with DSi concentrations of 50 – 80  $\mu\text{M}$  (1000 – 2000 m, 56°S) further north (Fig. 4.18). Despite high DSi concentrations at station 226, higher than expected  $\delta^{30}\text{Si}_{\text{DSi}}$  values (1.75 – 1.52 ‰) were recorded, possibly reflecting some influence of biological activity. This may be supported by the stimulation of primary production observed close to South America (Rutgers van der Loeff et al., 2011) in the region where station 248 was located during ANTXXIV/3. The  $\delta^{30}\text{Si}_{\text{DSi}}$  value recorded at 200 m at station 248 ( $2.13 \pm 0.07$  ‰) was higher than at station 226 ( $1.52 \pm 0.02$  ‰), indicating a possible high production near station 248, supported by the low DSi concentration (20  $\mu\text{M}$  at 200 m).

## II.4.2 Deep water masses in the Drake Passage and the 0° meridian

### II.4.2.1 Upper Circumpolar Deep Water (UCDW)

#### Antarctic Circumpolar Current (ACC)

A south-north gradient of DSi concentration was recorded through the Polar Front zone, which was in agreement with the upwelling of nutrient rich UCDW to the surface and nutrients lost during its northward flow (from stations 115 to 106) (Fig. 4.19). UCDW is not formed in the Atlantic Ocean (Morozov et al., 2010), and therefore, slight variations can be expected due to the entrainment of surrounding water masses as it flows south, even though the main change in water mass properties for the CDW occurred in the Drake Passage when the water enters in the Atlantic Ocean (Well et al., 2003). This may have resulted in the similar  $\delta^{30}\text{Si}_{\text{DSi}}$  values at stations 115, 106 and 248.

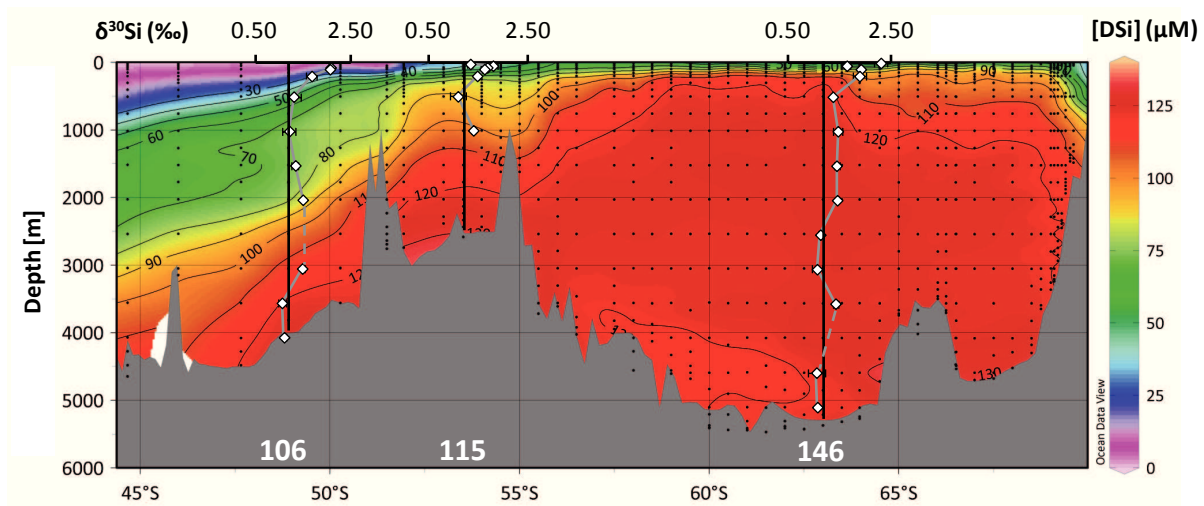


**Figure 4.19** Latitudinal transect through 0° meridian realized with data from the ANTXXIV/3 campaign. Our stations 106, 115 and 146 are indicated by vertical lines that represent in the same time the  $\delta^{30}\text{Si}_{\text{DSi}}$  of 1.2 ‰ characteristic of deep water masses value in the Southern Ocean. Grey lines with diamond markers represent  $\delta^{30}\text{Si}_{\text{DSi}}$  profiles. Thin horizontal lines indicate [DSi] boundaries. DSi concentration colour map was created with ODV (Schlitzer, Ocean Data View, <http://odv.awi.de>, 2013) using data from ANTXXIV/3 campaign.

Two distinct layers of UCDW were observed at station 248 in the Drake Passage, a shallower layer at 2100 m and the deeper layer at 2400 – 2700 m. The  $\delta^{30}\text{Si}_{\text{DSi}}$  of 1.4 ‰ in the shallower layer could be attributed to a Pacific Ocean influence due to the presence of the SPDSW above the UCDW, since  $\delta^{30}\text{Si}_{\text{DSi}}$  values of the Pacific Ocean are thought to be lower than the Atlantic Ocean values (De La Rocha et al., 2000; Cardinal et al., 2007; de Souza et al., 2012a).

## 0° meridian

The  $\delta^{30}\text{Si}_{\text{DSi}}$  value detected in the shallow (200 m) UCDW at station 146 (1.88 ‰, 0° meridian in the Weddell Gyre) was greater than the other stations (1.10 – 1.30 ‰) (Fig. 4.13), although, in comparison to the  $\delta^{30}\text{Si}_{\text{DSi}}$  values at depth for the other stations this value was expected, either directly or indirectly influenced by fractionation during biological uptake of DSi in the mixed layer. This somewhat anomalously high value and the proximity to the euphotic zone at the time of sampling may indicate isotopic fractionation during biological uptake followed by BSi dissolution and export.

### II.4.2.2 Lower Circumpolar Deep Water (LCDW)

LCDW was found below UCDW and NADW along the 0° meridian section. LCDW at station 226 had an elevated  $\delta^{30}\text{Si}_{\text{DSi}}$  average of  $1.69 \pm 0.05$  ‰ (500–750 m), which may be attributed to an influence from the NADW given the formation of the LCDW (see chapter 3) and previous studies showing that the NADW is expected to have  $\delta^{30}\text{Si}_{\text{DSi}}$  values  $\geq 1.7$  ‰ (de Souza et al., 2012b).

The relatively high  $\delta^{30}\text{Si}_{\text{DSi}}$  (1.5 ‰) recorded in the LCDW at station 106 also appears to be linked to the presence of NADW as well. On Figure 4.10 the appearance of NADW is observed in the ACC at approximately 1500 m, moving southeastward where LCDW and UCDW are detected. The formation of LCDW is the result of mixing processes in the Southern Ocean as LCDW comes from mixing between NADW and water from ACC. At the 0° meridian (station 106) this formation process was observed, with NADW influencing the LCDW layer. The influence of NADW seemed to influence LCDW further south (Fig. 4.10), as described by Middag et al., (2011). NADW becomes incorporated into the ACC at approximately 45 – 50°W (Morozov et al., 2010). This incorporation takes place at a location between the stations sampled in this study. This is further supported by how similar the  $\delta^{30}\text{Si}_{\text{DSi}}$  values of the NADW at station 106 ( $1.48 \pm 0.03$  ‰) and LCDW at station 115 ( $1.40 \pm 0.05$  ‰) are.

### II.4.3 The Weddell Gyre

During the cruise, the Weddell Gyre was mostly under ice-cover (from 0° to 25°W and from 43°W to 53°W) and the stations were located at the ice edge. Close to the ice edge, the water was clear and no phytoplankton bloom was noted, in keeping with the high DSi concentrations and low  $\delta^{30}\text{Si}$  values recorded (stations 211 and 189). In the Weddell Gyre, the export flux was determined as low in the central gyre, corresponding to a shallow depth of remineralisation (Rutgers van der Loeff et al., 2011), again, suggestive of an area not in the throes of a phytoplankton bloom.

#### Warm Deep Water (WDW)

The conclusion that can be drawn looking at the  $\delta^{30}\text{Si}_{\text{DSi}}$  values of stations in the Weddell Gyre is that the WDW water mass was homogenous at the time of sampling (late summer/beginning of autumn) between 200 m and 1500 m (Fig. 4.15).

#### Weddell Sea Deep Water (WSDW)

A slight westward, increasing  $\delta^{30}\text{Si}$  gradient was observed in the WSDW between stations 146 – 189 close to 1.2 ‰ and 211 closer to 1.4 ‰. Stations 146 and 189 were in the region of inflow of ACC water to the Weddell Gyre, whereas station 211 was located in the return flow eastward. This was in agreement with the flow pattern of the WSDW described by Fahrbach et al. (2011), who describe the circulation of deep and bottom water as cyclonic.

The high WSDW  $\delta^{30}\text{Si}_{\text{DSi}}$  values at station 211 could potentially be explained by the way the water mass is formed. According to Mackensen et al. (2001) and Huhn et al. (2013), WSDW is a mixture of WDW and WSBW and some of the WSDW can be the result of a mixing between WDW and surface water (Solomon, 1983). The location of station 211 on the slope of the Antarctic Peninsula did not allow for the sampling of the WSBW. Figure 4.13 E shows a lower DSi concentration on the slope of Antarctica (3547 – 3697 m), which is confirmed by the dive down of the subsurface water MWDW recorded deeper than 3547 m at station 211 (Fig. 4.16).

The influence of the Shelf Water potentially caused the difference in  $\delta^{30}\text{Si}_{\text{DSi}}$  between station 211 and 189 – 146. At the time of sampling, the ice cover at stations 146 and 189 were melting, whereas, station 211 was firmly under ice cover. Station 211 was located off Joinville Island and station 189 was a central Weddell Sea station. The Low Salinity Shelf Water at stations 189 and 211 was characterized by an average  $\delta^{30}\text{Si}_{\text{DSi}}$  of 1.50 ‰ and 1.75 ‰, respectively. Because the WDW was isotopically identical at all stations, the influence of Shelf Water was the most likely explanation for the difference between stations. As the Shelf Water was colder and denser than the surface water, it flowed along the shelf and mixed into the WSDW at depth in the water column.



## **Weddell Sea Bottom Water (WSBW) and Antarctic Bottom Water (AABW)**

The WSBW and AABW bottom water masses appear to be isotopically homogenous in the Weddell Gyre. The formation of WSBW occurred at two locations in the gyre, one close to the Filchner-Ronne Ice shelf (WSBWb) in the south and another at the Larsen Ice Shelf (WSBW<sub>s</sub>) on the western side of the gyre (Huhn et al., 2013). A significant amount of WSDW and WSBW recirculates in the gyre, increasing the possibility of a homogenization of the deep water mass through time (Orsi et al., 1995; Mackensen, 2001). The residence time in the gyre is  $\sim 5$  years (Huhn et al., 2013) for the deep and bottom water masses, supporting the previous observation of a homogenisation for the bottom water mass. The  $\delta^{30}\text{Si}_{\text{DSi}}$  values recorded for the bottom water were in agreement with de Souza et al. (2012b), who recorded an AABW  $\delta^{30}\text{Si}_{\text{DSi}}$  close to 1.20 ‰, effectively equivalent to the 1.10 ‰ measured in this study.

These lower  $\delta^{30}\text{Si}_{\text{DSi}}$  values recorded for the bottom water could be influenced by sediment. The residence time for the deep water in the Weddell Gyre is about five years and even if there is new production of deep water the fact that the water spent a long time in the gyre increases the influence of DSi released from the sediment. The Southern Ocean is the ocean where considerable deposits of biogenic silica are recorded (Ragueneau et al., 2000 and references therein) and now it is accepted that the Weddell Gyre is more productive than previously thought, especially regarding the export production (Hoppema et al., 2002).

The closest sediment core for which there is  $\delta^{30}\text{Si}_{\text{DSi}}$  data is too far north (52°38'S 00°08'W) to fall within the Weddell Gyre. Nonetheless, the BSi therein has a value of 1.20 ‰ at the top of the sediment core (De La Rocha et al., 1998).

### **II.4.4 Tropical and subtropical Atlantic Ocean**

#### **Atlantic Central Water (ACW)**

$\delta^{30}\text{Si}_{\text{DSi}}$  values recorded from the western North Atlantic Central Water (wNACW) were low, as expected at this depth due to the absence of biological activity. The only data available for comparison (de Souza et al., 2012b) supported the data of the present study. For the stations north of the Cape Verde Frontal Zone the station n°11 (only data for comparison) from de Souza et al. (2012b) recorded  $\delta^{30}\text{Si}_{\text{DSi}}$  of 1.46 ‰ at 943 m, close to  $\delta^{30}\text{Si}_{\text{DSi}}$  of 1.36 ‰ for our station 1. Conversely,  $\delta^{30}\text{Si}_{\text{DSi}}$  values recorded from the shallow (100 m) South Atlantic Central Water (SACW) recorded at station 21 showed the imprint of biological activity. This is expected as this station was in the euphotic zone where phytoplankton grow, and this was supported by the fact that the Cape Verde Island is in the area of upwelling that brings nutrient rich water to the surface.  $\delta^{30}\text{Si}_{\text{DSi}}$  values

for station 4 ( $1.16 \pm 0.07$  ‰ at 1000 m) were typical values of greater depth and unexpected at this intermediate depth. Data collected from the SACW (de Souza et al., 2012b) fell into our range, with an average of  $1.71 \pm 0.09$  ‰ (100 – 200 m). The spatial repartition of the two water masses indicated the presence of the front, a major boundary between these two central water masses (Stramma and Schott, 1999; Bory et al., 2001).

### ASIW - AAIW

ASIW was only observed north of the CVFZ.  $\delta^{30}\text{Si}_{\text{DSi}}$  values recorded these stations are quite high, with an average of 1.53 ‰ at depths deeper than 1000 m. Station 3 recorded unexpectedly elevated  $\delta^{30}\text{Si}_{\text{DSi}}$  values at these depths. The variability of the properties in this water mass could be an answer. The temperature varied while salinity was stable between 200 m to 700 m (appendix 2). No trend was observed for DSi concentrations and  $\delta^{30}\text{Si}_{\text{DSi}}$  values in this data set. At station 3, the slightly elevated  $\delta^{30}\text{Si}_{\text{DSi}}$  value of 2.02 ‰ may indicate an incorrect identification of the water mass. It is possible that NADW was observed at 2000 m rather than intermediate water, even though 2.02 ‰ is greater than the value noted for the NADW in the Labrador Sea (1.7 ‰, de Souza et al., (2012b)). The stations from the present study were however far south of the NADW formation sites in the North Atlantic increasing the time for this water mass to interact with surrounding water masses and so to have a different isotopic composition compare to the source.

AAIW from the Southern Ocean flows northward to reach latitudes of about 30N°, therefore, it was unsurprising to record AAIW in the tropical Atlantic Ocean with  $\delta^{30}\text{Si}_{\text{DSi}}$  values similar to those in the Southern Ocean. The  $\delta^{30}\text{Si}_{\text{DSi}}$  values recorded in the AAIW from the Southern Ocean (station 115,  $1.48 \pm 0.03$  ‰; station 106,  $1.67 \pm 0.12$ ) were in a similar range as the Tropical Atlantic Ocean (station 21,  $1.42 \pm 0.03$  ‰). The lower value may be attributed to processes, such as mixing with other water masses, during the northward flow. However, there is no further data available for the AAIW in the tropical North Atlantic Ocean for comparison.

## II.5 Global Atlantic Ocean

A compilation of all the data available for the intermediate and deep water masses of the Atlantic Ocean for which silicon isotopic composition and DSi concentrations are known, including the data from the present study, are presented in figure 4.10. This figure illustrates the idea of de Souza et al. (2012b), who described NADW with high  $\delta^{30}\text{Si}_{\text{DSi}}$  ( $\geq 1.7$  ‰) in the northern North Atlantic Ocean and AABW with low  $\delta^{30}\text{Si}_{\text{DSi}}$  (1.2 ‰) in the Southern Ocean. There is a meridional gradient in DSi concentrations, with a significant increase from low concentrations in the NADW formation area (formed from nutrient-depleted surface waters) to high concentrations in the Southern Ocean deep

water (linear regression of  $R^2 = 0.80$ ,  $p < 0.0001$ ,  $n = 140$ ). The  $\delta^{30}\text{Si}_{\text{DSi}}$  decrease from the North Atlantic Ocean to the Southern Ocean is observed, however, it only explains a part of the decrease due to the low but still significant linear regression ( $R^2 = 0.34$ ,  $p < 0.001$ ,  $n = 140$ ). Removing the intermediate water masses from this regression did not change the  $R^2$  or p-value, and therefore, latitudinal gradients observed for the DSi concentration and  $\delta^{30}\text{Si}$  were mainly due to the deep water masses. This illustrates the meridional overturning circulation representation of Toggweiler et al. (2006). According to de Souza et al. (2012b) the biological activity in surface water of the Atlantic Ocean, and processes such as BSi export and BSi dissolution, led to the increase in the DSi concentration of the deep water mass. This accumulates silicon all along its southward flow leading to the high DSi concentration in the Southern Ocean.

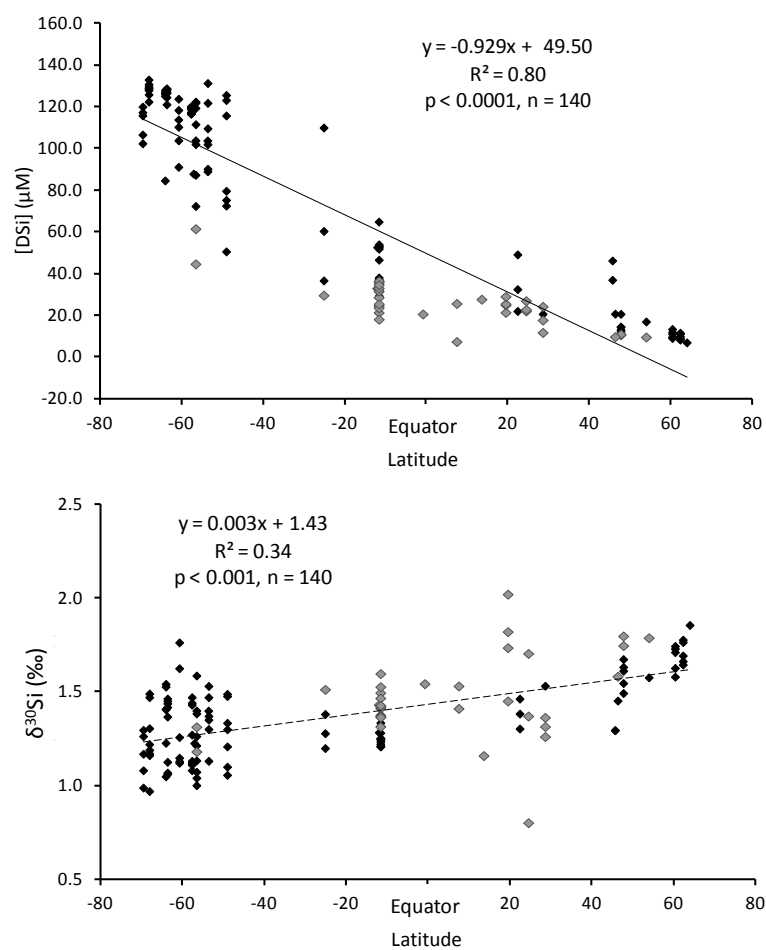


**Figure 4.20** Representation of the A) DSi concentration versus latitude and B)  $\delta^{30}\text{Si}$  versus latitude for data from intermediate and deep water masses of the Atlantic Ocean from the literature for which data for DSi concentration and  $\delta^{30}\text{Si}$  were available (de Souza et al., 2012b; Fripiat et al., 2012), including data from this study. A) Regression line:  $R^2 = 0.80$ ,  $p < 0.0001$  and  $n = 140$ , and B) Regression line:  $R^2 = 0.34$ ,  $p < 0.0001$  and  $n = 140$ . Black diamond: deep water masses, grey diamonds: intermediate water masses, both were used in the calculation of the regression lines.

The difference in DSi concentration is greater between the north and the Equator than between the equator and the south, with similar, less distinct trends occurring for  $\delta^{30}\text{Si}_{\text{DSi}}$  values. Given the

“high” DSi concentrations found in the South Atlantic Ocean and the highly variable  $\delta^{30}\text{Si}_{\text{DSi}}$  signal for the Southern Ocean, a linear regression of only the bottom water masses (WSBW, AABW and NADW) was conducted ( $R^2 = 0.51$ ,  $p < 0.0001$ ,  $n = 38$ ). This supports the presence of a north – south gradient, as previously mentioned by de Souza et al. (2012b), restricted to the bottom water masses.

The meridional gradient recorded through the Atlantic Ocean is due to the difference in  $\delta^{30}\text{Si}_{\text{DSi}}$  between the AAIW and AABW in the Southern Ocean (de Souza et al., 2012b). Our stations in the Weddell Gyre allowed the recording of WSBW and AABW with an average  $\delta^{30}\text{Si}_{\text{DSi}}$  of  $1.06 \pm 0.08 \text{ ‰}$  and stations on the  $0^\circ$  meridian (106 and 115) allow us to calculate an average  $\delta^{30}\text{Si}_{\text{DSi}}$  AAIW of  $1.41 \pm 0.09 \text{ ‰}$ , supporting that assumption. The northward flow brings AAIW to the Tropical North Atlantic Ocean, where  $\delta^{30}\text{Si}_{\text{DSi}}$  values of  $1.41 \pm 0.11 \text{ ‰}$  (station 21,  $7.6^\circ\text{N}$ ) were detected in the AAIW. We observed a similar value for the two locations in the Atlantic Sector of the Southern Ocean (stations 115 and 146) being sampled mid-summer / beginning of autumn and the Tropical Atlantic Ocean (station 21) mid-autumn. However as previously mentioned processes such as mixing and production and dissolution of BSi will influence the  $\delta^{30}\text{Si}_{\text{DSi}}$  linked to the season.

However the deduction these authors made to explain the  $\delta^{30}\text{Si}_{\text{DSi}}$  gradient, i.e. the difference between the AABW and the AAIW flowing to the North Atlantic Ocean should be considered with caution due to the AAIW formation in different areas in the Southern Ocean and due to the location of the mixing between the 3 sources. According to Rusciano et al. (2012) the AAIW found in the Southeast Atlantic Ocean (south of South Africa) is a mixture between three different AAIW, from Indian Ocean (I-AAIW), from Atlantic Ocean (A-AAIW) and a new AAIW identified by the authors and called Indo-Atlantic (AI-AAIW). South of South Africa the three sources converge and the I-AAIW flow return to the Atlantic Ocean. The turbulent environment at the tip of Africa leads to mesoscale turbulences and some A-AAIW leaves the front to move north where the IA-AAIW and the I-AAIW flow. Therefore, the AAIW signature detected in the Tropical Atlantic Ocean reflects not only the Atlantic Sector of the Southern Ocean but a mixture of the A-AAIW with water from the Indian Sector of the Southern Ocean.

## II.6 Conclusion

This study presented the first  $\delta^{30}\text{Si}_{\text{DSi}}$  data for the Weddell Gyre (eastern, southern and western side). Our data confirmed the existence of a gradient in DSi in surface waters from the western to eastern side (high DSi concentration) of the gyre to the eastern side (lower DSi concentration) as already mentioned in the literature. Our isotopic data revealed a  $\delta^{30}\text{Si}_{\text{DSi}}$  gradient going in the opposite direction, as expected. In terms of deep water masses, the Weddell Gyre is mainly a homogeneous area with a light gradient observed for the WSDW due to the circulation of the ACC

entering in the gyre on the eastern side. WSBW was homogeneous in terms of its DSi concentration and  $\delta^{30}\text{Si}_{\text{DSi}}$  at the time of the sampling, with a relatively low  $\delta^{30}\text{Si}_{\text{DSi}}$  of 1.10 ‰. The other bottom water (AABW) within the Weddell Gyre also appeared to be homogeneous during the campaign in terms of the concentration and isotopic composition of DSi.

For the ACC region our data recorded a DSi concentration gradient as well as a corresponding  $\delta^{30}\text{Si}_{\text{DSi}}$  gradient (going in the opposite direction) through the Polar Front, allowing the track of the UCDW upwelling at both locations. The  $\delta^{30}\text{Si}_{\text{DSi}}$  allowed observing as well a NADW influence in the ACC region of the LCDW, both in the Drake Passage and at the 0° meridian.

For the region of the Drake Passage it seems that we can track the influence of the deep Pacific Ocean on the  $\delta^{30}\text{Si}_{\text{DSi}}$  of UCDW as this latter recorded lower  $\delta^{30}\text{Si}_{\text{DSi}}$  than expected and knowing that the Pacific Ocean is thought to have lighter  $\delta^{30}\text{Si}_{\text{DSi}}$  values.

Stations in the Subtropical and Tropical North Atlantic Ocean allowed the observation of the Cape Verde Frontal Zone that separates central water masses coming from the North and the South. However, no differences were recorded in the  $\delta^{30}\text{Si}_{\text{DSi}}$ , although there were not many data presented.

From these data and those of other studies, we are beginning to have a good picture of the behaviour and distribution of  $\delta^{30}\text{Si}$  in the Atlantic Ocean, including the Atlantic sector of the Southern Ocean (De La Rocha et al., 2011; de Souza et al., 2012b). These results support the recent idea of de Souza et al. (2012b) that there is a gradient in the  $\delta^{30}\text{Si}$  of bottom water in the Atlantic, going from a relatively high value in the northern North Atlantic Ocean with NADW to a lower value in the Southern Ocean with AABW and its  $\delta^{30}\text{Si}$  of 1.1‰.

It will be of interest to increase the amount of data and the number of different locations in the Weddell Gyre for which  $\delta^{30}\text{Si}$  has been measured to confirm the trend observed that the deep water masses are homogeneous in the gyre as this area is a key site in the Southern Ocean (and, indeed, the world ocean) for bottom water production; the processes controlling  $\delta^{30}\text{Si}$  in the Weddell Gyre have an outsized impact on the concentration and isotopic composition of DSi in bottom waters that move through the world ocean. To have more silicon isotope data from depth profiles in the tropical Atlantic Ocean, both north and south of the equator, would also be of great interest, in this case to track the flow of intermediate water from the Southern Ocean to the tropics and to observe the evolution of the isotopic composition of the water during its flow due to processes of mixing and remineralisation.

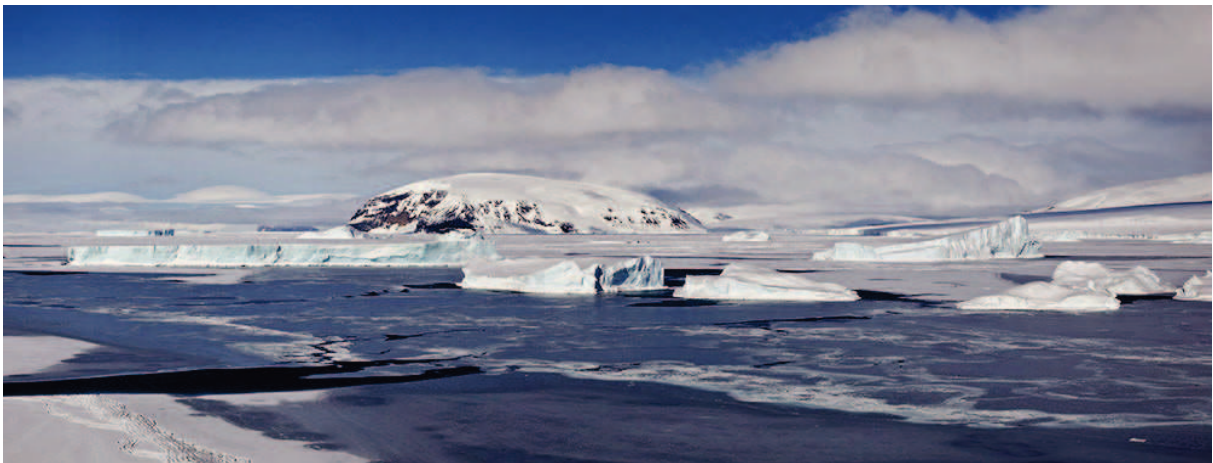


---

# Conclusions and perspectives

## — Chapter 5 —

---



## V Conclusions

Studies undertaken during this PhD improved our understanding of the distribution and behaviour of silicon isotopes in the Atlantic Ocean and in the Southern Ocean. The main areas of focus of the research were the Kerguelen Plateau in the Indian sector of the Southern Ocean; the Drake Passage, the Weddell Gyre and the 0° meridian in the Atlantic sector of the Southern Ocean; as well as the Subtropical and Tropical Atlantic Ocean. The questions raised at the beginning of this PhD were answered and their summary is presented as follow:

- ✓ **What processes affected the biogeochemical cycling of silicon and silicon isotopes in the area of Kerguelen Plateau? More precisely, what is responsible for the unexpectedly low  $\delta^{30}\text{Si}$  observed after the peak of the spring bloom along the edge of the Kerguelen Plateau? (chapter 3)**

Firstly, a new set of data from the Indian sector and the Atlantic sector of the Southern Ocean were presented (from expedition ANTXXIII/9). Then to answer the above questions, I built a box model of the biogeochemical silica cycle (dissolved silicon (DSi) and biogenic silica (BSi) concentrations and isotope composition) in the vicinity of the Kerguelen Plateau. The model simulated biological and physical processes occurring in the surface Mixed Layer (ML) and at the interface between the ML and Winter Water (WW). The biological processes modelled were diatom (BSi) production and mortality and the physical processes were mixing, BSi dissolution and BSi export via sinking. The key advantage of this model over previous box models of the silica cycle and silicon isotopes is that it takes into account the seasonal evolution of the ML depth.

This model revealed that the key driver of the observed and hitherto unexplained  $\delta^{30}\text{Si}$  decrease towards the end of summer seemed to be the switch from bloom growth to steady state growth (when slow but continuing production of BSi prevented significant net increase in DSi concentrations despite the diffusive input of DSi from WW but did not prevent a decrease in ML  $\delta^{30}\text{Si}$  towards WW values). This strongly implies that seasonal changes in export efficiency (e.g., favouring the export of bloom BSi versus the export of BSi produced during other times of the year) strongly influence the  $\delta^{30}\text{Si}$  of BSi accumulating in marine sediments and potentially confound attempts to use the  $\delta^{30}\text{Si}$  of this BSi as a paleoceanographic proxy of DSi utilization by diatoms. Secondly, fractionation during dissolution of BSi, when it was allowed to occur, had only a negligible effect on the  $\delta^{30}\text{Si}$  of BSi exported throughout the course of the year, a result which supports the use of the  $\delta^{30}\text{Si}$  of BSi accumulating in marine sediments as a paleoceanographic proxy. Finally and relating to the first point in this paragraph, the behaviour of silicon isotopes in the model is very sensitive to how the



mixing is constrained between ML and WW; if the the  $\delta^{30}\text{Si}$  of DSi input to the ML is allowed to vary throughout the year as the ML shoals away from the WW, the late summer drop in the  $\delta^{30}\text{Si}$  of DSi (and, ultimately BSi) is much less pronounced; although the overall decline is bigger and spread out over a much longer time frame. Altogether, these results suggest that as a paleoceanographic proxy,  $\delta^{30}\text{Si}$  may more reflect the dominant mode of production of the BSi that is exported (i.e. bloom versus steady state growth) rather than strictly the extent of DSi utilization by diatoms.

✓ **What is the distribution of the DSi concentration and  $\delta^{30}\text{Si}_{\text{DSi}}$  in the intermediate and deep water masses in the Atlantic Ocean from the Subtropical North Atlantic Ocean to the Atlantic sector of the Southern Ocean? (chapter 5)**

To answer these questions depth profiles from two campaigns were used, coming from the Atlantic sector of the Southern Ocean (seven profiles from expedition ANTXXIV/3) and from the tropical region in the North Atlantic Ocean (five profiles from the MSM10/1 campaign) to investigate the DSi concentration and  $\delta^{30}\text{Si}_{\text{DSi}}$ . In the Southern Ocean, the areas of greatest interest were the Weddell Gyre, for which the first  $\delta^{30}\text{Si}_{\text{DSi}}$  are presented here, the Drake Passage, and the 0° meridian. For the North Atlantic Ocean, samples came from north and south of the Cape Verde Island, in the coastal upwelling zone.

These data revealed a surface gradient in DSi concentration from the western to the eastern side of the Weddell Gyre with an opposite trend for the  $\delta^{30}\text{Si}_{\text{DSi}}$ . It was observed that each of the deep water masses in the Weddell Gyre was homogeneous in terms of its DSi concentration and  $\delta^{30}\text{Si}_{\text{DSi}}$  at the time of the sampling. WSBW had a low  $\delta^{30}\text{Si}_{\text{DSi}}$  ( $1.06 \pm 0.08 \text{ ‰}$ ) even lower than previously noted for bottom water in the Southern Ocean. This low value could be explained by DSi released from the dissolution of BSi in sediment, as the gyre is a high opal deposit area. Our data permit us to track the influence of NADW on the LCDW ( $1.49 \pm 0.03 \text{ ‰}$  at station 106 deeper than 2000 m with NADW influence vs.  $1.40 \pm 0.05 \text{ ‰}$  at 1000 m at station 115, no influenced of the NADW recorded) in the ACC from the Drake Passage to the 0° meridian. Finally, there were too few data from the Subtropical and Tropical North Atlantic Ocean to draw any strong conclusions. However, my dataset added to the small body of silicon isotope data available for the Atlantic Ocean, improving our picture of the isotopic composition of the deep water masses in this basin. The data support there being a meridional gradient in the deep water mass, going from high  $\delta^{30}\text{Si}_{\text{DSi}}$  for the NADW in the northern North Atlantic Ocean ( $\approx 1.7 \text{ ‰}$ ) to a lower  $\delta^{30}\text{Si}_{\text{DSi}}$  value of  $1.2 \text{ ‰}$  for the AABW in the Southern Ocean.

## VI Perspectives

### ✓ Perspectives to the work on modelling the silica cycle on the Kerguelen Plateau

To go further into the study of the silicon isotopes in the Southern Ocean, it will be necessary to quantify the influence of basalt weathering on the  $\delta^{30}\text{Si}$  of DSi and the DSi concentration of the water column in places such as the Kerguelen Plateau. Until now there are no available data about either how much DSi is input into the water column from basalt weathering or what the fractionation factor associated with marine basalt weathering is. Knowing this information, even to a rough extent, would help us to better understand silica cycling on the Kerguelen Plateau and allow us to improve currently very poorly constrained global estimates of DSi input (and  $\delta^{30}\text{Si}$ ) from the weathering of ocean crust (which is made of basalt).

To improve the model behaviour and to better reproduce the silica cycle (on the Kerguelen Plateau in our case) it will be important to acquire seasonal data for the  $\delta^{30}\text{Si}_{\text{DSi}}$  and  $\delta^{30}\text{Si}_{\text{BSi}}$  especially before the bloom period and during winter in the water and in the sediment. To date there is no information about  $\delta^{30}\text{Si}$  value for these periods. It will also be necessary to look at the species assemblage and to measure the seasonal BSi export efficiency to better understand the fraction exported and the fraction buried. All that parameters are needed to properly interpret opal sediment records used for paleoceanographic reconstruction of the silica cycle.

A good example is the Last Glacial Maximum (LGM) opal sediment record observation. Our model showed that BSi produced in winter will have a low  $\delta^{30}\text{Si}_{\text{BSi}}$  ( $\sim +0.8$  ‰), low values that are found as well in the LGM as low as  $+0.2$  to  $+0.8$  ‰. During this period, especially the area where the 2 cores are from (i.e.  $53^{\circ}53'S$ ,  $4^{\circ}56'W$  and  $52^{\circ}38'S$ ,  $00^{\circ}08'W$  - the Atlantic Sector of the Southern Ocean), there is a significant problem of opal preservation resulting in a better preservation of a heavily silicified diatom that is not representative of what was exported and buried in term of species at the time of export. Looking at abundance of species in these sediment cores, the winter resting stages of *Eucampia antarctica* that are very hard to dissolve are highly present compare to *Fragilariopsis kerguelensis* that are normally very abundant. If the winter resting stages are indeed produced during winter and so have these low  $\delta^{30}\text{Si}_{\text{BSi}}$  value, ascribing the low  $\delta^{30}\text{Si}_{\text{BSi}}$  during the LGM to less utilization of silicic acid during the growing season may be entirely incorrect.

Finally it will be of interest to improve the physical model by increasing the vertical resolution and the biological model by taking into account the diatom assemblage and communities when  $\delta^{30}\text{Si}$  is analyzed. It will be interesting to add an iron limitation term to simulate the “on” and “off” of the Kerguelen Plateau as iron conditions are different. Adding a zooplankton term and taking into account the Si:C ratio will be able to greatly improve the behaviour of the model.

✓ **Perspectives to the work on the DSi concentration and  $\delta^{30}\text{Si}$  in the intermediate and deep water masses of the Atlantic Ocean**

It will be interesting and necessary to improve the resolution of the silicon isotope dataset from the Weddell Gyre as this gyre is a key site of Antarctic Bottom Water (AABW) formation in the Southern Ocean and a major source of deepwater to the world ocean. A sampling of the East (entry of the Circumpolar Deep Water) and the West and North (outflow of AABW) of the gyre would help to improve our understanding about the gyre circulation and confirm the trend observed during this study, i.e. the observation of a gradient of DSi concentration for the surface water.

The Ross Sea being the 2<sup>nd</sup> producer of AABW, it is important to sample this area and to compare the results with DSi concentration and  $\delta^{30}\text{Si}$  of the Weddell Gyre. This will help to understand the circulation in the Southern Ocean and in the low latitudes.

Regarding the big picture of circulation in the Atlantic Ocean, it would be interesting to have more data from the Drake Passage, as it is a major choke point for the Antarctic Circumpolar Current (ACC). Moreover, it would help us to see the influence of the Drake Passage on the Pacific Ocean data once the ACC flow reaches the Atlantic Ocean, in term of water flow to the lower latitude and interaction of water masses.

Finally, it seems necessary to increase the quantity and resolution of sampling in the Subtropical and Tropical Atlantic Ocean to better track the delivery of nutrients in intermediate water from the Southern Ocean to the tropics and the movement of deep water from the North Atlantic to the Southern Ocean in order to understand how the isotopic signature of the water masses evolve along their flow.



---

## Bibliography

---

Arhan, M., Colin de Verdière, A., and Mémery, L.: The eastern boundary of the subtropical North Atlantic, *J. Phys. Oceanogr.*, 24, 1295 - 1316, 1994.

Baines, S. B., Twining, B. S., Brzezinski, M. A., Krause, J. W., Vogt, S., Assael, D., and McDaniel, H.: Significant silicon accumulation by marine picocyanobacteria, *Nature Geosci.*, 5, 886-891 12, <http://www.nature.com/ngeo/journal/v5/n12/abs/ngeo1641.html#supplementary-information>, 2012.

Basile-Doelsch, I., Meunier, J. D., and Parron, C.: Another continental pool in the terrestrial silicon cycle, *Nature*, 433, 399-402 7024, [http://www.nature.com/nature/journal/v433/n7024/supinfo/nature03217\\_S1.html](http://www.nature.com/nature/journal/v433/n7024/supinfo/nature03217_S1.html), 2005.

Berner, R. A., Lasaga, A. C., and Garrels, R. M.: The carbonate-silicate geochemical cycle and its effect on atmospheric carbon dioxide over the past 100 million years, *Am. J. Sci.*, 283, 641-683 7, 10.2475/ajs.283.7.641, 1983.

Beucher, C., Tréguer, P., Hapette, A.-M., Corvaisier, R., Metzl, N., and Pichon, J.-J.: Intense summer Si-recycling in the surface Southern Ocean, *Geophys. Res. Lett.*, 31, L09305, 10.1029/2003gl018998, 2004.

Beucher, C. P., Brzezinski, M. A., and Jones, J. L.: Sources and biological fractionation of silicon isotopes in the Eastern Equatorial Pacific, *Geochim. Cosmochim. Acta*, 72, 3063-3073 13, <http://dx.doi.org/10.1016/j.gca.2008.04.021>, 2008.

Beucher, C. P., Brzezinski, M. A., and Jones, J. L.: Mechanisms controlling silicon isotope distribution in the Eastern Equatorial Pacific, *Geochim. Cosmochim. Acta*, 75, 4286-4294 15, <http://dx.doi.org/10.1016/j.gca.2011.05.024>, 2011.

Bhattacharyya, P., and Volcani, B. E.: Sodium-dependent silicate transport in the apochlorotic marine diatom *Nitzschia alba*, *Proceedings of the National Academy of Sciences*, 77, 6386-6390 11, 1980.

Bidle, K. D., and Azam, F.: Accelerated dissolution of diatom silica by marine bacterial assemblages, *Nature*, 397, 508-512 6719, 1999.

Bory, A., Jeandel, C., Leblond, N., Vangriesheim, A., Khripounoff, A., Beaufort, L., Rabouille, C., Nicolas, E., Tachikawa, K., Etcheber, H., and Buat-Ménard, P.: Downward particle fluxes within different productivity regimes off the Mauritanian upwelling zone (EUMELI program), *Deep-Sea Res. I*, 48, 2251-2282 10, [http://dx.doi.org/10.1016/S0967-0637\(01\)00010-3](http://dx.doi.org/10.1016/S0967-0637(01)00010-3), 2001.

Brzezinski, M., Olson, R., and Chisholm, S.: Silicon availability and cell-cycle progression in marine diatoms, *Mar. Ecol. Prog. Ser.*, 67, 83-96 1, 1990.

Brzezinski, M. A., Nelson, D. M., Franck, V. M., and Sigmon, D. E.: Silicon dynamics within an intense open-ocean diatom bloom in the Pacific sector of the Southern Ocean, *Deep-Sea Res. II*, 48, 3997-4018, 2001.

Brzezinski, M. A., Pride, C. J., Franck, V. M., Sigman, D. M., Sarmiento, J. L., Matsumoto, K., Gruber, N., Rau, G. H., and Coale, K. H.: A switch from Si(OH)<sub>4</sub> to NO<sub>3</sub> depletion in the glacial Southern Ocean, *Geophys. Res. Lett.*, 29 (12), 10.1029/2001GL014349, 2002.

Brzezinski, M. A., Dickon, M. L., Nelson, D. M., and Sambrotto, R.: Ratios of Si, C and N uptake by microplankton in the Southern Ocean, *Deep-Sea Res. II*, 50, 619-633, 2003.

Brzezinski, M. A., Dumousseaud, C., Krause, J. W., Measures, C. I., and Nelson, D. M.: Iron and silicic acid concentrations together regulate Si uptake in the equatorial Pacific Ocean, *Limnol. Oceanogr.*, 53, 875-883, 2008.

Cardinal, D., Alleman, L. Y., de Jong, J., Ziegler, K., and Andre, L.: Isotopic composition of silicon measured by multicollector plasma source mass spectrometry in dry plasma mode, *J. Anal. Atom. Spectrom.*, 18, 213-218, 10.1039/b210109b, 2003.

Cardinal, D., Alleman, L. Y., Dehairs, F., Savoye, N., Trull, T. W., and Andre, L.: Relevance of silicon isotopes to Si-nutrient utilization and Si-source assessment in Antarctic waters, *Global Biogeochem. Cy.*, 19, GB2007, 10.1029/2004GB002364, 2005.

Cardinal, D., Savoye, N., Trull, T. W., Dehairs, F., Kopczynska, E. E., Fripiat, F., Tison, J.-L., and André, L.: Silicon isotopes in spring Southern Ocean diatoms: Large zonal changes despite homogeneity among size fractions, *Mar. Chem.*, 106, 46-62, 1-2, <http://dx.doi.org/10.1016/j.marchem.2006.04.006>, 2007.

Cardinal, D., Gaillardet, J., Hughes, H. J., Opfergelt, S., and André, L.: Contrasting silicon isotope signatures in rivers from the Congo Basin and the specific behaviour of organic-rich waters, *Geophys. Res. Lett.*, 37, 10.1029/2010GL043413, 10.1029/2010GL043413., 2010.

Claquin, P., Leynaert, A., Sferratore, A., Garnier, J., and Ragueneau, O.: Physiological ecology of diatoms along the land-sea continuum, in: *The silicon cycle: Human perturbations and impacts on aquatic systems*, Island Press, 18-24, 2006.

Cunningham, C. M.: Southern Ocean circulation, *Arch. Nat. Hist.*, 32, 265-280, 2005.

Davidson, A. T., Bramich, D., Marchant, H. J., and McMinn, A.: Effects of UV-B irradiation on growth and survival of Antarctic marine diatoms, *Mar. Biol.*, 119, 507-515, 10.1007/bf00354312, 1994.

de Brauwere, A., Fripiat, F., Cardinal, D., Cavagna, A.-J., De Ridder, F., André, L., and Elskens, M.: Isotopic model of oceanic silicon cycling: The Kerguelen Plateau case study, *Deep-Sea Res. I*, 70, 42-59, <http://dx.doi.org/10.1016/j.dsr.2012.08.004>, 2012.

De La Rocha, C. L., Brzezinski, M. A., and DeNiro, M. J.: Purification, recovery, and laser-driven fluorination of silicon from dissolved and particulate silica for the measurement of natural stable isotope abundances, *Anal. Chem.*, 68, 3746-3750, 10.1021/ac960326j, 1996.

De La Rocha, C. L., Brzezinski, M. A., and DeNiro, M. J.: Fractionation of silicon isotopes by marine diatoms during biogenic silica formation, *Geochim. Cosmochim. Acta*, 61, 5051-5056, 0016-7037/97, 1997.

De La Rocha, C. L., Brzezinski, M. A., DeNiro, M. J., and Shemesh, A.: Silicon-isotope composition of diatoms as an indicator of past oceanic change, *Nature*, 395, 680-683, 10.1038/3703, 1998.

De La Rocha, C. L., Brzezinski, A., and DeNiro, M. J.: A first look at the distribution of the stable isotopes of silicon in natural waters, *Geochim. Cosmochim. Acta*, 64, 2467-2477, S0016-7037(00)00373-2, 2000.

De La Rocha, C. L.: Measurement of silicon stable isotope natural abundances via multicollector inductively coupled plasma mass spectrometry (MC-ICP-MS), *Geochem. Geophys. Geosyst.*, 3, 1-8, 10.1029/2002gc000310, 2002.

- De La Rocha, C. L., Bescont, P., Croguennoc, A., and Ponzevera, E.: The silicon isotopic composition of surface waters in the Atlantic and Indian sectors of the Southern Ocean, *Geochim. Cosmochim. Acta*, 75, 5283-5295 18, <http://dx.doi.org/10.1016/j.gca.2011.06.028>, 2011.
- de Souza, G. F., Reynolds, B. C., Johnson, G. C., Bullister, J. L., and Bourdon, B.: Silicon stable isotope distribution traces Southern Ocean export of Si to the eastern South Pacific thermocline, *Biogeosciences*, 9, 4199-4213 11, 10.5194/bg-9-4199-2012, 2012a.
- de Souza, G. F., Reynolds, B. C., Rickli, J., Frank, M., Saito, M. A., Gerringa, L. J. A., and Bourdon, B.: Southern Ocean control of silicon stable isotope distribution in the deep Atlantic Ocean, *Global Biogeochem. Cy.*, 26, GB2035, 10.1029/2011gb004141, 2012b.
- DeFritas, A. S. W., McCulloch, A. W., and McInnes, A. G.: Recovery of silica from aqueous silicate solutions via trialkyl or tetraalkylammonium silicomolybdate., *Can. J. Chem.*, 69, 611-614, 1991.
- Demarest, M. S., Brzezinski, M. A., and Beucher, C. P.: Fractionation of silicon isotopes during biogenic silica dissolution, *Geochim. Cosmochim. Acta*, 73, 5572-5583 19, <http://dx.doi.org/10.1016/j.gca.2009.06.019>, 2009.
- DeMaster, D. J.: The supply and accumulation of silica in the marine environment, *Geochim. Cosmochim. Acta*, 45, 1715-1732 10, [http://dx.doi.org/10.1016/0016-7037\(81\)90006-5](http://dx.doi.org/10.1016/0016-7037(81)90006-5), 1981.
- DeMaster, D. J.: Marine silica cycle, *Ecosystems*, 4, 254 233, 2001.
- DeMaster, D. J.: The accumulation and cycling of biogenic silica in the Southern Ocean: revisiting the marine silica budget, *Deep-Sea Res. II*, 49, 3155–3167, 2002.
- Dessert, C., Dupré, B., Gaillardet, J., François, L. M., and Allègre, C. J.: Basalt weathering laws and the impact of basalt weathering on the global carbon cycle, *Chem. Geol.*, 202, 257-273 3–4, <http://dx.doi.org/10.1016/j.chemgeo.2002.10.001>, 2003.
- Ding, T., Wan, D., Bai, R., Zhang, Z., Shen, Y., and Meng, R.: Silicon isotope abundance ratios and atomic weights of NBS-28 and other reference materials, *Geochim. Cosmochim. Acta*, 69, 5487-5494 23, <http://dx.doi.org/10.1016/j.gca.2005.06.015>, 2005.
- Dong, J.: Water mass exchange between the Weddell Gyre and the Antarctic Circumpolar Current, PhD, The Florida state of University, Florida, 2012.
- Douthitt, C. B.: The geochemistry of the stable isotopes of silicon, *Geochimica and Cosmochimica Acta*, 46, 1449-1458 8, [http://dx.doi.org/10.1016/0016-7037\(82\)90278-2](http://dx.doi.org/10.1016/0016-7037(82)90278-2), 1982.
- Dugdale, R. C., Wilkerson, F. P., and Minas, H. J.: The role of a silicate pump in driving new production, *Deep-Sea Res. I*, 42, 697-719 5, 10.1016/0967-0637(95)00015-x, 1995.
- Emery, W. J.: Antarctic Polar Frontal Zone from Australia to the Drake Passage, *J. Phys. Oceanogr.*, 7, 811-822, 1977.
- Emery, W. J., and Meincke, J.: Global water masses: summary and review, *Oceanol. Acta*, 9, 383 - 391, 1986.
- Emery, W. J.: Water types and water masses, *Ocean circulation*, 2003.



Engström, E., Rodushkin, I., Baxter, D. C., and Öhlander, B.: Chromatographic purification for the determination of dissolved silicon isotopic compositions in natural waters by high-resolution multicollector inductively coupled plasma mass spectrometry, *Anal. Chem.*, 78, 250-257 1, 10.1021/ac051246v, 2006.

Engström, E.: Fractionation of the Stable Silicon Isotopes Studied Using MC-ICP-MS: Analytical Method Developments and Applications in Geochemistry, PhD, Department of Chemical Engineering and Geosciences, Division of Geosciences, Luleå University of Technology, 2009.

Epstein, E.: Silicon, *Annual Review of Plant Physiology and Plant Molecular Biology*, 50, 641-664 1, doi:10.1146/annurev.arplant.50.1.641, 1999.

Fahrbach, E., de Baar, H. J. W., Garçon, V. C., and Provost, C.: Introduction to physics, carbon dioxide, trace elements and isotopes in the Southern Ocean: The Polarstern expeditions ANT-XXIV/3 (2008) and ANT-XXIII/3 (2006), *Deep-Sea Res. II*, 58, 2501-2508 25-26, <http://dx.doi.org/10.1016/j.dsr2.2011.07.008>, 2011.

Field, C. B., Behrenfeld, M. J., Randerson, J. T., and Falkowski, P.: Primary production of the biosphere: integrating terrestrial and oceanic components, *Science*, 281, 237-240 5374, 10.1126/science.281.5374.237, 1998.

Frew, R. D., Dennis, P. F., Heywood, K. J., Meredith, M. P., and Boswell, S. M.: The oxygen isotope composition of water masses in the northern North Atlantic, *Deep-Sea Res. I*, 47, 2265-2286 12, [http://dx.doi.org/10.1016/S0967-0637\(00\)00023-6](http://dx.doi.org/10.1016/S0967-0637(00)00023-6), 2000.

Fripiat, F., Cavagna, A. J., Savoye, N., Dehairs, F., André, L., and Cardinal, D.: Isotopic constraints on the Si-biogeochemical cycle of the Antarctic Zone in the Kerguelen area (KEOPS), *Mar. Chem.*, 123, 11-22 1-4, <http://dx.doi.org/10.1016/j.marchem.2010.08.005>, 2011a.

Fripiat, F., Leblanc, K., Elskens, M., Cavagna, A. J., Armand, L., Andre, L., Dehairs, F., and Cardinal, D.: Efficient silicon recycling in summer in both the Polar Frontal and Subantarctic Zones of the Southern Ocean, *Mar. Ecol. Prog. Ser.*, 435, 47-61, 10.3354/meps09237, 2011b.

Fripiat, F., Cavagna, A.-J., Dehairs, F., De Brauwere, A., André, L., and Cardinal, D.: Processes controlling the Si-isotopic composition in the Southern Ocean and application for paleoceanography, *Biogeosciences*, 9, 2443-2457, 10.5194/bg-9-2443-2012, 2012.

Fuhrmann, T., Landwehr, S., El Rharbi-Kucki, M., and Sumper, M.: Diatoms as living photonic crystals, *Appl Phys B*, 78, 257-260 3-4, 10.1007/s00340-004-1419-4, 2004.

Georg, R. B., Reynolds, B. C., West, A. J., Burton, K. W., and Halliday, A. N.: Silicon isotope variations accompanying basalt weathering in Iceland, *Earth Planet. Sci. Lett.*, 261, 476-490 3-4, <http://dx.doi.org/10.1016/j.epsl.2007.07.004>, 2007.

Hamm, C. E., Merkel, R., Springer, O., Jurkojc, P., Maier, C., Prechtel, K., and Smetacek, V.: Architecture and material properties of diatom shells provide effective mechanical protection, *Nature*, 421, 841-843 6925, 2003.

Hildebrand, M.: Diatoms, biomineralization processes, and genomics, *Chem. Rev.*, 108, 4855-4874 11, 10.1021/cr078253z, 2008.

Hoefs, J.: Stable isotope geochemistry, 4th ed., Springer, 1996.

Hoppema, M., Goeyens, L., and Fahrbach, E.: Intense nutrient removal in the remote area off Larsen Ice Shelf (Weddell Sea), 2, Springer, Heidelberg, Germany, 2000.

Hoppema, M., de Baar, H. J. W., Bellerby, R. G. J., Fahrbach, E., and Bakker, K.: Annual export production in the interior Weddell Gyre estimated from a chemical mass balance of nutrients, *Deep-Sea Res. II*, 49, 1675-1689 9–10, [http://dx.doi.org/10.1016/S0967-0645\(02\)00006-1](http://dx.doi.org/10.1016/S0967-0645(02)00006-1), 2002.

Huhn, O., Rhein, M., Hoppema, M., and van Heuven, S.: Decline of deep and bottom water ventilation and slowing down of anthropogenic carbon storage in the Weddell Sea, 1984–2011, *Deep-Sea Res. I*, 76, 66-84 0, <http://dx.doi.org/10.1016/j.dsr.2013.01.005>, 2013.

Hurd, D. C., and Birdwhistell, S.: On producing a more general-model for biogenic silica dissolution, *Am. J. Sci.*, 283, 1-28 1, 1983.

Karl, D. M., and Tien, G.: MAGIC - A sensitive and precise method for measuring dissolved phosphorus in aquatic environments, *Limnol. Oceanogr.*, 37, 105-116 1, 1992.

Kröger, N., and Poulsen, N.: Diatoms - from cell wall biogenesis to nanotechnology, *Annu. Rev. Genet.*, 42, 83-107 1, doi:10.1146/annurev.genet.41.110306.130109, 2008.

Kuhlbrodt, T., Griesel, A., Montoya, M., Levermann, A., Hofmann, M., and Rahmstorf, S.: On the driving processes of the Atlantic meridional overturning circulation, *Rev. Geophys.*, 45, RG2001 2, 10.1029/2004rg000166, 2007.

Lacan, F.: Masses d'eau des mers nordiques et de l'Atlantique subarctique tracées par les isotopes du néodyme, PhD, Université de Toulouse III, 2002.

Laruelle, G. G., Roubéix, V., Sferratore, A., Brodherr, B., Ciuffa, D., Conley, D. J., Durr, H. H., Garnier, J., Lancelot, C., Phuong, Q. L. T., Meunier, J. D., Meybeck, M., Michalopoulos, P., Moriceau, B., Longphuir, S. N., Loucaides, S., Papush, L., Presti, M., Ragueneau, O., Regnier, P., Saccone, L., Slomp, C. P., Spiteri, C., and Van Cappellen, P.: Anthropogenic perturbations of the silicon cycle at the global scale: Key role of the land-ocean transition, *Global Biogeochem. Cy.*, 23, Gb4031 10.1029/2008gb003267, 2009.

Lewin, J. C.: Silicon metabolism in diatoms III. Respiration and silicon uptake in *Navicula pelliculosa*, *J. Gen. Physiol.*, 1 - 10 39, 1955.

Lewin, R. A.: *Physiology and Biochemistry of Algae*, Academic Press, 1962.

Loucaides, S., and Behrends, T.: Dissolution of biogenic silica from land to ocean: role of salinity and pH, *Limnol. Oceanogr.*, 53, 1614 4, 2008.

Mackensen, A.: Oxygen and carbon stable isotope tracers of Weddell Sea water masses: new data and some paleoceanographic implications, *Deep-Sea Res. I*, 48, 1401-1422 6, [http://dx.doi.org/10.1016/S0967-0637\(00\)00093-5](http://dx.doi.org/10.1016/S0967-0637(00)00093-5), 2001.

Martin-Jézéquel, V., Hildebrand, M., and Brzezinski, M. A.: Silicon metabolism in diatoms: implications for growth, *J. Phycol.*, 36, 821-840 5, 10.1046/j.1529-8817.2000.00019.x, 2000.

McCartney, M. S.: Recirculating components to the deep boundary current of the northern North Atlantic, *Prog. Oceanogr.*, 29, 283-383 4, [http://dx.doi.org/10.1016/0079-6611\(92\)90006-L](http://dx.doi.org/10.1016/0079-6611(92)90006-L), 1992.

- Middag, R., de Baar, H. J. W., Laan, P., Cai, P. H., and van Ooijen, J. C.: Dissolved manganese in the Atlantic sector of the Southern Ocean, *Deep-Sea Res. II*, 58, 2661-2677 25–26, <http://dx.doi.org/10.1016/j.dsr2.2010.10.043>, 2011.
- Milligan, A. J., and Morel, F. M. M.: A Proton Buffering Role for Silica in Diatoms, *Science*, 297, 1848-1850 5588, 10.1126/science.1074958, 2002.
- Milligan, A. J., Varela, D. E., Brzezinski, M. A., and Morel, F. M. M.: Dynamics of silicon metabolism and silicon isotopic discrimination in a marine diatom as a function of pCO<sub>2</sub>, *Limnol. Oceanogr.*, 49, 322-329 2, 2004.
- Morozov, E., Demidov, A., Tarakanov, R., and Zenk, W.: Deep water masses of the South and North Atlantic, in: *Abyssal Channels in the Atlantic Ocean*, Springer Netherlands, 25-50, 2010.
- Mosseri, J., Quéguiner, B., Rimmelin, P., Leblond, N., and Guieu, C.: Silica fluxes in the northeast Atlantic frontal zone of Mode Water formation (38–45°N, 16–22°W) in 2001–2002, *Journal of Geophysical Research: Oceans* (1978–2012), 110 C7, 2005.
- Nelson, D. M., Tréguer, P., Brzezinski, M. A., Leynaert, A., and Quéguiner, B.: Production and dissolution of biogenic silica in the ocean: revised global estimates, comparison with regional data and relationship to biogenic sedimentation, *Glob. Biogeochem. Cycles*, 9, 359-372, 1995.
- Nelson, D. M., and Brzezinski, M. A.: Diatom growth and productivity in an oligotrophic midocean gyre: a 3-yr record from the Sargasso Sea near Bermuda, *Limnol. Oceanogr.*, 42, 473-486, 1997.
- Opfergelt, S., and Delmelle, P.: Silicon isotopes and continental weathering processes: Assessing controls on Si transfer to the ocean, *C. R. Geosci.*, 344, 723-738 11-12, 10.1016/j.crte.2012.09.006, 2012.
- Orsi, A. H., Whitworth III, T., and Nowlin Jr, W. D.: On the meridional extent and fronts of the Antarctic Circumpolar Current, *Deep-Sea Res. I*, 42, 641-673 5, [http://dx.doi.org/10.1016/0967-0637\(95\)00021-W](http://dx.doi.org/10.1016/0967-0637(95)00021-W), 1995.
- Orsi, A. H., Johnson, G. C., and Bullister, J. L.: Circulation, mixing, and production of Antarctic Bottom Water, *Prog. Oceanogr.*, 43, 55-109 1, [http://dx.doi.org/10.1016/S0079-6611\(99\)00004-X](http://dx.doi.org/10.1016/S0079-6611(99)00004-X), 1999.
- Paasche, E.: Silicon and the ecology of marine plankton diatoms. II. Silicate-uptake kinetics in five diatom species, *Mar. Biol.*, 19, 262-269 3, 10.1007/bf02097147, 1973.
- Park, Y. H., Charriaud, E., Craneguy, P., and Kartavtseff, A.: Fronts, transport, and Weddell Gyre at 30 E between Africa and Antarctica, *Journal of Geophysical Research: Oceans* (1978–2012), 106, 2857-2879 C2, 2001.
- Passow, U., Engel, A., and Ploug, H.: The role of aggregation for the dissolution of diatom frustules, *FEMS Microbiol. Ecol.*, 46, 247-255 3, [http://dx.doi.org/10.1016/S0168-6496\(03\)00199-5](http://dx.doi.org/10.1016/S0168-6496(03)00199-5), 2003.
- Passow, U., French, M. A., and Robert, M.: Biological controls on dissolution of diatom frustules during their descent to the deep ocean: Lessons learned from controlled laboratory experiments, *Deep-Sea Res. I*, 58, 1147-1157 12, <http://dx.doi.org/10.1016/j.dsr.2011.09.001>, 2011.
- Pérez, F. F., Mintrop, L., Llinás, O., Glez-Dávila, M., Castro, C. G., Alvarez, M., Körtzinger, A., Santana-Casiano, M., Rueda, M. J., and Ríos, A. F.: Mixing analysis of nutrients, oxygen and inorganic carbon in

the Canary Islands region, *J. Mar. Syst.*, 28, 183-201 3–4, [http://dx.doi.org/10.1016/S0924-7963\(01\)00003-3](http://dx.doi.org/10.1016/S0924-7963(01)00003-3), 2001.

Platzner, I. T., Habfast, K., Walder, A. J., and Goetz, A.: Modern isotope ratio mass spectrometry, 1997.

Pondaven, P., Fravallo, C., Ruiz-Pino, D., Tréguer, P., Quéguiner, B., and Jeandel, C.: Modelling the silica pump in the Permanently Open Ocean Zone of the Southern Ocean, *J. Mar. Syst.*, 17, 587-619 1–4, [http://dx.doi.org/10.1016/S0924-7963\(98\)00066-9](http://dx.doi.org/10.1016/S0924-7963(98)00066-9), 1998.

Pondaven, P., Ragueneau, O., Tréguer, P., Hauvespre, A., Dezileau, L., and Reyss, J. L.: Resolving the 'opal paradox' in the Southern Ocean, *Nature*, 405, 168-172 6783, 10.1038/35012046, 2000.

Provost, C., Renault, A., Barré, N., Sennéchaël, N., Garçon, V., Sudre, J., and Huhn, O.: Two repeat crossings of Drake Passage in austral summer 2006: Short-term variations and evidence for considerable ventilation of intermediate and deep waters, *Deep-Sea Res. II*, 58, 2555-2571 25–26, <http://dx.doi.org/10.1016/j.dsr2.2011.06.009>, 2011.

Quéguiner, B., Tréguer, P., and Nelson, D. M.: The production of biogenic silica in the Weddell and Scotia Seas, *Mar. Chem.*, 35, 449-459 1–4, [http://dx.doi.org/10.1016/S0304-4203\(09\)90036-6](http://dx.doi.org/10.1016/S0304-4203(09)90036-6), 1991.

Quéguiner, B., Tréguer, P., Pecken, I., and Shareck, R.: Biogeochemical dynamics and the silicon cycle in the Atlantic sector of the Southern Ocean during Austral spring 1992, *Deep-Sea Res.*, 44, 68-89, 1997.

Ragueneau, O., Tréguer, P., Leynaert, A., Anderson, R. F., Brzezinski, M. A., DeMaster, D. J., Dugdale, R. C., Dymond, J., Fischer, G., François, R., Heinze, C., Maier-Reimer, E., Martin-Jézéquel, V., Nelson, D. M., and Quéguiner, B.: A review of the Si cycle in the modern ocean: recent progress and missing gaps in the application of biogenic opal as a paleoproductivity proxy, *Global Planet. Change*, 26, 317-365 4, [http://dx.doi.org/10.1016/S0921-8181\(00\)00052-7](http://dx.doi.org/10.1016/S0921-8181(00)00052-7), 2000.

Ragueneau, O., Schultes, S., Bidle, K., Claquin, P., and Moriceau, B.: Si and C interactions in the world ocean: Importance of ecological processes and implications for the role of diatoms in the biological pump, *Global Biogeochem. Cy.*, 20, GB4S02 4, 10.1029/2006gb002688, 2006.

Raven, J. A.: THE TRANSPORT AND FUNCTION OF SILICON IN PLANTS, *Biological Reviews of the Cambridge Philosophical Society*, 58, 179-207 2, 10.1111/j.1469-185X.1983.tb00385.x, 1983.

Rusciano, E., Speich, S., and Ollitrault, M.: Inter-ocean exchanges and the spreading of Antarctic Intermediate Water south of Africa, *J. Geophys. Res.*, 117, C10010 10.1029/2012jc008266, 2012.

Rutgers van der Loeff, M., Pinghe, H. C., Stimac, I., Bracher, A., Middag, R., Klunder, M. B., and van Heuven, S. M. A. C.: <sup>234</sup>Th in surface waters: Distribution of particle export flux across the Antarctic Circumpolar Current and in the Weddell Sea during the GEOTRACES expedition ZERO and DRAKE, 25-26, Elsevier, Kidlington, Royaume-Uni, 18 pp., 2011.

Sarmiento, J. L., Gruber, N., Brzezinski, M. A., and Dunne, J. P.: High-latitude controls of thermocline nutrients and low latitude biological productivity., *Nature*, 427, 56-60, 2004.

Sarmiento, J. L., Simeon, J., Gnanadesikan, A., Gruber, N., Key, R. M., and Schlitzer, R.: Deep ocean biogeochemistry of silicic acid and nitrate, *Global Biogeochem. Cy.*, 21, GB1S90 1, 10.1029/2006gb002720, 2007.

- Sarthou, G., Timmermans, K. R., Blain, S., and Tréguer, P.: Growth physiology and fate of diatoms in the ocean: a review, *J. Sea Res.*, 53, 25-42 1–2, <http://dx.doi.org/10.1016/j.seares.2004.01.007>, 2005.
- Schmitz, W. J.: On the world ocean circulation: volume 1, Woods Hole Oceanographic Institution, 1996.
- Sicko-Goad, L. M., Schelske, C. L., and Stoermer, E. F.: Estimation of intracellular carbon and silica content of diatoms from natural assemblages using morphometric techniques, *Limnol. Oceanogr.*, 29, 1170-1178 6, 1984.
- Sigman, D. M., Altabet, M. A., McCorkle, D. C., Francois, R., and Fischer, G.: The delta  $^{15}\text{N}$  of nitrate in the Southern Ocean: Consumption of nitrate in surface waters, *Global Biogeochem. Cy.*, 13, 1149-1166 4, 10.1029/1999gb900038, 1999.
- Smayda, T. J.: The suspension and sinking of phytoplankton in the sea, *Oceanogr. Mar. Biol. Ann. Rev.*, 8, 353-414, 1970.
- Smetacek, V., Assmy, P., and Henjes, J.: The role of grazing in structuring Southern Ocean pelagic ecosystems and biogeochemical cycles, *Antarctic Science*, 16, 541–558 4, 10.1017/S0954102004002317, 2004.
- Smethie, W. M., and Fine, R. A.: Rates of North Atlantic Deep Water formation calculated from chlorofluorocarbon inventories, *Deep-Sea Res. I*, 48, 189 - 215, 2001.
- Solomon, H.: Vertical mixed layer convection in the Weddell Sea, *Atmos.-Ocean*, 21, 187-206 2, 10.1080/07055900.1983.9649164, 1983.
- Speer, K., Rintoul, S. R., and Sloyan, B.: The Diabatic Deacon Cell, *J. Phys. Oceanogr.*, 30, 3212-3222 12, 10.1175/1520-0485(2000)030<3212:tddc>2.0.co;2, 2000.
- Sprintall, J., and Tomczak, M.: On the formation of central water and thermocline ventilation in the southern hemisphere, *Deep-Sea Res. I*, 40, 827-848 4, [http://dx.doi.org/10.1016/0967-0637\(93\)90074-D](http://dx.doi.org/10.1016/0967-0637(93)90074-D), 1993.
- Stramma, L., and Schott, F.: The mean flow field of the tropical Atlantic Ocean, *Deep-Sea Res. II*, 46, 279-303 1–2, [http://dx.doi.org/10.1016/S0967-0645\(98\)00109-X](http://dx.doi.org/10.1016/S0967-0645(98)00109-X), 1999.
- Stramma, L., Hüttl, S., and Schafstall, J.: Water masses and currents in the upper tropical northeast Atlantic off northwest Africa, *J. Geophys. Res-Oceans*, 110 C12, 10.1029/2005jc002939, 2005.
- Strickland, J. D. H., and Parsons, T. R.: A practical handbook of seawater analysis, Fish. Res. Board Can., Ottawa, 310 pp., 1972.
- Sudre, J., Garçon, V., Provost, C., Sennéchaël, N., Huhn, O., and Lacombe, M.: Short-term variations of deep water masses in Drake Passage revealed by a multiparametric analysis of the ANT-XXIII/3 bottle data, *Deep-Sea Res. II*, 58, 2592-2612 25–26, <http://dx.doi.org/10.1016/j.dsr2.2011.01.005>, 2011.
- Sullivan, C. W.: Silicification by diatoms in: Silicon biochemistry, Ciba Foundation Symposium 121, Chichester, 59-89, 1986.
- Sunda, W. G., and Huntsman, S. A.: Interrelated influence of iron, light and cell size on marine phytoplankton growth, *Nature*, 390, 389-392, 1997.

- Sutton, J. N., Varela, D. E., Brzezinski, M. A., and Beucher, C. P.: Species-dependent silicon isotope fractionation by marine diatoms, *Geochim. Cosmochim. Acta*, 104, 300-309 0, <http://dx.doi.org/10.1016/j.gca.2012.10.057>, 2013.
- Tegen, I., and Kohfeld, K. E.: Atmospheric transport of silicon, *Scope-scientific committee on problems of the environment international council of scientific unions*, 66, 81, 2006.
- Toggweiler, J. R., Russell, J. L., and Carson, S. R.: Midlatitude westerlies, atmospheric CO<sub>2</sub>, and climate change during the ice ages, *Paleoceanography*, 21, PA2005 2, 10.1029/2005pa001154, 2006.
- Tréguer, P., Nelson, D. M., Van Bennekom, A. J., DeMaster, D. J., Leynaert, A., and Quéguiner, B.: The silica balance in the world ocean: a reestimate, *Science*, 268, 375-379, 1995.
- Tréguer, P. J., and De La Rocha, C. L.: The World Ocean Silica Cycle, *Ann. Rev. Mar. Sci.*, 5, 477-501, 10.1146/annurev-marine-121211-172346, 2013.
- Van Cappellen, P., Dixit, S., and Van Beusekom, J.: Biogenic silica dissolution in the oceans: Reconciling experimental and field-based dissolution rates, 4, American Geophysical Union, Washington, DC, Etats-Unis, 2002.
- van Heuven, S. M., Hoppema, M., Huhn, O., Slagter, H. A., and de Baar, H. J.: Direct observation of increasing CO<sub>2</sub> in the Weddell Gyre along the Prime Meridian during 1973–2008, *Deep-Sea Res. II*, 58, 2613-2635 25, 2011.
- van Wijk, E. M., Rintoul, S. R., Ronai, B. M., and Williams, G. D.: Regional circulation around Heard and McDonald Islands and through the Fawn Trough, central Kerguelen Plateau, *Deep-Sea Res. I*, 57, 653-669 5, <http://dx.doi.org/10.1016/j.dsr.2010.03.001>, 2010.
- Varela, D. E., Pride, C. J., and Brzezinski, M. A.: Biological fractionation of silicon isotopes in Southern Ocean surface waters, *Global Biogeochem. Cy.*, 18, GB1047, 10.1029/2003gb002140, 2004.
- Villareal, T. A.: Positive buoyancy in the oceanic diatom *Rhizosolenia debaryana* H. Peragallo, *Deep-Sea Res.*, 35, 1037-1045 6, [http://dx.doi.org/10.1016/0198-0149\(88\)90075-1](http://dx.doi.org/10.1016/0198-0149(88)90075-1), 1988.
- Well, R., Roether, W., and Stevens, D. P.: An additional deep-water mass in Drake Passage as revealed by <sup>3</sup>He data, *Deep-Sea Res. I*, 50, 1079-1098 9, 2003.
- Weyer, S., and Schwieters, J. B.: High precision Fe isotope measurements with high mass resolution MC-ICPMS, *Int. J. Mass spectrom.*, 226, 355-368 3, [http://dx.doi.org/10.1016/S1387-3806\(03\)00078-2](http://dx.doi.org/10.1016/S1387-3806(03)00078-2), 2003.
- Whitworth III, T.: Zonation and geostrophic flow of the Antarctic circumpolar current at Drake Passage, *Deep-Sea Res.*, 27, 497-507 7, [http://dx.doi.org/10.1016/0198-0149\(80\)90036-9](http://dx.doi.org/10.1016/0198-0149(80)90036-9), 1980.
- Young, E. D., Galy, A., and Nagahara, H.: Kinetic and equilibrium mass-dependent isotope fractionation laws in nature and their geochemical and cosmochemical significance, *Geochim. Cosmochim. Acta*, 66, 1095-1104 6, [http://dx.doi.org/10.1016/S0016-7037\(01\)00832-8](http://dx.doi.org/10.1016/S0016-7037(01)00832-8), 2002.
- Ziegler, K., Chadwick, O. A., Brzezinski, M. A., and Kelly, E. F.: Natural variations of  $\delta^{30}\text{Si}$  ratios during progressive basalt weathering, Hawaiian Islands, *Geochim. Cosmochim. Acta*, 69, 4597-4610 19, <http://dx.doi.org/10.1016/j.gca.2005.05.008>, 2005.



---

# Appendix

---



Appendix 1. Data information about samples from Atlantic sector and the Indian sector of the Southern Ocean during the campaign ANTXXIV/9.

Stations	Date	Latitude	Longitude	Depth (m)	[DSi] ( $\mu\text{M}$ )	$\delta^{30}\text{Si} \pm \sigma$ (‰)	location
CTD1	02/11/07	69°24.03S	7°0.12'W	20	57	1.63 $\pm$ 0.06	Weddell Gyre
CTD1	02/11/07	69°24.03S	7°0.12'W	40	60.4	1.65 $\pm$ 0.0	
CTD1	02/11/07	69°24.03S	7°0.12'W	60	63.1	1.33 $\pm$ 0.03	
CTD1	02/11/07	69°24.03S	7°0.12'W	80	65.8	1.23 $\pm$ 0.08	
CTD1	02/11/07	69°24.03S	7°0.12'W	200	77.8	1.21 $\pm$ 0.07	
CTD1	02/11/07	69°24.03S	7°0.12'W	300	83.9	1.33 $\pm$ 0.06	
CTD1	02/11/07	69°24.03S	7°0.12'W	500	93.4	0.71 $\pm$ 0.0	
CTD1	02/11/07	69°24.03S	7°0.12'W	750	102.3	1.26 $\pm$ 0.08	
CTD1	02/11/07	69°24.03S	7°0.12'W	1000	106.5	1.17 $\pm$ 0.03	
CTD1	02/11/07	69°24.03S	7°0.12'W	1250	116.7	1.01 $\pm$ 0.0	
CTD1	02/11/07	69°24.03S	7°0.12'W	1500	114.4	1.18 $\pm$ 0.0	
CTD1	02/11/07	69°24.03S	7°0.12'W	1750	115.7	0.99 $\pm$ 0.07	
CTD1	02/11/07	69°24.03S	7°0.12'W	2000	117.2	1.08 $\pm$ 0.06	
CTD1	02/11/07	69°24.03S	7°0.12'W	2250	119.9	1.30 $\pm$ 0.01	
CTD4	02/24/07	68°43.34'S	70°40.66'E	20	36.8	2.13 $\pm$ 0.02	Prydz Bay
CTD4	02/24/07	68°43.34'S	70°40.66'E	40	48.8	1.71 $\pm$ 0.02	
CTD4	02/24/07	68°43.34'S	70°40.66'E	60	52.8	–	
CTD4	02/24/07	68°43.34'S	70°40.66'E	80	55.3	–	
CTD4	02/24/07	68°43.34'S	70°40.66'E	200	57.7	1.60 $\pm$ 0.02	
CTD4	02/24/07	68°43.34'S	70°40.66'E	500	58.7	–	
CTD6	03/21/07	65°20.98'S	82°39.48'E	20	53.5	1.44 $\pm$ 0.0	Prydz Bay
CTD6	03/21/07	65°20.98'S	82°39.48'E	40	50.2	1.42 $\pm$ 0.04	
CTD6	03/21/07	65°20.98'S	82°39.48'E	60	54	1.18 $\pm$ 0.06	
CTD6	03/21/07	65°20.98'S	82°39.48'E	80	57.3	1.13 $\pm$ 0.0	
CTD6	03/21/07	65°20.98'S	82°39.48'E	200	64.9	1.59 $\pm$ 0.03	
CTD6	03/21/07	65°20.98'S	82°39.48'E	500	88.1	1.35 $\pm$ 0.07	

Stations	Date	Latitude	Longitude	Depth (m)	[DSi] ( $\mu\text{M}$ )	$\delta^{30}\text{Si} \pm \sigma$ (‰)	location
CTD5	03/02/07	60°56.97'S	72°43.30'E	30	20.2	2.21 $\pm$ 0.08	Antarctic Circumpolar Current
CTD5	03/02/07	60°56.97'S	72°43.30'E	40	21.6		
CTD5	03/02/07	60°56.97'S	72°43.30'E	60	37.5	–	
CTD5	03/02/07	60°56.97'S	72°43.30'E	80	39.6	1.62 $\pm$ 0.06	
CTD5	03/02/07	60°56.97'S	72°43.30'E	200	72.9	1.25 $\pm$ 0.03	
CTD5	03/02/07	60°56.97'S	72°43.30'E	500	81.4	1.20 $\pm$ 0.04	
CTD5	03/02/07	60°56.97'S	72°43.30'E	1000	82	1.07 $\pm$ 0.03	
CTD5	03/02/07	60°56.97'S	72°43.30'E	1500	97.9	0.96 $\pm$ 0.05	
CTD5	03/02/07	60°56.97'S	72°43.30'E	2000	106.9	1.12 $\pm$ 0.0	
CTD5	03/02/07	60°56.97'S	72°43.30'E	2500	120.7	0.92 $\pm$ 0.07	
CTD5	03/02/07	60°56.97'S	72°43.30'E	3000	121.2	1.04 $\pm$ 0.0	
CTD5	03/02/07	60°56.97'S	72°43.30'E	3500	122.1	1.10 $\pm$ 0.05	
CTD5	03/02/07	60°56.97'S	72°43.30'E	4000	125.4	1.20 $\pm$ 0.0	
CTD7	03/24/07	59°37.25'S	85°40.52'E	20	28.1	1.90 $\pm$ 0.15	South of Antarctic Circumpolar Current
CTD7	03/24/07	59°37.25'S	85°40.52'E	40	41.5	2.21 $\pm$ 0.09	
CTD7	03/24/07	59°37.25'S	85°40.52'E	60	55.3	1.32 $\pm$ 0.06	
CTD7	03/24/07	59°37.25'S	85°40.52'E	80	60.9	1.53 $\pm$ 0.	
CTD7	03/24/07	59°37.25'S	85°40.52'E	200	76.2	1.25 $\pm$ 0.	
CTD7	03/24/07	59°37.25'S	85°40.52'E	500	88.1	1.44 $\pm$ 0.0	
CTD7	03/24/07	59°37.25'S	85°40.52'E	1000	94.2	–	
CTD7	03/24/07	59°37.25'S	85°40.52'E	1500	117.3	–	
CTD7	03/24/07	59°37.25'S	85°40.52'E	2000	120.8	–	
CTD7	03/24/07	59°37.25'S	85°40.52'E	2500	118.5	–	
CTD7	03/24/07	59°37.25'S	85°40.52'E	3000	118.1	–	
CTD7	03/24/07	59°37.25'S	85°40.52'E	3500	119.6	–	
CTD8	03/26/07	55°0.30'S	73°19.98'E	20	11.6	2.39 $\pm$ 0.06	Kerguelen Plateau
CTD8	03/26/07	55°0.30'S	73°19.98'E	40	11.7	2.20 $\pm$ 0.07	
CTD8	03/26/07	55°0.30'S	73°19.98'E	60	11.4	1.99 $\pm$ 0.0	
CTD8	03/26/07	55°0.30'S	73°19.98'E	80	31.5	0.94 $\pm$ 0.02	
CTD8	03/26/07	55°0.30'S	73°19.98'E	500	66.8	1.40 $\pm$ 0.0	
CTD8	03/26/07	55°0.30'S	73°19.98'E	1500	82.4	1.57 $\pm$ 0.02	

**Appendix 2. Data information about samples from the Atlantic sector of the Southern Ocean (ANTXXIV/3 campaign, stations 146 to 248) and for samples from the Subtropical and Tropical North Atlantic Ocean (MSM10/1 campaign, stations 1 to 21) used in this thesis.**

Stations	Date	Latitude	Longitude	Depth (m)	S (psu)	T (°C)	[DSi] (μM)	δ30Si ± σ (‰)	water mass	location
146	02/28/08	63°30.02'S	0°0.04'W	10	33.96	0.57	47.90	2.29 ± 0.12	AASW	0° meridian Weddell Gyre
146	02/28/08	63°30.02'S	0°0.04'W	25	33.97	0.45	48.32	–	AASW	
146	02/28/08	63°30.02'S	0°0.04'W	50	34.18	-1.67	56.84	1.64 ± 0.06	AASW	
146	02/28/08	63°30.02'S	0°0.04'W	75	34.26	-1.71	67.53	–	AASW	
146	02/28/08	63°30.02'S	0°0.04'W	100	34.40	-0.98	81.88	1.91 ± 0.02	AASW	
146	02/28/08	63°30.02'S	0°0.04'W	200	34.66	0.56	109.86	1.88 ± 0.13	UCDW	
146	02/28/08	63°30.02'S	0°0.04'W	500	34.69	0.46	121.00	1.37 ± 0.01	WDW	
146	02/28/08	63°30.02'S	0°0.04'W	1000	34.68	0.23	128.30	1.46 ± 0.08	WDW	
146	02/28/08	63°30.02'S	0°0.04'W	1500	34.67	0.04	128.66	1.44 ± 0.05	WDW	
146	02/28/08	63°30.02'S	0°0.04'W	2000	34.67	-0.12	128.30	1.45 ± 0.03	WSDW	
146	02/28/08	63°30.02'S	0°0.04'W	2500	34.66	-0.21	126.53	1.12 ± 0.03	WSDW	
146	02/28/08	63°30.02'S	0°0.04'W	3000	34.66	-0.29	126.53	1.06 ± 0.10	WSDW	
146	02/28/08	63°30.02'S	0°0.04'W	3500	34.66	-0.34	127.24	1.42 ± 0.05	WSDW	
146	02/28/08	63°30.02'S	0°0.04'W	4000	34.65	-0.38	125.83	± 0.07	WSDW	
146	02/28/08	63°30.02'S	0°0.04'W	4500	34.65	-0.44	122.36	1.05 ± 0.16	AABW	
146	02/28/08	63°30.02'S	0°0.04'W	5000	34.66	-0.42	124.43	1.07 ± 0.03	AABW	
189	03/16/08	67°59.20'S	20°2.06'W	10	33.85	-1.83	69.09	1.64 ± 0.05	ASW	Weddell Gyre
189	03/16/08	67°59.20'S	20°2.06'W	25	33.85	-1.84	72.25	2.25 ± 0.07	ASW	
189	03/16/08	67°59.20'S	20°2.06'W	50	34.36	-1.63	75.72	1.62 ± 0.06	LSSW	
189	03/16/08	67°59.20'S	20°2.06'W	75	34.47	-1.66	77.74	1.36 ± 0.05	LSSW	
189	03/16/08	67°59.20'S	20°2.06'W	100	34.49	-1.49	79.79	1.61 ±	MWDW	
189	03/16/08	67°59.20'S	20°2.06'W	200	34.64	0.1	101.94	1.48 ± 0.06	WDW	
189	03/16/08	67°59.20'S	20°2.06'W	500	34.69	0.55	122.31	1.30 ± 0.04	WDW	
189	03/16/08	67°59.20'S	20°2.06'W	1000	34.68	0.28	128.91	1.49 ± 0.07	WDW	
189	03/16/08	67°59.20'S	20°2.06'W	1500	34.67	0.08	129.62	1.47 ± 0.02	WDW	
189	03/16/08	67°59.20'S	20°2.06'W	2000	34.67	-0.08	130.70	1.19 ± 0.05	WSDW	
189	03/16/08	67°59.20'S	20°2.06'W	2500	34.66	-0.18	128.56	1.22 ± 0.03	WSDW	
189	03/16/08	67°59.20'S	20°2.06'W	3000	34.66	-0.25	125.75	1.17 ± 0.04	WSDW	
189	03/16/08	67°59.20'S	20°2.06'W	3500	34.66	-0.29	127.15	0.97 ± 0.24	WSDW	

189	03/16/08	67°59.20'S	20°2.06'W	4600	34.66	-0.31	127.85	1.16 ± 0.09	WSBW	
Stations	Date	Latitude	Longitude	Depth (m)	S (psu)	T (°C)	[DSi] (μM)	δ30Si ± σ (‰)	water mass	location
106	02/18/08	48°54.68'S	2°48.11'E	75	33.76	5.24	6.43	2.07 ± 0.04	SSW	0° meridian Antarctic Circumpolar Current
106	02/18/08	48°54.68'S	2°48.11'E	100	33.76	5.13	6.66	2.05 ± 0.02	SSW	
106	02/18/08	48°54.68'S	2°48.11'E	200	33.93	2.55	18.81	1.67 ± 0.12	AAIW	
106	02/18/08	48°54.68'S	2°48.11'E	500	34.31	2.6	50.46	1.30 ± 0.14	UCDW	
106	02/18/08	48°54.68'S	2°48.11'E	1000	34.61	2.41	75.17	1.21 ± 0.14	UCDW	
106	02/18/08	48°54.68'S	2°48.11'E	1500	34.75	2.33	72.41	1.33 ± 0.07	UCDW	
106	02/18/08	48°54.68'S	2°48.11'E	2000	34.77	1.93	79.53	1.49 ± 0.01	NADW/LDCW	
106	02/18/08	48°54.68'S	2°48.11'E	2500	34.72	1.25	103.66	—	NADW/LDCW	
106	02/18/08	48°54.68'S	2°48.11'E	3000	34.70	0.84	115.66	1.48 ± 0.04	NADW/LDCW	
106	02/18/08	48°54.68'S	2°48.11'E	3500	34.69	0.64	123.05	1.06 ± 0.08	WDW	
106	02/18/08	48°54.68'S	2°48.11'E	4000	34.69	0.62	125.48	1.10 ± 0.04	WDW	
115	02/21/08	53°31.25'S	0°0.10'E	25	33.80	1.26	38.25	1.34 ± 0.06	AASW	0° meridian Antarctic Circumpolar Current
115	02/21/08	53°31.25'S	0°0.10'E	50	33.80	1.22	39.04	1.79 ± 0.09	AASW	
115	02/21/08	53°31.25'S	0°0.10'E	75	33.80	1.21	38.64	1.68 ± 0.03	AASW	
115	02/21/08	53°31.25'S	0°0.10'E	100	33.81	1.19	39.85	1.62 ± 0.01	AASW	
115	02/21/08	53°31.25'S	0°0.10'E	200	34.41	1.04	77.97	1.48 ± 0.03	AAIW	
115	02/21/08	53°31.25'S	0°0.10'E	500	34.67	1.63	92.25	1.09 ± 0.16	UCDW	
115	02/21/08	53°31.25'S	0°0.10'E	1000	34.71	1.36	103.66	1.40 ± 0.05	LCDW	
248	04/08/08	56°25.10'S	63°18.63'W	200	34.09	2.62	20.47	2.13 ± 0.07	WW	Drake Passage Antarctic Circumpolar Current
248	04/08/08	56°25.10'S	63°18.63'W	500	34.28	2.6	44.49	1.31 ± 0.10	AAIW	
248	04/08/08	56°25.10'S	63°18.63'W	750	34.44	2.56	61.35	1.18 ± 0.09	AAIW	
248	04/08/08	56°25.10'S	63°18.63'W	1000	34.55	2.38	72.25	1.59 ± 0.03	SPDSW	
248	04/08/08	56°25.10'S	63°18.63'W	1500	34.68	2.11	87.18	1.40 ± 0.06	SPDSW	
248	04/08/08	56°25.10'S	63°18.63'W	2100	34.72	1.73	101.94	1.38 ± 0.03	UCDW	
248	04/08/08	56°25.10'S	63°18.63'W	2400	34.72	1.49	103.74	1.07 ± 0.08	UCDW	
248	04/08/08	56°25.10'S	63°18.63'W	2700	34.72	1.27	111.47	1.00 ± 0.11	UCDW	
248	04/08/08	56°25.10'S	63°18.63'W	3000	34.71	1.05	119.27	1.04 ± 0.03	LCDW	
248	04/08/08	56°25.10'S	63°18.63'W	3500	34.70	0.81	121.97	1.26 ± 0.02	SPDW	
248	04/08/08	56°25.10'S	63°18.63'W	3941	34.69	0.61	122.31	1.13 ± 0.10	SPDW	

Stations	Date	Latitude	Longitude	Depth (m)	S (psu)	T (°C)	[DSi] (μM)	δ30Si ± σ (‰)	water mass	location
211	03/26/08	63°55.44'S	48°38.73'W	10	33.78	-1.83	83.71	1.56 ± 0.08	ASW	Weddell Gyre
211	03/26/08	63°55.44'S	48°38.73'W	30	33.79	-1.82	82.65	1.25 ± 0.05	ASW	
211	03/26/08	63°55.44'S	48°38.73'W	50	34.34	-1.68	88.54	1.71 ± 0.02	LSSW	
211	03/26/08	63°55.44'S	48°38.73'W	75	34.45	-1.63	90.47	1.81 ± 0.04	LSSW	
211	03/26/08	63°55.44'S	48°38.73'W	100	34.49	-1.4	89.64	1.42 ± 0.03	MWDW	
211	03/26/08	63°55.44'S	48°38.73'W	200	34.64	0.22	105.56	1.31 ± 0.03	WDW	
211	03/26/08	63°55.44'S	48°38.73'W	500	34.68	0.5	114.35	–	WDW	
211	03/26/08	63°55.44'S	48°38.73'W	750	34.69	0.43	121.97	–	WDW	
211	03/26/08	63°55.44'S	48°38.73'W	1000	34.68	0.3	126.10	1.23 ± 0.06	WDW	
211	03/26/08	63°55.44'S	48°38.73'W	1500	34.67	0.05	127.85	1.54 ± 0.04	WDW	
211	03/26/08	63°55.44'S	48°38.73'W	2000	34.67	-0.09	124.71	1.33 ± 0.11	WSDW	
211	03/26/08	63°55.44'S	48°38.73'W	2500	34.66	-0.19	126.80	1.53 ± 0.02	WSDW	
211	03/26/08	63°55.44'S	48°38.73'W	3000	34.66	-0.23	126.10	1.41 ± 0.05	WSDW	
211	03/26/08	63°55.44'S	48°38.73'W	3250	34.66	-0.26	125.05	1.05 ± 0.06	WSDW	
211	03/26/08	63°55.44'S	48°38.73'W	3547	34.63	-0.59	106.48	0.89 ± 0.05	MWDW	
211	03/26/08	63°55.44'S	48°38.73'W	3697	34.61	-0.99	84.50	1.41 ± 0.11	MWDW	
226	04/01/08	60°37.59'S	53°49.88'W	10	34.35	0.54	78.25	1.39 ± 0.05	AASW	Drake Passage
226	04/01/08	60°37.59'S	53°49.88'W	25	34.35	0.55	78.76	1.18 ± 0.06	AASW	
226	04/01/08	60°37.59'S	53°49.88'W	50	34.35	0.53	77.49	1.75 ± 0.08	AASW	
226	04/01/08	60°37.59'S	53°49.88'W	75	34.39	0.36	79.02	1.50 ± 0.06	AASW	
226	04/01/08	60°37.59'S	53°49.88'W	100	34.40	0.33	79.02	1.47 ± 0.08	AASW	
226	04/01/08	60°37.59'S	53°49.88'W	200	34.45	0.35	82.92	1.52 ± 0.02	AASW	
226	04/01/08	60°37.59'S	53°49.88'W	500	34.59	0.43	91.02	1.76 ± 0.04	LCDW	
226	04/01/08	60°37.59'S	53°49.88'W	750	34.67	0.53	103.74	1.62 ± 0.06	LCDW	
226	04/01/08	60°37.59'S	53°49.88'W	1000	34.68	0.63	110.21	1.13 ± 0.05	LCDW	
226	04/01/08	60°37.59'S	53°49.88'W	1500	34.67	0.47	123.67	1.15 ± 0.02	LCDW	
226	04/01/08	60°37.59'S	53°49.88'W	2000	34.66	0.2	118.28	1.12 ± 0.04	WSDW	
226	04/01/08	60°37.59'S	53°49.88'W	2500	34.66	0	113.70	1.26 ± 0.09	WSDW	
226	04/01/08	60°37.59'S	53°49.88'W	2699	34.66	-0.03	118.61	1.22 ± 0.27	WSDW	

Stations	Date	Latitude	Longitude	Depth (m)	S (psu)	T (°C)	[DSi] (μM)	$\delta^{30}\text{Si} \pm \sigma$ (‰)	water mass	location
1	11/02/08	28°42.03'N	26°19.95'W	100	36.88	20.37	3.17	—	SMW	Subtropical North Atlantic Ocean north Cape Verde Frontal Zone
1	11/02/08	28°42.03'N	26°19.95'W	200	36.55	17.81	4.13	—	SMW	
1	11/02/08	28°42.03'N	26°19.95'W	400	35.93	12.71	5.88	—	wNACW	
1	11/02/08	28°42.03'N	26°19.95'W	700	35.51	10.1	11.61	$1.31 \pm 0.07$	wNACW	
1	11/02/08	28°42.03'N	26°19.95'W	1000	35.36	8.14	17.55	$1.36 \pm 0.04$	wNACW	
1	11/02/08	28°42.03'N	26°19.95'W	1500	35.28	5.98	24.09	$1.26 \pm 0.12$	wNACW	
1	11/02/08	28°42.03'N	26°19.95'W	2000	35.10	4.3	20.52	$1.53 \pm 0.08$	ASIW	
2	11/04/08	24°37.12'N	26°39.42'W	45	37.329	24.1	3.02	—	SMW	Subtropical North Atlantic Ocean north Cape Verde Frontal Zone
2	11/04/08	24°37.12'N	26°39.42'W	100	37.172	21.03	3.17	—	SMW	
2	11/04/08	24°37.12'N	26°39.42'W	200	36.662	18.27	3.97	—	wNACW	
2	11/04/08	24°37.12'N	26°39.42'W	400	35.897	13.87	6.69	—	wNACW	
2	11/04/08	24°37.12'N	26°39.42'W	700	35.361	9.79	15.83	—	wNACW	
2	11/04/08	24°37.12'N	26°39.42'W	1000	35.141	7.07	21.94	$1.70 \pm 0.07$	ASIW	
2	11/04/08	24°37.12'N	26°39.42'W	1500	35.164	5.36	22.65	$1.37 \pm 0.06$	ASIW	
2	11/04/08	24°37.12'N	26°39.42'W	2000	35.053	4.02	26.82	$1.12 \pm 0.37$	ASIW	
3	11/04/08	19°33.88'N	27°1.80'W	35	36.719	25.28	3.10	—	SMW	Subtropical North Atlantic Ocean north Cape Verde Island
3	11/04/08	19°33.88'N	27°1.80'W	100	37.083	21.22	3.49	—	SMW	
3	11/04/08	19°33.88'N	27°1.80'W	200	36.169	16.06	7.17	—	SMW	
3	11/04/08	19°33.88'N	27°1.80'W	400	35.591	12.37	12.28	—	wNACW	
3	11/04/08	19°33.88'N	27°1.80'W	700	35.113	8.3	21.23	$1.73 \pm 0.05$	ASIW	
3	11/04/08	19°33.88'N	27°1.80'W	1000	34.995	6.26	24.81	$1.82 \pm 0.04$	ASIW	
3	11/04/08	19°33.88'N	27°1.80'W	1500	35.034	4.63	25.36	$1.45 \pm 0.09$	ASIW	
3	11/04/08	19°33.88'N	27°1.80'W	2000	34.985	3.61	28.85	$2.02 \pm 0.09$	ASIW	
4	11/05/08	13°29.99'N	27°30'W	45	35.882	20.81	5.08	—	SACW	Tropical North Atlantic Ocean south Cape Verde Frontal Zone
4	11/05/08	13°29.99'N	27°30'W	100	35.503	13.75	10.78	—	SACW	
4	11/05/08	13°29.99'N	27°30'W	200	35.213	11.71	12.61	—	SACW	
4	11/05/08	13°29.99'N	27°30'W	400	35.131	10.37	17.21	—	SACW	
4	11/05/08	13°29.99'N	27°30'W	700	34.907	7.72	24.45	—	SACW	
4	11/05/08	13°29.99'N	27°30'W	1000	34.899	6.08	27.56	$1.16 \pm 0.07$	SACW	
4	11/05/08	13°29.99'N	27°30'W	1500	34.978	4.44	24.27	—	NADW	

Stations	Date	Latitude	Longitude	Depth (m)	S (psu)	T (°C)	[DSi] (μM)	δ30Si ± σ (‰)	water mass	location
21	11/08/08	7°30.21'N	24°59.81'W	50	35.966	25.91	3.36	–	SACW	
21	11/08/08	7°30.21'N	24°59.81'W	100	35.682	16.25	7.23	1.53 ± 0.05	SACW	
21	11/08/08	7°30.21'N	24°59.81'W	200	35.507	13.14	9.12	–	SACW	Tropical North
21	11/08/08	7°30.21'N	24°59.81'W	310	35.092	11.37	11.23	–	SACW	Altantic Ocean
21	11/08/08	7°30.21'N	24°59.81'W	410	34.986	10.09	14.72	–	SACW	south Cape
21	11/08/08	7°30.21'N	24°59.81'W	800	34.668	5.57	27.89	–	AAIW	Verde Frontal
21	11/08/08	7°30.21'N	24°59.81'W	1200	34.852	4.72	25.51	1.42 ± 0.03	AAIW	Zone
21	11/08/08	7°30.21'N	24°59.81'W	1600	34.964	4.11	20.62	–	NADW	
21	11/08/08	7°30.21'N	24°59.81'W	2000	34.958	3.54	22.87	–	NADW	

---

## Participation at conferences

---



## $\delta^{30}\text{Si}$ of DSi in the Atlantic and Indian Sectors of the Southern Ocean

Coffineau N.<sup>1\*</sup>, De La Rocha C.L.<sup>1</sup>, Bescont P., Croguennoc A. and Ponzevera E.<sup>2</sup>

<sup>1</sup> 6539, LEMAR, IUEM, Université de Bretagne Occidentale,  
Technopôle Brest-Iroise, Place Nicolas Copernic, 29280 Plouzané, France  
<sup>2</sup> IFREMER, Dept Geosciences Marines, Pointe du Diable, Plouzané, France

\* Corresponding author  
Phone: +33-(0)- 2 9849 8660  
E-mail: nathalie.coffineau@univ-brest.fr

### Introduction:

Because of its large size and High Nutrient, Low Chlorophyll status (i.e. potential for further productivity and nutrient and carbon dioxide draw down), reconstructing nutrient cycling in the Southern Ocean of the past has been a prime focus of many paleoceanographic studies. Our confidence in reconstructions of the cycling of silica in surface waters, which are based on the silicon isotopic composition ( $\delta^{30}\text{Si}$ ) of diatom silica that has accumulated in the sediments, would be enhanced by a better understanding of the distribution and behavior of Si isotopes in the modern day Southern Ocean.

We know that during the uptake of dissolved silicon (DSi) for the production of biogenic silica (BSi), diatoms discriminate against the heavier isotopes of silicon in favor of the lightest one ( $^{28}\text{Si}$ ). This fractionation is on the order of -1.1 ‰ to -1.5 ‰ and results in surface waters with low concentrations of DSi due to biological removal having as well high values of  $\delta^{30}\text{Si}$  due to Rayleigh distillation. At the same time, episodes of upwelling occurring throughout the growing season, ocean circulation and mixing, and the fractionation of silicon isotopes during BSi dissolution all complicate the use of diatom  $\delta^{30}\text{Si}$  as a proxy for DSi removal during the growing season. This is especially true in the Southern Ocean, which is split into Atlantic, Pacific, and Indian Ocean sectors, is fractionated into several circumpolar zones by numerous fronts, and is where the deep waters of the world meet (and, in places, form).

In this study, we attempt to shed light on this complexity through a series of depth profiles and a surface water transect of  $\delta^{30}\text{Si}$  of DSi in the Indian sector (offshore and Kerguelen plateau) and the Atlantic sector of the Southern Ocean.

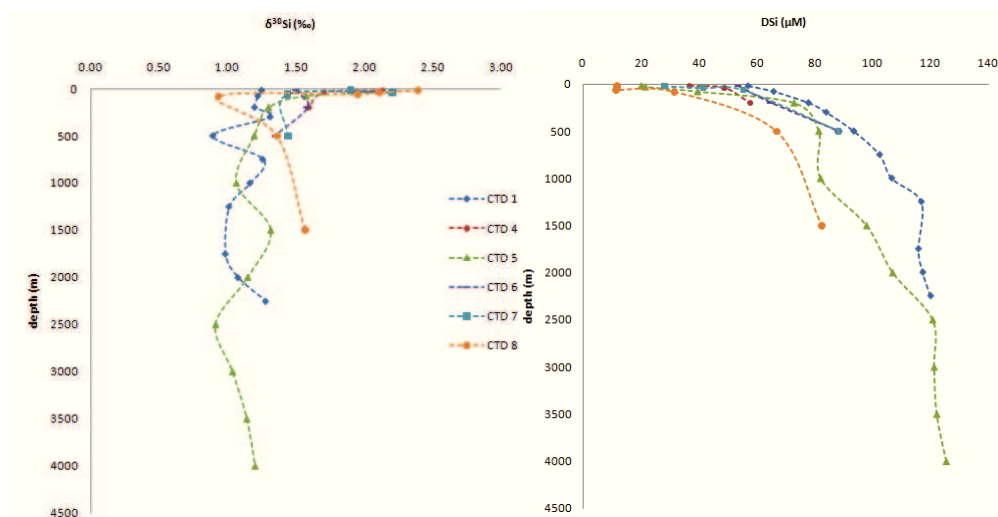
### Methods:

Seawater samples were collected between February and March 2007 during cruise ANTXXIII/9 for the Indian sector (6 CTD profiles) and the Atlantic sector (42 surface water samples) of the Southern Ocean, respectively. Samples were purified by ion-exchange chromatography following either preconcentration via  $\text{Mg}(\text{OH})_2$  precipitation or extraction using TEA-moly. Isotopic analyses were carried on a Neptune MC-ICP-MS at medium resolution.

### Results:

In general,  $\delta^{30}\text{Si}$  varied inversely with DSi concentration, as expected (c.f. fig.1). Values of  $\delta^{30}\text{Si}$  ranged from +0.9 to +2.4 ‰ in surface waters and from +0.9 to +1.6 ‰ in waters deeper than 200 m.

**Figure 1:** DSi and  $\delta^{30}\text{Si}$  in the CTD profiles.



### Discussion:

In the 42 surface water samples, which spanned a range in DSi concentration of  $50 \mu\text{mol L}^{-1}$ ,  $\delta^{30}\text{Si}$  generally increased with decreasing DSi, supporting the use of  $\delta^{30}\text{Si}$  as a proxy for DSi removal and suggesting isotope fractionation on the order of -1.4 ‰. The vertical profiles and surface samples from the Kerguelen Plateau, however, had lower  $\delta^{30}\text{Si}$  than expected given their DSi concentrations, potentially reflecting damping due to isotope fractionation during the dissolution of biogenic silica. As a whole, the surface water and vertical profile data are a good match for previous Southern Ocean data, both filling gaps in our map of the Si isotopic composition of the modern Southern Ocean, and confirming other published results in areas where there is overlap.

Behavior of Silicon Isotopes ( $\delta^{30}\text{Si}$ ) of dissolved Si in the Atlantic and Indian  
Sectors of the Southern Ocean

COFFINEAU N<sup>1</sup>, DE LA ROCHA C. L<sup>1</sup>, BESCONT P, CROGUENOC A AND PONZEVEIRA E<sup>2</sup>

<sup>1</sup> UMR 6539, LEMAR, IUEM, Université de Bretagne Occidentale, Technopôle Brest-Iroise, Place Nicolas Copernic, 29280 Plouzané, France

<sup>2</sup> IFREMER, Dept Geosciences Marines, Pointe du Diable, Plouzané, France

Silicon isotopes are a paleoceanographic proxy whose use in the Southern Ocean would be improved by a more detailed understanding of the distribution and behavior of these isotopes in the modern day Atlantic and Indian sectors. We report here the silicon isotopic composition ( $\delta^{30}\text{Si}$ ) of dissolved silicon (DSi) from 42 surface water samples, spanning the Drake Passage to the Kerguelen Plateau and the Atlantic Polar Front to the edge of the shelf ice, taken between the beginning of February and the end of March 2007. We also report results from 6 CTD profiles taken during the cruise. The  $\delta^{30}\text{Si}$  of DSi in surface waters were strongly correlated to DSi concentrations, supporting the use of  $\delta^{30}\text{Si}$  as a proxy for DSi removal. The “open system” fractionation observed,  $\epsilon = -1.4 \text{ ‰}$ , agree well with results from previous work in other areas. The estimate of the initial  $\delta^{30}\text{Si}$  of DSi of  $+1.4 \text{ ‰}$  matches observations of the  $\delta^{30}\text{Si}$  of DSi in deep waters in the CTD profiles and in the Pacific sector. Using these values gave reasonable estimates for DSi draw down in the past from the  $\delta^{30}\text{Si}$  of sediment cores. However, isotopic fractionation during silica dissolution appeared to influence the  $\delta^{30}\text{Si}$  of some surface water samples, inviting further study of this phenomenon.



# The silicon isotopic composition ( $\delta^{30}\text{Si}$ ) of water masses in the Atlantic Ocean



Nathalie Coffineau<sup>(1)</sup>, C.L. De La Rocha<sup>(1)</sup>, C. Schlosser<sup>(2)</sup>, D.A. Wolf-Gladrow<sup>(3)</sup>

(1) LEMAR-UMR 6539, Institut Universitaire Européen de la Mer, Place Nicolas Copernic, 29280 Plouzané, France

(2) National Oceanography Center, Southampton, UK

(3) Alfred Wegener Institute for Marine & Polar Research, Bremerhaven, Germany

nathalie.coffineau@univ-brest.fr; +33 (0)2 98 49 86 60

Ifremer

## Introduction

Use of silicon isotopes ( $\delta^{30}\text{Si}$ ) as a paleoceanographic proxy requires sound knowledge of the distribution and behaviour of silicon isotopes. Over the past few years considerable effort has been made to map the silicon isotope composition ( $\delta^{30}\text{Si}$ ) of silicic acid (dissolved silicon, DSi) and biogenic silica (BSi) in the ocean.

We present here new data for the  $\delta^{30}\text{Si}$  of DSi of water masses in the South Atlantic and eastern North Atlantic. These data include transects from the Drake Passage to the Weddell Gyre, through the Antarctic Circumpolar Current, and through the oxygen minimum zone in the tropical eastern North Atlantic.

## Objectives:

To increase our understanding of the distribution of Si isotopes in major Atlantic water masses and the evolution of  $\delta^{30}\text{Si}$  as these water masses travel through the Atlantic Ocean and are subjected to mixing and biogeochemical processes.

## Study Areas

### Samples come from 2 campaigns

- the Zero and Drake campaign in the Southern Ocean (February - April 2008) from Punta Arenas (Chili) to Cape Town (South Africa)
- the MSM/10-1 campaign for the Tropical Atlantic Ocean (October - December 2008) from Ponta Delgada (Azores) to Mindelo (Cape Verde) to sample the Oxygen Minimum Zone (OMZ).

### And from 3 zones

#### Antarctic Circumpolar Current

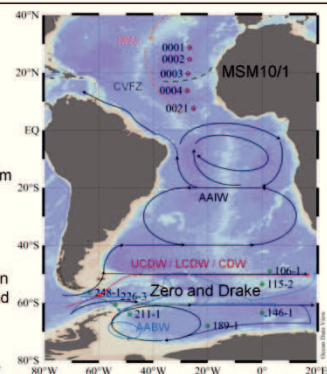
The ACC is a large volume, circumpolar flow of cold and well-mixed water combining and redistributing deep and intermediate waters from all the major ocean basins. The ACC enters the Atlantic Sector of the Southern Ocean from the Pacific Sector through the constriction of the Drake Passage.

#### Weddell Gyre

The cyclonic Weddell Gyre sits to the south of the ACC, in the lee of the Antarctic Peninsula, and its subsurface waters have not been previously sampled for Si isotopes. It is also the main source of Antarctic Bottom Water (AABW). The main inflow is deep water located on the east side that becomes incorporated in the gyre and the outflow occurs on the western side at the Scotia Ridge. Continental slope and shelf waters also contribute to Weddell Sea water masses.

#### Tropical Oxygen Minimum Zone

The oxygen minimum zone is located offshore of west Africa, south of the Cape Verde Islands, in central and intermediate water masses. The OMZ zone is characterised by the Cape Verde Frontal Zone (CVFZ) serves as a boundary between the North Atlantic Central Water (NACW) and the South Atlantic Central Water (SACW). Both upwelling and downwelling of water occur, further complicating circulation in this region.



---

# Curriculum Vitae

---

<i>Name</i>	Nathalie Carole Coffineau
<i>Date of Birth</i>	5 <sup>th</sup> January 1984
<i>Place of birth</i>	Montmorency, France
<i>Nationality</i>	French

## Education

<i>2013</i>	<b>PhD</b> in marine geochemistry, University of Brest (France)
<i>2008</i>	<b>M.Sc.</b> in marine biology and ecology, University of Brest (France)
<i>2006</i>	<b>B.Sc.</b> in organisms and population biology, University of Brest (France)

## Work Experience

<i>2009 – 2010</i>	6 months research internship, Maurice-Lamontagne Institute, (Canada) Work on marine mammal's ecology supervised by Dr V. Lesage
<i>2009</i>	6 months research internship, Mediterranean and Tropical Halieutic Research Center - IRD (France) ➤ Ménard, F., Benivary, H. D., Bodin, N., <b>Coffineau, N.</b> , Le Loc'h, F., Mison, T., and Potier, M. (2013). Stable isotope patterns in micronekton from the Mozambique Channel. <i>Deep Sea Research Part II: Topical Studies in Oceanography</i> , 100, 153-163.
<i>2008</i>	<b>M.Sc.</b> research internship, Laboratoire d'Observation de Villefranche (LOV) - CNRS (France) ▪ Thesis title: " <i>The role of lipids in winter survival and breeding strategies in copepods of the sub-Antarctic area. Case of multi-generational species. Drepanopus pectinatus</i> " supervised by Dr P. Mayzaud <b>M.Sc.</b> research internship, Chizé Centre for Biological Studies (CEBC) - CNRS (France) ▪ Thesis title: " <i>Estimate of the Sperm whale population which interacts with Patagonian toothfish fisheries, in Crozet Archipelagos</i> " supervised by Dr C. Guinet
<i>2006</i>	1.5 months research internship, Laboratory of Marine Environmental Sciences, (LEMAR) - CNRS (France) ▪ " <i>Effect of co-culture with copepods Calanus helgolandicus on the rate of silicification of the diatom Thalassiosira weissflogii</i> " supervised by Dr P. Pondaven